A STUDY OF PARAMETER MEASUREMENT IN A LONG-BASELINE NEUTRINO OSCILLATION EXPERIMENT

David Anthony Petyt

The Queen's College

A thesis submitted for the degree of Doctor of Philosophy

at the University of Oxford, Hilary Term, 1998.

Abstract

This thesis presents a study of the capability of the proposed MINOS long-baseline neutrino experiment to measure the neutrino mixing parameters, if oscillations are assumed to occur with the parameters suggested by the results of atmospheric neutrino experiments.

It is shown that the observation of a neutrino energy dependent suppression of ν_μ events in MINOS could provide a measurement of the mixing parameters to greater than 10% accuracy for $0.005 < \Delta m^2 < 0.2$ eV^2 if $\sin^2 2\theta \geq 0.7$. The performance of a putative low energy beam for MINOS has been studied and it is shown that this beam could allow neutrino oscillations to be observed in MINOS above $\Delta m^2 = 0.002$ eV^2. An independent and complementary method to measure the mixing parameters by using the energy distributions of ν_e CC events is also presented.

A test has been developed that is sensitive to $\nu_\mu \rightarrow \nu_\tau$ oscillations in MINOS by searching for event topologies that are characteristic of tau leptons. The sensitivity of the test to neutrino oscillations has been evaluated for a variety of possible detector configurations of the MINOS far detector. A fine grained detector (2 cm steel plates and 2 cm transverse pitch) is shown to provide the greatest sensitivity; a limit of $\sin^2 2\theta < 0.2$ could be set at 90% confidence at large Δm^2 for a 20 kiloton year exposure of MINOS. A five standard deviation effect or greater could be observed if $\nu_\mu \rightarrow \nu_\tau$ oscillations occur with $\sin^2 2\theta = 1$ and $\Delta m^2 \geq 10^{-2}$ eV^2.

The prospects of analysing MINOS data in the framework of three-flavour neutrino oscillations have been assessed and a preliminary Monte Carlo analysis in three-generations is presented. The results of the CHOOZ reactor neutrino experiment and the solar neutrino experiments are shown to rule out the possibility of observing a large CP violating amplitude in MINOS. Finally it is shown how the future results of MINOS are complementary to other searches for neutrino oscillations.

Acknowledgements

Although I have asserted that the work presented in this thesis is entirely my own (for which I am likely to be dragged over hot coals if this is not the case), I would like to acknowledge here the important contributions that many people have made over the past few years which have allowed me to get where I am today.

Having been ensconced in office number 665 (the last stop before Hell?) over the past three and a half years, it is a pleasure to thank my fellow office-mates Ursula Wielgosz and Argyris Stassinakis. They helped to create an informal and congenial atmosphere in the lab that, in my opinion, makes thesis writing a much less onerous task than it otherwise might be. I would like to thank Ursula for her warm-hearted encouragement and support and Argyris for, among other things, sharing my obsession with Formula 1 racing simulators. Fortunately for him, he discovered their attractions *after* finishing his thesis. I am also grateful to Argyris for discovering all the bugs in a well-known word processing package before I did.

Numerous friends and acquaintances have helped to take my mind off work from time to time. I would especially like to acknowledge the contribution of Kitson Cheung who has been a good mate over these past eight years. Ever since he discovered e-mail, we have engaged in friendly discussion (and occasional agreement) over a wide range of issues, although they have usually gravitated around soccer and Formula 1. His special brand of irreverent and highly amusing messages were much appreciated. I would also like to thank Xin Chen for numerous conversations about soccer and neutrino oscillations (in that order) and Stefan Piperov for his entertaining descriptions of life in Bulgaria and at CERN.

I would like to thank my supervisor, Dr. John Cobb, for sharing his thoughts with me and suggesting the way forward at several points in my research. I would also like to express my gratitude to Jenny Thomas and Hugh Gallagher for their encouragement and enthusiasm for my work during my time at Oxford. I am grateful to Peter Litchfield for his support and for encouraging me to develop the tau analysis that became a part of this thesis

It is a tribute to the talents of Nick West, Pete Gronbech and John McAllister that the computer facilities generally ran smoothly while I was in Oxford. I would like to extend special thanks to Nick for the way he handled the infamous disk crash of 1997 where, for 20 minutes at least, it appeared that all my work from the previous nine months had been lost. His prompt actions have meant that I am writing this in early 1998, rather than in 1999.

I would like to thank my fellow MINOS collaborators for their encouragement, feedback and numerous suggestions. Robert Hatcher, Geoff Pearce, Lynn Miller and Jeff Nelson have provided excellent Monte Carlo support over the years and they were always willing to answer my questions and satisfy my requests. Special thanks must go to Robert and Jenny Thomas for providing me with several plots that are used in Chapter 3 and to Ursula and Hugh for their careful proof-reading of this thesis.

It would, of course, be completely amiss for me to end my acknowledgements without recognising the immense contribution that my family has made to my work. Despite living 161 miles away, they are constantly in my thoughts and their love and support has been a major stabilising force over these past three years. Their unquestioning faith in me and my abilities has helped to make all this possible and for that, and everything else, I dedicate this thesis to them.

Table of Contents

Chapter 1 Introduction

The Standard Model of Particle Physics is the result of many years of experimental and theoretical endeavour. The model has been subjected to stringent experimental tests over a wide range of energies and the agreement between data and theory is remarkable, given that it is widely believed that physics beyond the Standard Model must exist. There are a number of arbitrary parameters in the model, for example neutrino masses are set to zero 'by hand' although there is no fundamental reason why this should be the case. The phenomenon of neutrino oscillations can occur if neutrinos are not massless and, over the past few years, it has become clear that the search for neutrino oscillations is a promising probe of physics beyond the Standard Model. The possible existence of neutrino oscillations is supported by the deficit of solar neutrinos and the anomalous flavour ratio of atmospheric neutrinos observed by large underground experiments.

The proposed MINOS (Main Injector Neutrino Oscillation Search) experiment plans to conduct a comprehensive investigation of neutrino oscillations using a neutrino beam produced by the Fermilab Main Injector and a large new detector located at the Soudan Mine in Minnesota, 730 km away. The experiment will be sensitive to neutrino oscillations in the same region of parameter space as the atmospheric neutrino experiments. Most discussions of the physics capability of MINOS have focussed on the limits that could be set on the oscillation parameters if no effect is observed. In this thesis I will assume that neutrino oscillations do exist, with parameters similar to those indicated by the atmospheric neutrino anomaly. The role of MINOS is therefore to provide a precision measurement of the

oscillation parameters. In the subsequent chapters I describe, with the aid of Monte Carlo simulations, several complementary methods to achieve this aim in MINOS.

The design of the MINOS detector has evolved significantly while this thesis was in preparation; the steel plate thickness has changed from 4 cm to 1 inch and the active detectors have evolved from limited streamer tubes to plastic scintillator. I have therefore attempted to make my arguments largely independent of the specifics of the detector design. The results of Appendix B were, however, used by the collaboration in deciding the optimum detector parameters for MINOS.

Chapter 2 summarises the results of experimental searches for neutrino oscillations. Experiments probing solar and atmospheric neutrinos have produced results that are strongly suggestive of oscillations and the excess of events observed by the LSND experiment can also be interpreted in terms of neutrino mixing. The recent results from CHOOZ and Super-Kamiokande are described and their implications for MINOS are assessed in the subsequent chapters.

The forthcoming MINOS experiment, which is designed to check the atmospheric neutrino anomaly, is described in Chapter 3. MINOS can perform a large number of measurements that are sensitive to neutrino oscillations. In Chapter 4 I describe how the neutrino oscillation phase can be measured by analysing the energy distribution of ν_μ charged-current events. This measurement is one of the most convincing demonstrations of neutrino oscillations in MINOS. I calculate the expected measurement errors on the mixing parameters for a range of oscillation scenarios. The effect of systematic errors on parameter measurement is studied. I have also investigated the physics potential of a preliminary low energy neutrino beam design for MINOS in Chapter 5, which may extend the sensitivity of

the experiment to the values of the mixing parameters that are suggested by the recent Super-Kamiokande atmospheric neutrino results.

Chapter 6 studies an independent and complementary method to measure the neutrino mixing parameters by analysing the energy distribution of ν_e charged-current events. This analysis is sensitive to $\nu_\mu \rightarrow \nu_e$ oscillations and can, when combined with the results of the ν_μ charged-current energy analysis described in Chapter 4, indicate whether the oscillation mode is $\nu_\mu \rightarrow \nu_e$, $\nu_\mu \rightarrow \nu_\tau$ or both.

Given that three-flavours of neutrino exist in nature, it is natural to assume that all three take part in the oscillations. Unlike previous experiments, MINOS data will be analysed in a three-flavour framework rather than the more restrictive two-flavour model. Moreover, MINOS has the statistical power and flavour identification capabilities to play a major role in the measurement of three-generation mixing parameters or in the exclusion of large regions of parameter space. In Chapter 7 I study the methods and prospects of a three-generation analysis of MINOS data. I also study the progress that MINOS could make to the measurement of a new CKM matrix for leptons and the prospects of observing CP violation in MINOS. The important consequences of the CHOOZ result for a three-generation analysis of MINOS are also discussed.

The atmospheric neutrino anomaly, which can be explained by $\nu_\mu \rightarrow \nu_\tau$ oscillations with large mixing strength, motivates the search for tau leptons in MINOS. The observation of tau lepton interactions would be a powerful indication of neutrino mixing since none are expected if oscillations do not occur. Chapter 8 describes a method to search for events of a particular topology that is more common in tau lepton interactions than in the background of ν_μ interactions. An excess of events with this topology is therefore indicative of $\nu_\mu \rightarrow \nu_\tau$ oscillations. Appendix B investigates how the sensitivity of this test changes as the major

parameters of the far detector (steel thickness, transverse granularity, active detector technology) are varied.

The important results of the thesis are summarised in Chapter 9. The interplay between MINOS measurements and those of other neutrino oscillation experiments and the implications of future MINOS results for models of neutrino mass and mixing are also discussed.

Chapter 2 Neutrino Physics

2.1 Introduction

In the early part of the twentieth century experimenters studying nuclear beta decay were faced with an unexpected conundrum; the range of electron energies observed from neutron decay could not be explained in terms of the mass difference between the neutron and proton. In order to account for these observations, the experimenters were forced to postulate a new particle which invisibly carried energy away from the system. This new neutral particle was dubbed the neutrino, or *'little neutron'*, by Fermi.

The neutrino truly proved to be an elusive particle; it possesses no electric charge and interacts weakly with matter. It was not until the 1950's that a direct neutrino signature was observed by Reines and Cowan [1]. Their pioneering experiment observed the reaction:

$$\overline{\nu}_e + p \rightarrow n + e^+$$

by utilising a reactor as a source of 1 MeV anti-neutrinos and a target of cadmium chloride ($CdCl_2$) and water. The signature of a neutrino interaction is a fast pulse of gamma rays from the positron and a slow gamma ray pulse from radiative capture of the neutron in cadmium. The high neutrino fluxes and large detector volume required are a consequence of the low neutrino-nucleon interaction cross-section, which for this process is a mere 10^{-43} cm^2/nucleon.

Today the neutrino remains similarly elusive; we still cannot answer the question of whether or not it possesses a non-zero rest mass. Despite this, the neutrino has been put forward as one of the most promising probes of new physics and as a solution to some of the most fundamental and puzzling mysteries in modern particle physics and cosmology.

2.2 Neutrino Properties

Several properties of neutrinos have been measured:

- the classic experiment of Wu *et. al.* [2] in 1957 determined that the weak interaction maximally violates parity conservation. Applying this result to massless neutrinos leads to the condition that neutrinos must be fully polarised with a helicity of +1 or –1. In 1958, an experiment by Goldhaber *et. al.* [3] measured the helicity of the neutrino and determined that only left-handed neutrinos (spin anti-parallel to neutrino direction) participate in the weak interaction;

- experimental results indicate that neutrinos observe lepton number conservation, that is they are always associated with their like-flavour charged lepton;

- studies of the Z boson line width at LEP and SLC have determined that there are only three neutrino species with standard couplings to the Z and masses less than 45 GeV/c^2 [4]. Neutrinos with non-standard (much weaker) couplings, so-called 'sterile' neutrinos, could exist in addition to the three standard species.

2.2.1 Neutrino mass

The neutrino masses, however, are not known. They are assumed to be zero in the Standard Model, although there is no fundamental aspect of the Standard Model that forbids non-zero neutrino masses. Indeed, it is quite straightforward to insert neutrino mass terms into the Standard Model Lagrangian. There are two basic methods to generate neutrino mass terms that are both gauge and Lorentz invariant [5].

- **Dirac mass**. This is obtained by introducing extremely heavy right-handed neutrinos which have not yet been observed. These neutrinos appear in many Grand Unified Theories. The mass term in the Lagrangian is therefore:

$$L_{Dirac} = -(\overline{\nu}_L M \nu_R + \overline{\nu}_R M \nu_L), \tag{2.1}$$

  where $\nu_{L,R}$ are the neutrino flavour eigenstates and M is the 3×3 neutrino mass matrix.

- **Majorana mass**. A massive Majorana neutrino can be created by modifying the Higgs sector in the Standard Model. An additional singlet, doublet or triplet is added to the original Higgs doublet, although this introduces a new mass scale in the form of the Higgs vacuum expectation value. The mass term in the Lagrangian is:

$$L_{Majorana} = -\frac{1}{2}\overline{\nu}_L^C M \nu_L + h.c. \tag{2.2}$$

  In this case neutrinos are their own anti-particles since ν_L^C is a right-handed neutrino. These mass terms violate lepton number conservation by two units and their presence could be indicated by the observation of neutrinoless double beta decay, nuclear transitions of the type $(Z, A) \rightarrow (Z-2, A) + 2e^-$, which are only possible in the presence of massive Majorana-type neutrinos. The non-

observation of this transition in current experiments sets a limit on the mass of the electron neutrino of $m_{\nu_e} < 0.5$ eV if the ν_e is assumed to be a Majorana particle [6].

2.2.2 Direct searches for neutrino mass

A direct measurement of neutrino mass can be performed by studying decay processes that involve neutrinos. If neutrinos possess mass, the decay kinematics will be different from the massless case and could lead to observable effects. Studies of the endpoint of tritium decay have been used to search for non-zero electron neutrino masses via the process:

$$ {}^{3}_{1}H \rightarrow {}^{3}_{2}He + e^{-} + \overline{\nu}_e . $$

If the electron neutrino has a non-zero mass, it will induce potentially measurable distortions near the endpoint of the electron energy spectrum. This measurement is complicated by the fact that corrections must be made for nuclear screening effects and final state interactions for the tritium itself. Two experiments, one at the University of Mainz [7] and the other at Troitsk [8] in Russia, are currently taking data. Their fits to current data yield upper limits at 95% confidence level for the electron anti-neutrino mass of 5.6 and 3.9 eV/c^2 respectively. However, both experiments obtain best-fit values for m^2_ν that are negative and there are some apparent systematic effects associated with the data. In particular, the Troitsk group observes a bump-like structure near the end-point which changes position over time. These uncertainties mean that it is difficult to produce a definitive limit on the electron neutrino mass using this technique, although the two groups feel that if the electron neutrino had a mass of 25 eV/c^2 then they should be able to observe a clear signal above the systematic effects.

An entirely independent method of obtaining a limit on the electron neutrino mass was obtained by analysing the time structure of electron neutrinos detected in the Kamiokande and IMB water Cerenkov detectors from the recent supernova SN1987A. If the electron neutrino has a finite mass, the propagation time from the supernova core to the Earth will be correlated with the neutrino energy since high energy neutrinos will be observed sooner than those of low energy (the mean neutrino energy is approximately 15 MeV). By analysing the time structure of the 11 neutrino interactions that were observed in Kamiokande [9] and the 8 interactions recorded by IMB [10] over a period of ten seconds, Bahcall and Glashow have obtained a conservative upper limit on the electron neutrino mass of 11 eV/c^2 [11].

An upper limit for the mass of the ν_μ can be obtained by studying the following decay:

$$\pi^+ \rightarrow \mu^+ + \nu_\mu ,$$

with the pion at rest. Only π^+ decays can be studied because π^- at rest are captured by nuclei. Since the above process is a two-body decay, a measurement of the muon momentum and knowledge of both the pion and muon masses to sufficient accuracy allow an upper limit to be placed on the mass of the muon neutrino. The latest results obtained at the Paul Scherrer Institute, Switzerland yield an upper limit of 170 keV/c^2 at 90% C.L. [12].

Limits on the mass of the ν_τ are obtained by studying the following tau decays:

$$\tau \rightarrow 5\pi + \nu_\tau , \tau \rightarrow 3\pi + \nu_\tau .$$

These decays are chosen to minimise the amount of phase space available to the tau neutrino. A limit on the neutrino mass is obtained by reconstructing the invariant mass of the hadronic

system. The experiment that currently sets the most stringent limit on the mass of the tau neutrino is the ALEPH experiment at LEP which sets an upper limit of 23.1 MeV/c^2 at 90% C.L. [13].

Neutrino masses also have consequences for big-bang cosmology. Over the past 60 years, a number of measurements have led to the conclusion that a large fraction (between 90 and 99%) of the mass in the universe is in the form of non-luminous, or dark, matter. Bounds placed by nucleosynthesis limit the baryonic content of dark matter to 10%. However, neutrinos were prodigiously produced in the aftermath of the big-bang and if they possess a small non-zero mass, they could constitute a significant fraction of the dark matter in the universe. In order to prevent an overclosed universe (i.e $\Omega \geq 1$) then the sum of all neutrino masses must satisfy the following relationship [14]:

$$h^2 \sum_{i=e,\mu,\tau} m_i \leq 100eV, \tag{2.3}$$

where h is a factor that can take on values between 0.5 and 1.0 and encapsulates the current level of uncertainty in the value of the Hubble constant.

2.2.3 The see-saw mechanism

Several theories have been put forward to explain the smallness of neutrino masses, assuming of course that they are not zero. The simplest of these is the so-called "see-saw" mechanism [15] which is a natural consequence of many Grand Unified Theories. This model assumes that the right-handed neutrinos are extremely massive and that the neutrino masses are related to the quark masses in the following way [5]:

$$m(\nu_1) : m(\nu_2) : m(\nu_3) = \frac{m_u^n}{M_R} : \frac{m_c^n}{M_R} : \frac{m_t^n}{M_R}, \tag{2.4}$$

where M_R is the mass-scale associated with the theory. The exponent n can take on the values 1 or 2; $n = 1$ is referred to as the linear see-saw mechanism and $n = 2$ is the quadratic see-saw mechanism. The precise ratios and the value of M_R, which is related to the GUT scale (~10^{16} GeV), depend on the particular GUT model (e.g. $SU(5)$, $SO(10)$). It is expected that M_R lies between 10^{10} and 10^{15} eV^2. This naturally explains the smallness of the neutrino masses and predicts that the neutrino mass hierarchy is qualitatively similar to that of the charged leptons and quarks.

2.3 Neutrino Oscillations

If neutrinos possess mass then the phenomenon of neutrino mixing is possible. Neutrino mixing is a powerful method to probe for neutrino masses far below the kinematic limits of the direct searches described in section 2.2.2. In general, the neutrino flavour eigenstates – the ν_e, ν_μ and ν_τ of the weak interaction – may not be the same as the neutrino mass eigenstates that exist in the Standard Model Lagrangian. The weak eigenstates ν_α are therefore related to the mass eigenstates ν_i, by a unitary transformation matrix U such that $\nu_\alpha = U\nu_i$. If the mixing matrix is non-diagonal, the weak eigenstates are linear combinations of the mass eigenstates. For N generations of Dirac-type neutrinos, the matrix U contains $N(N-1)/2$ Euler angles and $(N-1)(N-2)/2$ complex phases [16]. In the case of three neutrino generations, the matrix U is the analogue of the familiar Cabibbo-Kobayashi-Maskawa mixing matrix for quarks.

In a neutrino oscillation experiment, a neutrino beam consisting of a particular flavour eigenstate ν_α is produced at $t = 0$ and sampled at a later time t, at a distance x from the source. The ν_α produced in the beam will be a linear combination of the mass eigenstates and if these possess finite and non-degenerate masses, they will propagate at different speeds

in a vacuum. The admixture of mass eigenstates in the beam at (t, x) will therefore be different from that at $t = x = 0$. When the beam is sampled, there is a finite probability that a neutrino of flavour ν_β is detected, where $\beta \neq \alpha$.

The transition probability can be written as:

$$P(\alpha \to \beta) = \left| \sum_i U_{\beta i} e^{-i(E_i t - p_i x)} U^*_{\alpha i} \right|^2, \tag{2.5}$$

where the factor $U_{\alpha i}$ is the probability amplitude of mass eigenstate ν_i being produced at the source, the exponential factor describes the propagation of the mass eigenstate in space and time and the factor $U_{\beta i}$ is the probability amplitude of observing a ν_β interaction in the neutrino detector. This result is independent of the number of neutrino flavours. Expanding the above equation yields:

$$P(\alpha \to \beta) = \sum_i \left| U_{\beta i} \right|^2 \left| U_{\alpha i} \right|^2 + \mathrm{Re} \sum_{i \neq j} U_{\beta i} U^*_{\beta j} U^*_{\alpha i} U_{\alpha j} e^{-i[(E_i - E_j)t - (p_i - p_j)x]}. \tag{2.6}$$

The first term in equation (2.6) is the classical transition probability from flavour eigenstate ν_α to ν_β. The second term contains a quantum mechanical phase which leads to a space-time dependence of the transition probability. An observation of neutrino mixing would therefore be the demonstration of a non-zero transition probability between neutrino flavour eigenstates. On the other hand, an observation of neutrino oscillations requires the demonstration of an oscillation probability which varies with space and/or time.

Since the neutrino masses probed in oscillation experiments are of $O(\mathrm{eV/c^2})$ and the neutrino momenta are typically in the MeV or GeV region, the approximation of highly relativistic neutrinos is valid. Under this assumption, the neutrino momenta and energies are related in the following way:

$$p_i = p_j = p,$$

$$E_i = (p^2 + m_i^2)^{1/2} = p(1 + m_i^2 / p^2)^{1/2} \approx p + m_i^2 / 2p. \quad (2.7)$$

The transition probability therefore assumes the following form:

$$P(\alpha \to \beta) = \sum_i \left|U_{\beta i}\right|^2 \left|U_{\alpha i}\right|^2 + \mathrm{Re} \sum_{i \neq j} U_{\beta i} U_{\beta j}^* U_{\alpha i}^* U_{\alpha j} e^{-i\Delta m_{ij}^2 L/2E}, \quad (2.8)$$

where L is the source-detector distance and $\Delta m_{ij}^2 = \left|m_i^2 - m_j^2\right|$.

2.3.1 Two-flavour oscillations

The form of the oscillation probability is much simplified if only two neutrino generations are assumed to take part in the oscillations. In this case, the mixing matrix U takes the form:

$$U = \begin{pmatrix} \cos\theta & \sin\theta \\ -\sin\theta & \cos\theta \end{pmatrix}.$$

The matrix U contains only one free parameter, the mixing angle θ. There is one Δm^2 parameter between the two neutrino mass eigenstates ν_1 and ν_2. The oscillation probability $P_{\alpha\beta}$, between neutrino flavours α and β is given by the following simplified form:

$$P_{\alpha\beta} = \left|\delta_{\alpha\beta} - \sin^2 2\theta \sin^2(1.27\Delta m^2 L / E_\nu)\right|, \quad (2.9)$$

where L is the neutrino path length in km, E_ν is the neutrino energy in GeV and Δm^2 is in units of eV^2/c^4. The advantage of adopting this formalism is its simplicity. There are only two parameters and they are directly linked to experimental observables.

Figure 2.1 shows a neutrino energy distribution of ν_α with (dashed line) and without (solid line) $\nu_\alpha \to \nu_\beta$ oscillations. The number of ν_α converting to ν_β depends on the neutrino energy, hence the dip in the oscillated distribution. The size of the dip is related to $\sin^2 2\theta$. The energy where the deficit is greatest, E_{dip}, is related to Δm^2 by:

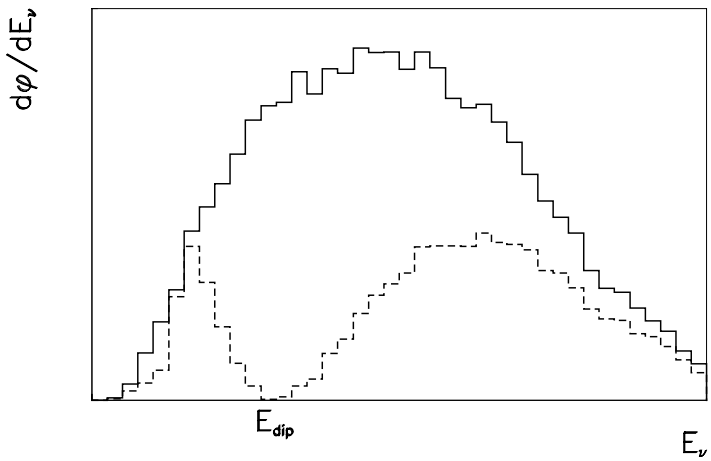

Figure 2.1 - Neutrino oscillations in a two-generation framework. The solid line shows the flux of neutrino flavour ν_α as a function of the neutrino energy E_ν for a fictional beam spectrum. The dashed line shows the flux spectrum of ν_α that would be observed if $\nu_\alpha \rightarrow \nu_\beta$ oscillations occur with mixing parameters Δm^2 and $\sin^2 2\theta$.

$$E_{dip} = 2.53\Delta m^2 L / n\pi, \tag{2.10}$$

where n is an integer. Maximum sensitivity to neutrino oscillation occurs when the following condition is satisfied:

$$2.53\Delta m^2 L / E = n\pi / 2. \tag{2.11}$$

Results from the study of the Z^0 linewidth at LEP and elsewhere have shown that three light neutrino generations exist in nature. It is natural to assume that all three-generations participate if oscillations occur. It is therefore possible to have $\nu_\mu \rightarrow \nu_e$ and $\nu_\mu \rightarrow \nu_\tau$ oscillations occurring simultaneously. The two-generation formalism is inadequate in this case and it is necessary to consider three-flavour oscillations.

2.3.2 Three-flavour oscillations

Three-flavour neutrino oscillations are described by a 3×3 mixing matrix U and two independent Δm^2. The matrix U is parameterised by three angles and one complex phase [17]:

$$\begin{pmatrix} \nu_e \\ \nu_\mu \\ \nu_\tau \end{pmatrix} = \begin{pmatrix} c_1 c_2 & s_1 c_2 & s_2 \\ -c_1 s_2 s_3 e^{i\delta} - s_1 c_3 & c_1 c_3 - s_1 s_2 s_3 e^{i\delta} & c_2 s_3 e^{i\delta} \\ -c_1 s_2 c_3 + s_1 s_3 e^{-i\delta} & -s_1 s_2 c_3 - c_1 s_3 e^{-i\delta} & c_2 c_3 \end{pmatrix} \begin{pmatrix} \nu_1 \\ \nu_2 \\ \nu_3 \end{pmatrix},$$

where $c_1 = \cos\theta_1$, $s_1 = \sin\theta_1$ and δ is a complex CP violating phase. The real angles θ_1, θ_2 and θ_3 have no obvious physical meaning. They specify the three orthogonal rotations that transform between the flavour basis and the mass basis. Setting θ_2 and θ_3 to zero results in two-generation $\nu_\mu \to \nu_e$ oscillations. Setting θ_1 and θ_3 to zero gives $\nu_e \to \nu_\tau$ and setting θ_1 and θ_2 to zero results in $\nu_\mu \to \nu_\tau$. This formalism has six independent parameters. It is possible to reduce the number of free parameters and simplify the oscillation probabilities by assuming that the neutrino masses are strongly ordered, that is $\Delta m^2_{32} << \Delta m^2_{21}$ [18]. If, for a particular experiment, $\Delta m^2_{21} L / E_\nu << 1$ then it is legitimate to ignore the contribution of Δm^2_{21}, effectively eliminating one free parameter. The oscillation probabilities simplify greatly because only the matrix elements that couple the neutrino flavours to the heavy mass eigenstate, ν_3, are important. The probabilities take on the following form:

$$P_{\alpha\alpha} = 1 - 4U^2_{\alpha 3}(1 - U^2_{\alpha 3}) \sin^2(1.27\Delta m^2 L / E_\nu), \tag{2.12}$$

$$P_{\alpha\beta} = 4U^2_{\alpha 3} U^2_{\beta 3} \sin^2(1.27\Delta m^2 L / E_\nu). \tag{2.13}$$

There is a simple transformation between two and three-generation oscillation probabilities:

$$\sin^2 2\theta_{\alpha\alpha} \leftrightarrow 4U^2_{\alpha 3}(1 - U^2_{\alpha 3}), \tag{2.14}$$

$$\sin^2 2\theta_{\alpha\beta} \leftrightarrow 4U^2_{\alpha 3} U^2_{\beta 3}. \tag{2.15}$$

When the unitarity condition $U_{e3}^2 + U_{\mu 3}^2 + U_{\tau 3}^2 = 1$ is imposed then this assumption, known as one mass-scale dominance (OMSD), reduces the number of free parameters from six to three. The OMSD formalism will be described in greater detail in Chapter 7 where the prospects of a three-generation analysis of MINOS are discussed.

2.4 Neutrino oscillation experimental techniques

Neutrino oscillation experiments generally fall into one of two categories:

- **Disappearance experiments**: these experiments look for a suppression in the rate of neutrino events of flavour ν_α (as a function of L/E);
- **Appearance experiments**: these experiments search for neutrinos of flavour ν_β from a beam that is originally of flavour ν_α (as a function of L/E).

To observe neutrino *oscillations*, it is necessary to observe flavour conversion as a function of L/E. If no L/E dependence is observed then only neutrino mixing can be inferred. This definition of the nomenclature is important because the observation of an oscillatory dependence of the neutrino transition probability with L/E is an unambiguous demonstration of oscillations whereas a change in the number of events of a particular flavour could easily be explained by an error in the rate normalisation, a systematic effect in the experiment or spurious events due to background contamination of the data.

There are three key ingredients for a neutrino oscillation experiment:

1. **Neutrino beam.** This can be produced by many sources. Accelerator beams produce copious quantities of pions and kaons which decay primarily to muon neutrinos. Thermonuclear reactors produce electron antineutrinos. The sun

produces a steady flux of electron neutrinos from nuclear fusion in the solar interior. Finally, cosmic rays impinging on the upper atmosphere produce a flux of electron and muon neutrinos and antineutrinos.

2. **Prediction of neutrino flux (no oscillations).** For accelerator based neutrino beams, the measurement of neutrino interactions in a beam monitor calorimeter that is near to the neutrino source can, with the aid of a Monte Carlo simulation, be used to predict the flux expected at the main detector site. The flux of reactor neutrinos can be determined on-site by monitoring the neutron flux, which is directly related to the flux of neutrinos. The solar neutrino and atmospheric neutrino fluxes are predicted by detailed Monte Carlo calculations.

3. **Detector.** A single detector situated at a distance L from the source must have the ability to do one of the following: detect original flavour ν_α; detect the appearance of ν_β; measure the ν_α (or ν_β) energy spectrum. A second approach is to place several detectors at different distances from the source. Each detector measures the flux of ν_α. Neutrino oscillations are inferred if the flux does not drop off as $1/L^2$. Since the neutrino-nucleon cross-section is small ($\sim 10^{-38}$ cm^2/GeV), all neutrino experiments are characterised by large (multi-ton to multi-kiloton) masses. The detectors are placed (deep) underground to suppress the large cosmic ray induced background.

2.5 Experimental Searches for Neutrino Oscillations

A large number of experiments have searched for the existence of neutrino oscillations over the past thirty years. They have used both natural sources of neutrinos

(cosmic rays, the sun and supernovae) and man-made sources (from fission reactors and accelerators). Several experiments have obtained results that can be interpreted as being due to neutrino mixing and these are discussed below.

2.5.1 Solar Neutrinos

The Sun is powered by thermonuclear fusion in the solar core, driven by the burning of Hydrogen to form Helium-4. This is an exothermic process (Q= 26 MeV) and is almost entirely responsible for the solar luminosity of 3.8×10^{26} W. The process of turning Hydrogen into Helium is governed by the pp cycle. The neutrino producing reactions are listed below.

$$p + p \rightarrow {}^{2}D + e^{+} + \nu_{e}$$

$$p + p + e^{-} \rightarrow {}^{2}D + \nu_{e}$$

$${}^{7}Be + e^{-} \rightarrow {}^{7}Li + \gamma + \nu_{e}$$

$${}^{8}B \rightarrow 2{}^{4}He + e^{+} + \nu_{e}$$

Electron-type neutrinos are produced at three points in the chain. The pp neutrinos, which are the most numerous, have energies of up to 0.4 MeV. The neutrinos from ^{7}Be and the pep reaction are monoenergetic. The ^{8}B neutrinos are only produced in the rare ppIII branch and are emitted with a continuous energy spectrum with an endpoint of 14.1 MeV.

Figure 2.2 shows the energy spectrum of neutrinos emitted by the sun, along with the experimental thresholds of the detectors designed to observe them. These neutrino fluxes are predicted by the standard solar models [20] which are complex numerical calculations that predict the stellar temperature and density as a function of radius and therefore the neutrino flux expected on Earth. Reaction cross-sections, measured solar abundances, solar opacities and the solar luminosity are all inputs to the models. The largest uncertainties in neutrino rates are in the ^{8}B neutrinos, since the reaction cross-section is strongly temperature dependent ($\sigma \propto T^{18}$). The ^{7}Be and ^{8}B fluxes are correlated since Boron-8 is produced by Beryllium-7. The pp neutrino flux calculations are the most secure because they are produced in the ppI branch of the pp cycle, which is responsible for 91% of the energy output of the sun and can therefore be directly related to the solar luminosity.

The solar models appear to be in excellent agreement with data from other methods that probe the solar interior (e.g. helioseismology) [21] although numerous authors have contested the validity of cross-section measurements used in the models and the fine details

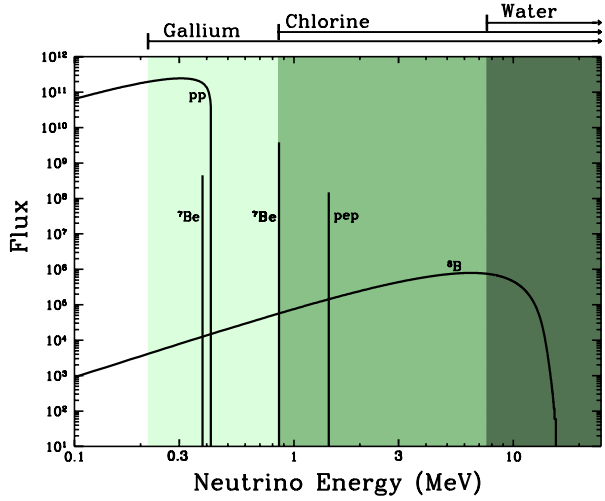

Figure 2.2 – The solar neutrino spectrum, from [19].

of the simulations. It appears, however, that the most robust experimental measurement of solar neutrinos is the neutrino energy spectrum. The analysis of spectral information from solar neutrinos by comparing the results from experiments with different energy thresholds, solar neutrino spectroscopy, is a powerful tool in unravelling the physics behind the experimental measurements of solar neutrino fluxes [22].

2.5.1.1 Solar neutrino experiments

The pioneering experiment in the field is the Homestake [23] solar neutrino experiment which is located in a salt mine in South Dakota, USA. The experiment consists of a large tank filled with 680 tonnes of C_2Cl_4. Electron neutrinos react with the chlorine in the solution to produce Argon-37. The tank is periodically purged with Helium gas and any Argon atoms are captured in a charcoal trap. The Argon then decays producing a 2.2 MeV Auger electron which is detected by a proportional counter. The count rate of these electrons is thus proportional to the electron neutrino flux at the mine. The threshold of the experiment is 0.813 MeV, which means that the detector is sensitive to the ^{7}Be and ^{8}B neutrinos from the sun, but not the pp neutrinos. The experiment has been taking data for over twenty years and has recorded an average neutrino flux of 2.54±0.16±0.14 SNU[1] [24], which is only 28% of the flux predicted by the standard solar model.

Two experiments, SAGE [25] and GALLEX [26], use a similar technique to the Homestake experiment to detect the low energy pp neutrinos that form the bulk of the solar neutrino flux. The experiments consist of large tanks of Gallium which undergoes the reaction:

$$^{71}Ga + \nu_e \rightarrow {}^{71}Ge + e^-.$$

[1] 1 SNU = 1 capture/second/10^{36} target atoms.

The low threshold of this reaction (0.233 MeV) means that the experiments are sensitive to the pp, ^{7}Be and ^{8}B neutrinos. The experiments are exposed to the solar neutrino flux for a period of a month, after which the tanks are purged and the germanium (which has a half-life of 16.5 days) is placed in a proportional counter for several months and allowed to decay. The SAGE experiment measures a neutrino rate of 72±12±7 SNU and the GALLEX experiment measures 70±8 SNU. The standard solar model prediction is 137±8 SNU. Both experiments have performed an independent calibration of their counting method using a high intensity ^{51}Cr source. The isotope has a half-life of 27 days and produces neutrinos with an energy of 746 keV, which closely matches the pp and ^{7}Be solar neutrinos. Both experiments report a measured to expected flux ratio that is consistent with unity: GALLEX measures 0.92±0.07 [26] and SAGE measures 0.95±0.11±0.07 [25].

A different class of experiment uses a large tank of purified water to observe Cerenkov light from neutrino-electron scattering:

$$\nu + e^{-} \rightarrow \nu + e^{-}.$$

The threshold for this type of reaction is set by background Cerenkov light from radioactivity and cosmic rays and is typically 5-7 MeV. This technique can therefore only be used to detect Boron-8 neutrinos from the sun.

The Kamiokande [27] detector has observed the solar neutrino flux between 1983 and 1996. The experiment consisted of a 4.5 kiloton cylindrical tank of purified water, 16.1 metres in height and 15.6 metres in diameter. The detector walls were lined by 948 photomultiplier tubes. The detector was situated in the Kamioka mine between Tokyo and Nagoya in Japan at a depth of 2700 m.w.e. The fiducial mass of the detector for solar neutrinos was 680 tonnes. The experiment detected electron neutrinos via the distinctive Cerenkov ring pattern observed on the phototubes from electrons produced by elastic

Experiment	Threshold	Observed	Expected	% of SSM
SAGE	0.223 MeV	72±12±7 SNU	137±8	51%
GALLEX	0.223 MeV	70±8 SNU	137±8	53%
HOMESTAKE	0.813 MeV	2.54±0.16±0.14 SNU	9.3±1.3	28%
KAMIOKANDE	7.5 MeV	$2.80\pm0.19\pm0.33\times10^{6}$ $cm^{-2}s^{-1}$	6.6±1.1	42%
SUPER-K	6.5 MeV	$2.44\pm0.06\pm0.07\times10^{6}$ $cm^{-2}s^{-1}$	6.6±1.1	37%

Table 2.1 – The Solar neutrino problem.

neutrino-electron scattering. In contrast to the radiochemical solar neutrino experiments, the detection of these Cerenkov rings is done in real time. Temporal variations in the solar neutrino flux, either diurnal or seasonal, can therefore be searched for. In addition, the direction of travel of the recoil electron is correlated with the direction of the incoming neutrino (to within 30^{o}) so it is possible to verify that the neutrinos observed in the detector indeed originate from the sun. The Kamiokande experiment has measured a flux of neutrinos from the sun that is only 42% of the expected flux from standard solar models.

On April 1st 1996, the Kamiokande experiment was superseded by Super-Kamiokande, a high-mass (50 kiloton) water Cerenkov detector surrounded by 11200 phototubes. The fiducial mass of Super-Kamiokande for solar neutrinos is 22 kilotons, providing a dramatic increase in statistics over Kamiokande. A preliminary analysis of the first 300 days of data produces a flux of neutrinos that is only 37% of that expected by the standard solar model [27].

The results of these five experiments are shown in Table 2.1 and together constitute what is known as the solar neutrino problem.

2.5.1.2 Solutions to the solar neutrino problem

There are three possible solutions to the solar neutrino problem:

1. the experiments are wrong;

2. the standard solar model is wrong;

3. neutrinos are changing flavour between source and detector.

The first option is seen as unlikely, especially since the SAGE and GALLEX experiments have been successfully calibrated with a ^{51}Cr source. The second solution is the subject of some debate in the physics community [21] although the general consensus is that no reasonable variation in the input parameters to the solar model can account for the experimental data. The third option has attracted a great deal of attention over the past 20 years. The model that most closely fits the current data is that of resonant neutrino oscillations in the solar interior via the Mikheyev-Smirnov-Wolfenstein (MSW) mechanism [28].

The basic premise of the MSW mechanism is that as neutrinos pass through the solar interior they undergo multiple small angle scatters via the reactions $\nu + e \rightarrow \nu + e$ and $\nu + N \rightarrow \nu + N$. For the elastic neutrino-nucleon scatters, the cross-section will be the same for all neutrino flavours. For neutrino-electron scattering, there will be an additional contribution for electron neutrinos due to the contribution of W boson exchange. The net result of this is that there will be an additional term in the Lagrangian for electron neutrinos that is proportional to the neutrino energy and electron density at a particular region of the solar interior. If there is two-flavour mixing between ν_e and ν_μ then the ν_e will be a linear combination of the two mass eigenstates ν_1 and ν_2. As the ν_e- like state propagates through

matter in the solar interior, it picks up an effective mass due to neutrino-electron scattering. After a time t the mass of the state has changed such that what was initially ν_e- like now contains an admixture of ν_μ. The electron density is a function of solar radius and there is in principle a region where the initial ν_e state is almost totally converted into ν_μ.

The experimental results isolate two regions of parameter space for MSW-induced neutrino oscillations, the small angle solution at $\Delta m^2 \sim 10^{-5}$ eV^2 and $\sin^2 2\theta \sim 10^{-3}$ and the large angle solution at $\Delta m^2 \sim 10^{-5}$ eV^2 and $\sin^2 2\theta \sim 0.8$. These solutions are shown in Figure 2.8. The fact that Kamiokande and Super-Kamiokande see no significant distortion in the electron energy spectrum excludes a region of parameter space above $\Delta m^2 \sim 10^{-4}$ eV^2 and the non-observation of a day-night effect (due to resonant flavour conversion in the Earth) rules out a region between the small and large angle solutions [29]. A solution for vacuum oscillations with $\Delta m^2 \sim 10^{-10}$ eV^2 and $\sin^2 2\theta \sim 1$ is also allowed. Solar neutrino spectroscopy reveals that the low energy neutrinos appear to be present at the predicted rate, the ^{7}Be neutrinos appear to be entirely absent and the high energy ^{8}B neutrinos are suppressed to a lesser degree. To reproduce this energy dependence in the vacuum oscillation solution requires a degree of fine-tuning of the parameters and it has hence been named the 'just-so solution'. It has also been shown that it is possible in principle to distinguish between the just-so and MSW explanations of the solar neutrino problem by searching for an oscillation probability that results from the eccentricity of the earth's orbit around the sun [30]. The sun-earth distance varies by ±1.7% over the course of a calendar year and an observation of an (energy dependent) asymmetry in the neutrino rates between perihelion (July 4th) and aphelion (January 4th) over and above the ±3.3% rate variation expected from geometry alone, is a signal of just-so oscillations with $\Delta m^2 \sim 10^{-10}$ eV^2.

2.5.1.3 Future experiments

In the next few years three experiments will help to unravel the physics behind the solar neutrino problem:

1. Super-Kamiokande will accumulate more statistics and will lower its threshold to 5 MeV. It will search for subtle spectral distortions in the recoil electron energy spectrum and for diurnal and seasonal variations of the neutrino flux.

2. The Sudbury Neutrino Observatory (SNO) [31] is expected to begin taking data in 1998. The unique feature of this experiment is the ability to measure the rate of the neutral current reaction $\nu + D \rightarrow p + n + \nu$. This reaction is sensitive to all neutrino flavours whereas the charged-current electron scattering process applies only to ν_e. If the NC and CC rates are equally suppressed and there is a deficit of the neutrino flux then the solar models are wrong[2]. If only the CC rate is suppressed then neutrino oscillations have occurred.

3. The BOREXINO [32] experiment will be operational in the next few years. This experiment will be a scintillator-based detector that will operate with a very low threshold (246 keV) provided the background from radioactivity is sufficiently low. The high event rate (50 events/day are expected) and good energy resolution of this device will allow spectral distortions and temporal variations to be studied with high statistical precision.

[2] Oscillations to sterile neutrinos which, by definition, do not produce CC or NC interactions could also explain this observation.

2.5.2 Atmospheric Neutrinos

A second source of neutrinos is the upper atmosphere. Cosmic rays, mostly protons, impinge on the Earth's atmosphere from every direction in space and produce cascades of elementary particles as spallation products from the nuclei in the upper atmosphere. These pions and kaons then decay producing muons, electrons and neutrinos. The pion decay chain:

$$\pi^- \rightarrow \mu^- + \overline{\nu_\mu},$$
$$\mu^- \rightarrow e^- + \overline{\nu_e} + \nu_\mu,$$

produces a ν_μ / ν_e ratio of 2:1. There are small corrections due to kaon decay and the ratio increases for neutrino energies above 1 GeV because more muons reach the surface of the earth before decaying. The ratio is predicted with an error of 5%, although the absolute fluxes of ν_μ and ν_e are known only to 20% due to uncertainties in the primary cosmic ray flux and hadron production in the upper atmosphere [33].

Atmospheric neutrinos are the background to proton decay since they produce events that are contained within the detector volume with approximately 1 GeV of visible energy. The detectors that were built to search for proton decay have devoted a great deal of effort to studying and understanding this background. It is somewhat ironic that while a proton decay signal has not been observed, the background has proved to be extremely interesting in its own right.

2.5.2.1 Atmospheric neutrino experiments

The experiments measure the ratio of muon-like to electron-like events. It is conventional to measure the double ratio R, which is the ratio of the μ / e ratio measured by experiment to the μ / e ratio predicted by Monte Carlo simulations. If the data is correctly

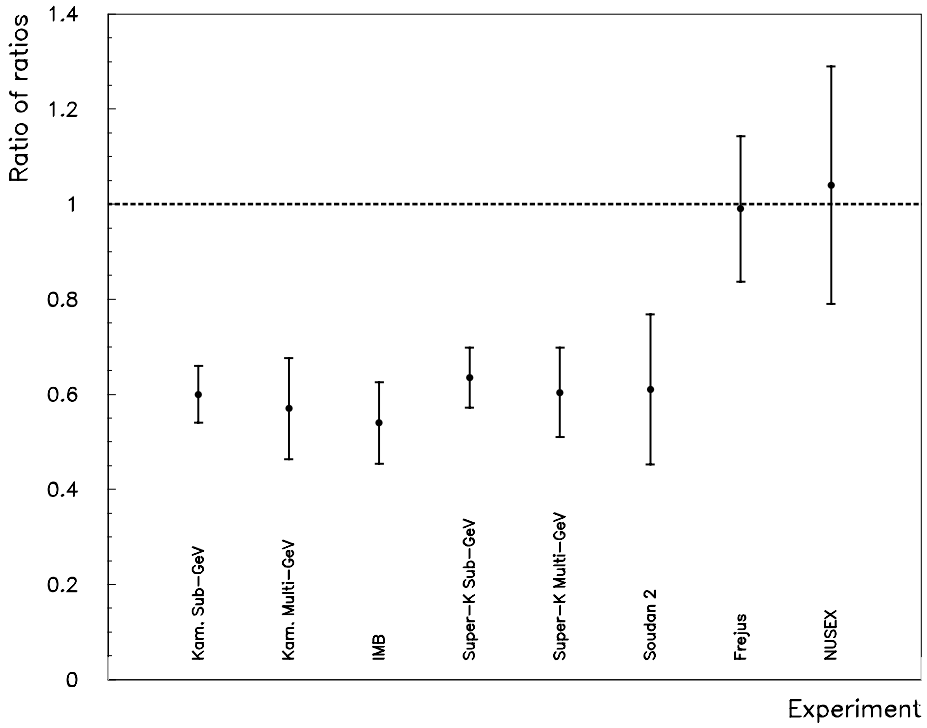

Figure 2.3 – The atmospheric neutrino anomaly.

described by the Monte Carlo, the value of R should be 1.0. Figure 2.3 shows the value of R measured by six different experiments. Many of the experiments find a value of R that is significantly less than one, implying that the mixture of muon-like and electron-like events from atmospheric neutrino interactions is different from the predictions of the Monte Carlo simulations. Large effects are seen in the water Cerenkov detectors: IMB [34], Kamiokande [35], and Super-Kamiokande [36]. On the other hand, the small iron calorimeter detectors, NUSEX [37] and FRÉJUS [38], see no significant deviation from unity. The Soudan 2 detector [39], which is also an iron calorimeter, supports the water Cerenkov results, implying that a large systematic effect that is peculiar to the water Cerenkov detectors is not likely to be an explanation for the low values of R.

The water Cerenkov experiments, IMB, Kamiokande and Super-Kamiokande, identify muon and electron events by the pattern of Cerenkov light on the photomultiplier tubes that line the walls of the detectors. Quasi-elastic events, which produce a single Cerenkov ring, are the easiest to analyse (the analyses of the water Cerenkov experiments and the Soudan 2 tracking calorimeter experiment are based entirely on samples of quasi-elastic neutrino interactions). A muon track will produce a sharply defined ring whereas an electron shower, which is the sum of many particles, will produce a more diffuse pattern of hits. A sophisticated pattern recognition algorithm computes the likelihood that a particular Cerenkov ring is due to the passage of a muon or an electron. All three experiments find a value of R that is significantly smaller than unity using this technique. The Kamiokande collaboration has exposed a 1 kiloton water detector to a test beam at the 12 GeV KEK PS to check that the deficit is not due to mis-identification of events. The results show that there is, on average, only a 1.9% chance that a muon event will be incorrectly identified as an electron and vice versa [40].

An anomalous value of R sets a lower limit on Δm^2 if it is interpreted in the framework of neutrino oscillations. A more convincing demonstration of oscillations is provided by the zenith angle distribution of the ratio of ratios for the Kamiokande multi-GeV data, shown in Figure 2.4. The ratio of ratios for downward going events ($\cos\theta = 1$) is consistent with unity, whereas the ratio for upward going events ($\cos\theta = -1$) is heavily suppressed, suggesting that the neutrino oscillation wavelength is longer than the height of the atmosphere (20 km) but shorter than the diameter of the Earth (12000 km). The data is well-described by both $\nu_\mu \to \nu_e$ and $\nu_\mu \to \nu_\tau$ oscillations with $\sin^2 2\theta \sim 1$ and $\Delta m^2 \sim 1.6\times10^{-2}$ eV^2 for $\nu_\mu \to \nu_\tau$ and $\Delta m^2 \sim 1.8\times10^{-2}$ eV^2 for $\nu_\mu \to \nu_e$ [41]. The sub-GeV zenith angle distribution shows no significant variation of R with $\cos\theta$.

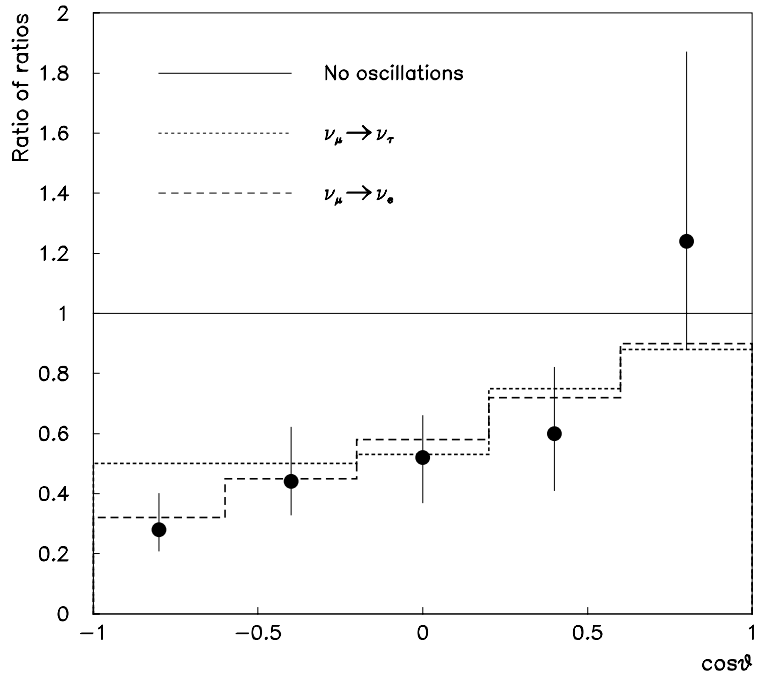

Figure 2.4 - Distribution of the ratio of ratios as a function of zenith angle of the outgoing lepton for the Kamiokande multi-GeV data sample of atmospheric neutrino interactions. The dashed and dotted lines show the best fit distributions if neutrino oscillations are assumed in the modes $\nu_\mu \to \nu_e$ and $\nu_\mu \to \nu_\tau$ respectively. From [41].

A preliminary analysis of the first 326 days of data from the Super-Kamiokande experiment [36] also suggests that the ratio of ratios depends on zenith angle. Figure 2.5 shows the ratio of ratios as a function of $\cos\theta$ for the sub-GeV (E_{vis}< 1.33 GeV) and the multi-GeV (E_{vis}> 1.33 GeV) data samples. The zenith angle distributions of R for both sub-GeV and multi-GeV samples are not flat, somewhat at variance with the results from Kamiokande, which pushes the neutrino oscillation fit to lower values of Δm^2. The best fit for the combined sub-GeV and multi-GeV Super-Kamiokande data in the mode $\nu_\mu \rightarrow \nu_\tau$ is $\sin^2 2\theta \sim 1$ and $\Delta m^2 \sim 3\times10^{-3}$ eV^2.

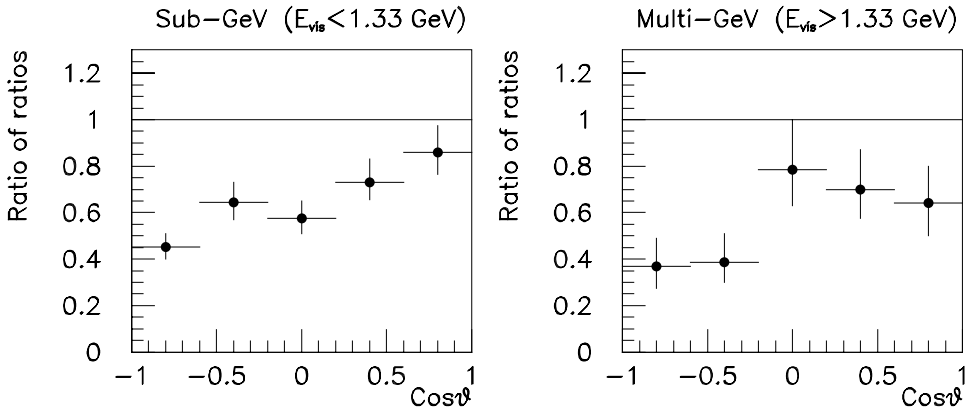

Figure 2.5 – Zenith angle distribution of R for a preliminary analysis of Super-Kamiokande atmospheric neutrino data. The left-hand plot is for the sub-GeV sample and the right-hand plot is for the multi-GeV sample. From [36].

The Soudan 2 detector [39] is a 963 tonne iron tracking calorimeter located in the Soudan Mine in Northern Minnesota at a depth of 2100 m.w.e. The detector consists of 224 identical modules which consist of drift tubes sandwiched between layers of 1.6 mm thick corrugated steel sheets. The tubes are filled by a 85% argon/15% CO_2 mixture. Ionisation deposited in the gas by the passage of a charged particle through a tube drifts towards the closest end of the tube under the influence of an uniform electric field. The ionisation is

amplified and detected at the end of the tube by vertical anode wires and horizontal cathode strips. A three-dimensional picture of an event can be reconstructed from the hits on the cathode strips and anode wires and the drift time. The detector is surrounded by a 4π veto shield which rejects events due to charged particles that originate outside of the detector volume.

The analysis of atmospheric neutrinos performed by Soudan 2 first isolates a sample of contained events, which are defined as events that originate within the fiducial volume of the detector and have no shield activity. These events are then scanned by experienced physicists who decide whether the event is track-like or shower-like. Quasi-elastic ν_μ CC interactions are generally track-like and quasi-elastic ν_e CC events are shower-like. The analysis does not yet include inelastic interactions. An orthogonal approach to the task of event selection and flavour classification in Soudan 2 is also underway [42]. This method uses sophisticated event selection algorithms to classify the events and eliminates the involvement of the human scanner. Both approaches produce values of the ratio of ratios that are consistent with one another and inconsistent with the standard model prediction at the level of 2-3 standard deviations.

The Fréjus [38] experiment operated from 1984 to 1998 in a road tunnel beneath the Alps connecting France and Italy. The detector was an 900 tonne iron calorimeter with dimensions of 6 m × 6 m × 12.3 m and consisted of a sandwich of 3 mm thick iron plates and 912 flash chambers. The fiducial mass of the detector was 554 tonnes. Atmospheric neutrino events in the detector are classified as charged-current muon interactions, charged-current electron interactions or neutral current interactions. The events are also classified as contained or uncontained. The analysis of atmospheric neutrino interactions in Fréjus reports

no significant deviation of the ratio of ratios from unity, although the statistical errors are large.

The NUSEX [37] experiment operated for a period of 6 years between 1982 and 1988 in a road tunnel under Mont Blanc with an overburden of 4800 m.w.e. The detector was a 150 tonne cubical iron calorimeter measuring 3.5 m on each side, consisting of a sandwich of 134 one cm thick iron plates and 9 cm × 9 cm × 3.5 m plastic streamer tubes. The flavour ratio of atmospheric neutrino interactions reported by NUSEX is also consistent with unity, with large statistical errors.

Table 2.2 shows the results of the atmospheric neutrino experiments that have measured the ratio of ratios, R. The fact that two of the iron calorimeter experiments disagree with the water Cerenkov results has been viewed as evidence that there is a large systematic uncertainty associated with the water Cerenkov results. Both NUSEX and Fréjus are situated much deeper underground than the water Cerenkov detectors and it has been postulated [44] that the much greater cosmic ray flux at shallower depths produces a large neutron flux in the detectors due to muon interactions in the surrounding rock. This hypothesis has been refuted by the Kamiokande collaboration, who have analysed the vertex

Experiment	Exposure (kt-yr)	Ratio of ratios
Kamiokande Sub-GeV	7.7	0.60±0.06
Kamiokande Multi-GeV	8.2	0.57±0.08±0.07
IMB	7.7	0.54±0.05±0.07
Super-Kamiokande Sub-GeV	22.5	0.635±0.034±0.010±0.052
Super-Kamiokande Multi-GeV	22.5	0.604±0.065±0.018±0.065
Soudan 2	2.83	0.61±0.14±0.07
Fréjus	2.0	0.99±0.13±0.08
NUSEX	0.74	1.04±0.25

Table 2.2 – Summary of atmospheric neutrino results. The exposures are quoted in units of kiloton years. Adapted from [43].

position distribution of atmospheric neutrino events with vertices that are contained within the fiducial volume of the detector and have found no evidence of neutron contamination [45]. The Soudan 2 collaboration does observe an excess of events at the edges of the fiducial volume but these are taken into account in the analysis and do not significantly bias the ratio of ratios [39].

A second concern is that the water Cerenkov experiments and the Soudan 2 experiment only use quasi-elastic events in their analysis. It has been suggested that poorly understood nuclear effects in low energy (< 1 GeV) quasi-elastic interactions may be responsible for the anomaly that is seen in the water Cerenkov detectors and in Soudan 2. The Fréjus experiment, which sees no anomaly, analyses the full data sample upto an energy of 50 GeV. Analyses of inelastic interactions in Soudan 2 are currently underway and may go some way to resolving this problem.

The most plausible explanation for the anomaly is neutrino oscillations. The data is consistent with oscillations in the modes $\nu_\mu \rightarrow \nu_e$ and $\nu_\mu \rightarrow \nu_\tau$ with $\Delta m^2 \sim 10^{-2}$ eV^2 and $\sin^2 2\theta \sim 1$. The $\nu_\mu \rightarrow \nu_e$ solution has very recently been checked (November 1997) by the CHOOZ experiment located in the Ardennes region of France.

2.5.3 The CHOOZ experiment

The neutrino source for CHOOZ [46] is a pair of pressurised water reactors with a total thermal output of 8.5 GW. Both reactors have been running at full power since August 1997 and produce a flux of $\overline{\nu}_e$ with a mean energy of 3 MeV. The neutrino flux is known to 1.4%. The neutrino detector is situated at a distance of 1 km from the reactor source and at a depth of 300 m.w.e. The neutrino target is a 5 tonne mass of hydrogen-rich parafinnic liquid scintillator (loaded with 0.09% gadolinium) that is contained within an acrylic vessel. The

vessel is immersed in a unloaded liquid scintillator solution which is subdivided into a 17 tonne containment region that is observed by 192 eight-inch photomultiplier tubes and a 90 tonne cosmic ray veto shield that is monitored by two rings of 24 PMT's. The entire assembly is contained within a steel tank and a 1 m thick gravel shielding.

The neutrinos are detected via the following reaction:

$$\bar{\nu}_e + p \rightarrow e^+ + n,$$

and the $\bar{\nu}_e$ signal is a delayed coincidence between the prompt positron and the signal from neutron capture on gadolinium. A signal of 25 events per day is recorded with a background rate due to cosmic ray interactions of 1 event per day. The ratio of the measured to expected neutrino signal for the period March to October 1997 is 0.98 ± 0.04 (stat) ± 0.04 (syst) [47]. The ratio measured as a function of positron energy is also consistent with unity. This result sets, at 90% C.L., a limit of $\Delta m^2 > 0.9 \times 10^{-3}$ eV^2 for maximal mixing and $\sin^2 2\theta < 0.18$ for large Δm^2 and effectively excludes the region of parameter space suggested by the Kamiokande atmospheric neutrino analysis in the mode $\nu_\mu \rightarrow \nu_e$[3].

2.5.4 The LSND experiment

The Liquid Scintillator Neutrino Detector [48] at the LAMPF facility at Los Alamos, New Mexico, is designed to search for $\bar{\nu}_\mu \rightarrow \bar{\nu}_e$ and $\nu_\mu \rightarrow \nu_e$ oscillations with $\Delta m^2 > 0.1$ eV^2. Protons of energy 800 MeV from the LAMPF accelerator are directed onto a water target and 97% of the pions thus produced decay at rest in a copper beam stop. The

[3] CHOOZ sets a limit on $\bar{\nu}_e$ disappearance and hence an upper limit on $\bar{\nu}_e \rightarrow \bar{\nu}_\mu$ oscillations. By the CPT theorem, $P(\bar{\nu}_e \rightarrow \bar{\nu}_\mu) = P(\nu_\mu \rightarrow \nu_e)$ so the CHOOZ result sets the same upper limit on $\nu_\mu \rightarrow \nu_e$ oscillations.

resulting muons produce a beam of $\overline{\nu}_\mu$ with a maximum energy of 52.8 MeV. A monoenergetic ν_μ line is produced by pion decay at rest. The contamination due to $\overline{\nu}_e$ is at the level of 8×10^{-4} of the $\overline{\nu}_\mu$ flux. The LSND detector is a 167 tonne tank of mineral oil with a 0.31 g/l concentration of PBD-butyl. The detector is roughly cylindrical in shape, 8.3 m long and 5.7 m in diameter, and is situated 30 m downstream of the beam stop. The detector is lined by 1220 8'' photomultiplier tubes which detect signals via Cerenkov light and scintillator light.

The LSND collaboration has published the results of a search for $\overline{\nu}_\mu \to \overline{\nu}_e$ oscillations using data collected between 1993 and 1995 [49]. The signature for oscillations is the observation of positrons in the detector via the reaction $\overline{\nu}_e p \to e^+ n$. Positron candidates are defined as events with energies between 36 and 60 MeV correlated in space and time with a photon of 2.2 MeV from the reaction $np \to d\gamma$. The energy cut of 36 MeV is needed to eliminate the background from ν_e interactions since the detector cannot distinguish between electrons and positrons. The background from cosmic ray interactions is reduced by a veto shield which envelopes all but the bottom of the detector. Any remaining beam-unrelated background is well-measured by the beam-off data between spills which is a factor of 14 larger than the beam-on data. The LSND collaboration find 22 events in the data that satisfy the criteria outlined above. The expected background is 4.6±0.6 events. If this excess is attributed to neutrino oscillations then the oscillation probability is $(0.31 \pm 0.12 \pm 0.05)$ %.

The ν_μ produced by pion decay in flight can also be used to search for neutrino oscillations. If there are $\overline{\nu}_\mu \to \overline{\nu}_e$ oscillations, then $\nu_\mu \to \nu_e$ must also occur. The oscillation probabilities derived from both methods should be the same, otherwise this is a signature for CP violation. The LSND collaboration have produced an analysis of $\nu_\mu \to \nu_e$ oscillations

from pion decay in flight [50]. The analysis demands a electron candidate in the detector with energy between 60 and 200 MeV. The upper limit on the electron energy rejects a region of large cosmic ray background. This analysis is more difficult than the decay at rest analysis due to the low ν_μ flux at these energies and the fact that there are no space and time correlated photons in this channel to reduce the background contamination. The LSND experiment also observes an excess of events in this channel, corresponding to an oscillation probability of $(0.26 \pm 0.1 \pm 0.05)$ %, which is consistent with the result of the decay at rest analysis.

The KARMEN detector [51], which is situated at the ISIS spallation neutron facility at the Rutherford Appleton Laboratory, is sensitive to neutrino oscillations over a comparable region of parameter space to that explored by LSND. The unique feature of this experiment is the pulsed nature of the 800 MeV proton beam which is the source of the neutrinos. The time structure of the beam is well matched to the different lifetimes of the pion (26 ns) and the muon (2.2 μs). The time distribution of ν_μ follows the time structure of the proton beam whereas the ν_e and $\overline{\nu}_\mu$ are characterised by the muon decay time constant. This timing information provides a powerful means of background rejection.

The detector is a 56 tonne segmented liquid scintillator calorimeter that is situated at a distance of 17.5 metres downstream of the beam stop. The detector is subdivided into 512 modules, each module is constructed with acrylic glass walls and measures 18 cm by 18 cm by 350 cm. The modules are monitored by two 3'' photomultiplier tubes at each end. Light is transmitted by total internal reflection at the wall/air-gap boundary between modules. Gadolinium-loaded paper is inserted between modules to detect neutrons via the observation of a de-excitation photon that results from neutron capture by the Gadolinium. A veto counter that reduces the cosmic ray background by a factor of 10^3 surrounds the detector and

the entire apparatus is shielded from neutrons from the spallation source by a 600 tonne steel blockhouse.

The signature that would indicate $\bar{\nu}_\mu \rightarrow \bar{\nu}_e$ oscillations in KARMEN is a positron of energy between 10 and 50 MeV correlated in space and in delayed time coincidence by a photon from neutron capture. The positrons are also expected between 0.5 and 10 μs after beam on target. The number of such events observed is consistent with the expected background rate, which sets a limit on the oscillation probability of $P(\bar{\nu}_\mu \rightarrow \bar{\nu}_e) \leq 3.75 \times 10^{-3}$ at 90% confidence. A null result in the mode $\nu_\mu \rightarrow \nu_e$ is also obtained which yields $P(\nu_\mu \rightarrow \nu_e) \leq 1.9 \times 10^{-2}$ at 90% confidence [51].

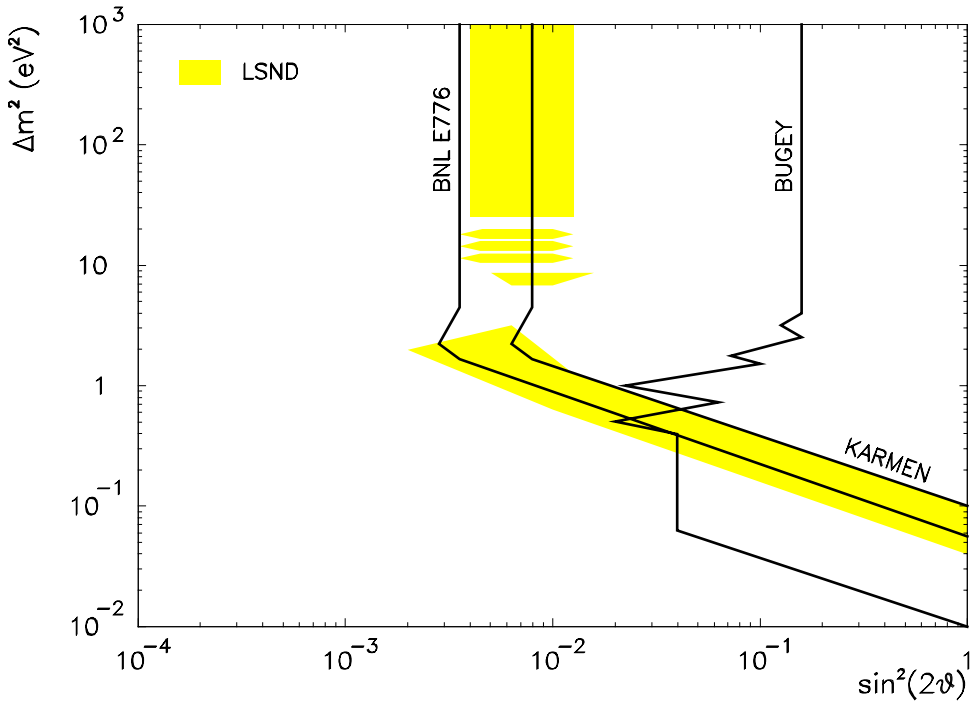

Figure 2.6 – Neutrino oscillation searches in the mode $\bar{\nu}_\mu \leftrightarrow \bar{\nu}_e$. The shaded area represents the 90% C.L. allowed region found by the LSND experiment. The regions to the right of the heavy lines are excluded at 90% confidence.

The current status of experimental searches for $\overline{\nu}_\mu \to \overline{\nu}_e$ oscillations is shown in Figure 2.6. The favoured region of parameter space suggested by the LSND result is shown by the shaded area. The exclusion regions implied by the null results of BNL E776 [52], KARMEN [51] and the BUGEY reactor experiment [53] are also shown. A small region of the LSND allowed region between $0.3 < \Delta m^2 < 2$ eV^2 is not excluded by the other experiments. Within the next two years, the KARMEN experiment will run with an improved veto shield and increased neutron detection efficiency and will fully explore the region of parameter space suggested by the LSND positive result.

2.5.5 Neutrino oscillation interpretation

If the solar neutrino problem, the atmospheric neutrino anomaly and the LSND excess are due to neutrino oscillations then they must all be explained in a unified framework. If the result from LEP of three species of light neutrino is taken into account then there is an immediate problem. The three experiments probe very different regimes of L/E: solar neutrinos have $L/E \sim 10^{10}$ km/GeV; atmospheric neutrinos span the range $20 - 20000$ km/GeV and the LSND experiment has $L/E \sim 10$ km/GeV. All three classes of experiment claim to see an energy dependent suppression of the neutrino flux (the LSND evidence for this is somewhat weak). If this is taken at face value then it suggests that there are three distinct mass-squared differences responsible for the oscillations. Only two independent Δm^2 values are possible for three neutrino species so the data seems to be suggesting the need for a fourth (sterile) neutrino [54][55].

The evidence is not conclusive. It has been shown that if the zenith angle dependence of the ratio of ratios in the Kamiokande experiment is discarded, then it is possible to reconcile all three anomalies in a three-generation framework [56]. The recent results from

Super-Kamiokande, however, seem to support the Kamiokande zenith angle dependence, and even push down the value of Δm^2. It must also be noted that the LSND anomaly is the result of a single experiment and, unless the result can be replicated by another, it should be treated with a degree of caution.

One model which can fit the world data on neutrino oscillations, with the exception of the LSND experiment, is the so-called "threefold maximal mixing" scheme [57]. In this model, the mixing matrix elements are the complex cube roots of unity. This results in the following properties:

- survival probabilities are the same, regardless of generation;
- transition probabilities are cyclical;

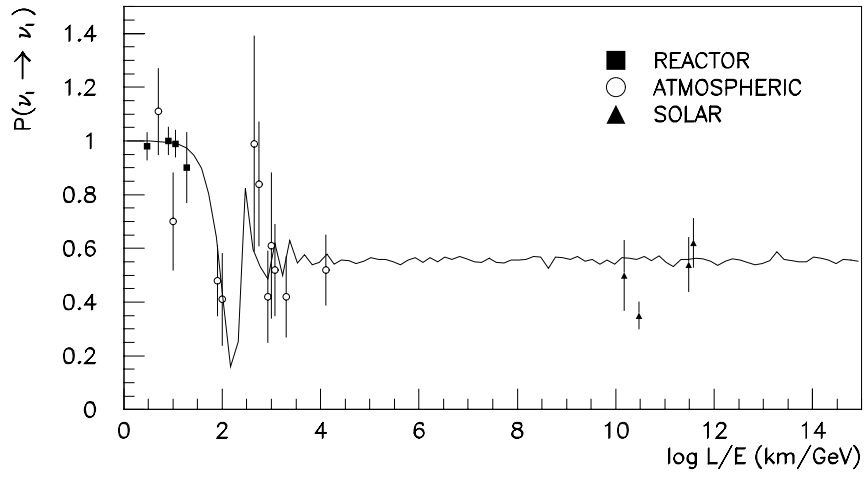

Figure 2.7 - Neutrino survival probability as a function of L / E. The experimental results are represented by the data points and the prediction of threefold maximal mixing with $\Delta m^2 = 0.0072$ eV^2 is indicated by the solid line. This plot is adapted from [57] and does not include the recent CHOOZ and Super-Kamiokande results.

- the symmetry transformation CP is maximally violated.

Given that the mixing angles are fixed *a priori*, the only parameters that are extracted from experimental data are the two independent Δm^2's. Figure 2.7 shows the neutrino survival probability plotted as a function of L/E. The data points are the results of reactor, accelerator, atmospheric and solar neutrino experiments. The solid line is the prediction of maximal mixing. The dip in survival probability from the atmospheric neutrino data sets one Δm^2 at 0.72×10^{-2} eV^2. The mean value of the survival probability for $L/E >> 10^3$ km/GeV is therefore predicted to be 5/9. This is good in agreement with the solar neutrino data (which have $L/E \sim 10^{10}$ km/GeV), with the exception of the Homestake experiment. The positioning of a second value of Δm^2, between $10^{-2} < \Delta m^2 < 10^{-10}$ eV^2 will result in an average survival probability of 1/3 provided that $L/E >> (\Delta m^2)^{-1}$. The Homestake experiment can therefore be reconciled with the theory if $\Delta m^2 \sim 10^{-11}$ eV^2 but the Gallium experiments, SAGE and GALLEX, which benefit from more accurate theoretical predictions, are not consistent with this value of Δm^2. Harrison, Perkins and Scott argue that the Homestake result is consistent with no second Δm^2 (and hence a neutrino survival probability of 5/9) given the uncertainties in the theoretical predictions of the ^{8}B flux from the sun [58].

The recent result from CHOOZ, however, seems to exclude this hypothesis since maximal mixing would imply $\overline{\nu}_e \rightarrow \overline{\nu}_x$ oscillations with an effective $\sin^2 2\theta$ of 8/9. This can presumably be reconciled with the model by setting a lower value of Δm^2 ($\sim 10^{-3}$ eV^2) at the expense of a inferior level of agreement with the Kamiokande multi-GeV atmospheric neutrino data.

Other authors have performed more general three-generation fits to the existing neutrino oscillation data and have found regions of parameter space that are allowed by both

atmospheric and solar neutrino data. The fits favour a low value of Δm^2 (a few times 10^{-3} eV^2) for the atmospheric neutrino anomaly and small angle MSW oscillations for the solar neutrino problem [59]. The LSND result is difficult to accommodate in these fits.

2.5.6 Current status and future prospects

The status of neutrino oscillations searches is summarised by Figure 2.8 and Figure 2.9, where Figure 2.8 is for $\nu_\mu \to \nu_e$ oscillations and Figure 2.9 is for $\nu_\mu \to \nu_\tau$. The experimental hints of neutrino oscillation signals are indicated by shaded areas and exclusion limits are shown by thick lines. All limits and allowed regions are at 90% confidence. Only the experiments that produce the most restrictive limits in their respective modes are shown to avoid cluttering the plots.

2.5.6.1 Status of $\nu_\mu \to \nu_e$ oscillation searches

The most restrictive limit at high Δm^2 in the mode $\nu_\mu \to \nu_e$ has recently been set by the NOMAD [60] experiment. NOMAD is a large fine-grained tracking calorimeter situated at a distance of 1 km downstream of the CERN SPS neutrino beam target which produces a beam of ν_μ with an average neutrino energy of 20 GeV. The main purpose of the experiment is to search for neutrino oscillations in the mode $\nu_\mu \to \nu_\tau$ by studying the event kinematics which are different for events containing tau leptons. The experiment is able to set a limit on $\nu_\mu \to \nu_e$ oscillations due to powerful electron identification capabilities. Preliminary results of a subset of the 1995-6 data have been presented. For Δm^2 above 100 eV^2 a limit of $\sin^2 2\theta < 2 \times 10^{-3}$ is set at 90% confidence.

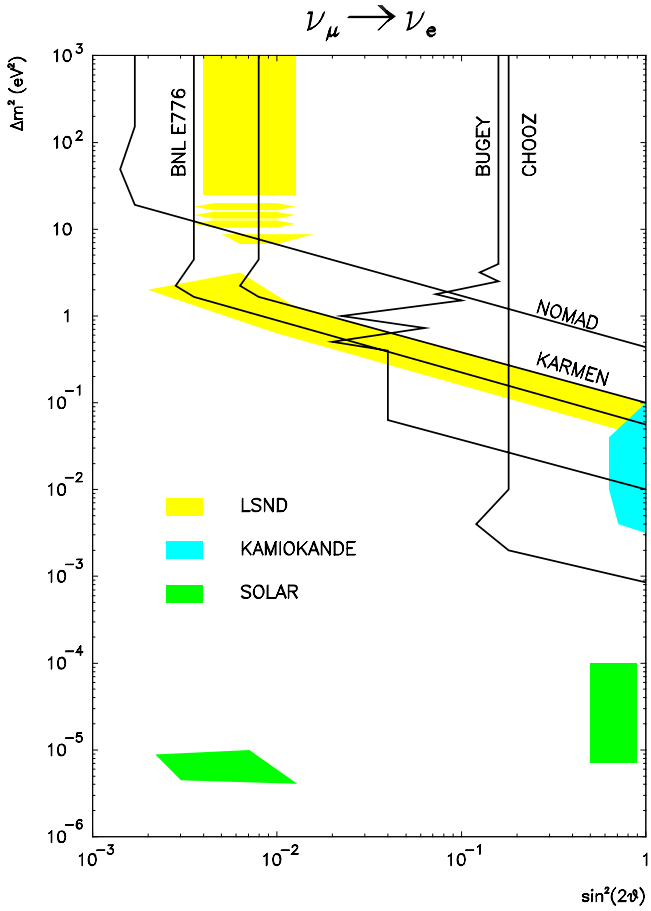

Figure 2.8 – Current experimental limits and favoured regions in the mode $\nu_\mu \rightarrow \nu_e$. Adapted from [43]. The 90% C.L. exclusion limits of E776 [52], KARMEN [51], BUGEY [53], CHOOZ [47] and NOMAD [60] are shown by the solid lines and the 90% C.L. allowed regions of LSND [49], the Kamiokande atmospheric neutrino analysis [41] and the combined results of the solar neutrino experiments [59] are shown by the shaded areas.

The recent CHOOZ result is inconsistent with the interpretation of the Kamiokande multi-GeV zenith angle distribution of atmospheric neutrinos in the mode $\nu_\mu \rightarrow \nu_e$. The CHOOZ result will be further checked by the Palo Verde reactor experiment [61] which is sensitive to $\nu_\mu \rightarrow \nu_e$ oscillations with $\Delta m^2 > 10^{-3}$ eV^2 and $\sin^2 2\theta > 0.1$ and is expected to produce results in 1998.

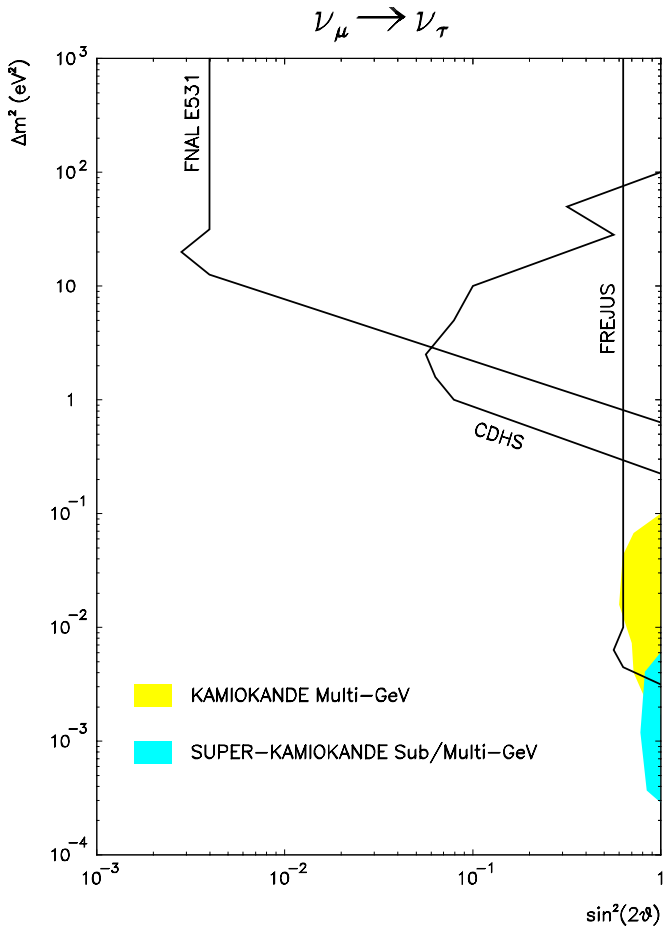

Figure 2.9 – Current experimental limits and favoured regions in the mode $\nu_\mu \rightarrow \nu_\tau$. Adapted from [43]. The 90% C.L. exclusion limits of E531 [62], CDHS [63] and Frejus [64] are shown by the solid lines and the 90% C.L. allowed regions from the Kamiokande [41] and Super-Kamiokande [36] atmospheric neutrino analyses are shown by the shaded areas.

2.5.6.2 Status of $\nu_\mu \rightarrow \nu_\tau$ oscillation searches

NOMAD has produced a preliminary limit on $\nu_\mu \rightarrow \nu_\tau$ oscillations at high Δm^2 of $\sin^2 2\theta < 4 \times 10^{-3}$ eV^2. The CHORUS experiment [65] which uses the same SPS neutrino beam as NOMAD, searches for decay kinks in photographic emulsion which are characteristic of tau lepton decays. No such events have been observed in 50000 charged-current events that have been analysed by CHORUS, which corresponds to a limit of

$\sin^2 2\theta < 8\times10^{-3}$ eV^2. These limits are currently competitive with that from the E531 experiment which set the previous best limit for $\Delta m^2 > 5$ eV^2. The projected limit that could be set on $\sin^2 2\theta$ for a full analysis of four-year CHORUS and NOMAD data sets is 10^{-4}, which is an order of magnitude better than the present limits. This limit is set to be improved by a further order of magnitude by the COSMOS experiment [66] which will run at the NuMI neutrino beam facility at Fermilab. The detector is similar in design to CHORUS and expects to begin taking data in 2002.

2.5.7 Long-baseline experiments

Several new neutrino oscillation projects with accelerator-produced neutrino beams and long baselines have been proposed to fully explore the regions of parameter space suggested by the atmospheric neutrino anomaly in the modes $\nu_\mu \to \nu_e$ and $\nu_\mu \to \nu_\tau$. The value of L/E for these experiments is chosen to provide maximum sensitivity to neutrino oscillations with $\Delta m^2 \sim 10^{-2}$-10^{-3} eV^2. The optimal value of L/E is therefore:

$$L/E \sim \pi/2.53\Delta m^2 \sim 100-1000 \text{ km/GeV}.$$

Since it is desirable to have high (~10 GeV) neutrino energies to maximise the neutrino event rate and to be above the tau production threshold (3.5 GeV on free nucleons), baselines of approximately 1000 km are required. The detectors therefore have to be multi-kiloton devices to produce an acceptable event rate.

Three proposals to build long-baseline neutrino experiments are currently at an advanced stage of planning:

1. **KEK to Super-Kamiokande (K2K) experiment** [67]. This experiment will use a neutrino beam from the 12 GeV KEK-PS with a mean energy of 1 GeV. The beam is directed towards the existing Super-Kamiokande experiment, which is

250 km away. A 1 kiloton water Cerenkov detector close to the beam source will monitor the neutrino flux. The experiment is currently in construction and expects to commence data taking in 1999. The detector is sensitive to $\nu_\mu \rightarrow \nu_\tau$ oscillations by comparing the rate of ν_μ CC events observed in the detector to that expected for no oscillations. Measurement of the muon energy spectrum can give information on the value of Δm^2 if a positive effect is found. The detector is also sensitive to $\nu_\mu \rightarrow \nu_e$ oscillations. The experiment will explore neutrino oscillations with $\Delta m^2 > 10^{-3}$ eV^2 and $\sin^2 2\theta > 0.1$.

2. **CERN to GRAN SASSO** [68]. This experiment plans to direct a neutrino beam from the CERN-SPS to a large underground detector in the Gran Sasso laboratory in Northern Italy. The baseline for this experiment is 732 km. Several possible detector designs are currently being considered and the experiment may begin to take data early in the next century. As an example, ICARUS is a large (6 kiloton) liquid Argon-Methane TPC detector which can produce event pictures of comparable quality to bubble chamber experiments. The detector is expected to have powerful electron identification abilities and is predicted to reach a sensitivity of $\sin^2 2\theta \sim 10^{-3}$ at large Δm^2 and $\Delta m^2 \sim 10^{-3}$ at $\sin^2 2\theta = 1$ in the $\nu_\mu \rightarrow \nu_e$ channel. The mean neutrino energy (27 GeV) means that the detector is sensitive to $\nu_\mu \rightarrow \nu_\tau$ oscillations via the observation of events that have topologies that are consistent with tau lepton interactions.

3. **MINOS experiment** [69]. This experiment is the subject of this thesis and will be explained in detail in subsequent chapters.

Chapter 3 The MINOS Experiment

In 1991 a proposal was submitted to the Fermilab Physics Advisory Committee to direct a neutrino beam from the Main Injector TEVATRON upgrade at Fermilab to the Soudan 2 detector in Northern Minnesota [70]. With a baseline of 731 km and a mean neutrino interaction energy of 17 GeV, the experiment would have maximum sensitivity to neutrino oscillations with:

$$\Delta m^2 = \pi E / 2.53L \sim 0.03 \text{ eV}^2, \tag{3.1}$$

close the parameters suggested by the atmospheric neutrino anomaly ($\Delta m^2 > 10^{-3}$ eV^2 and $\sin^2 2\theta \sim 1$).

A subsequent proposal, submitted in January 1995, by the newly formed MINOS collaboration, opted to build a new 10 kiloton detector at the Soudan mine to intercept the Main Injector beam [69]. This new detector, although more coarsely grained than Soudan 2, would record ten times as many events and therefore explore a larger area of neutrino oscillation parameter space. This proposal (P875) was approved by the Fermilab PAC in April 1995.

The construction of the MINOS cavern and detector is projected begin in late 1998-1999. The detector will be constructed in three stages. The neutrino beam is expected reach Soudan in 2002 with at least a third of the detector in place. The full detector is expected be complete by the year 2004 and the experiment will initially run for two years. Subsequent running will depend on the results of the initial run. If $\nu_\mu \rightarrow \nu_\tau$ oscillations are discovered then an emulsion-based upgrade may be considered in order to search for the presence of

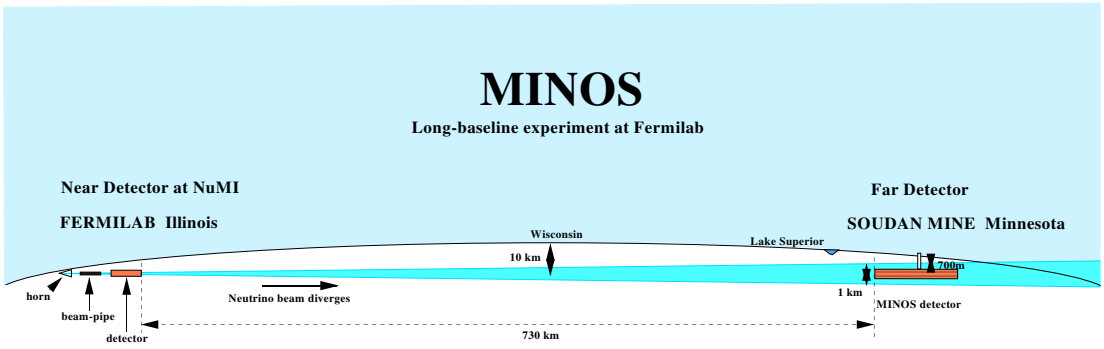

Figure 3.1 – Schematic of the MINOS experiment (not to scale).

characteristic tau decay kinks that could be produced in the emulsion by ν_τ CC interactions. Narrow band or low energy beams may also be desirable to measure the mixing parameters with greater precision than is possible with the default beam design.

The MINOS experiment will consist of three elements: the neutrino beam at Fermilab, the near detector downstream of the beam target at the Fermilab site and the far detector in the Soudan mine. Figure 3.1 shows a sketch of the experiment.

3.1 Neutrino beam

The NuMI neutrino beam will be used by the MINOS near and far detectors and the COSMOS short-baseline experiment [66]. The steps that will be necessary to produce this beam are as follows [71]. A 120 GeV proton beam is extracted from the Fermilab main injector (a 1 ms spill every 2 seconds) and is brought to a focus at the carbon production target. A flux of 3.7×10^{20} protons on target are expected per calendar year. The secondary particles resulting from proton-nucleus interactions are produced with a range of production angles. These secondaries are efficiently focussed by a system of three magnetic horns. The focussed π's and K's then enter the decay pipe, an evacuated space in which the secondaries may decay. The decay pipe is 750 m long, which is comparable to the mean

decay length for a 15 GeV pion, and 1 m in radius, which prevents a significant fraction of the secondaries from interacting with the decay pipe walls before decaying. A water-cooled aluminium and copper hadron absorber stops any primaries or secondaries that reach the end of the decay pipe and a 240 m dolomite absorber eliminates the muon component of the beam.

The NuMI neutrino beam is predominantly of ν_μ flavour, produced by the decay $\pi^+ \rightarrow \mu^+\nu_\mu$. The neutrino energy distribution is approximated by the following expression [71]:

$$E_\nu = \frac{0.427 E_\pi}{(1+\gamma^2\theta^2)}, \tag{3.2}$$

where E_π is the pion energy, γ is the Lorentz boost and θ is the angle (in radians) between the pion line of flight and the detector. Figure 3.2 shows the neutrino flux spectrum expected

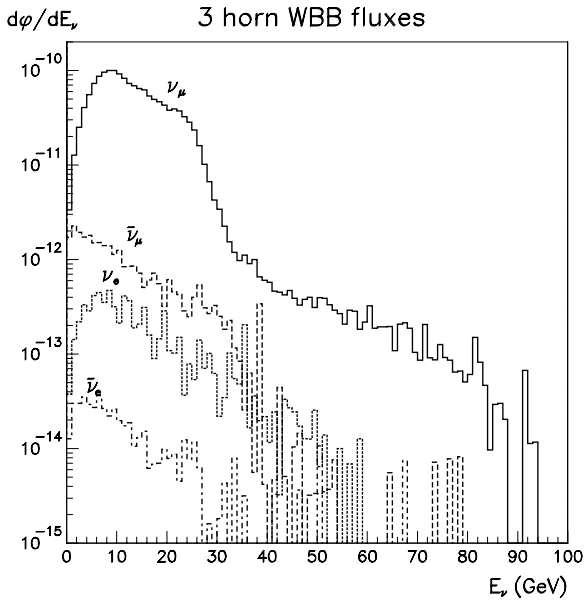

Figure 3.2 – Neutrino flux distributions (in units of neutrinos/m^2/GeV/protons on target) as a function of energy expected at the far detector site.

in the far detector. The bulk of the ν_μ flux is between 5 and 30 GeV, peaking at approximately 10 GeV. This beam has been designed to maximise the flux of high energy neutrinos at the far detector site in order to be sensitive to $\nu_\mu \rightarrow \nu_\tau$ oscillations via the observation of tau leptons (tau production threshold ~ 3.5 GeV). The relative interaction rates for all flavours are: 98.7% ν_μ (from π, K decays); 0.85% $\overline{\nu}_\mu$ (largely π^- decays); 0.48% ν_e (μ and K decays) and 0.02% $\overline{\nu}_e$ (K_L^0 decays) [71].

3.2 Far detector

The MINOS far detector will be placed in a cavern in the Soudan mine, North Minnesota, which is at a distance of 731 km from Fermilab. The detector will be at a depth of 2100 metres of water equivalent (m.w.e.), which reduces the cosmic ray flux by a factor of 10^5 from the surface rate. The neutrino beam has a half-width of ~1 km at the mine so the nearby Soudan 2 experiment [39] can also be used to search for neutrino oscillations in addition to the MINOS far detector.

The analyses described in this thesis were performed at a time when the detailed design of the far detector was uncertain. A reference detector was used in the simulations that differs from the current design. The differences between the two designs are small and do not significantly differ in terms of the physics capabilities of the experiment.

The reference detector used in this thesis is a large tracking iron calorimeter comprising of planar steel sheets which are octagonal in shape and 8 m wide. Figure 3.3 shows a sketch of the reference far detector. The steel thickness is nominally 2 cm, although a reference detector with 4 cm steel plates is studied in Appendix B to investigate the physics consequences of adopting a coarser grained detector. The detector mass of 10 kilotons is

made up of 1200 2 cm thick steel planes which are physically divided into three equal length supermodules. This sub-division allows the experiment to begin taking data once 1/3 of the far detector has been constructed. A current-carrying copper coil runs through the centre of each supermodule and provides a toroidal magnetic field (average field strength ~ 1.5 tesla) which focuses and increases the containment of muons in the detector. The field also provides a measurement of the momentum of muons that exit the detector volume.

Active detector elements are interleaved between the steel planes. In the reference design, these take the form of extruded plastic cells which are 8 m in length with 2 cm pitch. The cells are filled with a mineral oil based liquid scintillator. The passage of a charged particle through a particular cell produces de-excitation photons which are transmitted to the readout end of the cell by means of a 1 mm diameter wave-shifting fibre. Each fibre is optically coupled to an individual pixel of a multi-channel photomultiplier tube, which amplifies the signal and passes the resulting pulses to the readout electronics. There are

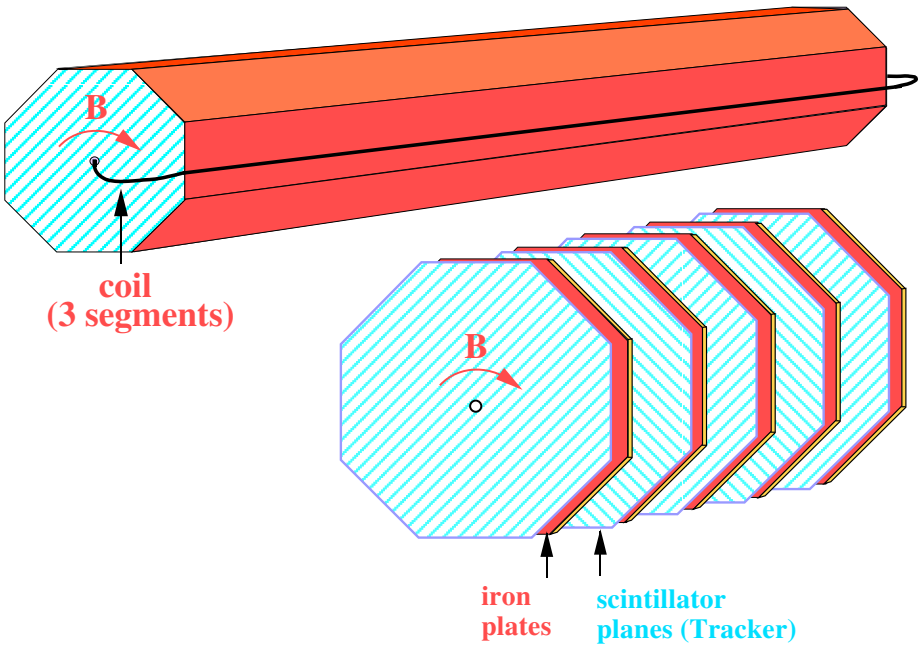

Figure 3.3 – Sketch of the reference MINOS far detector.

480,000 electronics channels for a detector with 2 cm steel plates. Light is attenuated down the fibre and there is roughly a factor of four in the relative light yield between the near and far ends of the fibre. The orientation of each successive active plane is rotated by 90°.

In Chapter 8 a simulated reference detector with aluminium proportional tube active detectors is studied to compare its physics performance with the reference detector outlined above.

The 10 kiloton reference detector expects to record 82200 ν_μ charged-current and neutral current interactions in a two year run if there are no neutrino oscillations.

The current far detector design for MINOS, which was decided in September 1997 [72], differs from the reference detector in a number of aspects:

- 8 kT total mass rather than 10 kT;
- 730 one inch steel plates rather than 1200 2 cm plates;
- solid scintillator active detectors rather than liquid scintillator.

3.3 Near detector

The purpose of the near detector is to measure the properties of the neutrino beam close to the source; the near detector will be situated 500 m downstream of the end of the decay pipe. Measurements in the near detector can be used to refine Monte Carlo beam simulations that predict the neutrino flux and energy at the far detector site. Comparing results from the near and far detectors will in principle cancel many sources of systematic

error, both beam and detector related. It is therefore important that the near and far detectors are closely similar in design.

The neutrino energy spectra at the near and far detector sites are not the same. The near detector subtends a much larger solid angle to the decay pipe than the far detector so neutrinos that are emitted at large angles are more likely to intercept the near detector than the far. Figure 3.4 shows a comparison of the shapes of the far detector and near detector ν_μ CC energy spectra (top plot) and the ratio of the far and near spectra (bottom plot). There are

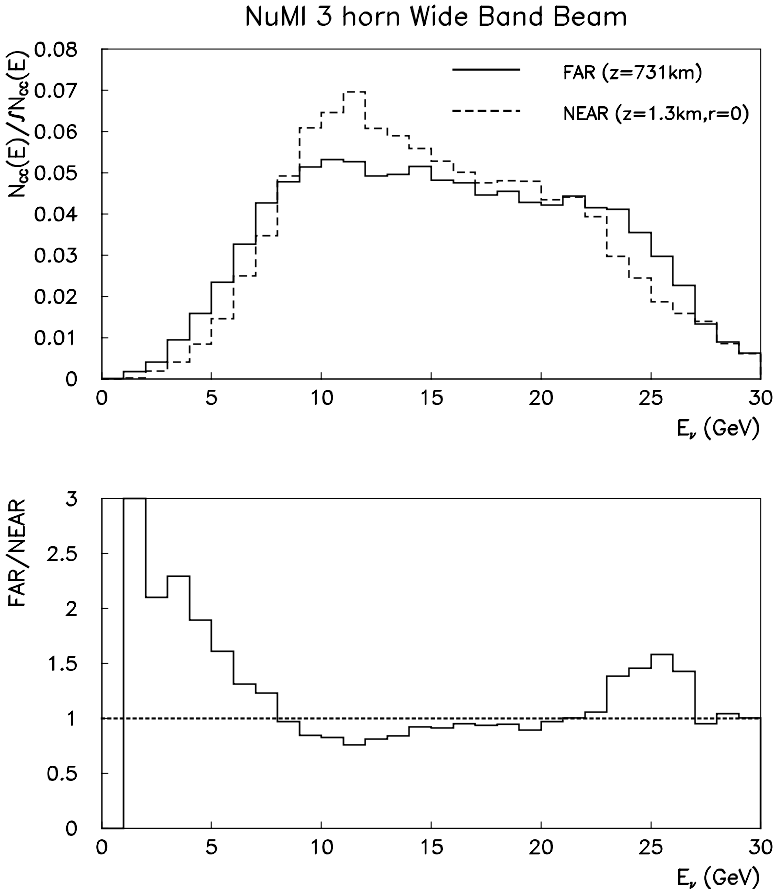

Figure 3.4 - Predicted near and far detector ν_μ CC energy spectra for the NuMI 3 horn WBB. Top plot: energy distributions for the far detector (solid histogram) and the central portion of the near detector (dashed histogram). The two histograms are normalised to the same area. Bottom plot: the ratio far/near as a function of neutrino energy.

(relatively) more neutrinos at very low and very high energies in the far detector than in the near detector. This is because the pion decay kinematics produce neutrinos which are more collimated at these energies and are thus more likely to hit the far detector than neutrinos of moderate (10 GeV) energy.

Three effects contribute to the differences between the near and far detector energy spectra [71].

1. Low energy pions decay at the beginning of the decay pipe (pion decay length ~ $\gamma c\tau$ ~ 500 m for a 10 GeV pion). The neutrinos that emerge from the end of the decay pipe have small angles. This effect is exactly calculable and produces more low energy neutrinos in the far detector relative to the near.

2. Well-focussed pions are more likely to decay at small angles than badly focussed pions. This effect depends on focussing misalignments and the hadronic p_T distribution.

3. Pions at large radii with respect to the centre of the decay pipe are more likely to produce neutrinos at large angles. The relative chance of these neutrinos intercepting the near detector to the far detector therefore increases. This effect also depends on the focussing and p_T. These last two effects produce more neutrinos at medium (10 GeV) energies in the near detector and relatively more at high energy in the far detector.

These differences are reduced by selecting only neutrinos in the near detector that subtend small angles to the beam. This is achieved by only using events with vertices that are within the central 25 cm of the beam spot.

Monte Carlo simulations using the reference near detector design are not used in this analysis although the consequences of the beam differences between near and far detector sites for the measurement of neutrino oscillation parameters are investigated in Chapter 4.

The current near detector design is a smaller version of the baseline far detector. It consists of magnetised octagonal steel planes that are 6 m wide and one inch thick. Layers of active detector are sandwiched between the steel plates. The detector has a total mass of approximately 1 kiloton. The current design is logically divided into four longitudinal regions [73]:

1. veto region (20 planes of steel) to eliminate any background from neutrons that are produced in the rock upstream of the detector. Neutrino events in this region are not used;

2. target region (40 planes of steel) within which the vertices of neutrino events must lie;

3. hadron shower region (60 planes of steel) to contain the hadronic component of events originating in the target region;

4. muon spectrometer (160 planes of steel) which is used to contain the muons from events originating in the target region or provide a measurement of the muon momentum via magnetic bending for those that exit the detector.

The beam is offset from the centre of the detector by 1.5 m and, since the beam size is small (~1 m), only one quadrant of the first three logical regions is instrumented, as shown in Figure 3.5.

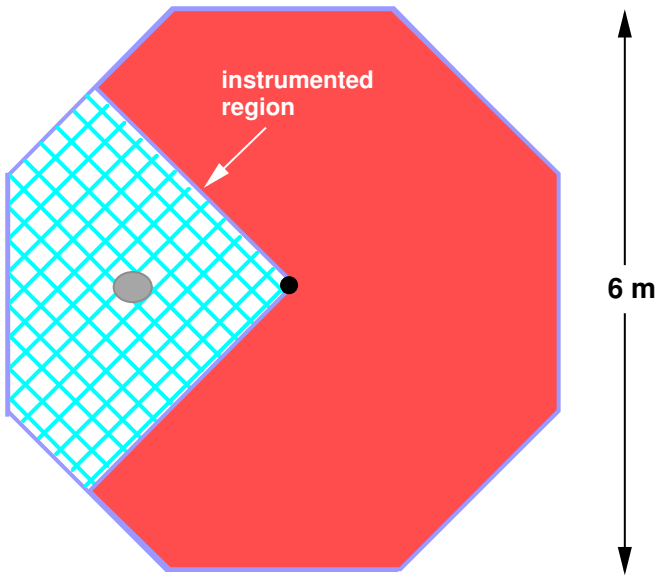

Figure 3.5 – The instrumented upstream face of the current near detector design. The central 25 cm of the beam spot is shown by the shaded area in the middle of the instrumented region.

The event rate in the near detector will be significantly higher than in the far detector, 150 neutrino events and 50 muon events from upstream neutrino interactions are expected in the detector per 1 ms spill. The number of CC events expected in the near detector per kiloton per year is roughly 10^6 of that expected in the far detector.

3.4 The GMINOS Monte Carlo package

The Monte Carlo package used by the MINOS collaboration is a GEANT based system written in FORTRAN 77 and uses the NEUGEN event generator that was originally written for the Soudan 2 Monte Carlo [74]. The data structure takes the form of ADAMO [75] tables which specify the details of the detector geometry and hold the hits and digitisation information for each simulated event. An event display package, VINES, exists to view the generated events in three dimensions.

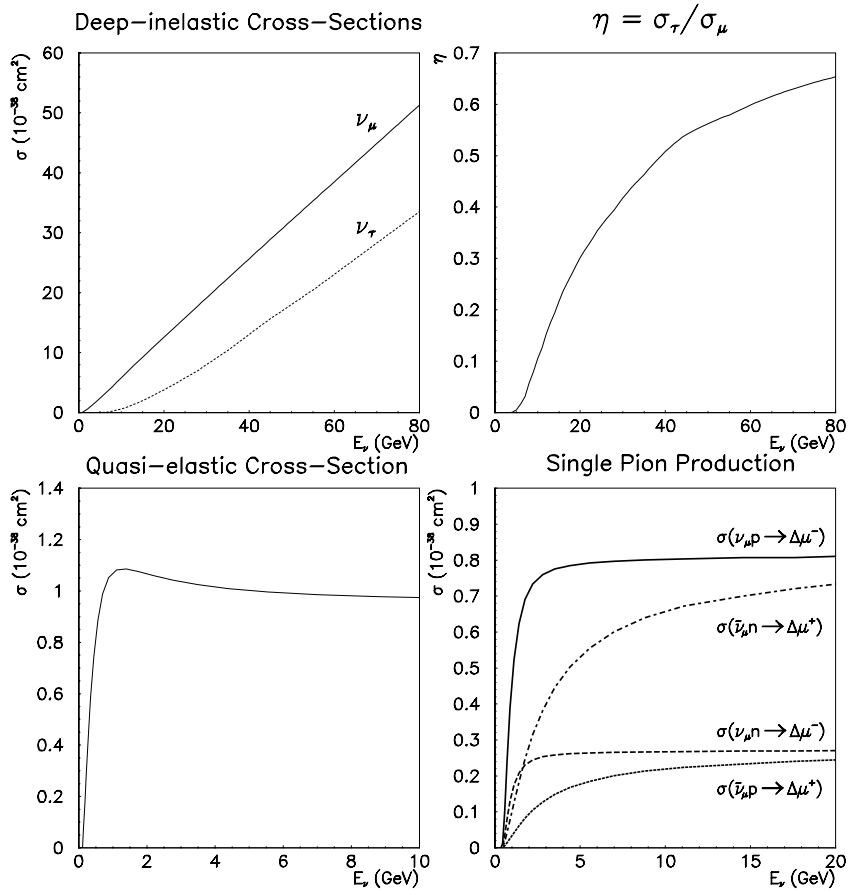

Figure 3.6 – Neutrino cross-sections from the NEUGEN event generator package. Top left: ν_μ CC and ν_τ CC deep-inelastic cross-sections. Top right: ratio of ν_τ CC/ν_μ CC cross-sections. Bottom left: ν_μ quasi-elastic cross-section. Bottom right: single pion production cross-sections.

The NEUGEN event generator package generates neutrino events in the range 0 to 120 GeV according to the neutrino fluxes and cross-sections that are shown in Figure 3.6. The ν_τ CC cross section is suppressed with respect to the ν_μ CC cross-section due to the mass of the τ lepton. The threshold for creating a tau from ν_τ- nucleon scattering is 3.5 GeV. At low energies (< 2 GeV) the cross-sections for quasi-elastic, resonance production and deep inelastic processes are comparable in magnitude, above this energy deep inelastic scattering dominates. The cross-sections that are calculated by NEUGEN are in

excellent agreement with experimental data from bubble chamber neutrino experiments at low energy (~1 GeV) and are in agreement with large sampling calorimeter neutrino experiments at higher energy (10-100 GeV) [74]. The decay of tau leptons is modelled by the TAUOLA [76] package which includes the effects of tau polarisation.

The particle four-vectors are passed from NEUGEN to GEANT for tracking through the detector medium. The reference MINOS detector design is specified by a series of control cards that are passed to GEANT, describing the detector geometry, details of active and passive media and active detector response parameters (attenuation lengths in scintillator, for example). The magnetic field strength at any point within a steel plane is given by a field map that is the result of a finite element calculation. Tracking and energy loss are handled by GEANT, and the active detector response is simulated by applying response functions to the GEANT tracking hits. These functions are derived from first principles calculations and are calibrated by experimental data where available.

The component steps of the detector simulation are listed below:

1. a particle passing through a scintillator cell loses energy. This energy loss, which is the integral of dE / dx over a small distance Δx, is calculated by GEANT.

2. The energy loss is converted into light (or number of photoelectrons) by applying Birks' Law [4]:

$$dL/dx = \frac{A \times dE/dx}{1 + B \times dE/dx}, \tag{3.3}$$

where L is the light yield (in photoelectrons), A is the light yield for a low specific ionisation density (19.56 photoelectrons are produced for an energy deposition of 2.8 MeV) and B is Birks' constant, which must be determined for each scintillator

by measurement. GMINOS uses a value of $B = 13.3$ cm/GeV, which is derived from measurements made in the MACRO detector. Figure 3.7 shows the number of photoelectrons predicted by equation (3.3) as a function of dE/dx. The scintillator does not respond linearly to the ionisation density; the light yield saturates for highly ionising particles ($dE/dx > 100$ MeV/cm), which are generally slow-moving nuclear fragments.

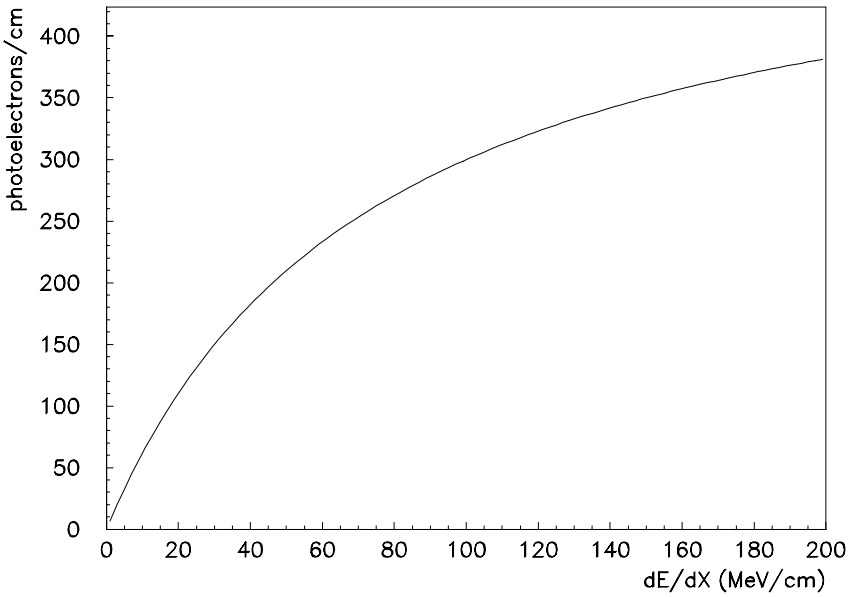

Figure 3.7 - The light yield (in photoelectrons) as a function of ionisation density for the liquid scintillator detector response used in GMINOS.

3. The photons are collected by a 1 mm diameter wave-shifting fibre, which can be up to 8 metres in length. The fibre is optically coupled to a photodetector and the far end of the fibre is mirrored with a reflectivity of 70%. The relative light yield is attenuated as the distance from the readout end of the fibre is increased. The attenuation is given by the following equation:

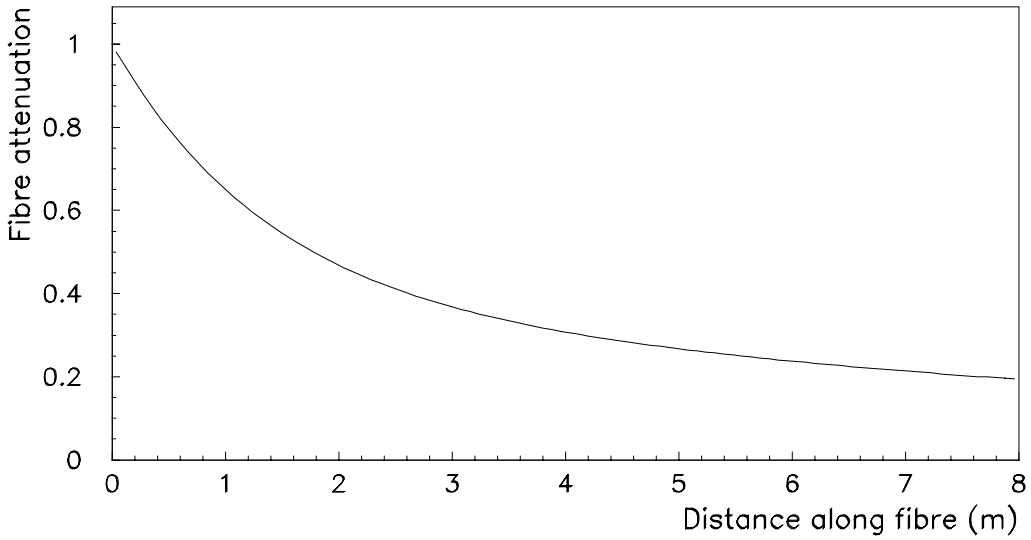

Figure 3.8 - The attenuation of light down the wave-shifting fibre.

$$L(x) = \frac{L_o}{1.66}\left(e^{\frac{-x}{1.35}} + 0.66e^{\frac{-x}{11}}\right) \tag{3.4}$$

where L is the light yield (in photoelectrons) measured at the readout end of the fibre, L_o is the light yield produced by the energy loss of the particle and x is the distance (in metres) between the point of production and the readout end. The two attenuation lengths (1.35 m and 11 m) have relative normalisations of 1.0 and 0.66 respectively and are taken from experimental measurements. Figure 3.8 shows the attenuation of light as a function of distance from the readout end of the fibre, predicted by equation (3.4). There is a factor of four in light yield between the near and far ends of the fibre.

4. The quantum efficiency of the photodetector is 10%. An average of 22 photoelectrons are expected from the passage of a muon through a scintillator cell at the near end. The resulting digitisations are placed in ADAMO tables to be used for physics analyses.

The MARS (MAster Reference System) co-ordinate system used by GMINOS for the far detector is described in [77] and sketched in Figure 3.9. The z- axis runs along the centreline of the detector. The neutrino beam from Fermilab is orientated at an angle of +3° relative to the positive z direction due to the curvature of the Earth between the beam source and the far detector site. The positive y axis is defined to be up (opposite local gravity) and the positive x axis points in a westerly direction to form a right-handed co-ordinate system. The origin is located on the front face of the detector hall.

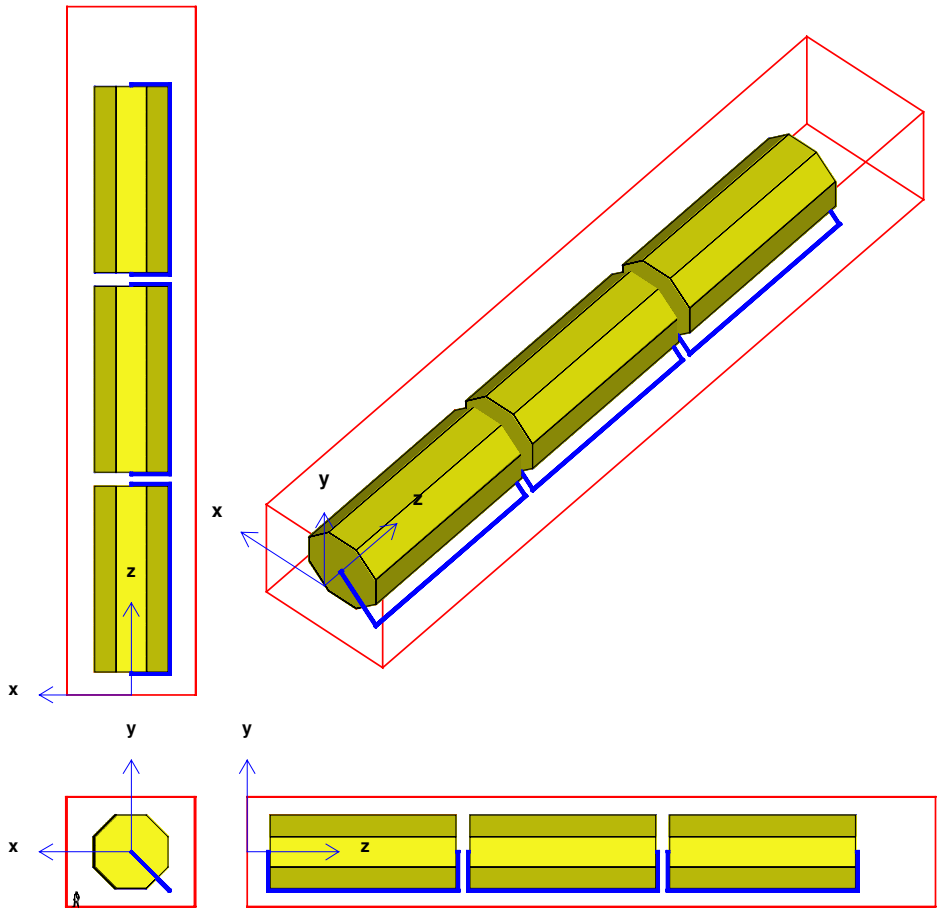

Figure 3.9 – The MARS co-ordinate system, from [77]. This figure shows a reference far detector which is divided into three super-modules. The current-carrying coil is visible in the $(-x,-y)$ quadrant. The orientation of the neutrino beam is +3° relative to the $+z$ direction.

Figure 3.10 shows a VINES picture of a typical GMINOS ν_μ CC event, projected in the $x-z$ plane. The two pairs of parallel lines at the top and bottom of the plot represent the boundaries of the far detector cavern and the two rectangular boxes in the centre of the plot represent two far detector super-modules. The neutrino direction is approximately left-to-right. The small box-like markers represent individual hits in the active detector media between the passive planes; the vertical lines connecting hits in the same detector plane have no physical meaning. The vertex of the event is at the left-hand side of the plot, close to the cross. This event consists of a hadronic shower at the vertex and a long muon track which is bent by the influence of the magnetic field before ranging out at the right-hand side of the plot. The gap in the centre of the muon track is caused by the ~1 metre air-gap between super-modules.

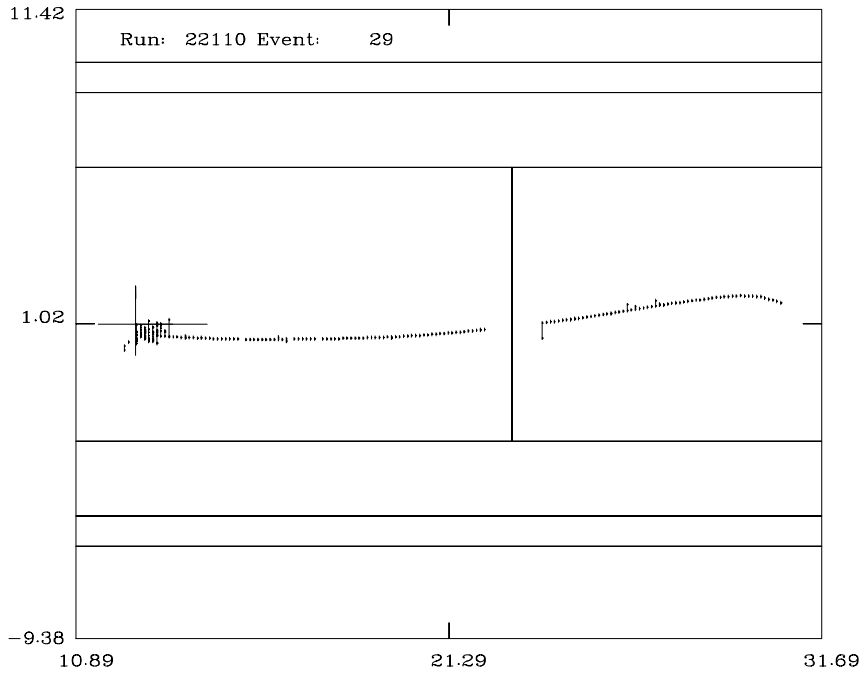

Figure 3.10 - A typical GMINOS simulated ν_μ CC event viewed with the VINES event display package. The $x-z$ projection of the event is shown. The axis scales are in metres.

3.5 Detector performance

The neutrino oscillation probability depends on the incident neutrino energy which can be estimated for ν_μ CC events, such as Figure 3.10, in MINOS by summing the components from the muon track and hadronic shower. This principle will be used in Chapter 4 where the oscillation parameters are measured by examining the reconstructed neutrino energy distribution of ν_μ CC events.

3.5.1 Muon energy resolution

Muon energy can be estimated from range or magnetic bending. For the three horn NuMI beam, ~ 75% of events with a vertex that is > 3 m from the most downstream plane of the detector are fully contained within the detector volume. The muon energy can be estimated from its track length for these events. The left-hand plot of Figure 3.11 shows the mean track length (in cm) as a function of muon momentum for a detector with 4 cm thick

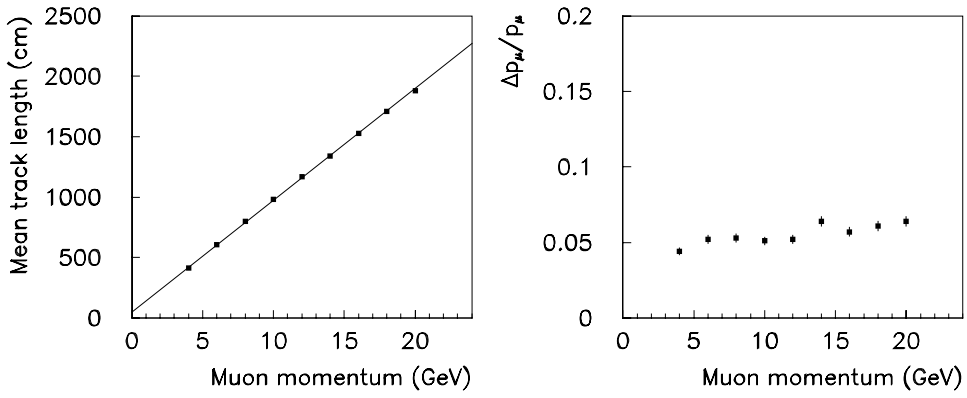

Figure 3.11 - Left-hand plot: track length as a function of muon momentum. Right-hand plot: fractional error on muon momentum for a measurement of the muon track length.

steel plates. The line corresponds to a scale factor of 93 cm/GeV. The right-hand plot of Figure 3.11 shows the fractional error on muon momentum from a measurement of track length. The fractional error, $\Delta p / p$, is typically 5% [78] and is limited by multiple coulomb scattering.

For events that exit the detector, an estimate of the muon momentum can be obtained by fitting the muon track to a combination of magnetic bending and coulomb scattering (taking the slowing down of the muon into account). The fractional error on p_μ is reduced as the muon momentum and usable track length increase, reaching an asymptotic value of 10% for a track length of 10 metres (corresponding to $p_\mu > 10$ GeV). This is limited by coulomb scattering rather than measurement errors [79].

3.5.2 Hadron shower energy resolution

The hadron shower energy can be estimated by counting the number of hits or summing the pulse height in the first few interaction lengths downstream of the event vertex. Monte Carlo simulations [78] give $\Delta E / E \sim 70\% / \sqrt{E}$ for gas detectors or $\sim 50\% / \sqrt{E}$ for scintillator based detectors, where E is in GeV. Figure 3.12 shows the resolution on the number of hits (*rms* of the number of hits divided by the mean number of hits) as a function of $1 / \sqrt{E}$ for a detector with 4 cm thick steel and gas-based active detectors. The resolution on the hadron shower energy derived from Figure 3.12 is $\Delta E / E = 66\% / \sqrt{E}$ and is limited by intrinsic fluctuations in the shower itself.

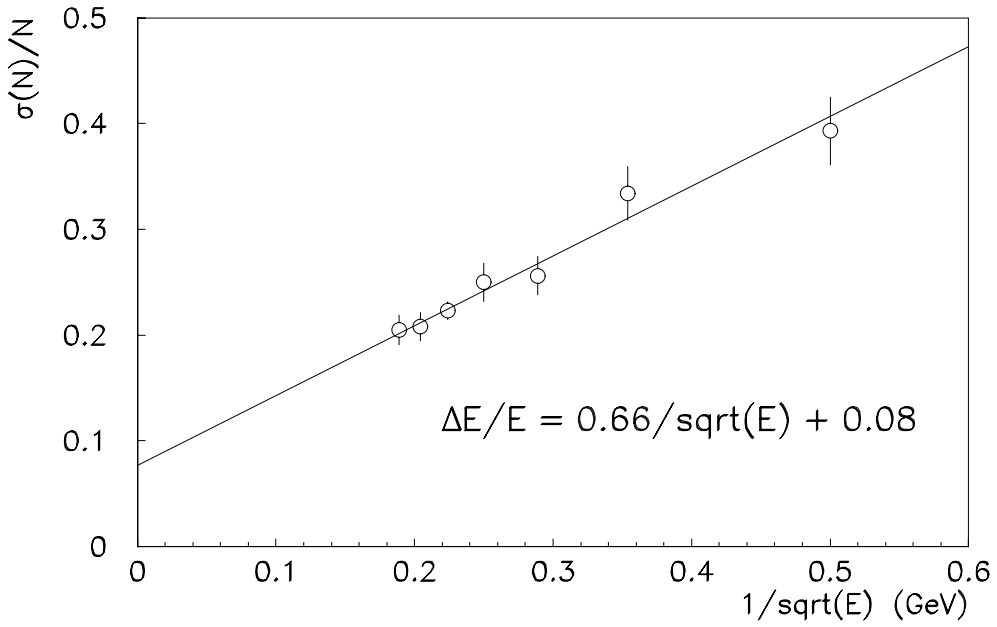

Figure 3.12 – Energy resolution for a simulated detector with 4 cm steel plates and gas-based active detectors.

An APT instrumented calorimeter which ran in a test beam at Fermilab in the Spring of 1997 measured a hadron energy resolution of $\sim 65\% / \sqrt{E}$ for 1.5" steel plates and an electromagnetic energy resolution of $\sim 32\% / \sqrt{E}$ for 2 cm steel plates [80]. These results showed that hadron and electron energy measurement by counting hits or summing pulse height was straightforward and that the measurements were consistent with the Monte Carlo calculations.

Chapter 4 Measuring Mixing Parameters in MINOS

4.1 Introduction

The aim of this and subsequent chapters is to investigate the potential of MINOS to measure the neutrino oscillation parameters if oscillations occur with parameters similar to those suggested by the atmospheric neutrino experiments.

Recall from section 2.5.2 that most atmospheric neutrino experiments measure a value of the flavour ratio, R, that is significantly smaller than unity, the value predicted by the Standard Model. This suggests large mixing ($\sin^2 2\theta > 0.5$) if it is interpreted in terms of neutrino oscillations. The Δm^2 parameter, however, is not well measured. The anomalous values of R only suggest that $\Delta m^2 > 10^{-3}$ eV^2. The exclusion limits from accelerator and reactor neutrino experiments set an upper limit of $\Delta m^2 \sim 10^2 - 10^{-1}$ eV^2, as shown in Figure 2.8 and Figure 2.9. Moreover, the atmospheric neutrino experiments have difficulty in distinguishing between $\nu_\mu \to \nu_\tau$ and $\nu_\mu \to \nu_e$ oscillations. It is therefore clear that the role of MINOS is to attempt to resolve this confusion by making a precision measurement of the mixing parameters and determining the oscillation mode.

This chapter investigates a method to measure the mixing parameters by using energy measurements of ν_μ CC events in MINOS. This analysis is largely independent of the neutrino oscillation mode and can make a direct measurement of Δm^2. The parameter measurement capabilities of a proposed low energy beam for MINOS are studied in Chapter

5. This beam is designed to confront the recent results of the Super-Kamiokande atmospheric neutrino analysis, which suggests that neutrino oscillations occur with $\Delta m^2 \sim 10^{-3}$ eV^2. Chapter 6 studies an analysis that is complementary to that of Chapter 4 which searches for neutrino oscillations in the mode $\nu_\mu \rightarrow \nu_e$ by using energy measurements of ν_e CC events. The prospects of performing a three-flavour mixing analysis in MINOS, by combining the information from the two analyses, are studied in Chapter 7. To complete the picture, Chapter 8 studies the prospects of observing a clear $\nu_\mu \rightarrow \nu_\tau$ signal in MINOS.

4.2 A test for neutrino oscillations using ν_μ CC events

The term *parameter measurement* when applied to neutrino oscillations implies that oscillations have already been shown to occur. This means that a *hypothesis test* must first be performed to demonstrate the existence of neutrino oscillations before the parameters can be measured by the usual methods of χ^2 minimisation or maximum likelihood.

The MINOS proposal [69] describes several tests that are sensitive to neutrino oscillations. The analysis method that is most relevant to this thesis is the ν_μ CC energy test (or Z-test) which is described fully in [81]. The test examines the energy distributions of ν_μ CC events and is therefore sensitive to Δm^2 because of the energy dependence of the ν_μ survival probability, $P_{\mu\mu}$:

$$P_{\mu\mu} = 1 - \sin^2 2\theta \sin^2(1.27\Delta m^2 L / E). \qquad (4.1)$$

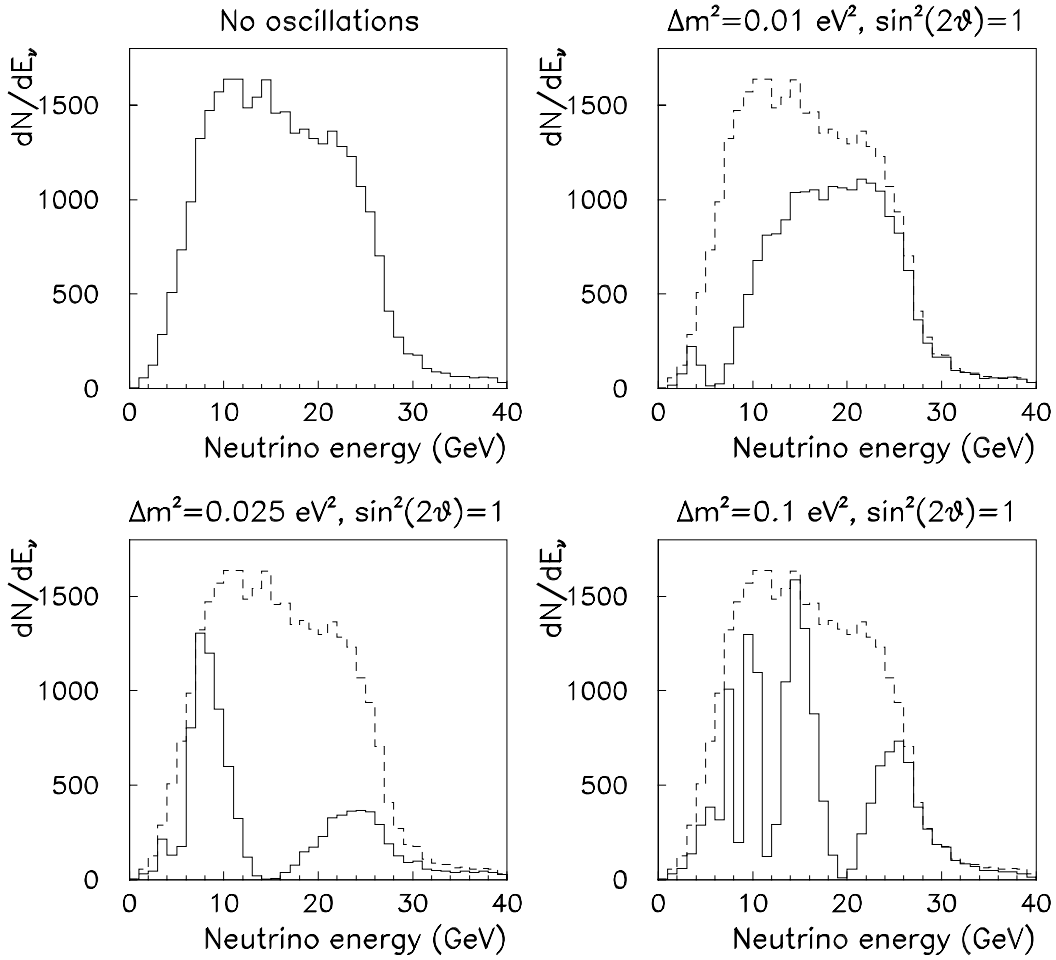

Figure 4.1 – Distributions of true neutrino energy of ν_μ CC events in the NuMI three-horn wide band beam for various neutrino oscillation scenarios.

Figure 4.1 shows ν_μ CC energy distributions for a number of oscillation scenarios. The top-left panel shows the true neutrino energy distribution of ν_μ CC events in the NuMI three-horn wide band beam for no oscillations. The other three panels show the energy distributions of ν_μ CC events for neutrino oscillations with $\sin^2 2\theta = 1$ and $\Delta m^2 = 0.01, 0.025, 0.1$ eV^2 respectively. The no-oscillation distribution is indicated by the dashed histogram in these plots.

The shape and extent of the suppression depends on the value of Δm^2. For $\Delta m^2 = 0.025$ eV^2, one complete oscillation wavelength is visible in the energy distribution and the maximum suppression occurs at approximately the mean interaction energy of the NuMI 3 horn beam (~ 15 GeV). For $\Delta m^2 = 0.1$ eV^2, many oscillation wavelengths are contained in the energy distribution and the fractional widths of the dips are smaller than for $\Delta m^2 = 0.025$ eV^2. It is therefore expected to be more difficult to resolve the dips in the energy distribution for oscillations with $\Delta m^2 = 0.1$ eV^2 than oscillations with $\Delta m^2 = 0.025$ eV^2 for a detector with imperfect energy resolution.

An estimate of the suppression in neutrino event rate that is expected for neutrino oscillations can be obtained by examining, $\overline{S}$, the quantity $\sin^2(1.27\Delta m^2 L/E)$ averaged over the neutrino beam spectrum:

$$\overline{S} = \frac{\int_0^\infty \phi(E_\nu)\sigma_{CC}(E_\nu)\sin^2(1.27\Delta m^2 L/E_\nu)dE_\nu}{\int_0^\infty \phi(E_\nu)\sigma_{CC}(E_\nu)dE_\nu}. \qquad (4.2)$$

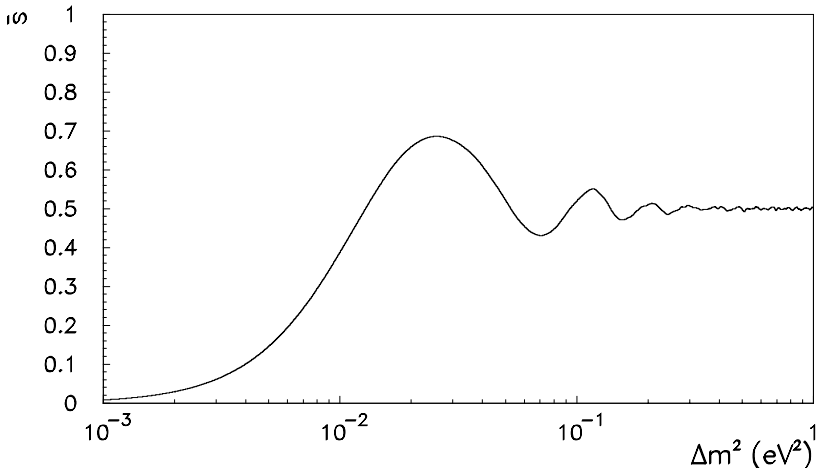

Figure 4.2 – The value of $\overline{S}$, defined by equation (4.2), as a function of Δm^2.

where E_ν is the neutrino energy in GeV, $\phi(E_\nu)$ is the ν_μ flux distribution and $\sigma_{CC}(E_\nu)$ is the ν_μ CC cross-section as a function of neutrino energy. The value of $\overline{S}$ calculated for the NuMI 3 horn beam as a function of Δm^2 is shown in Figure 4.2.

For a constant oscillation probability P, the value of $\sin^2 2\theta$ is given by $\sin^2 2\theta = P / \overline{S}$. At low Δm^2, the value of $\overline{S}$ grows as the square of Δm^2 and reaches a maximum at $\Delta m^2 = \pi\langle E\rangle/2.53L$, where $\langle E\rangle$ is the average neutrino interaction energy. At high Δm^2, $\overline{S}$ averages to 0.5. The bottom plot shows that the suppression of neutrino event rate is maximised at $\Delta m^2 \sim 0.025$ eV^2, where up to 70% of the ν_μ CC interactions oscillate into other neutrino species. Notice that $\overline{S}$ does not reach unity due to the finite width of the E_ν distribution.

The Z-test examines the shapes of ν_μ CC interaction energy distributions and is therefore sensitive to Δm^2 by the position of dips in the energy spectrum and to $\sin^2 2\theta$ by the size of the dips.

Expanding equation (4.1) yields:

$$P_{\mu\mu} = 1 - \frac{1}{2}\sin^2 2\theta + \frac{1}{2}\sin^2 2\theta \cos(2.53\Delta m^2 L / E_\nu). \tag{4.3}$$

The test is based on the normalised statistic Z, which is calculated from the reconstructed energies of ν_μ CC events as:

$$Z(\Delta m^2) = \frac{1}{N}\sum_{i=1,N} \cos(2.53\Delta m^2 L / E_i), \tag{4.4}$$

where N is the number of events observed. The quantity Z, which is an approximation to the Fourier cosine transform of the differential energy distribution $dN / d(E^{-1})$, can be calculated as a function of Δm^2 for events in the near and far detectors. A statistically

significant difference between these two numbers, $Z_n(\Delta m^2)$ and $Z_f(\Delta m^2)$, can be interpreted as evidence for neutrino oscillations.

Figure 4.3 shows the signal expected in this test if neutrino oscillations exist with

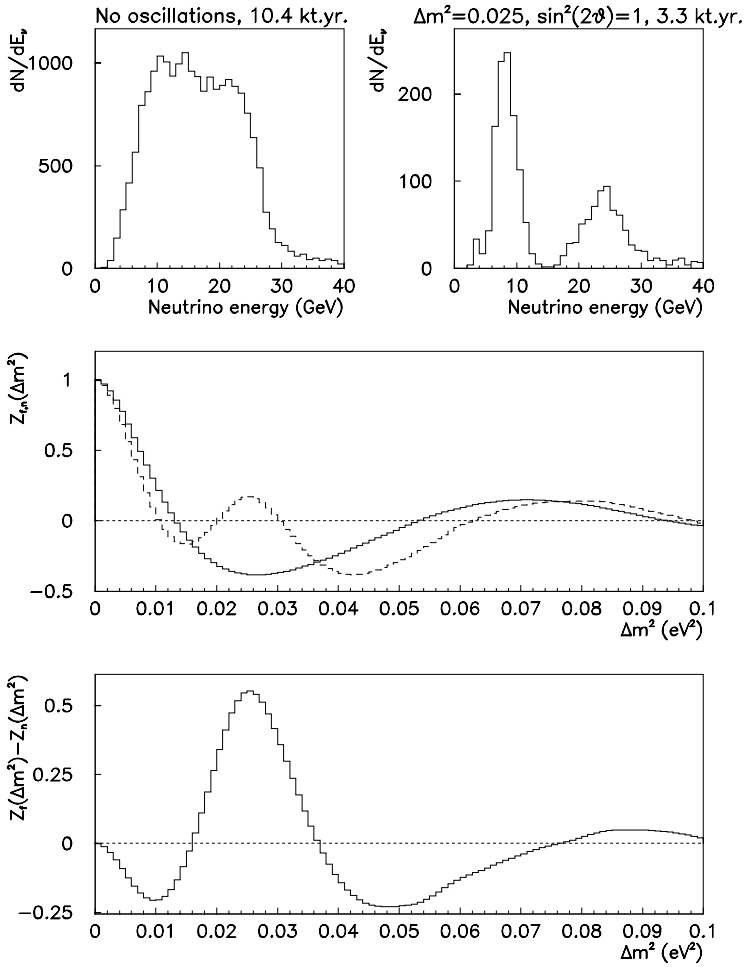

Figure 4.3 – Expected oscillation signals in MINOS using the ν_μ CC energy test for $\Delta m^2 = 0.025$ eV^2 and $\sin^2 2\theta = 1$. The top two plots show the true ν_μ CC energy distributions for the near detector (left-hand plot, no oscillations) and the far detector (right-hand plot, oscillations with $\Delta m^2 = 0.025$ eV^2 and $\sin^2 2\theta = 1$). The centre plot shows the Fourier cosine amplitudes of the $1/E_\nu$ distributions of ν_μ CC events for the near detector (solid histogram) and the far detector (dashed histogram) as a function of Δm^2. The bottom plot shows the difference between the two distributions.

parameters $\sin^2 2\theta = 1$ and $\Delta m^2 = 0.025$ eV^2. These parameters are similar to those suggested by the atmospheric neutrino anomaly. The top two plots show the neutrino energy distributions for the no oscillation hypothesis (left-hand plot) and neutrino oscillations with $\sin^2 2\theta = 1$ and $\Delta m^2 = 0.025$ eV^2 (right-hand plot). The right-hand distribution assumes a 3.3 kiloton year exposure of MINOS. The centre plot shows the distributions of Z_n (solid histogram) and Z_f (dashed histogram) as a function of Δm^2. True neutrino energies have been used to calculate both distributions, although energy resolution is not important at this value of Δm^2 since the oscillation wavelength is much larger than the expected energy resolution in MINOS.

The two distributions are inconsistent with each other and this is more clearly shown by plotting the difference $\Delta Z(\Delta m^2) = Z_f(\Delta m^2) - Z_n(\Delta m^2)$, as shown in the bottom plot of Figure 4.3. This distribution is a clear demonstration of neutrino oscillations; the position of the maximum of ΔZ is an indication of the value of Δm^2 and the height of the maximum is related to $\sin^2 2\theta$. The significance of this effect is given by the following equation:

$$\chi(\Delta m^2) = \frac{\Delta Z(\Delta m^2)}{\sqrt{\mathrm{var}(Z)}}, \tag{4.5}$$

where $\mathrm{var}(Z)$, the variance of $Z_n(\Delta m^2)$, is given by [81]:

$$\mathrm{var}(Z) = \frac{1}{2N}(1 - 2Z_f^2(\Delta m^2) + Z_f(2\Delta m^2)). \tag{4.6}$$

The signal shown in Figure 4.3, which is for a 3.3 kiloton year exposure of MINOS, has $\Delta Z = 0.56$ and $\mathrm{var}(Z) = 7 \times 10^{-3}$ at $\Delta m^2 = 0.025$ eV^2 and is therefore equivalent to a 80 standard deviation effect.

In the subsequent analysis, which concentrates on selecting ν_μ CC events, estimating their energies and using these energy distributions to measure the mixing parameters, it is

assumed that a) the ν_μ CC energy test (and other tests, such as the T-test, which measures the ratio of the number of ν_μ CC events to the total number of interactions) has demonstrated that neutrino oscillations exist and b) the test has indicated the region of parameter space in which the signal is expected to lie.

4.3 Selecting ν_μ CC events

It is necessary to devise a selection procedure that isolates a relatively pure sample of ν_μ CC events in order to investigate the measurement of neutrino oscillation parameters using the CC energy test in MINOS. The neutrino energy distribution for a simulated experiment with mixing parameters Δm^2 and $\sin^2 2\theta$ is then reconstructed by summing the observed hadron and muon energies for each event. This distribution is then fitted to a high statistics Monte Carlo sample to determine the favoured regions of neutrino oscillation parameter space and the errors on the mixing parameters.

The event length is a good discriminator between ν_μ CC and NC events. The typical energy of a ν_μ CC event in MINOS is 17 GeV. Assuming a flat y distribution, the muon will carry on average approximately 9 GeV. For a steel detector dE/dx~1.2 GeV/m. A 9 GeV muon will therefore pass through ~ 8 m of steel before ranging out. A typical NC event with 9 GeV of visible energy has a longitudinal extent of less than ten interaction lengths, or 1.7 metres (λ_I=16.7 cm). A cut on the event length will therefore effectively separate ν_μ CC and NC interactions.

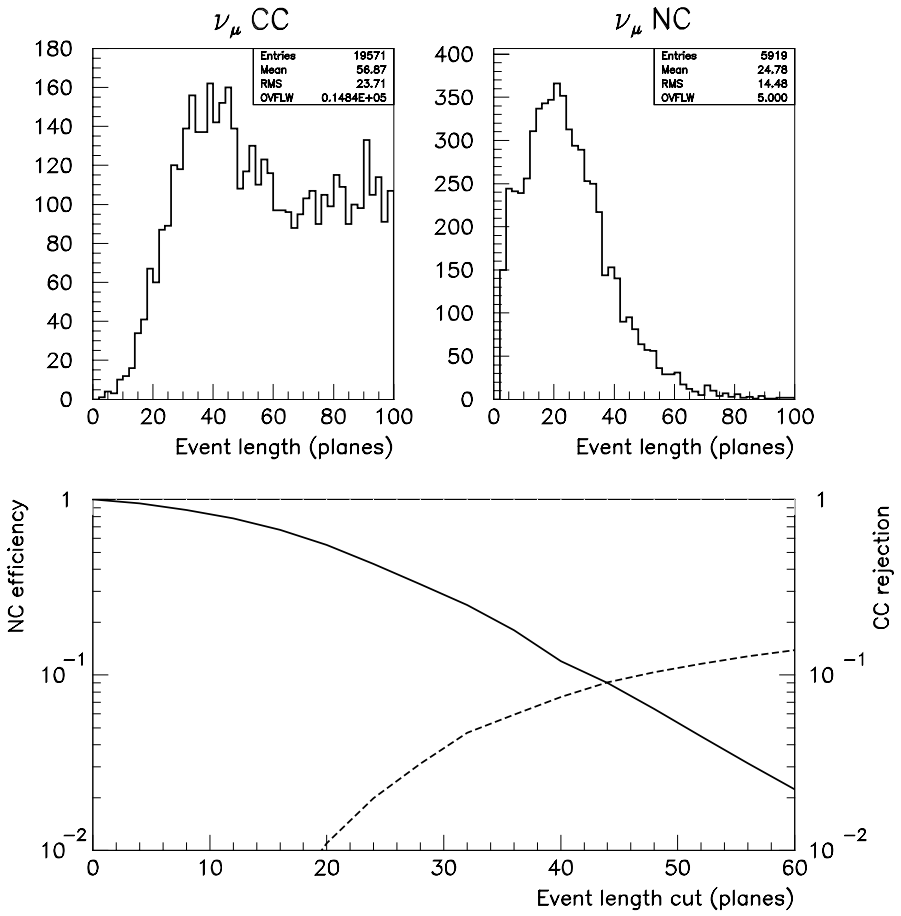

Figure 4.4 - Defining an event length cut to select ν_μ CC events. Top plots: event length distributions for ν_μ CC and NC events in 2 cm steel. Bottom plot: cumulative NC efficiency and CC inefficiencies as a function of the cut on the event length.

Figure 4.4 shows the separation between CC and NC events that could be achieved by a simple event length cut in a detector with 2 cm steel plates. The vertex of an event is defined as the first of three contiguous planes containing hits with a pulse height of 2 photo-electrons or greater (the events were generated with liquid scintillator active detectors). This threshold is designed to eliminate low pulse height hits caused by neutron-hydrogen scattering in liquid scintillator, that may occur upstream of the true vertex. The end of the event is defined as being the last of three contiguous planes containing at least one hit (no

pulse height threshold is applied). The event length is therefore defined as the distance (in detector planes) between the vertex plane and the end of the event. The following fiducial cuts are applied to this and all other data in this thesis:

- vertex > 1 m from front face of detector;
- vertex > 3 m from back face of detector;
- vertex > 20 cm from the central hole;
- vertex > 50 cm from edge of detector.

The top two figures show the distributions of event length, `EVLENGTH`, in steel planes for simulated ν_μ CC and NC events. Note the large overflow for the CC sample; 75% of ν_μ CC events are longer than 100 planes.

The bottom plot shows the NC efficiency (number of NC events longer than length L/total number of NC events) and the CC rejection (number of CC events shorter than L/total number of CC events) as a function of event length. A cut on event length is made at the point of intersection of the two curves. The cut of `EVLENGTH` > 44 planes yields a CC efficiency of 91% and a NC contamination of 9%.

Figure 4.5 shows the CC selection efficiency and NC inefficiency as a function of true neutrino energy. At low E_ν the CC efficiency is reduced since the muons produced at low energy penetrate through less than 44 planes of steel. This inefficiency at low E_ν will limit the sensitivity of the CC energy test to oscillations at low Δm^2. The dotted line in Figure 4.5 is a prediction of the CC selection efficiency that is calculated by assuming a muon momentum cut-off of 1.47 GeV (the minimum muon energy required to penetrate 44

planes of 2 cm steel) and a flat y distribution. The CC selection efficiency as a function of neutrino energy is therefore:

$$\varepsilon_{CC}(E_\nu) = 1 - \frac{1.47}{E_\nu}, \tag{4.7}$$

where E_ν is the neutrino energy in GeV. The agreement between this prediction and the measured efficiency is good.

In section Chapter 5, where a low energy beam is considered to explore the low Δm^2 region suggested by the Super-Kamiokande experiment, it is shown that it is possible to pattern recognise short muon tracks and hence improve the CC selection efficiency at low E_ν. For the purposes of the current analysis, the sensitivity to low Δm^2 is already seriously limited by the small number of events at 5 GeV or lower so this inefficiency is not a critical problem here.

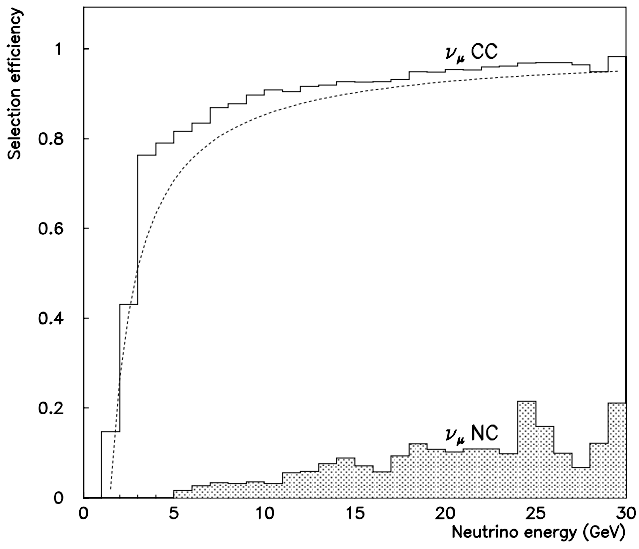

Figure 4.5 – Event selection efficiency as a function of true neutrino energy, E_ν. The open histogram is for ν_μ CC events and the shaded histogram is for NC interactions. The dotted line is the prediction of equation (4.7).

4.4 Reconstructing E_ν

The neutrino energy in a ν_μ CC event is estimated by summing the reconstructed hadronic shower energy and the muon momentum. The hadron shower energy can be estimated by simply counting the number of hits (or summed pulse height) in the first few interaction lengths of the events. If the muon ranges out in the detector then its momentum can be estimated from track length, if not then it is necessary to estimate its momentum from magnetic bending.

4.4.1 Estimating hadron shower energies

The first few interaction lengths of a typical ν_μ CC event (such as the event shown in Figure 3.10) will contain hits from the hadronic shower and hits due to the muon. These muon hits must be subtracted before an estimate of the hadron energy can be made. Since muon tracks are not being fitted in this analysis, it is not necessary to identify the muon hits in the shower region, rather it is simply necessary to subtract the pulse height due to an average minimum ionising particle passing through the first few interaction lengths.

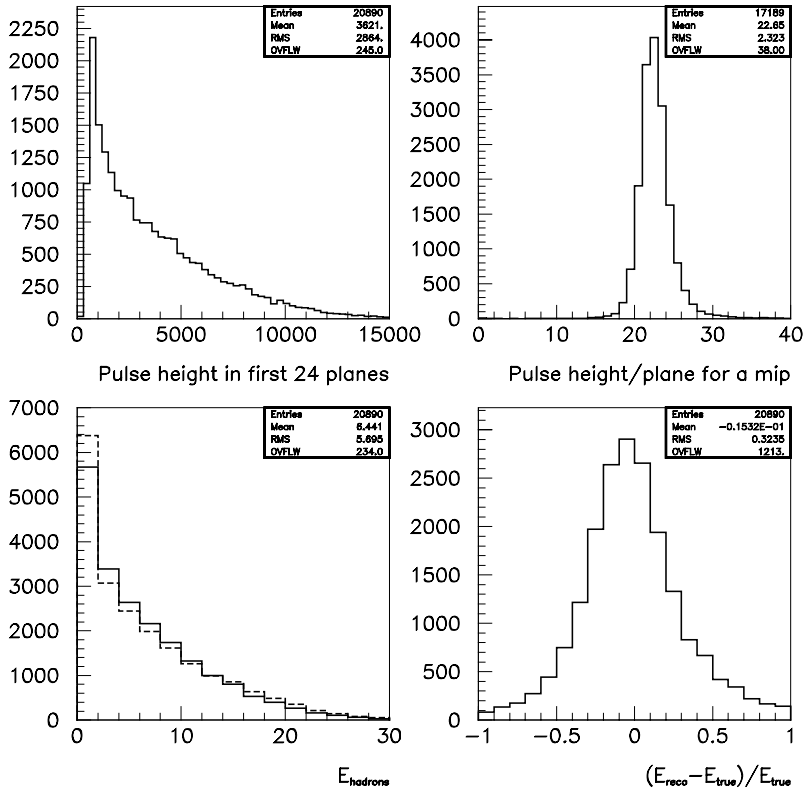

Figure 4.6 – Measuring hadron shower energies.

The top-left plot in Figure 4.6 shows the distribution of summed pulse height in the first 24 planes downstream of the event vertex (approximately three interaction lengths) for CC-like events (events satisfying `EVLENGTH` > 44 planes). The top-right plot shows the mean pulse height per plane produced by a minimum ionising particle (m.i.p.) in the detector. This plot shows that a m.i.p. will produce on average 22 photoelectrons (p.e.) per plane, which equates to about 500 p.e. for 24 planes. For NC events, 500 p.e. is equivalent to 1 GeV of visible energy. Figure 4.7 shows a scatter plot of the true hadron shower energy (in GeV) against the summed pulse height in the first 24 planes of CC-like events. The thick line represents 500 photoelectrons per GeV. An estimate of the hadron energy for CC-like events is:

$$E_{hadrons} = \frac{\sum_{plane=1}^{24} pulseheight - 500\,p.e.}{500\,p.e.}. \quad (4.8)$$

The bottom-left plot of Figure 4.6 shows this estimate of the hadron energy (solid histogram) and the true hadron energy (dashed line). The bottom-right plot shows the fractional difference between reconstructed and true hadron energy. This distribution has a mean of zero and a width of 32%, which, if the errors are assumed to be Gaussian distributed and the average hadron energy is taken to be ~ 6 GeV, roughly corresponds to a resolution of $\Delta E / E \sim 80\% / \sqrt{E}$.

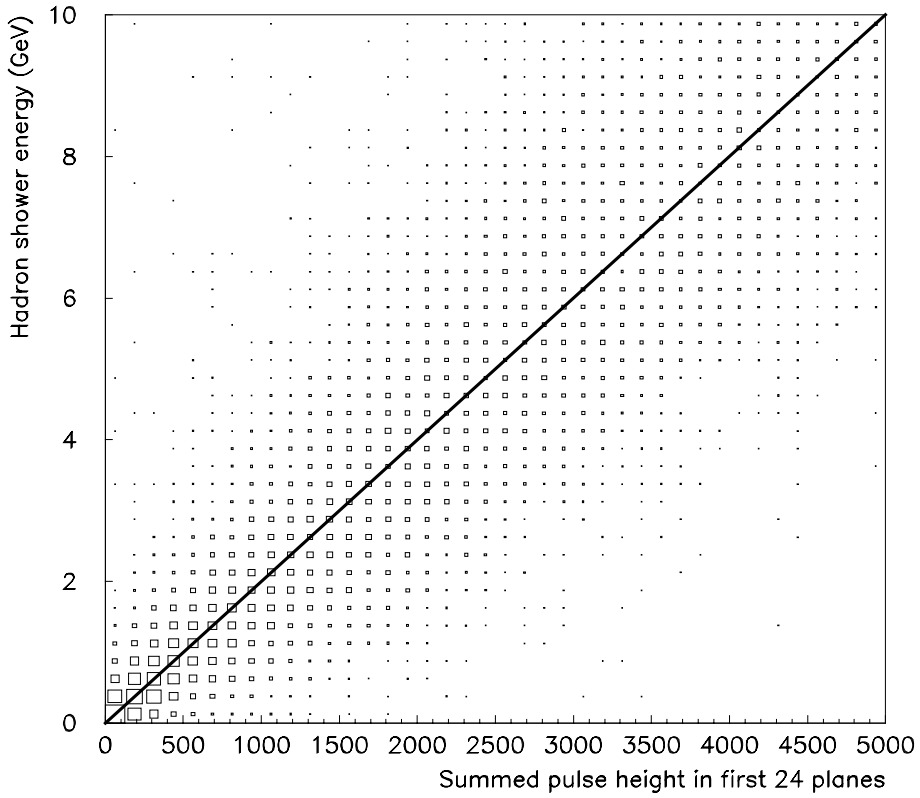

Figure 4.7 – Scatter plot of true hadron shower energy against the summed pulse height in the first 24 planes of CC-like events. The scale factor, 500 photoelectrons per GeV, is indicated by the thick line.

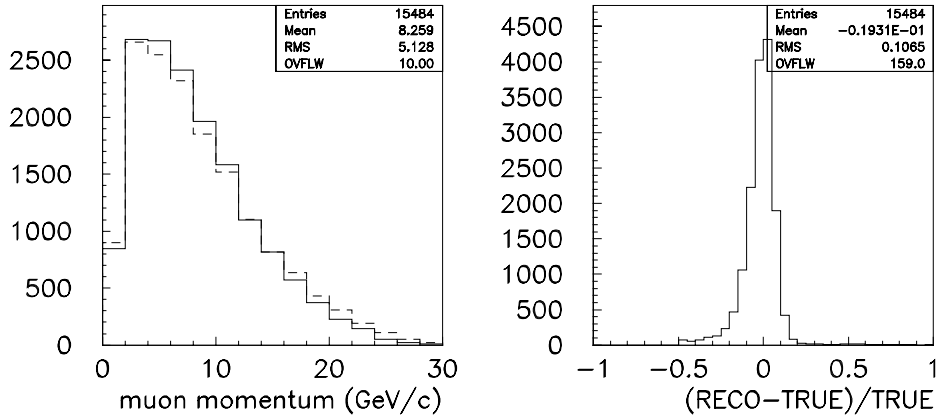

Figure 4.8 – Measuring muon momentum by range.

4.4.2 Estimating muon energies

The top-left plot of Figure 4.8 shows the reconstructed muon momentum for the 76% of all events that range out in the detector (solid histogram), which is estimated by the event length divided by 30 planes. The dashed line represents the true muon momentum. The top-right plot shows the fractional error on muon momentum for all events.

Routines exist in `GMINOS` to fit muon tracks in a magnetic field and provide an estimate of the muon momentum [82]. For the purposes of this analysis, a parameterisation which gives the mean fractional error on muon momentum measurement, $\Delta p/p$, is used for events that do not range out in the detector volume which takes into account coulomb scattering and the slowing down of the muon. The parameterisation is obtained as follows:

A muon track is deflected under the influence of a magnetic field. In a distance dx the direction of the muon changes by $d\theta$:

$$d\theta = \frac{dx}{R} = \frac{0.3Bdx}{p}, \tag{4.9}$$

where R is the radius of curvature of the muon track (in metres) and the relation [4]:

$$R = \frac{p}{0.3B} \tag{4.10}$$

has been used, where p is the muon momentum (in GeV/c) and B is the magnetic field (in tesla).

The muon loses energy as it passes through the steel plates of the MINOS detector and the momentum p after a track length x is related to the initial momentum, p_o, by:

$$\begin{aligned} p &= p_o - kx, \\ k &= \frac{1}{\beta c}\frac{dE}{dx}. \end{aligned} \tag{4.11}$$

Substituting equation (4.11) into equation (4.9) yields:

$$d\theta = \frac{0.3Bdx}{(p_o - kx)}. \tag{4.12}$$

The muon is therefore deflected by an angle θ over a total track length L:

$$\theta = \int_0^L \frac{0.3Bdx}{(p_0 - kx)} = \frac{0.3B}{k}\ln\left(\frac{p_o}{p_0 - kL}\right). \tag{4.13}$$

In addition to the effects of slowing down, the muon also undergoes multiple small angle scatters in the detector medium. The mean square coulomb scattering angle, $d\theta_{ms}^2$, over a small distance dx is related to the muon momentum, p, and the radiation length of the detector medium, X_o, by [4]:

$$d\theta_{ms}^2 = \frac{0.0136}{p^2}\frac{dx}{X_o}. \tag{4.14}$$

Substituting the result of equation (4.11) into equation (4.14) and integrating over a track length L yields:

$$\theta_{ms}^2 = \int_0^L \frac{(0.0136)^2}{(p_o - kx)^2}\frac{dx}{X_o} = \frac{0.0136^2}{kX_o}\frac{kL}{(p_o - kL)p_o}. \quad (4.15)$$

The rms scattering angle $\left\langle \theta_{ms}^2 \right\rangle^{1/2}$ is therefore given by:

$$\left\langle \theta_{ms}^2 \right\rangle^{1/2} = \frac{0.0136}{\sqrt{p_o(p_o - kL)}}\sqrt{\frac{L}{X_o}}. \quad (4.16)$$

The resolution on the true muon momentum ,Δp_o, can therefore be calculated:

$$\Delta p_o = \left(\frac{d\theta}{dp_o}\right)^{-1}\Delta\theta. \quad (4.17)$$

Using the result of equation (4.13):

$$\frac{d\theta}{dp_o} = \frac{0.3BL}{p_o(p_o - kL)}. \quad (4.18)$$

Combining equation (4.17) and equation (4.18) and setting $\Delta\theta \equiv \left\langle \theta_{ms}^2 \right\rangle^{1/2}$ yields:

$$\Delta p_o = \frac{0.0136}{0.3B}\frac{\sqrt{p_o(p_o - kL)}}{L}\sqrt{\frac{L}{X_o}}. \quad (4.19)$$

The simulated detector configuration used in this analysis consists of 2 cm steel plates separated by 3 cm of active detector medium. The density of the active detector medium is much lower than the density of the steel. The effective magnetic field in the detector is therefore a factor of 2/5 of the average field in the steel (1.5 tesla) and the effective radiation length is a factor of 5/2 of the radiation length in steel (1.76×10^{-2} m). The constant k is determined from Monte Carlo simulations to be 0.667 GeV/m.

The fractional error on muon momentum, $\Delta p_o / p_o$, is therefore given by the following expression:

$$\frac{\Delta p_o}{p_o} = 7.56\times10^{-2}\times\frac{\sqrt{(p_o - 0.667L)}}{L\sqrt{p_o}}\times\sqrt{\frac{L}{0.044}}\oplus 5\%, \quad (4.20)$$

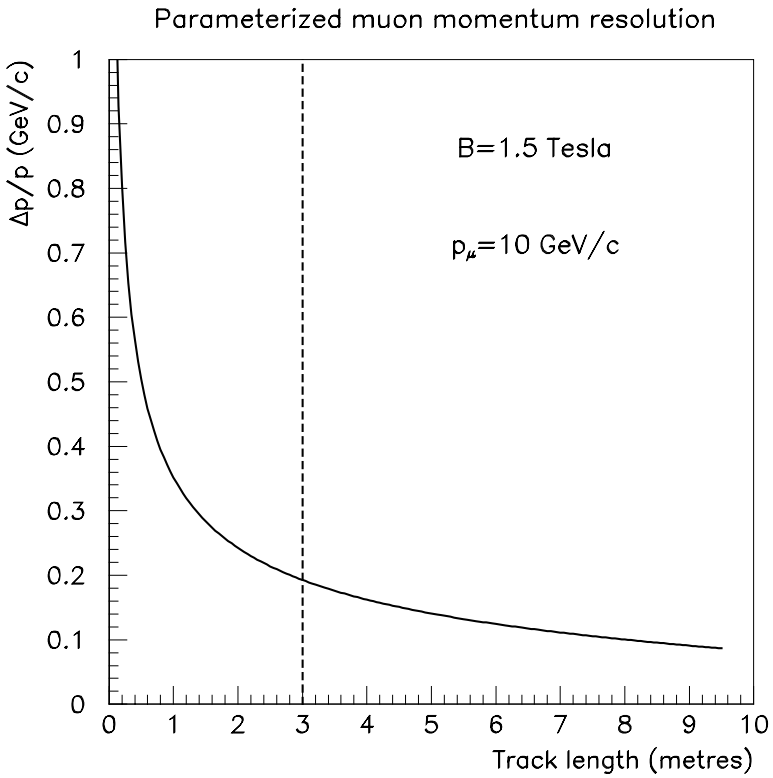

Figure 4.9 – Parameterised muon momentum measurement error as a function of track length in the detector. The parameterisation, which is given by equation (4.20) is explained in the text.

where Δp_o is in units of GeV/c, p_o is the true muon momentum (in GeV/c) and L is the track length in metres. A constant $\Delta p_o / p_o$ of 5% is added in quadrature to the above expression because $\Delta p_o / p_o$ would otherwise tend to zero as $L \to \infty$. Figure 4.9 shows a plot of $\Delta p / p$ versus track length in the detector for a 10 GeV muon for this parameterisation.

Figure 4.10 shows true and reconstructed muon momenta and the fractional error on momentum measurement for the 24% of events that exit the detector. For these events, the true muon momentum and muon track length in the detector are used to calculate $\Delta p/p$ using equation (4.20) from the parameterisation outlined in section 4.4. This number is then smeared with a Gaussian distribution to produce the final estimate of p_μ.

4.4.3 Measurement of E_ν

Figure 4.11 shows distributions of reconstructed neutrino energy (solid histogram), which is constructed by summing the reconstructed hadron and muon energies, and true E_ν (dashed histogram). The right-hand plot shows the fractional error on the measurement of the initial neutrino energy. This distribution has a mean of zero and a width of 16%, and is dominated by the measurement error on the hadronic shower.

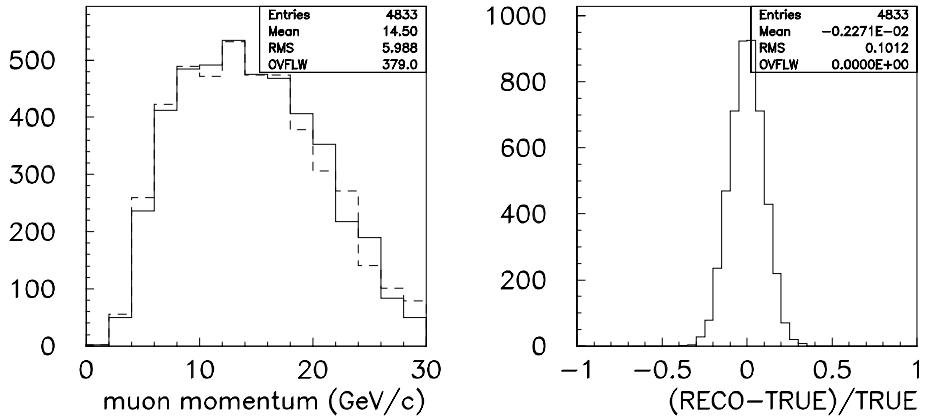

Figure 4.10 – Measuring muon momentum via magnetic bending.

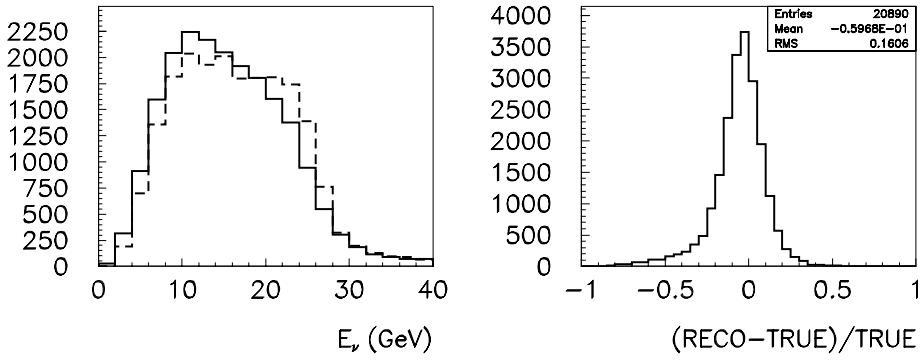

Figure 4.11 – Measurement of neutrino energy.

4.5 Determination of neutrino oscillation parameters

4.5.1 Fitting procedure

A sample of Monte Carlo events is generated with no oscillations. This sample is named `MCNO` (Monte Carlo, no oscillations) and contains 20890 events that pass the cut `EVLENGTH` > 44 planes, corresponding to a 10.3 kiloton year exposure of MINOS. A distribution of reconstructed neutrino energy, E_{reco}, with 60 bins and a range of 0-30 GeV is then constructed. The bin size of 0.5 GeV is comparable to the average energy resolution for these events and, since >100 events are expected in each bin for no oscillations, Gaussian statistics can be used.

A second sample of Monte Carlo events is generated and the quantity $W = \sin^2 2\theta \sin^2(1.27\Delta m^2 L / E_\nu)$ for a particular pair of oscillation parameters $(\Delta m^2, \sin^2 2\theta)$ is calculated for each event. The true neutrino energy is used to calculate W.

A random number R is generated with possible values $0 < R < 1$ and the event is rejected if $R > W$. This sample of events is named MCEXP (Monte Carlo experiment) and consists of 6629 events, which is equivalent to an exposure of 3.3 kiloton years. A distribution of E_{reco} from 0 to 30 GeV is then constructed for this sample with 60 bins.

A binned likelihood method is then used to perform a fit of the 'data' (MCEXP) to the Monte Carlo expectation (MCNO) in order to extract the values of the mixing parameters. The fit is performed using the two E_{reco} distributions. A grid of $\Delta m^2, \sin^2 2\theta$ values is set up and, for each pair of parameters, the MCNO events are *weighted* by the factor W and a new E_{reco} distribution for these events is created. The log likelihood ratio is then calculated for the MCNO and MCEXP energy distributions:

$$\log L = \sum_{i=1}^{n} \log P_i(E_{reco}, \Delta m^2, \sin^2 2\theta) - C$$
$$\log P_i = \frac{(m(i) - A \times n(i))^2}{2 \times A \times n(i)} \tag{4.21}$$
$$C = \sum_{i=1}^{n} \log P_i(E_{reco}, \Delta m^2 = 0, \sin^2 2\theta = 0)$$

where $m(i)$ is the number of events in bin i of the E_{reco} distribution for the MCEXP sample, $n(i)$ is the number of events in bin i of the MCNO sample and A is the relative normalisation of the MCEXP and MCNO samples. The log likelihood ratio can be interpreted as the 'betting odds' that a particular hypothesis is favoured over the null hypothesis ($\Delta m^2 = 0$, $\sin^2 2\theta = 0$).

Subsequent fits in this chapter assume fixed or free normalisation. Fixed normalisation assumes that the relative normalisation of the MCEXP and MCNO samples is perfectly known. The factor A is therefore given by the number of events in the MCEXP sample divided by the number of events in the MCNO sample:

$$A = 6629 / 20890 = 0.317 . \tag{4.22}$$

Free normalisation assumes that the relative normalisation of the two samples is unknown and only the shapes of the E_{reco} distributions are used in the fit. The value of A is therefore calculated for each pair of parameters $(\Delta m^2, \sin^2 2\theta)$ to ensure that the two distributions are normalised to the same number of events:

$$A = \frac{\sum_{i=1}^{n} m(i)}{\sum_{i=1}^{n} n(i)}. \tag{4.23}$$

4.5.2 Example fits

Figure 4.12 shows the results of fits to single MCEXP samples with mixing parameters $\Delta m^2 = 0.025$ eV^2 and $\sin^2 2\theta = 0.7$ (the optimal case) and $\Delta m^2 = 0.01$ eV^2 and $\sin^2 2\theta = 0.7$ (the Kamiokande parameters). The left hand plots show the 68%, 90% and 95% confidence level contours (corresponding to a change in the log likelihood ratio of $\Delta L = 1.13, 2.25, 3.0$) drawn relative to the maximum value of log likelihood in the plot, assuming two degrees of freedom. The favoured fit parameters are consistent (within the 68% confidence limit) with the input parameters, which are indicated by the stars. The right-hand plots show the distributions of E_{reco} for the MCEXP sample (error bars) the MCNO sample with no oscillations (dashed histogram) and the MCNO sample weighted with the best fit parameters (solid histogram).

For $\Delta m^2 = 0.025$ eV^2, the dip at 15 GeV is clearly resolved and the fit quality is good ($\chi^2 = 46.5/58$). The oscillation signal at $\Delta m^2 = 0.01$ eV^2 is less convincing. The oscillation probability is maximised at ~ 6 GeV for these parameters and the CC energy spectrum is rising rapidly at this energy. The dip in event rate is therefore not clearly resolved and the shape information is weaker than in the fit at $\Delta m^2 = 0.025$ eV^2. This results in larger error contours that show a strong anti-correlation between Δm^2 and $\sin^2 2\theta$.

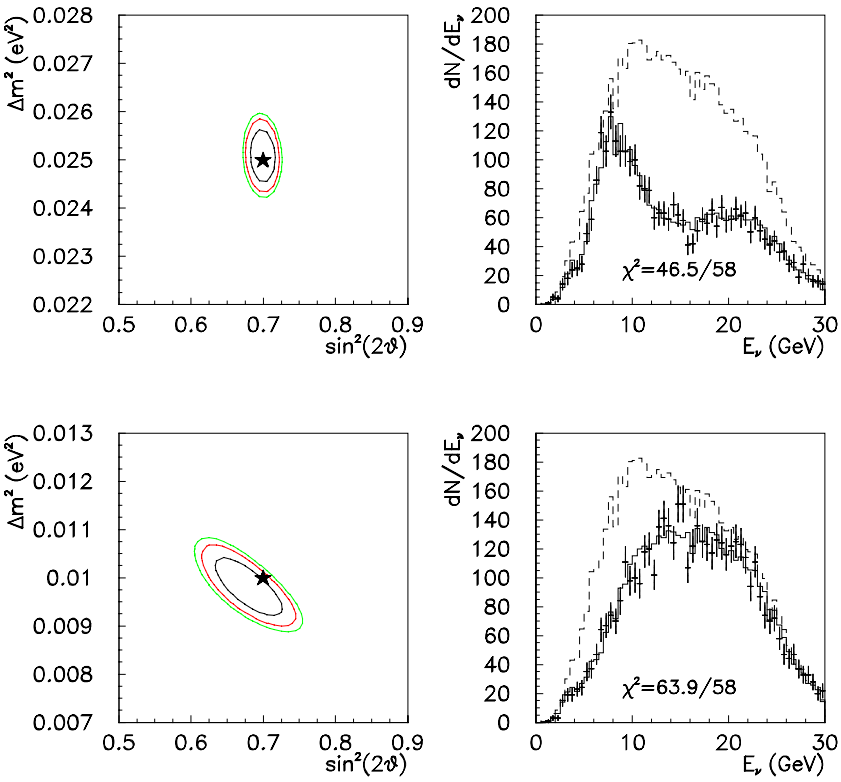

Figure 4.12 - Fixed normalisation fits to MCEXP samples with $\Delta m^2 = 0.025$ eV^2 (top plots), $\Delta m^2 = 0.01$ eV^2 (bottom plots) and $\sin^2 2\theta = 0.7$. The left-hand plots show the error contours drawn with respect to the log likelihood maximum. The stars represent the input parameters. The right-hand plots show the MCEXP reconstructed neutrino energy distributions (error bars), the best fit MCNO sample (solid histogram) and the unoscillated MCNO sample (dashed histogram). The plots assume a 3.3 kiloton year exposure of MINOS.

4.5.3 Effect of uncertain normalisation

Section 4.5.2 shows how well the mixing parameters can be measured in the Wide Band Beam if only statistical errors are considered. In general there will be a number of systematic errors associated with the extrapolation of the ν_μ CC energy spectrum measured in the near detector to that expected in the far detector for no oscillations.

A major uncertainty is in the prediction of the absolute rate of neutrino interactions in the far detector. This depends on the secondary hadron production spectrum and the corresponding p_T distribution. Unfortunately, this is not well measured at the high proton energies planned for the Main Injector beam and the current predictions involve extrapolations from hydrogen target measurements to a carbon target and an extrapolation in beam energy. The far detector rates predicted by NUADA (which calculates the neutrino rates by convolving distributions that are derived from experimental data on hadron production) and GNuMI (which uses `GEANT` to model hadron production and includes the effects of interactions between the secondaries and the decay pipe walls) differ by as much as 20% [71]. A study of the relative changes in the near and far detectors when the p_T distribution of secondary hadrons is allowed to vary within the range suggested by the models of hadron production has been made. The conclusion is that the relative changes in the near/far spectra are predicted to be between 2 and 4% for the low energy (< 10 GeV) part of the spectrum and less that 8% for the upper edge (~ 25 GeV) [71].

Experimental uncertainties, such as imperfect knowledge of the masses of the detectors and the live-time of the beam, can also contribute to an error in the prediction of the absolute normalisation of neutrino interactions.

Figure 4.13 shows an example of the effect of an incorrect prediction of the far detector rate on parameter determination. The fits are made to a MCEXP sample with $\Delta m^2 = 0.015$ eV^2 and $\sin^2 2\theta = 0.7$. The percentage errors quoted are on the interaction rate in the far detector for no oscillations. A positive error implies that too many events are expected and a negative error means that too few are expected. The effect of a positive error is to shift the best fit parameters to larger values of Δm^2 and $\sin^2 2\theta$, because the apparent size of the dip is greater, resulting in a larger value of $\sin^2 2\theta$. The increase in Δm^2 results from an increased deficit at high neutrino energy. The converse argument applies to the fits with a negative error. In these cases the fits favour lower values of $\sin^2 2\theta$ and Δm^2. For a +20% shift in the absolute normalisation, the fitted value of Δm^2 increases by 10% and $\sin^2 2\theta$ increases by 15%.

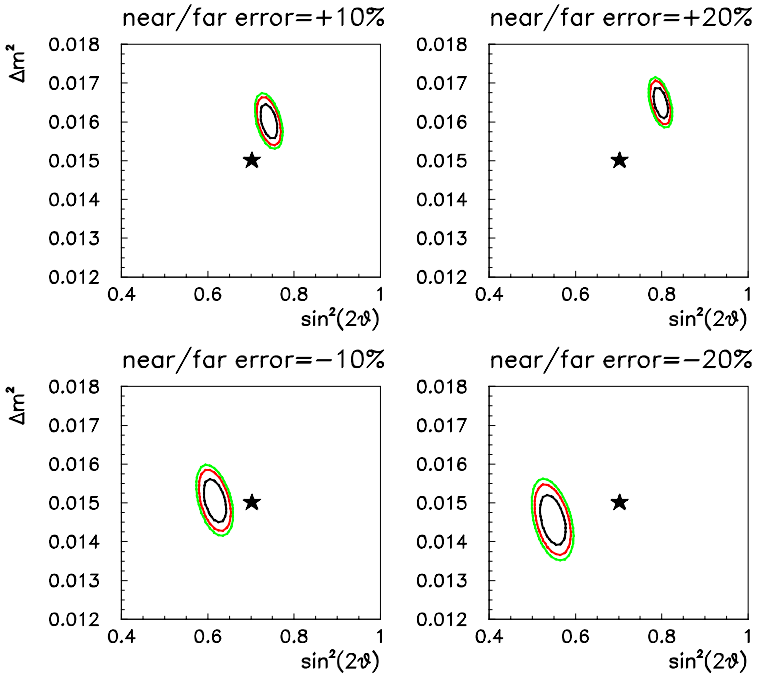

Figure 4.13 – The effect of an incorrect prediction of the neutrino interaction rate on parameter measurement. The fits are all for $\Delta m^2 = 0.015$ eV^2 and $\sin^2 2\theta = 0.7$. The quoted errors are on the interaction rate in the far detector for no oscillations.

An uncertainty in the relative rates in the near and far detectors can be accounted for in the fits. Figure 4.14 shows a summary of parameter measurement errors for various values of Δm^2 and $\sin^2 2\theta = 0.7$. The plots show the errors expected on Δm^2 and $\sin^2 2\theta$, which are defined as one half of the maximum extent of the 68% C.L. contours in Δm^2 and $\sin^2 2\theta$ respectively. The four curves in each plot correspond to perfect normalisation, a 2% or 4% uncertainty in the relative rate between near and far detectors[4] and free normalisation (shape-only fit with three degrees of freedom).

The error contours for a particular value of Δm^2 increase in size as the normalisation uncertainty increases because the normalisation information is extremely important in fixing $\sin^2 2\theta$ and, to a lesser extent Δm^2. The parameters $\Delta m^2 = 0.025$ eV^2 and $\sin^2 2\theta = 0.7$, which are close to optimal for this beam, can be measured with a precision of between 2-3% for Δm^2 and between 3-6% for $\sin^2 2\theta$, depending on the normalisation uncertainty. The Kamiokande best-fit parameters from the atmospheric neutrino analysis ($\Delta m^2 = 0.01$ eV^2 and large $\sin^2 2\theta$) can be measured to ~10% in both Δm^2 and $\sin^2 2\theta$. This result emphasises the fact that the beam energy is not optimal for a precision measurement of the Kamiokande parameters. The arrows on the plot indicate that the 68% C.L. error contours are not closed (i.e. they extend up to $\sin^2 2\theta = 1$, fits with $\sin^2 2\theta > 1$ are unphysical and are not allowed in this analysis) and the errors shown on the plot are therefore underestimates.

[4] The relative normalisation is allowed to float within this range and the value of log likelihood is maximised for each value of the mixing parameters.

The regions marked ‘unresolved’ on the plots refer to the upper and lower limits of Δm^2 for which a precision measurement of the parameters can be made. The lower limit is set by the beam energy spectrum. For $\Delta m^2 = 0.005$, the oscillation probability is maximised at 3 GeV and in the 3 horn Wide Band Beam, there are simply very few neutrinos at this

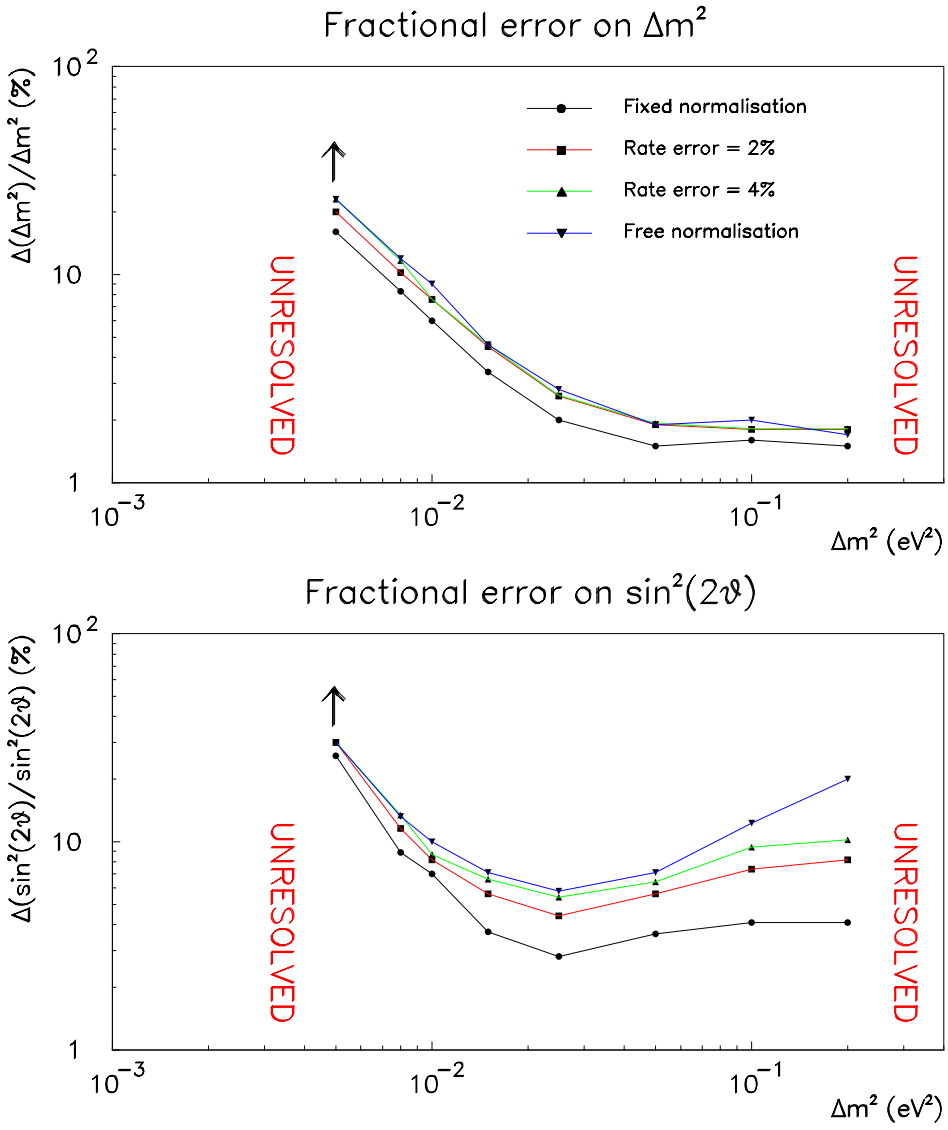

Figure 4.14 – Summary of parameter measurement errors for fits to neutrino oscillations with various values of Δm^2 and $\sin^2 2\theta = 0.7$. The lines correspond to different assumptions about the relative near/far rate normalisation.

energy. The shape and normalisation information therefore becomes very weak and the error contours become prohibitively large. The high Δm^2 limit is set by energy resolution. For $\Delta m^2 > 0.2$ eV^2 the oscillation probability varies rapidly as a function of energy between 0 and 30 GeV. It is simply not possible to resolve the dips in the CC energy spectrum. For shape-only tests, this results in increasing errors in the mixing parameters below $\Delta m^2 = 0.2$ eV^2 and large shifts in the fitted parameters above this value. Fixed normalisation fits rely more heavily on the normalisation information as the dips become harder to resolve.

Figure 4.15 shows the results of a fit to a MCEXP sample with $\Delta m^2 = 0.1$ eV^2 and $\sin^2 2\theta = 0.7$. The effect of energy resolution can clearly be seen when the right-hand plot of Figure 4.15 is compared to the bottom right-hand plot of Figure 4.1, which shows the true neutrino energy distribution of ν_μ CC events for oscillations with $\Delta m^2 = 0.025$ eV^2 and $\sin^2 2\theta = 1$. The dips in the energy distribution at high energy (> 10 GeV) are smeared out when energy resolution is accounted for and it is impossible to resolve the narrow dips that occur below 10 GeV. The dips become narrower as Δm^2 is increased and eventually, above $\Delta m^2 = 0.2$ eV^2, it becomes impossible to measure Δm^2 using this method.

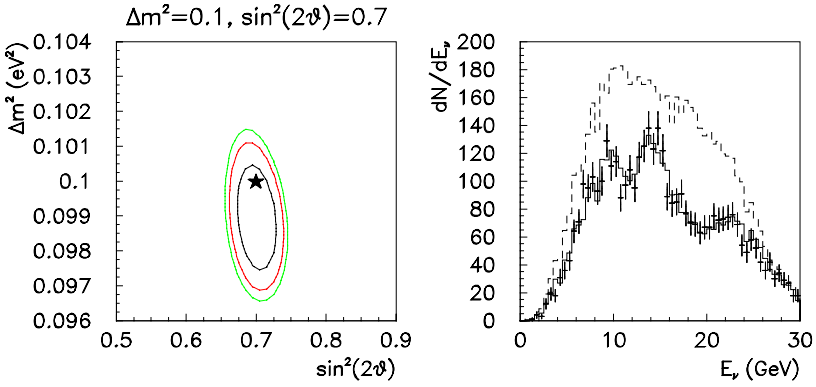

Figure 4.15 – Fixed normalisation fit to a MCEXP sample with $\Delta m^2 = 0.1$ eV^2 and $\sin^2 2\theta = 0.7$. A 3.3 kiloton year exposure of MINOS is assumed.

4.5.4 Effect of near/far energy shift

Another potential source of systematic error in the fits is a shift in the energy measurement scales between the near and far detectors. A change in the steel thickness or density between near and far detectors could easily produce such a bias. For the purposes of this study, this shift is parameterised by ε, where $E_{far} = (1+\varepsilon)E_{near}$, which simulates a linear shift in the two energy scales. Figure 4.16 shows the 68% confidence limit contours for five fits to a MCEXP sample with $\Delta m^2 = 0.015$ eV^2 and $\sin^2 2\theta = 0.7$ and an uncorrected bias in the energy scales with values of ε between –0.2 and 0.2.

The best-fit contours move toward large values of $\sin^2 2\theta$ and slightly large values

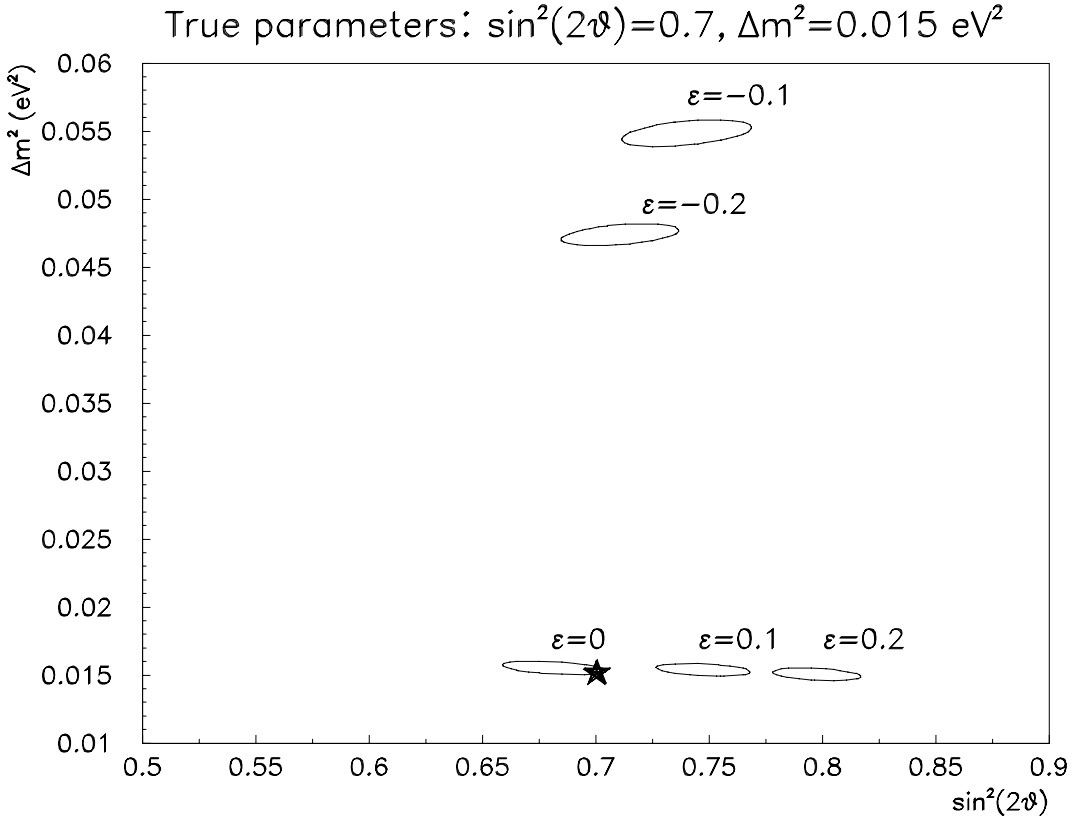

Figure 4.16 – Fixed normalisation fits with $\Delta m^2 = 0.015$ eV^2 and $\sin^2 2\theta = 0.7$ and several linear near/far energy shifts, ε, between the near and far detectors. The 68% C.L. contours are drawn.

of Δm^2 for positive values of ε. On the other hand, a negative energy shift produces best-fit contours at $\sin^2 2\theta \sim 0.7$ and $\Delta m^2 \sim 0.05$. This drastic shift in the values of the fitted parameters can be explained by examining the best-fit energy distributions, which are shown in Figure 4.17.

For positive values of ε, the dip in the neutrino energy distribution moves to higher

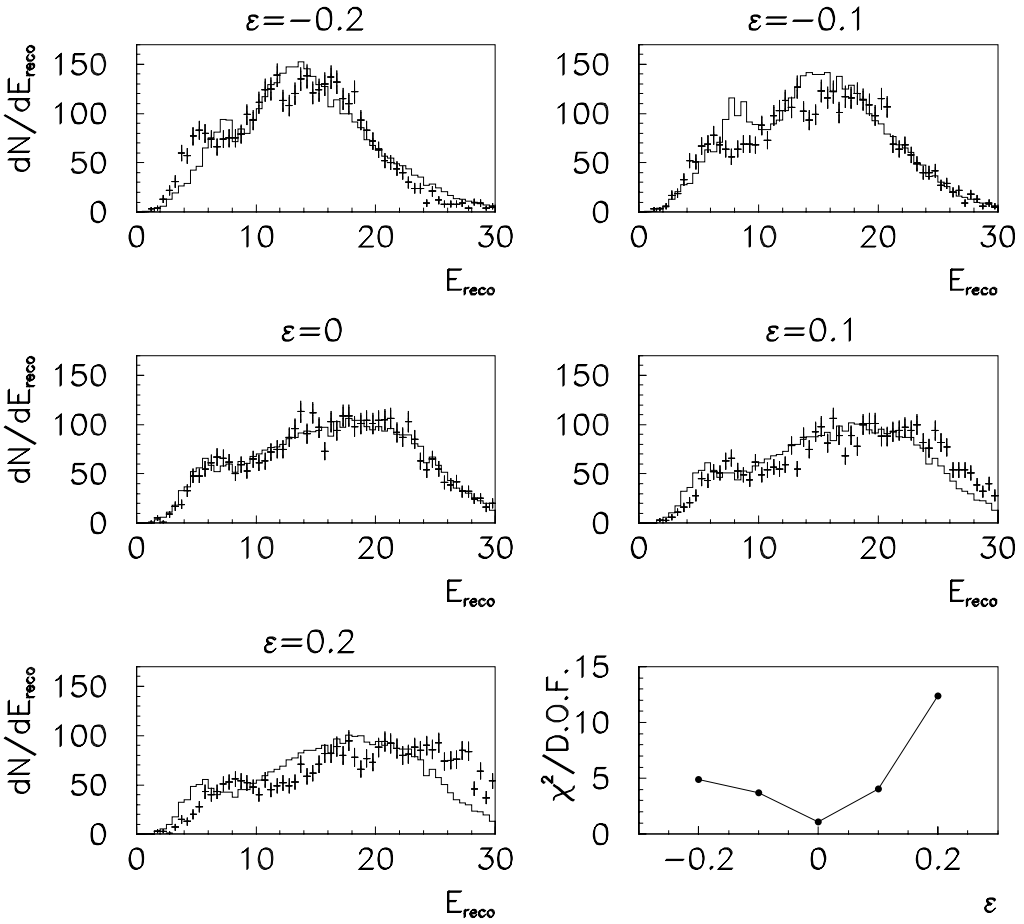

Figure 4.17 – Best-fit neutrino energy distributions for the fits shown in Figure 4.16. The error bars represent the MCEXP samples and the histograms represent the best-fit MCNO samples. The bottom right plot shows the χ^2 per degree of freedom for the fits.

energies, which increases the best fit values of Δm^2 and $\sin^2 2\theta$. Positive ε also results in too many neutrinos at high energy in the MCEXP sample. This cannot be fitted by any oscillation scenario and results in poor values of χ^2. A negative energy shift on the other hand, results in too few neutrinos at high energy in the MCEXP sample. This appears as a deficit above 20 GeV which can be fitted by a large value of Δm^2. There are now too many neutrinos at low energy and the fit quality is poor ($\chi^2 \sim 5$ per degree of freedom). Shape-only fits show the same characteristics as those with fixed normalisation but produce slightly better values of χ^2. This is because the normalisation information is largely responsible for the poor fits at low energy for negative ε and high energy for positive ε.

It is possible to avoid these large shifts in the fitted parameters by regarding the near/far energy scale as a free parameter in the fits. For each value of Δm^2 and $\sin^2 2\theta$, the log likelihood is maximised for a range of ε between –0.25 and 0.25. The true values of the parameters are regained although the contours increase in size relative to the fixed normalisation fits with no energy shift. Table 4.1 shows how much the errors on Δm^2 and $\sin^2 2\theta$ increase for two oscillation hypotheses when the energy scale is allowed to float. The errors on the parameters generally increase by 10-30% although the errors increase more for $\Delta m^2 = 0.05$ than for $\Delta m^2 = 0.015$. This is because, as has been shown in Figure 4.16, energy shifts can induce spurious signals at $\Delta m^2 \sim 0.05$ and large $\sin^2 2\theta$ and the likelihood surface is therefore more distorted in this region.

Mixing Hypothesis	$\Delta(\Delta m^2)$ (%) (no shift)	$\Delta(\Delta m^2)$ (%) (floating energy shift)	Increase in error on Δm^2	$\Delta(\sin^2 2\theta)$ (%) (no shift)	$\Delta(\sin^2 2\theta)$ (%) (floating energy shift)	Increase in error on $\sin^2 2\theta$
$\Delta m^2 = 0.015$ $\sin^2 2\theta = 0.7$	3.4	4.2	24%	3.7	4.1	11%
$\Delta m^2 = 0.05$ $\sin^2 2\theta = 0.7$	1.5	2.0	33%	3.6	4.6	28%

Table 4.1 – The 68% C.L. errors on the mixing parameters for fixed normalisation fits to two MCEXP samples. The second and fifth columns show the fractional errors on the mixing parameters for fits where the energy scales of the near and far detectors are assumed to be identical. The third and sixth columns show the fractional errors on the mixing parameters when the relative energy scale is allowed to float and the fourth and seventh columns show how much the errors increase when this additional degree of freedom is used in the fits.

4.5.5 Effect of near/far beam systematics

Section 3.3 has shown how the shapes of the predicted neutrino energy spectra at the near and far detector sites are different and has outlined the effects that are responsible for these differences. At the present time, it is not clear how well these effects can be corrected for. It is certain, however, that the worst possible case is that the near detector spectrum in Figure 3.4 is the prediction in the far detector for no oscillations (no correction) and the best case is when the far detector spectrum is the no oscillation prediction (perfect correction).

Figure 4.18 shows how the fitted parameters change between the best case (100% far) and the worst case (100% near) for two MCEXP samples with $\sin^2 2\theta = 0.7$ and $\Delta m^2 = 0.01, 0.025$ eV^2. The fits assume fixed normalisation and a MCNO beam spectrum which is a linear combination of the near and far spectra. The near beam fraction is plotted on the x-axis and the difference between the best fit parameters and the input parameters divided by the 68% C.L. errors on the fitted parameters are plotted on the y-axes. The fits for true $\Delta m^2 = 0.01$ eV^2 move to larger values of Δm^2 and smaller $\sin^2 2\theta$ as the near beam fraction is increased. For a beam with a 40% far and 60% near admixture, the true

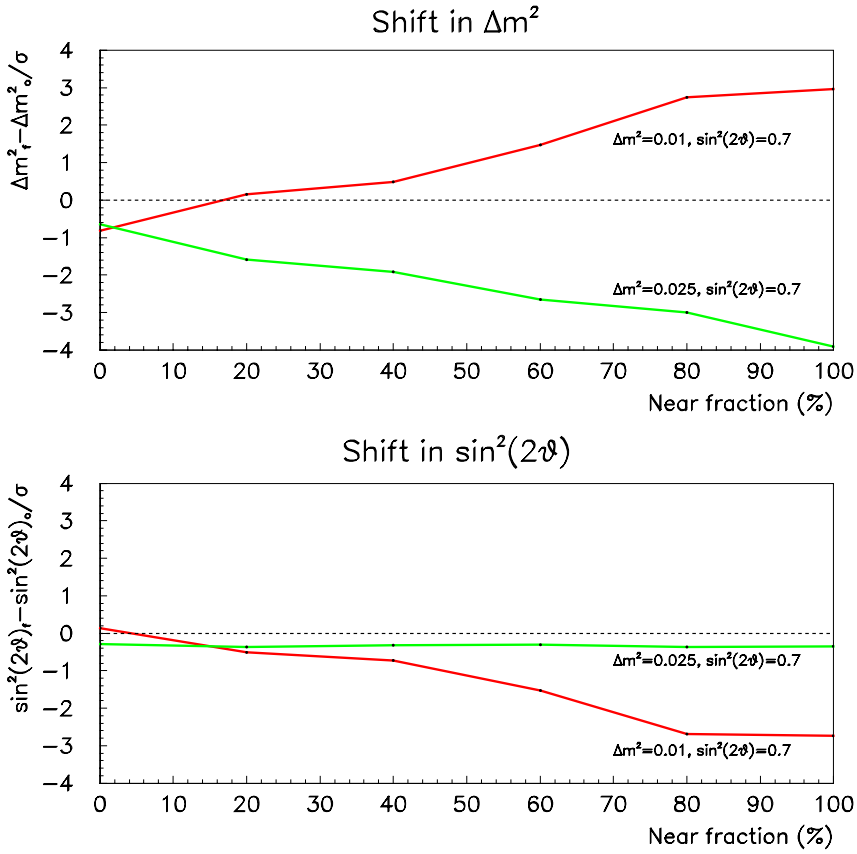

Figure 4.18 – Effect of near/far spectral differences on parameter measurement. Two MCEXP samples are fitted with a MCNO sample of the form: x% near + (100-x)% far. The y-axes show the difference between best fit and true parameters divided by the 68% C.L. errors on the fitted parameters.

parameters are outside of the 68% confidence level contour drawn with respect to the best-fit parameters. The shift in Δm^2 is caused by an increase in the number of neutrinos with energies around 12 GeV as the near beam concentration is increased. The deficit therefore appears to be larger at these energies, which can be simulated by larger values of Δm^2 and $\sin^2 2\theta$. On the other hand, an increase in the near beam concentration produces a discrepancy at low (< 10 GeV) and high (> 20 GeV) energies. The `MCEXP` sample, which uses the far detector spectrum, has an excess of neutrinos at high energy. This forces the fits to lower values of $\sin^2 2\theta$. The net effect of increasing the near beam concentration is therefore to increase Δm^2 and decrease $\sin^2 2\theta$.

The dominant effect in these fits is the near/far difference at 12 GeV. This corresponds to $\Delta m^2 = 0.02$ eV^2. For $\Delta m^2 = 0.025$ eV^2, the effect of increasing the near beam contamination is therefore to decrease the fitted value of Δm^2. There is no decrease in $\sin^2 2\theta$ because this value of Δm^2 more effectively suppresses the higher energy neutrinos than $\Delta m^2 = 0.01$ eV^2.

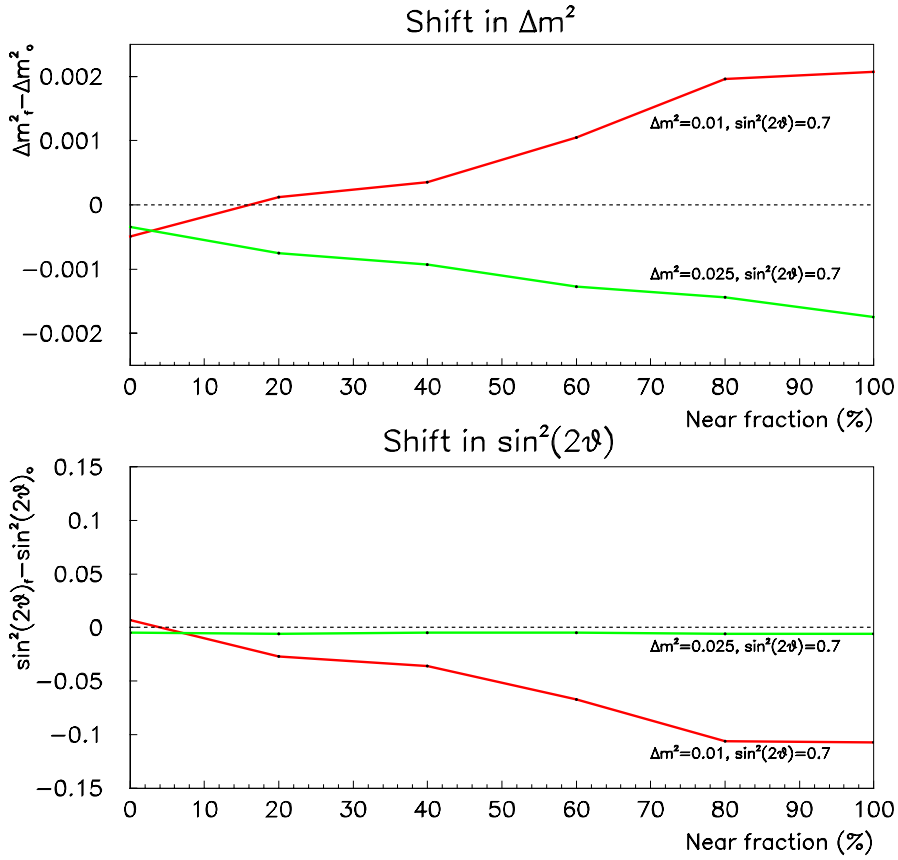

Figure 4.19 – As Figure 4.18, but showing the raw values of the shifts in the mixing parameters.

Figure 4.19 shows the absolute shifts in Δm^2 and $\sin^2 2\theta$ that result from the differences between the near and far energy spectra. The figure shows that, if the near-far difference cannot be corrected at all (i.e. the near detector beam is assumed to be the no oscillation expectation), then the mixing hypothesis $\Delta m^2 = 0.01$ eV^2 and $\sin^2 2\theta = 0.7$ will be fitted as $\Delta m^2 = 0.012$ eV^2 and $\sin^2 2\theta = 0.6$.

Figure 4.20 shows the cumulative χ^2 (for 58 degrees of freedom) versus the reconstructed neutrino energy. The fits with large near beam contamination give poor overall fits (χ^2/d.o.f > 2). Moreover the discrepancy occurs at high neutrino energy (greater than 20 GeV) where there are too many neutrinos in the MCEXP sample. The net effect in these fits is to move the favoured regions to larger Δm^2. This situation is alleviated somewhat if shape-only fits are considered (χ^2/d.o.f < 2 for all cases).

Figure 4.21 shows the error contours in parameter space and the best-fit neutrino energy distributions for two of the cases considered above. Both cases are for a MCEXP sample with $\Delta m^2 = 0.01$ eV^2 and $\sin^2 2\theta = 0.7$. The top two plots assume that the MCNO sample consists of 80% of the far detector spectrum and 20% of the near detector spectrum. The top left-plot shows that the true values of the parameters are regained when the fit is performed and the right hand plot shows that the MCEXP energy distribution (error bars) is well-described by the best-fit MCNO energy distribution (histogram).

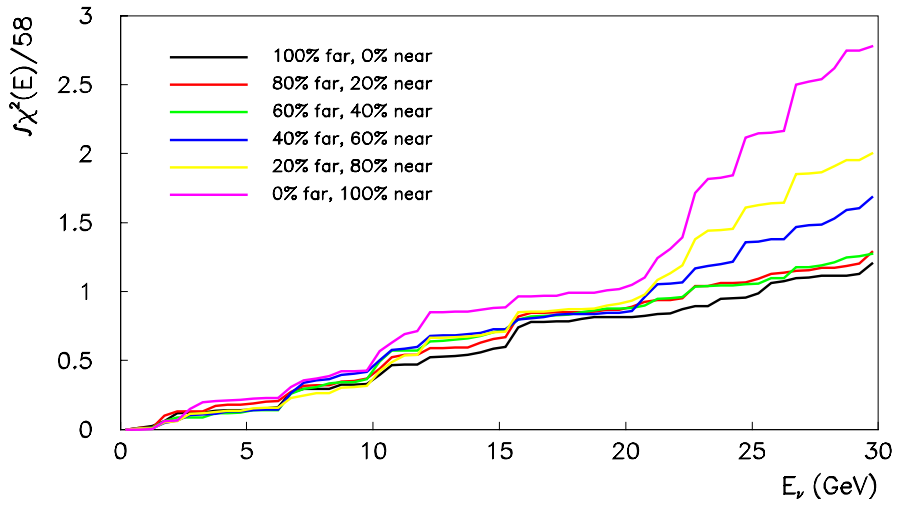

Figure 4.20 – Cumulative χ^2 distributions, plotted as a function of neutrino energy, for the best fit parameters of the MCEXP sample with $\Delta m^2 = 0.01$ eV^2 from Figure 4.18. The values of χ^2 are divided by the 58 degrees of freedom in the fits.

The bottom two plots of Figure 4.21 assume that the MCNO energy distribution is identical to the near detector distribution. The bottom left-hand plot shows that the values of the parameters favoured by the fit are not consistent with the true parameters. The bottom right-hand plot, however, shows that the agreement between the MCEXP energy distribution and the best-fit MCNO distribution is poor. This implies that the observation of a large effect with a poor value of χ^2 between the MCEXP energy distribution and the best-fit MCNO distribution could indicate the presence of a systematic effect in the fit.

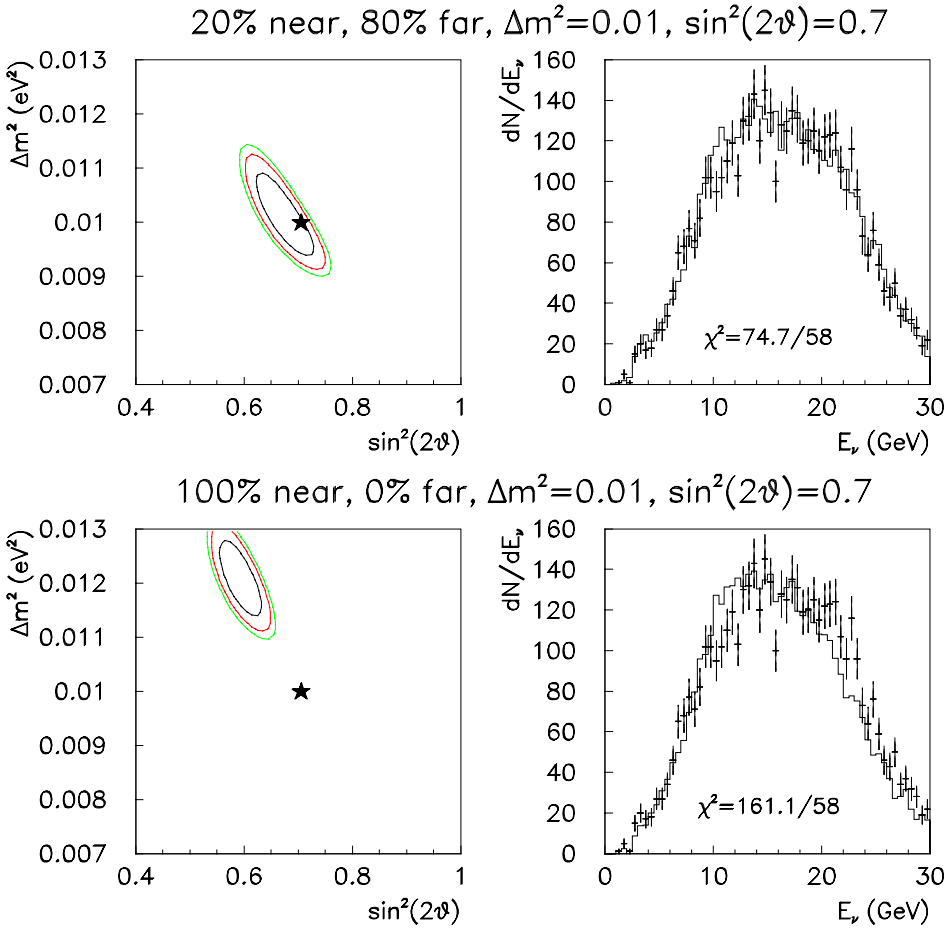

Figure 4.21 – The result of fits to MCEXP samples with $\Delta m^2 = 0.01$ eV^2 and $\sin^2 2\theta = 0.7$ with a MCNO sample that is 20% of the near detector spectrum and 80% of the far detector spectrum (top plots) and a MCNO sample that is 100% of the near detector spectrum.

4.5.6 Effect of near/far systematics for no oscillations

The previous section has shown that there are potentially large shifts in fitted parameters if there are systematic uncertainties associated with the prediction of the unoscillated far detector spectrum from measurements in the near detector. Errors associated with the relative neutrino rates in the two detectors and the relative energy scales can be accounted for in the fits to eliminate these shifts. This assumes that these systematics exist on top of a large neutrino oscillation signal. If there are no oscillations then these systematics may induce spurious signals that can be fitted with non-zero values of the mixing parameters.

Figure 4.22 shows the results of shape-only fits to a MCEXP sample with the far detector beam spectrum and no oscillations with MCNO samples that are a mixture of the near and far spectra. Mixtures with 20%, 40%, 60%, 80% and 100% of the near detector spectrum are considered. A favoured region is found in all cases with $\Delta m^2 \sim 0.02$ eV^2 and $\sin^2 2\theta > 0.1$. These fits are driven by the large near-far difference at 12 GeV. The top plot shows the value of $\sin^2 2\theta$ favoured by the fits as a function of near spectrum fraction. The ν_μ CC energy test, which is described in section 4.2, is expected to set a limit of $\sin^2 2\theta < 0.06$ for $\Delta m^2 = 0.02$ eV^2 at 90% confidence for a 3.3 kiloton year exposure of MINOS, assuming no systematic error between the near and far detectors. This is indicated by the dotted line in the plot.

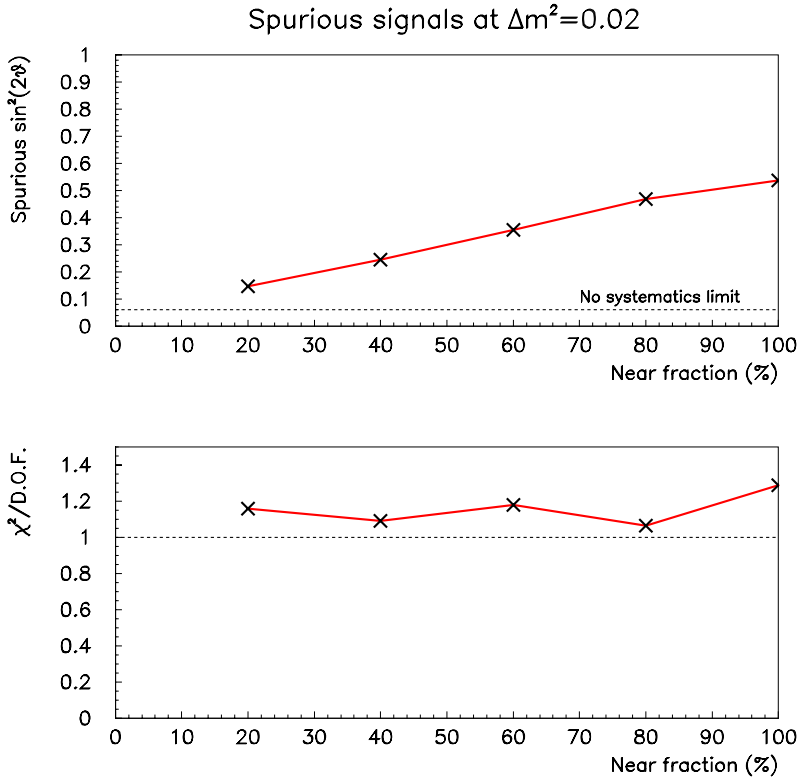

Figure 4.22 – Free normalisation fits to no oscillation MCEXP samples with a predicted energy spectrum that is an admixture of the near and far detector energy spectra with x% near and (100-x)% far. The top plot shows the size (in $\sin^2 2\theta$) of the spurious signal that occurs at $\Delta m^2 \sim 0.02$ eV^2 as a function of the near spectrum fraction, x. The bottom plot shows the value of χ^2 per degree of freedom between the MCEXP and the best fit MCNO energy distributions.

If no attempt is made to correct the near-far difference then a large apparent signal occurs at $\Delta m^2 \sim 0.02$ eV^2 and $\sin^2 2\theta = 0.5$ in the absence of neutrino oscillations. The left-hand plot of Figure 4.23 shows the favoured region of parameter space for this case and the right-hand plot shows a comparison of the shapes of the neutrino energy distributions for the MCEXP sample with no oscillations (which uses the far detector spectrum and is represented by the error bars) and the MCNO sample for no oscillations (which uses the near detector spectrum and is represented by the histogram). This plot clearly shows that the near-far difference at ~12 GeV is responsible for the apparent oscillation signal.

The bottom plot of Figure 4.22 shows the value of χ^2 calculated from the reconstructed neutrino energy distributions. The χ^2 is acceptable (χ^2/d.o.f. ~ 1) in all cases. The large near-far spectral difference at 12 GeV is therefore problematic for the CC energy test as it can produce large signals with parameters similar to those suggested by the atmospheric neutrino anomaly. This difference must therefore be correctable to = 20% of its raw value in order for MINOS to be sensitive to oscillations with $\sin^2 2\theta \geq 0.1$.

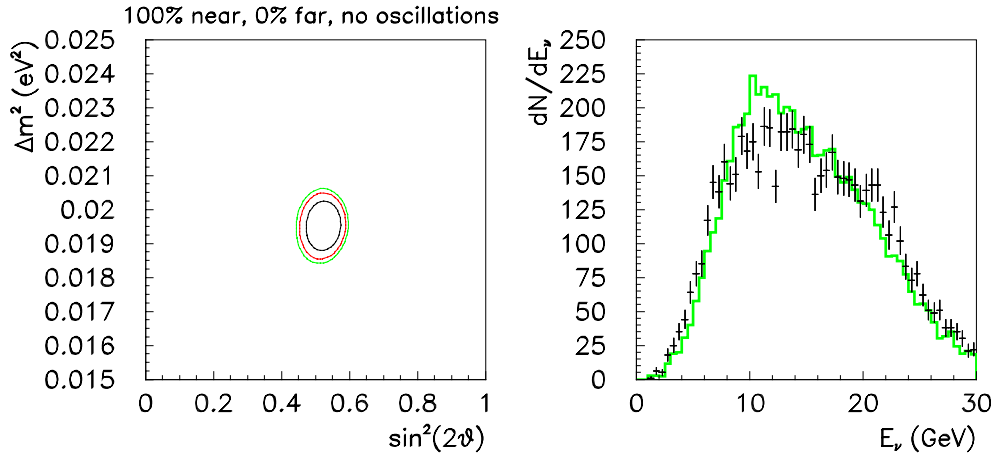

Figure 4.23 – The result of a shape-only fit to a no oscillation MCEXP sample with a MCNO sample that assumes the near detector energy spectrum. The left-hand plot shows the favoured region of parameter space found by the fit and the right-hand plot shows a comparison between the no oscillation MCEXP energy distribution (error bars) and the no oscillation MCNO energy distribution (histogram).

4.6 Summary and conclusions

The analysis of ν_μ CC energy distributions is the only way to provide a direct measurement of Δm^2 in MINOS and an observation of an energy dependent suppression of the number of CC events would be a convincing demonstration of neutrino oscillations. The reference NuMI three horn wide band beam for MINOS has been designed to maximise the

neutrino flux at high energies and has maximum sensitivity to neutrino oscillations at $\Delta m^2 = 0.025$ eV^2. The beam energy is therefore higher than optimal for the values of the parameters suggested by the Kamiokande atmospheric neutrino analysis ($\Delta m^2 \sim 0.01$ eV^2, $\sin^2 2\theta \sim 1$). These parameters can be measured with an accuracy of ±10% for a 3.3 kiloton year exposure. The relative lack of neutrinos below 5 GeV limits the test to values of Δm^2 above 0.005 eV^2. Energy resolution limits the test to below $\Delta m^2 \sim 0.2$ eV^2.

Systematic effects between the near and far stations can induce sizeable shifts on the measurement of neutrino oscillation parameters. For large signals, many of these effects can be alleviated by letting the near/far rate normalisation or the near/far energy shift float, at the expense of larger errors on the measured parameters. If there are no oscillations, however, these systematics can induce spurious signals. Systematics therefore limit the range of parameter space in which neutrino oscillation signals can be measured.

The most insidious systematic error is the difference in neutrino energy spectra between the near and far detectors. This difference depends on the secondary hadron production spectrum, which is uncertain at the present time and therefore cannot be fully corrected for. An estimate of the spectral difference between the near and far detectors is x% of the raw near/far difference, where x can range from 0 to 100%. A shape-only fit to a no-oscillation sample with this systematic error induces a signal at $\Delta m^2 \sim 0.02$ eV^2 and $\sin^2 2\theta > 0.15$. Unless the spectral difference can be corrected to better than 20% of the current value, it appears that this systematic error limits the measurement of neutrino oscillation parameters to $\sin^2 2\theta > 0.2$.

An experiment to measure the secondary hadron spectrum resulting from 120 GeV protons on a carbon target and hence reduce the systematic error on the prediction of the far detector spectrum has been proposed. This analysis shows that such an experiment is highly

desirable to prevent this uncertainty from seriously limiting the sensitivity of MINOS to neutrino oscillations using the CC energy test.

Chapter 5 Parameter fitting with a low energy beam

The recent preliminary results [36] from Super-Kamiokande on the zenith angle distribution of atmospheric neutrinos seem to suggest oscillations with a lower value of Δm^2 than that suggested by its precursor, Kamiokande, which indicated a value of $\Delta m^2 \sim 10^{-2}$ eV^2 [41]. The Super-Kamiokande best fit point to the zenith angle distributions of sub and multi-GeV data is $\Delta m^2 \sim 2\times10^{-3}$ eV^2 and $\sin^2 2\theta \sim 1$ [36]. Although the value of R quoted by Super-Kamiokande ($R \sim 0.60$) indicates a somewhat higher value of Δm^2, this new data demands that forthcoming experiments such as MINOS should take the prospect of a low value of Δm^2 seriously and ensure that they are sensitive to oscillations with these parameters.

The three horn WBB that was discussed in the previous chapter is optimised for $\Delta m^2 \sim 2.5\times10^{-2}$ eV^2 and has limited sensitivity to low Δm^2. It is impossible to perform a precision measurement of the neutrino oscillation parameters with this beam if $\Delta m^2 < 5\times10^{-3}$ eV^2.

Two options are available to improve the sensitivity of MINOS at low Δm^2. The first option, to increase the baseline of the experiment, is only feasible for new proposals and is impossible for MINOS which is at an advanced stage of planning. The second option is to reduce the beam energy, maximising the flux at low energy at the expense of the overall rate. For $\Delta m^2 = 2\times10^{-3}$ eV^2, the ideal beam would have a mean neutrino energy of ~1 GeV. A putative beam design which, although not quite satisfying this criteria, provides a greater sensitivity to low Δm^2 has been proposed. The beam spectrum is shown in Figure 5.1.

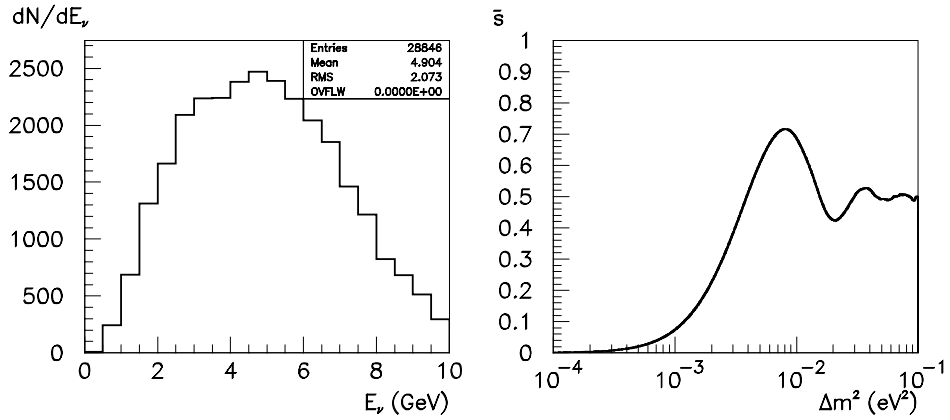

Figure 5.1 – Left-hand plot: low energy WBB beam spectrum. Right-hand plot: the quantity $\bar{S}$ (defined in equation(4.2)) as a function of Δm^2 for the low energy beam.

This beam has only 1/6th of the event rate of the three horn WBB, producing about 800 events per kiloton year at the far detector site, but has maximum sensitivity to neutrino oscillations at $\Delta m^2 \sim 0.008$ eV^2 (the point at which $\bar{S}$ is maximised) which is about a factor of three lower than the standard WBB. This chapter studies the parameter measurement capability of this beam, using the techniques that were developed in Chapter 4.

5.1 ν_μ CC identification at low E_ν

If neutrino oscillations occur with $\Delta m^2 < 5\times10^{-3}$ eV^2 then the important neutrinos have energies below 3 GeV. The difficulty in performing a parameter fit in this case lies in the ability of a relatively coarse grained detector such as MINOS to identify ν_μ CC events at these energies and to reconstruct the neutrino energy.

The left hand plot of Figure 5.2 shows the CC efficiency and NC inefficiency as a function of true E_ν if the simple event length cut of 44 planes is applied to `GMINOS` events

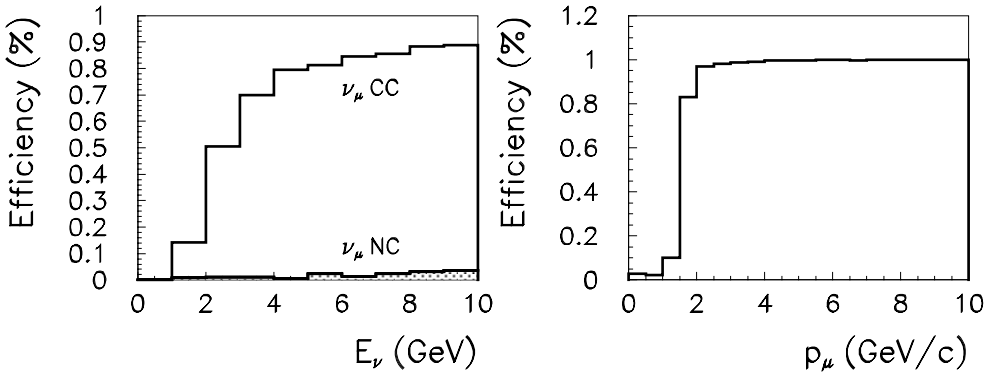

Figure 5.2 – Selection efficiency for low energy events with the cut EVLENGTH>44 planes.

generated with the low energy WBB spectrum. The right hand plot shows the CC efficiency as a function of muon momentum. Both plots show that there is a sharp drop in efficiency below 2 GeV, limiting the sensitivity to oscillations with low Δm^2.

A scan of these low energy events with the event display package VINES reveals that it is possible to decide by eye in most cases whether a particular event is a ν_μ CC or NC

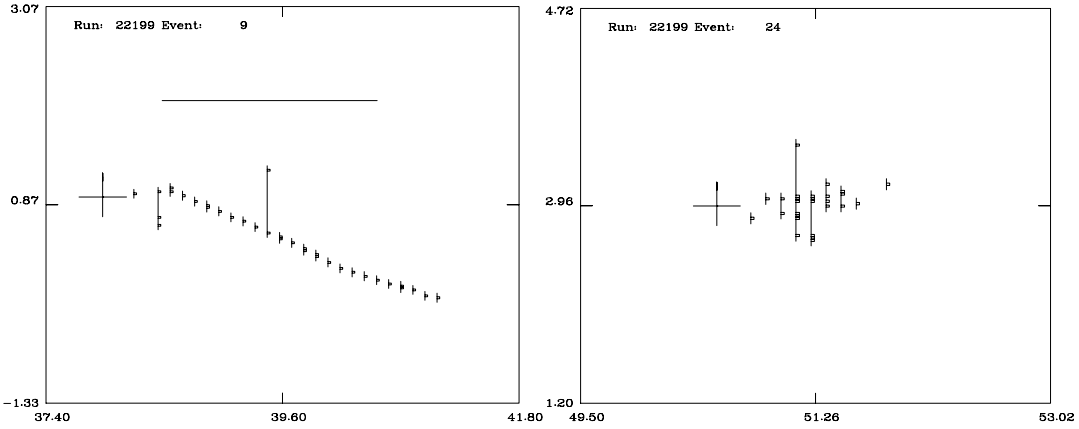

Figure 5.3 – GMINOS events generated with the low energy beam. Left-hand plot: quasi-elastic ν_μ event with short muon track. Right-hand plot: NC event with low energy hadronic shower.

interaction. A significant proportion of the ν_μ CC sample are quasi-elastic so only a short track appears in the detector. In many cases where a short muon track is accompanied by hadronic activity, it is usually clear that the event contains a muon since the muon track is generally longer than the hadronic shower. Figure 5.3 shows VINES event pictures of typical ν_μ CC and NC events generated with the low energy beam. A better CC selection algorithm for these energies would therefore be to demand the presence of a track and require low hadronic activity at the downstream end of the event. The following analysis uses a simple form of the Hough Transform to flag the presence of a track in an event.

5.2 Finding tracks with the Hough Transform

The Hough transform [83] is a method to find tracks in digitised images. It does not examine the microscopic structure of the events and is therefore insensitive to gaps in tracks and scattered background noise hits. In addition, the efficiency of the transform does not depend at all on an accurate reconstruction of the event vertex. This section briefly describes the Hough transform and explains how it is used to identify tracks in `GMINOS` events. Appendix A explores the transform in more detail and evaluates the expected performance of the track finding algorithm under a variety of conditions.

The Hough transform was introduced in 1962 by Paul Hough and was originally used to find tracks in bubble chambers. These days, it is commonly used in the domain of artificial vision and in astrophysics. The function of the Hough transform is to find analytically representable features (straight lines, circles, ellipses) in two-dimensional images. For this analysis, the transform is used to find straight lines (tracks) in the digitised detector readout.

The image to be analysed by the Hough transform is a set of two-dimensional co-ordinates x_i, y_i. A straight line is characterised by the relation $y_i = mx_i + c$, where m and c are the gradient and intercept respectively. The function of the Hough transform is to transform the detector co-ordinates (x_i, y_i) into lines in the parameter space (m, c). These lines are given by the equation $y_i - mx_i - c = 0$. If the image co-ordinates form a straight track, the lines should cross at a particular value of m and c. This principle is illustrated in Figure 5.4.

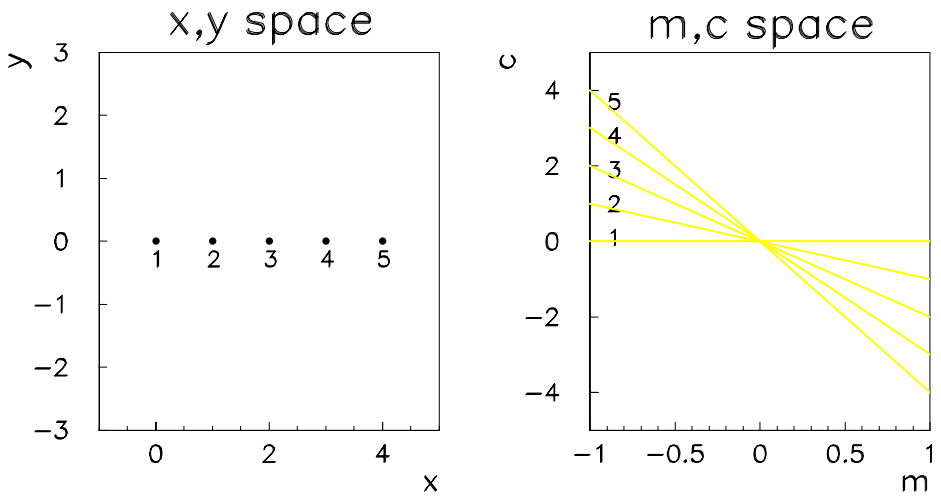

Figure 5.4 – The Hough Transform in action. The left-hand plot shows five points in x, y space that lie in a straight line. The right-hand plot shows the lines in m, c space that correspond to these co-ordinates. The lines converge at a single value of m and c, yielding the parameters of the line.

Formally, the Hough Transform is represented by:

$$H(m,c) = \sum_{hits} \Delta(y_i - mx_i - c) \tag{5.1}$$

where Δ is an indicator such that $\Delta(t) = 1$ if $t = 0$ and $\Delta(t) = 0$ if $t \neq 0$. (m, c) space is referred to as the Hough Space.

Simulated GMINOS events give two orthogonal views of each event in the detector. A set of axes is defined such that z is parallel to the long axis of the detector. Alternate planes give either (x_i, z_i) or (y_i, z_i) co-ordinates. Since there are two two-dimensional images per event, there will be two Hough spaces. Each Hough space is a two dimensional array or histogram of points in (m, c) space.

The Hough space is filled as follows for the set of (x_i, z_i) co-ordinates in an event:

1. a pair of co-ordinates (x_i, z_i) is chosen;
2. a value of the gradient is chosen, corresponding to the first m bin in Hough space;
3. for this value of m and (x_i, z_i), the value of the intercept c satisfying the equation $x_i - mz_i - c = 0$ is calculated;
4. the bin in Hough space corresponding to this particular value of m and c is found and its contents are incremented by one;
5. steps 3-4 are repeated for all bins of m in Hough space;
6. steps 2-5 are repeated for all (x_i, z_i) in the event.

The same procedure is used to fill a separate Hough space for the (y_i, z_i) co-ordinates in the event.

Figure 5.5 shows a straight track from a ν_μ CC interaction. Figure 5.6 is the Hough space of this particular image. There is a large localised peak in the Hough space corresponding to the presence of a track in the event. The position of the peak in Hough space gives the parameters of the track. Figure 5.7 shows a shower from a ν_μ NC

interaction. The Hough space of this event (Figure 5.8) does not show a localised accumulation point, rather there is a large ridge which is the result of the overlap of many parallel lines.

The signature of a track in an event is the presence of a localised peak in Hough space. Both Hough spaces should contain peaks if the event contains a straight track. The Hough space used in this analysis is a two-dimensional histogram with 40×40 bins. The axes of both Hough spaces are renormalised so that they range from 1 to 40 in both dimensions. This renormalisation is necessary because of the very different scales used in the two dimensions (-1< *gradient* < +1 and –200 < *intercept* < +200). The bins with entries that are ≥ 75% of the peak value are found and the *rms* of the co-ordinates of these bins with respect to the co-ordinates of the peak are then calculated in each Hough space. The values of *rms* in the two Hough spaces are named `XRMS75` and `YRMS75` respectively. They are an estimate of the localisation of the peak in Hough space and should be small for a track and large for a shower.

To flag an event as containing a track, the following procedure is adopted:

- both Hough spaces are filled and the *gradient* and *intercept* dimensions are renormalised to the range 1 to 40;
- the Hough spaces are scanned and the peak values in each are recorded;
- the bins in $x-z$ Hough space which contain entries ≥ 75% of the peak value are found. The *rms* of the co-ordinates of these bins with respect to the co-ordinates of the peak is then calculated. This number is `XRMS75`;
- the above step is repeated for $y-z$ Hough space and `YRMS75` is obtained;

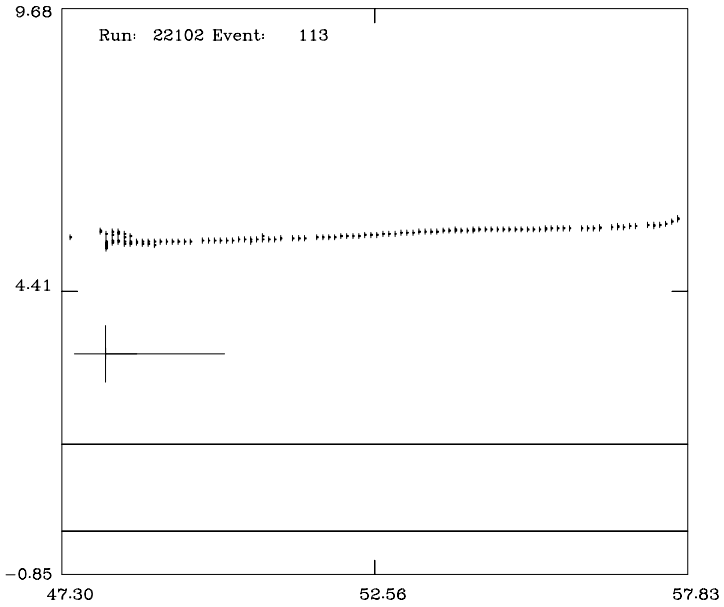

Figure 5.5 – A typical ν_μ CC event.

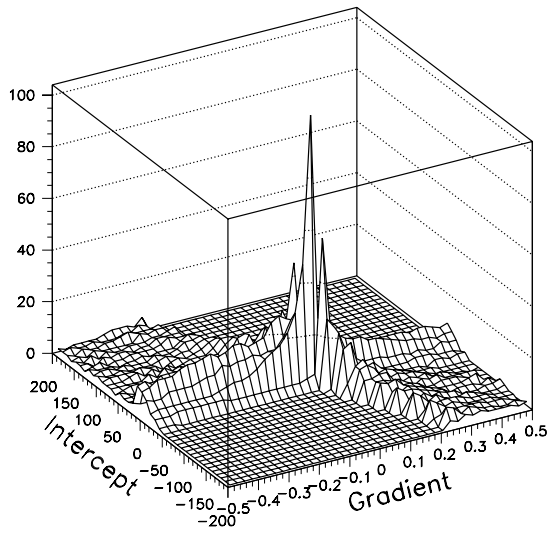

Figure 5.6 – Hough space of event in Figure 5.5.

- for an event to be classified as containing a track, the conditions `XRMS75,YRMS75` < 10 must hold.

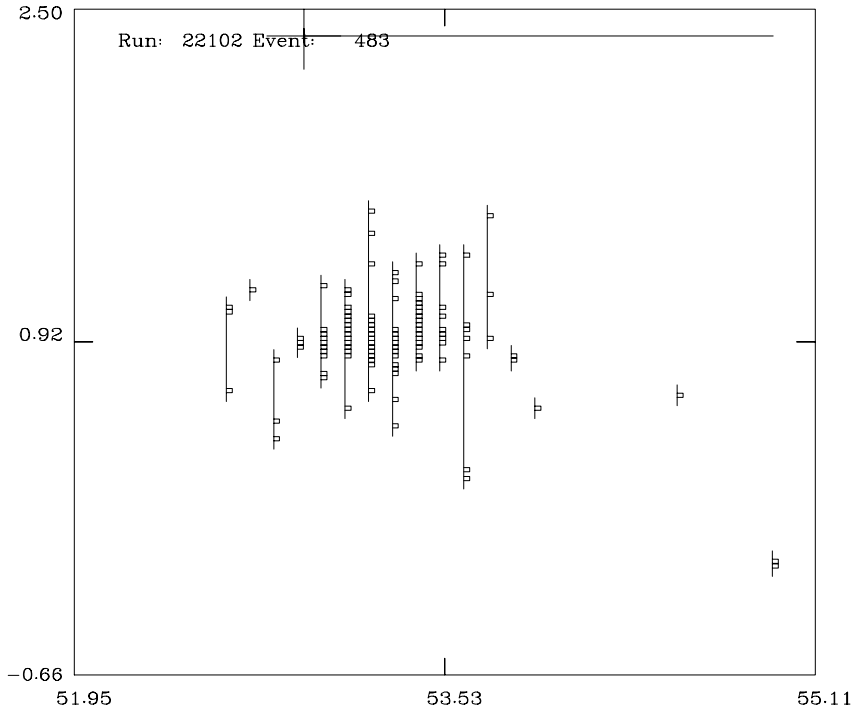

Figure 5.7 – A typical NC event.

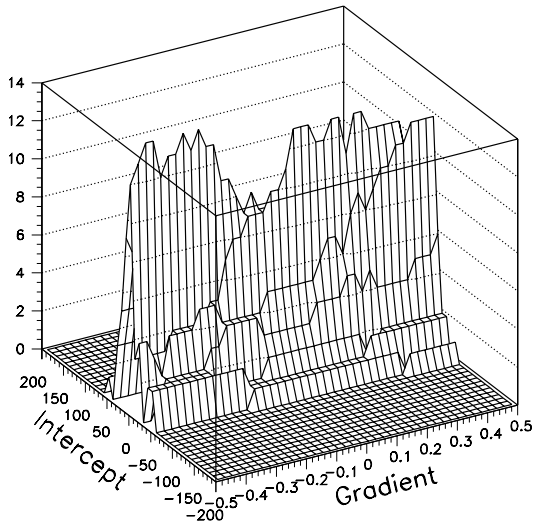

Figure 5.8 - Hough space of the event in Figure 5.7.

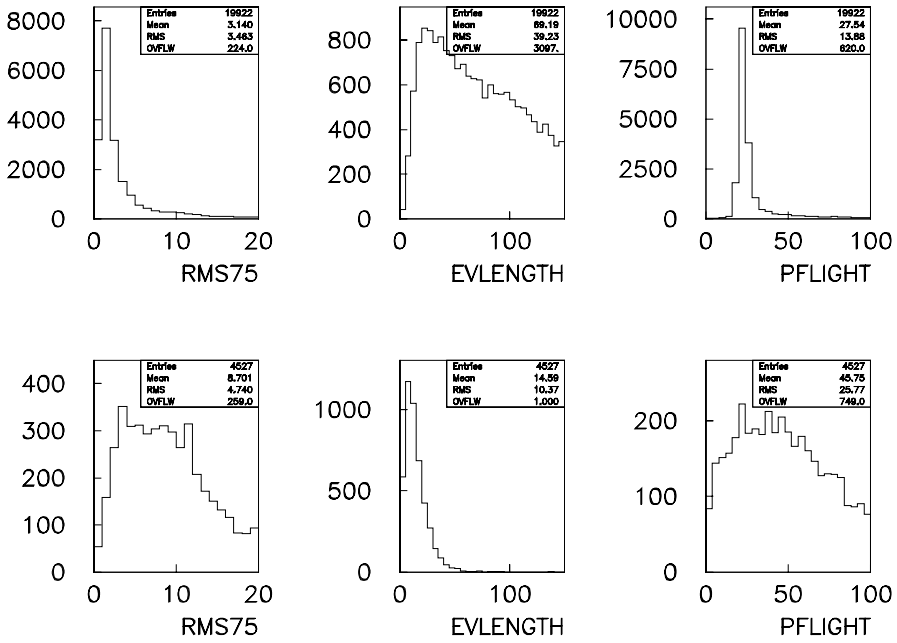

Figure 5.9 – The discriminating variables that are used in the low energy ν_μ CC analysis. The top row is for ν_μ CC events and the bottom row is for NC events.

The two left-hand plots of Figure 5.9 show distributions of `RMS75` for CC and NC events. The CC events tend to have low (< 10) values of `RMS75` while the NC events exhibit a much broader distribution. There is, however, a large set of NC events with low `RMS75`. These are typically low energy events with a single pion which appears as a short track in the detector. This implies that it is more difficult to obtain a clear separation between CC and NC events in the low energy beam.

The two centre plots of Figure 5.9 show distributions of event lengths for ν_μ CC and NC events. There are very few NC events with event lengths greater than 40 planes. A cut of event length > 10 planes rejects a useful fraction of these NC events although it imposes a low energy cut off on the muon momentum, p_μ, for ν_μ CC events of approximately

330 MeV. For very low Δm^2 it may be desirable to relax this cut at the expense of higher background contamination.

The two right-hand plots show the average pulse height per plane (PFLIGHT) in the second (downstream) half of the event for ν_μ CC events (top plot) and NC events (bottom plot). A minimum ionising particle (mip) produces an average pulse height of 22 photoelectrons per plane for liquid scintillator active detectors. ν_μ CC events tend to have few mips per plane in the second half of the event whereas NC events have several mips per plane.

The following cut sequence is applied to the low energy data:

- EVLENGTH > 10 planes;
- PFLIGHT < 60 p.e. (equivalent to 3 mips per plane);
- PLANEOCC > 0.9 (90% of planes between vertex and end of event contain 1 or more hit);
- (EVLENGTH > 50) .OR. (RMS75 < 10). If the event is long (> 50 planes) then it is very likely to be a ν_μ CC interaction. If the event is shorter than 50 planes then it must contain a straight track.

Figure 5.10 shows the CC selection efficiency (open histogram) and the NC inefficiency (shaded histogram) as a function of E_ν. The dotted curve is the predicted CC selection efficiency assuming a cut-off muon momentum of 0.33 GeV (the threshold energy required for a muon to penetrate 10 planes of 2 cm steel). The measured selection efficiency is lower than the predicted efficiency, because further cuts (involving RMS75 and PFLIGHT) are required to select low energy CC events in this analysis. The right-hand plot

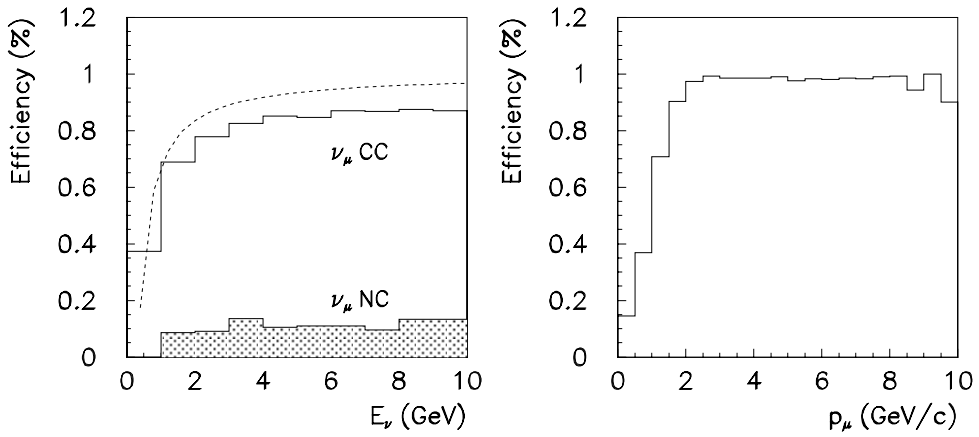

Figure 5.10 – Selection efficiency for low energy events.

shows the CC efficiency as a function of p_μ and shows that, for the reasons discussed above, the selection algorithm is not 100% efficient at identifying events with muons with $p_\mu \geq 0.33$ GeV. A comparison of Figure 5.10 and Figure 5.2, which is for events that are longer than 44 planes, shows that the new cuts have increased sensitivity at low neutrino energies and muon momenta, at the expense of higher background contamination.

5.3 Energy measurement for low energy events

The hadron shower energy for low energy events is estimated from the summed pulse height in the first eight detector planes downstream of the event vertex, corresponding to approximately one interaction length in the detector. This definition differs from that for high energy events because the hadronic showers are less energetic and are therefore shorter. The contribution due to the passage of the muon through the first eight planes is subtracted from the total pulse height. The top left-hand plot of Figure 5.11 shows the reconstructed hadron energy (solid histogram), which is estimated by:

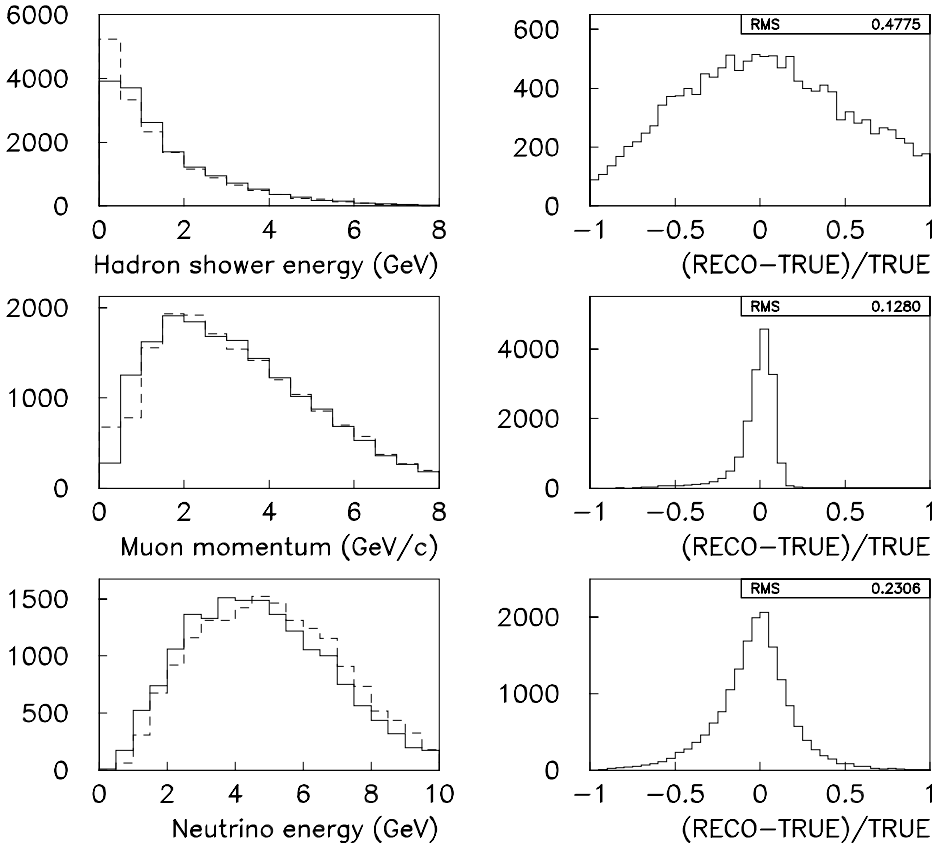

Figure 5.11 – Energy measurement in the low energy beam. The left-hand plots show reconstructed (solid histogram) and true (dashed histogram) energies. The right-hand plots show the fractional difference between reconstructed and true energies.

$$E_{hadrons} = \frac{\sum_{plane=1}^{8} pulseheight - 140\,p.e.}{350\,p.e.}, \tag{5.2}$$

the pulse height in the first 8 planes minus a 140 pe contribution due to the muon, divided by 350 pe. The true hadron energy distribution is indicated by the dashed histogram. The top right-hand plot shows the fractional error on the measurement of hadron energy. The width of the distribution is rather wider than the corresponding distribution for the high energy three horn WBB in Figure 4.6.

The muon energy is estimated in the same way as for high energy events. The centre-left plot of Figure 5.11 shows the true and reconstructed muon momentum for events that stop in the detector volume. For these energies, only 3% of ν_μ CC events exit the detector so 97% of muons have their energies estimated by range.

The bottom left plot of Figure 5.11 shows distributions of true and reconstructed neutrino energy. The *rms* width of the bottom right plot is slightly larger than for the high energy beam due to larger measurement errors on the hadron shower energy.

5.4 Example fits

A large MCNO sample of 25000 events and a MCEXP sample of 13700 events have been generated with the low energy WBB spectrum, corresponding to approximate exposures of 36.5 and 20 kiloton years respectively. These samples are reduced to 11014 and 5959 events respectively when fiducial volume and low energy CC identification cuts are applied .

Figure 5.12 shows the results of fixed normalisation fits to two MCEXP samples (both with $\sin^2 2\theta = 0.7$) with $\Delta m^2 = 0.008$ eV^2 (the optimum value) and $\Delta m^2 = 0.003$ eV^2 (the Super-Kamiokande parameters). The favoured regions of parameter space in the fits are consistent with the true parameters and the fit quality is good in both cases. The fact that the contours are elongated for $\Delta m^2 = 0.003$ eV^2 suggests that these parameters are at the limit of sensitivity of the low energy beam. For $\Delta m^2 = 0.003$ eV^2, the dip in the energy spectrum occurs at 1.8 GeV and there are few neutrinos at this energy, even in the low energy beam. It is therefore impossible to perform a precision measurement of the parameters if Δm^2 is much lower than 0.003 eV^2.

The parameter measurement capability of the low energy beam as a function of Δm^2 is summarised in Figure 5.13, which is the analogue of Figure 4.14 for the high energy beam. The plot assumes a 20 kiloton year exposure with the low energy beam. The parameters can be measured between $\Delta m^2 = 0.003$ and 0.05 eV^2, above which the dips in the energy spectrum are unresolved. The best measurement of neutrino oscillation parameters occurs around $\Delta m^2 = 0.01$ eV^2 which suggests that this beam may be more suitable than the high

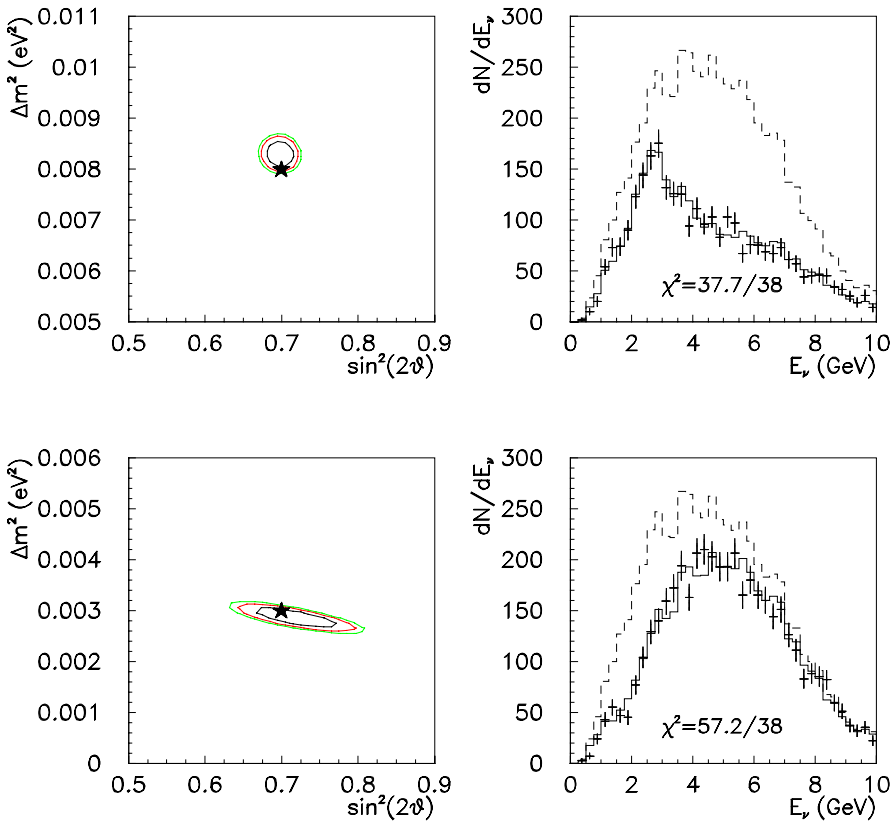

Figure 5.12 – Fixed normalisation fits to MCEXP samples in the low energy beam with $\Delta m^2 = 0.008$ eV^2 (top plots), $\Delta m^2 = 0.003$ eV^2 (bottom plots) and $\sin^2 2\theta = 0.7$. The left-hand plots show the 68%, 90% and 95% C.L. error contours drawn with respect to the log likelihood maximum. The stars represent the input parameters. The right-hand plots show the MCEXP reconstructed neutrino energy distributions (error bars), the best fit MCNO sample (solid histogram) and the unoscillated MCNO sample (dashed histogram). A 20 kiloton year exposure of MINOS is assumed.

energy beam for measuring the Kamiokande parameters. The Super-Kamiokande best-fit point ($\Delta m^2 = 0.003$ eV^2) can be measured with ±10% precision in both Δm^2 and $\sin^2 2\theta$.

Figure 5.14 shows the effect of near/far energy shifts on fits to a MCEXP sample with $\Delta m^2 = 0.003$ eV^2 and $\sin^2 2\theta = 0.7$. Fits with positive energy shifts favour larger values of $\sin^2 2\theta$ and Δm^2 whereas fits with negative shifts favour $\sin^2 2\theta \sim 0.5$ and $\Delta m^2 \sim 0.015$ eV^2.

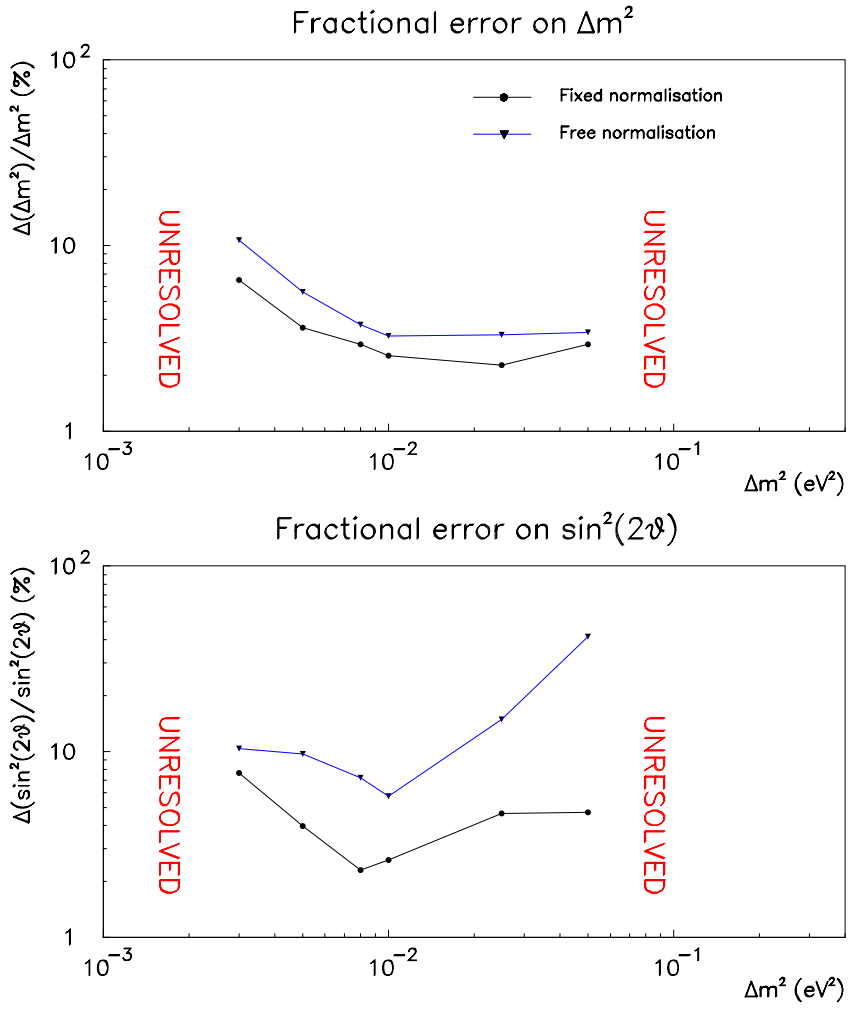

Figure 5.13 – Summary of parameter measurement errors for fits to neutrino oscillations with various values of Δm^2 and $\sin^2 2\theta = 0.7$.

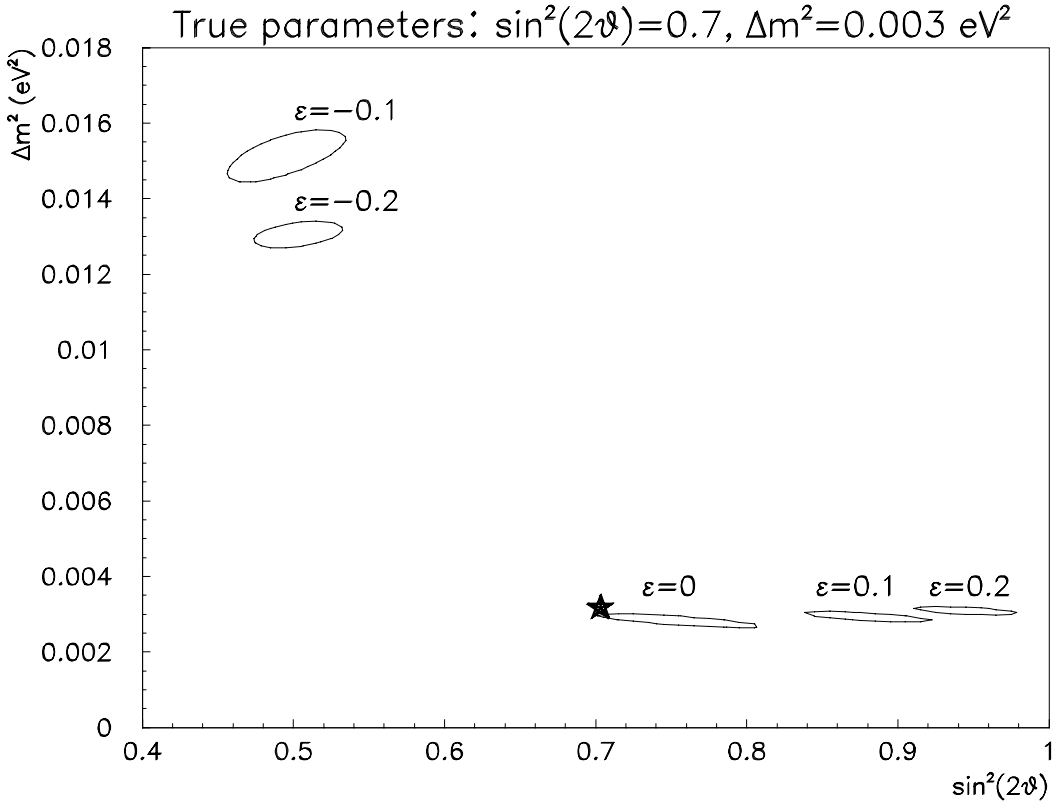

Figure 5.14 – Fixed normalisation fits to MCEXP samples with $\Delta m^2 = 0.003$ eV^2, $\sin^2 2\theta = 0.7$ and various near/far energy shifts between the near and far detectors.

For positive values of ε, the parameter that simulates a linear shift between the near and far detector energy scales, the situation is similar to the high energy beam fits in section 4.5.4. The fits are poor because there are too many high energy neutrinos in the MCEXP sample. For negative ε, there is a deficit in the MCEXP sample at 8 GeV which is fitted by neutrino oscillations with $\Delta m^2 = 0.015$ eV^2. This then creates a discrepancy at low energy since there are now too many neutrinos in the MCEXP sample below 4 GeV, which is alleviated somewhat by fitting with a smaller value of $\sin^2 2\theta$. The fit quality is still poor however (χ^2/d.o.f >2).

5.5 Effect of systematic error for no oscillations

The low energy beam is expected to be subject to the same systematic effects as the high energy beam. Since the low energy beam design is extremely preliminary, there is no near detector beam spectrum available at the present time. The study of near-far spectral differences, which is the most important source of systematic error for the CC energy test in the high energy beam, cannot therefore be studied, although the other sources of systematic error described in section 4.5.5 can be investigated in the low energy beam.

Figure 5.15 shows the effect of a near/far energy shift on a fit to a MCEXP sample

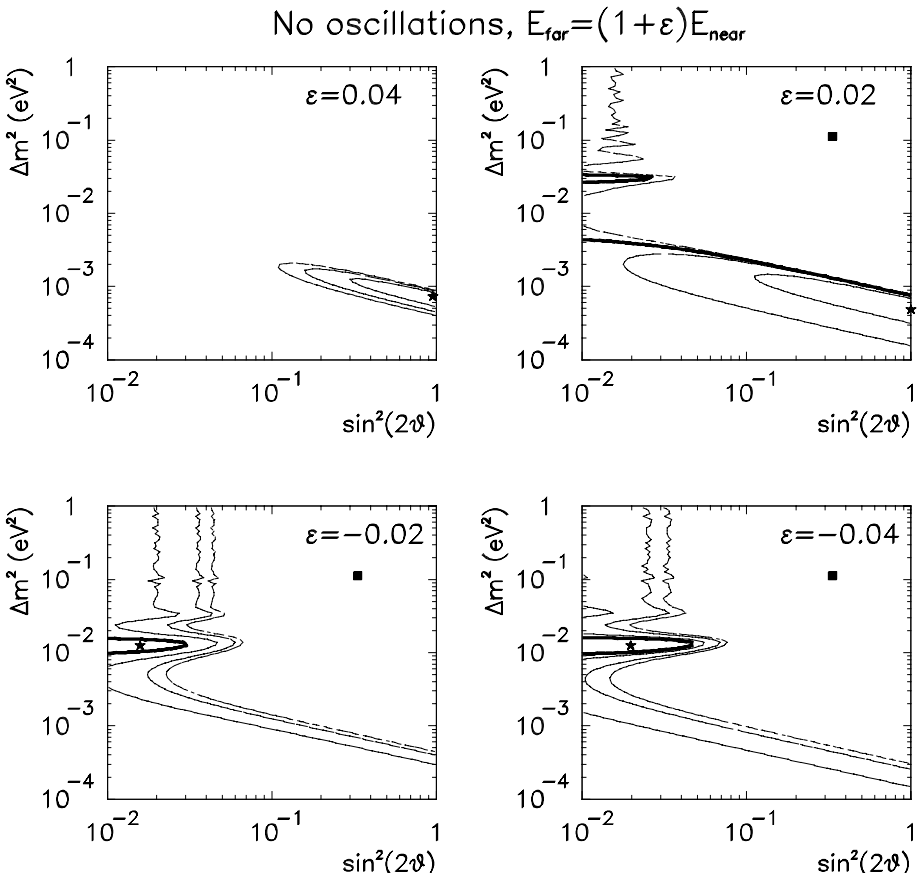

Figure 5.15 – Fixed normalisation fits to a MCEXP sample with no oscillations with four values of the near/far energy shift between near and far detectors.

with no oscillations. For a positive energy shift, the effect is to create a deficit at very low neutrino energy. This is fitted by very small Δm^2 (10^{-3} eV^2) and large $\sin^2 2\theta$. A negative energy shift produces a deficit at high energy which is fitted by very small $\sin^2 2\theta$ (10^{-2}) and $\Delta m^2 \sim 0.01$ eV^2. The thick line indicates a zero value of log likelihood and the regions that are marked with the black square are less likely than the no oscillation hypothesis. The stars mark the log likelihood maxima in each plot.

Figure 5.16 shows the result of fits to a MCEXP sample with no oscillations with a shift in the near/far event rate of +2% and +4% respectively. For a 2% energy shift, there is a weak allowed region (maximum log likelihood ratio=1.6) at large Δm^2 and $\sin^2 2\theta \sim 0.03$ and one at large $\sin^2 2\theta$ and $\Delta m^2 < 10^{-3}$ eV^2.

A 4% shift in the relative near/far event rate produces a stronger solution (maximum log likelihood ratio = 5.6) at $\Delta m^2 \sim 0.03$ eV^2 and $\sin^2 2\theta \sim 0.08$. The favoured region extends up to large Δm^2 for $\sin^2 2\theta \sim 0.06$ and there is a second region at large $\sin^2 2\theta$ and $\Delta m^2 < 10^{-3}$ eV^2. These features occur because an oscillation signature does not in general

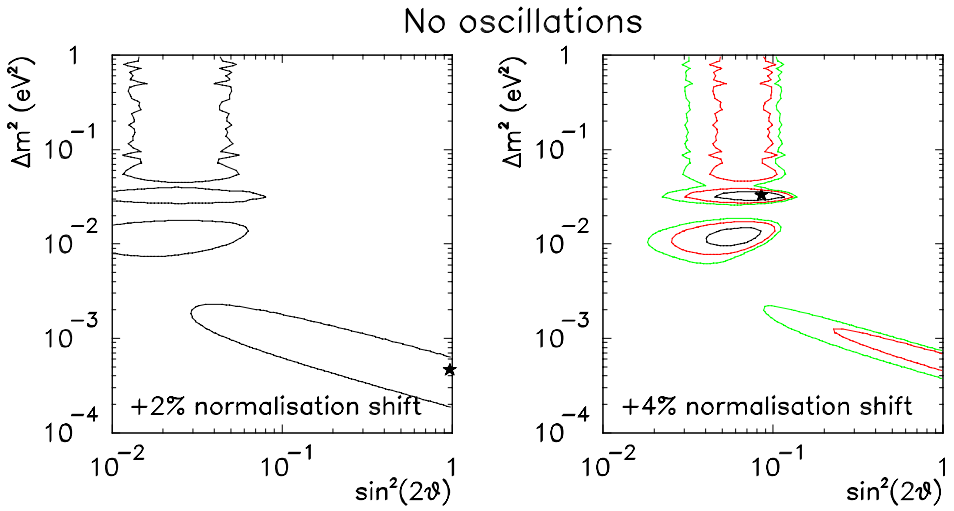

Figure 5.16 – Fits to a no oscillation MCEXP sample with a +2% shift (left-hand plot) and a +4% shift (right-hand plot) in the relative near/far event rate.

produce a suppression of the neutrino flux that is independent of energy. Such a situation can occur, however, at very low Δm^2, where the highest energy minimum occurs at very low energy, and at very high Δm^2, where the rapidly varying oscillations are averaged out. For intermediate values of Δm^2 (10^{-3} to 10^{-2} eV^2), the distortion of the low energy spectrum depends strongly on neutrino energy and these regions are disfavoured in the fit.

This point is illustrated by Figure 5.17 which shows neutrino energy distributions for various neutrino oscillation scenarios in the low energy beam. The top-left plot shows the dN/dE distribution expected for no oscillations. The other three plots show the true neutrino energy distributions expected for neutrino oscillations with $\sin^2 2\theta = 1$ and

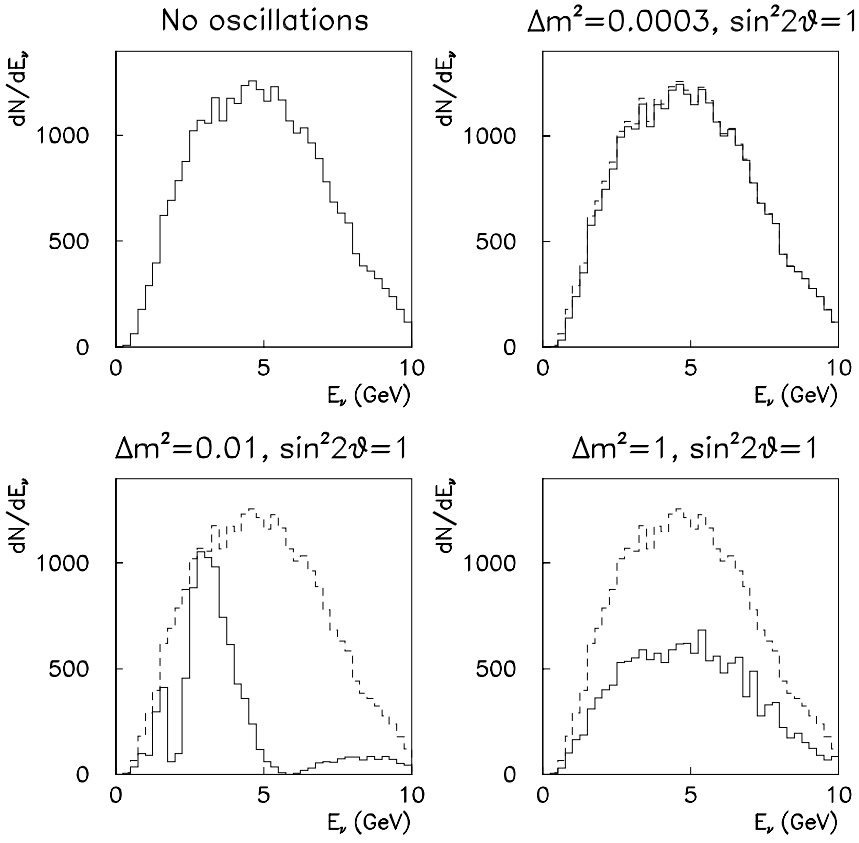

Figure 5.17 – True neutrino energy distributions for various oscillation scenarios in the low energy beam. The no oscillation distribution is indicated by the dotted histograms.

$\Delta m^2 = 3\times10^{-4}, 10^{-2}, 1$ eV^2 respectively. The no oscillation distribution is indicated by the dashed histogram on these plots. For $\Delta m^2 = 3\times10^{-4}$ eV^2 (top-right plot), the suppression is small and energy independent; for $\Delta m^2 = 10^{-2}$ eV^2, the suppression is large and is strongly dependent on the neutrino energy and for $\Delta m^2 = 1$ eV^2, the suppression is large but is independent of neutrino energy. An energy independent shift in the relative normalisation of the near and far detectors can therefore be described by neutrino oscillations with very small or very large values of Δm^2. For a fixed shift in the normalisation, the value of $\sin^2 2\theta$ indicated by the fits is larger for small Δm^2 than for large values of Δm^2. These features are apparent in Figure 5.16.

5.6 Conclusions

The recent Super-Kamiokande and CHOOZ results suggest that Δm^2 may be lower than indicated by Kamiokande. The best fit to the Super-Kamiokande zenith angle distribution of atmospheric neutrinos suggests a value of $\Delta m^2 \sim$ 2-3$\times10^{-3}$ eV^2. For the MINOS baseline of 731 km, this means that the low energy (< 5 GeV) neutrinos are important. A low energy beam that could be produced by reducing the beam energy and redesigning the horns has been proposed to address the implications of this new data. Identification of ν_μ CC events is more difficult at these energies and a more sophisticated method is required than a simple event length cut. The low energy beam has a mean interaction energy of 5 GeV and therefore has maximum sensitivity to oscillations at $\Delta m^2 \sim 0.008$ eV^2. This beam, like the high energy beam, has higher than optimal energies for the signal it is designed to probe (the Super-Kamiokande solution) although, for an exposure of 20 kiloton years, it is possible to measure the Super-Kamiokande parameters to an accuracy of ±10%. This beam is limited to values of Δm^2 between 0.003 and 0.05 eV^2 so

it is unable to push the limit on Δm^2 in the mode $\nu_\mu \rightarrow \nu_e$ below that ruled out by the recent CHOOZ results ($\Delta m^2 < 8\times10^{-4}$ eV^2 at $\sin^2 2\theta = 1$).

The effect of systematic errors on parameter measurement in the low energy beam has also been studied. The near/far rate error must be smaller than 4% for the MINOS experiment to be sensitive to neutrino oscillations with $\sin^2 2\theta \sim 0.1$. At the present moment in time, an error of 4% appears feasible but it has not yet been demonstrated that a smaller uncertainty can be achieved. A linear shift in the near/far energy scales of 4% can induce signals at large $\sin^2 2\theta$ and $\Delta m^2 \sim 10^{-3}$ eV^2 in the low energy beam. This implies that the uncertainty in the near/far energy scale must be smaller than 4% in order for MINOS to be sensitive to neutrino oscillations over the full region of parameter space suggested by the Super-Kamiokande atmospheric neutrino analysis.

Chapter 6 Electron identification in MINOS

Chapter 4 showed how it is possible to measure the mixing parameters in a two-generation framework by identifying ν_μ CC events and measuring the ν_μ disappearance probability, $P_{\mu\mu}$. If it is also possible to identify ν_e CC or ν_τ CC events then an independent and complementary analysis is possible. This describes a simple method to identify ν_e CC events and fit the energy distribution of electron-like events to measure the neutrino mixing parameters. The identification of ν_τ CC events is more difficult and is studied in Chapter 8.

6.1 Electron identification

Several algorithms exist to identify ν_e CC events in MINOS [72][85]. The algorithms typically search for events that are short compared to ν_μ CC events, are more compact than NC events and reach shower maximum earlier than hadronic events. A ν_e CC efficiency of ~15% with less than 1% background of ν_μ events has been obtained by using sophisticated pattern recognition algorithms on simulated MINOS data.

The electron identification algorithm described in this chapter uses simple cuts to produce a ν_e CC efficiency and a ν_μ background inefficiency that is comparable to the simple procedure outlined in the MINOS proposal [69] (ν_e CC efficiency = 27% and ν_μ background efficiency = 1%). Since the purpose of this section is to investigate $\nu_\mu \rightarrow \nu_e$ oscillations with large $\sin^2 2\theta$, it is not necessary to achieve better than 1% background suppression here.

Figure 6.1 shows the discriminating variables used in this analysis. The top three plots are for ν_e CC events and the bottom three plots are for NC events. The two left-hand plots show the summed pulse height in the first 10 planes (approximately 12 radiation lengths) divided by the total pulse height. Electromagnetic showers develop earlier than their hadronic counterparts and so the fraction of total pulse height deposited in the first 10 planes is larger. The centre plots show the RMS width (in centimeters) of events, calculated with respect to the z- axis. Electron showers tend to be somewhat narrower than hadronic showers. The two right-hand plots show distributions of total pulse height. Neutral current events have large missing energy and usually have smaller values of total pulse height than ν_e CC events. A harsh cut on total pulse height, however, would affect the sensitivity of electron identification to neutrino oscillations with low Δm^2, since pulse height is directly

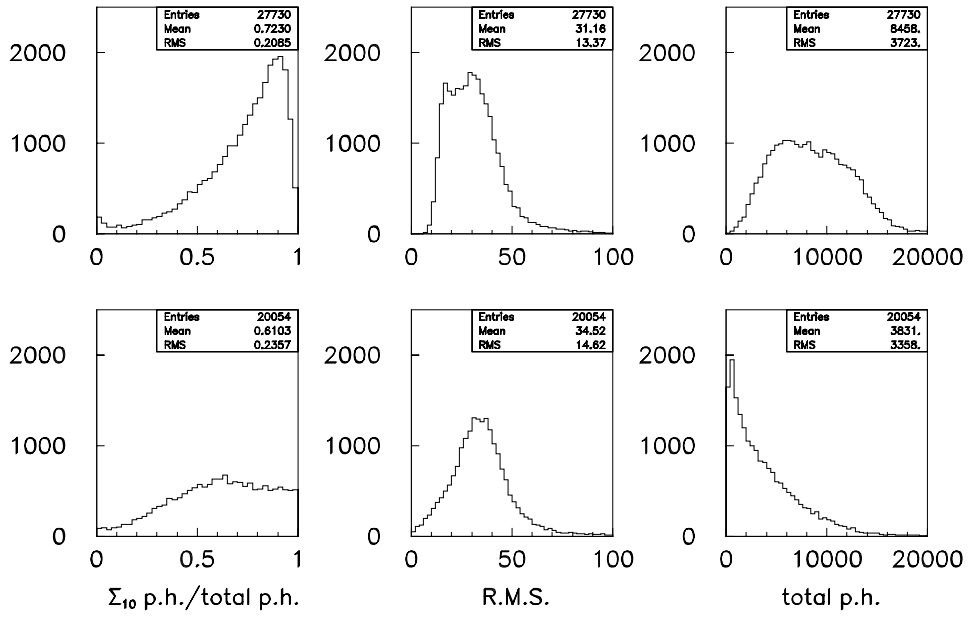

Figure 6.1 – The discriminating variables that are used for electron identification. The top plots are for ν_e CC events and the bottom plots are for NC events. The variables are defined in the text.

related to neutrino energy.

Electron-like events in this analysis are defined by the following cuts:

- event length < 44 planes;
- pulse height in first 10 planes/total pulse height > 0.8;
- RMS < 20 cm;
- total pulse height > 1500 photoelectrons (this corresponds to approximately 3 GeV of visible energy. It has a very small effect on the ν_e CC acceptance since the previous cuts favour ν_e CC events with large visible energy).

Figure 6.2 shows the ν_e CC efficiency and NC inefficiency plotted as a function of

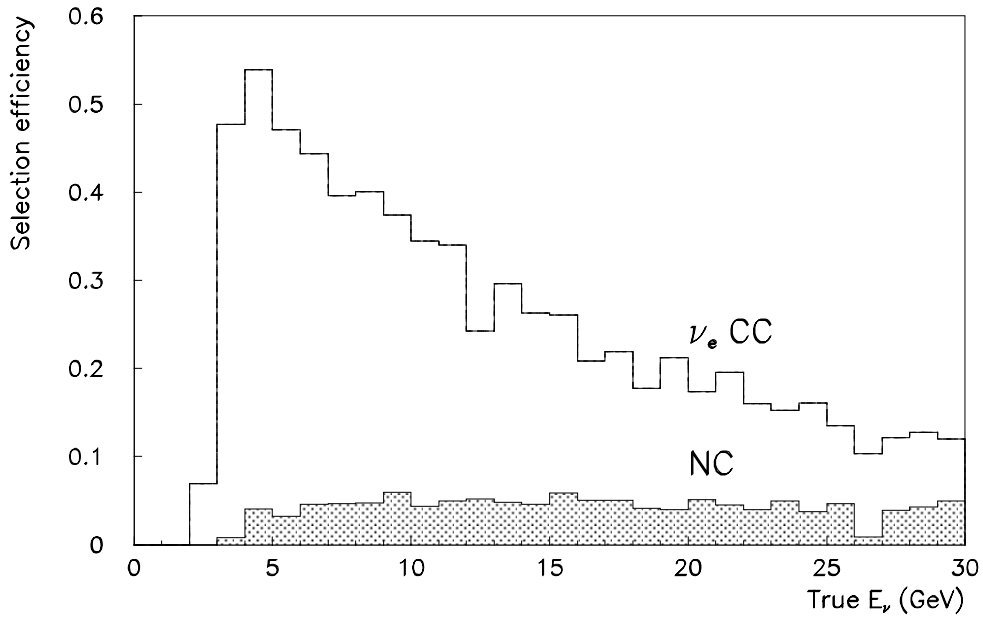

Figure 6.2 - ν_e CC selection efficiency (open histogram) and NC inefficiency (shaded histogram) as a function of true neutrino energy.

true neutrino energy. The average ν_e CC efficiency is 26% and the NC inefficiency is 4%. This background rate can be understood in the following way: the major background to ν_e CC events is inelastic NC events where most of the energy goes into creating a single π^0. Assuming 33% of NC events have a large π^0 fraction, these events have $y > 0.5$ and the selection efficiency is 26%, then the expected background is 0.33×0.5×0.26 = 4.3% which is consistent with the Monte Carlo result.

The ν_e CC selection efficiency is a strong function of neutrino energy. It is zero below 2 GeV and rises sharply to a maximum of ~ 50% at 5 GeV. The efficiency then falls towards a value of 15% at 30 GeV. The reason for this is that electromagnetic showers become longer as the neutrino energy increases. As a consequence a smaller fraction of the total pulse height is contained in the first 10 planes. At very high energy, the showers become longer than 44 planes and therefore fail the event length cut.

The total pulse height is a good measure of electron neutrino energies. The left-hand plot of Figure 6.3 shows reconstructed neutrino energy (solid line), which is defined as total

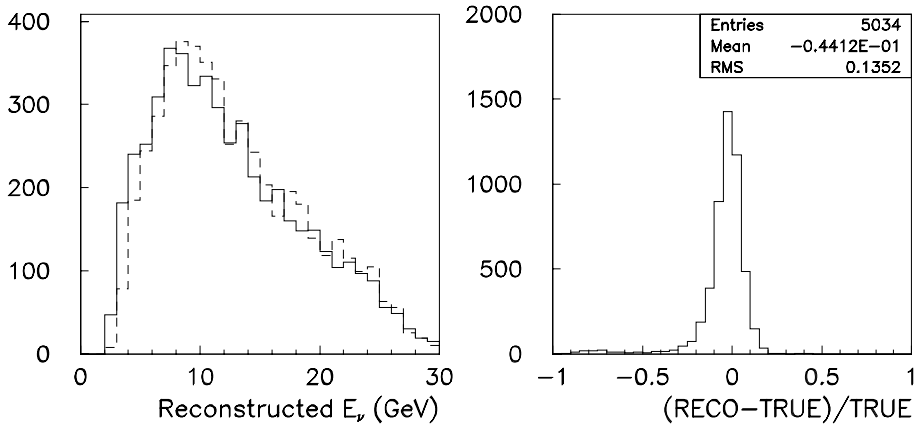

Figure 6.3 – Left-hand plot: reconstructed neutrino energy (solid histogram) and true neutrino energy (dashed histogram) for electron-like events. Right-hand plot: fractional error in energy measurement for these events.

pulse height/540, and true neutrino energy (dashed line) for electron-like events. There is good agreement between the two histograms. The right hand plot shows the fractional difference between reconstructed and true energies. This distribution has a *rms* of 13%, which, given a mean neutrino energy of 10 GeV, roughly corresponds to an energy resolution of $\Delta E_\nu / E_\nu \sim 40\% / \sqrt{E_\nu}$.

6.2 ν_e CC energy test in MINOS

If $\nu_\mu \to \nu_e$ oscillations occur with large $\sin^2 2\theta$ then it is possible to identify electron-like events using the cuts described above and to fit the resulting energy distribution in order to obtain a complementary (and independent) measurement of the mixing parameters to the ν_μ CC energy analysis described in Chapter 4.

The fitting procedure is similar to that described in section 4.5.1. Two Monte Carlo samples of ν_e events are generated. The electron identification cuts are applied to the samples. The large 9.63 kiloton year exposure `MCNO` sample contains 3651 electron-like events and the 3.3 kiloton year exposure `MCEXP` sample contains 1383 events. Two-generation $\nu_\mu \to \nu_e$ oscillations with mixing parameters $\sin^2 2\theta$ and Δm^2 are assumed. The weight $W = \sin^2 2\theta \sin^2(1.27\Delta m^2 L / E_\nu)$ is calculated for each event and the event is accepted into the `MCEXP` sample if the random number R is less than W, where $0 < R < 1$. The 0.5% $\nu_e + \bar{\nu}_e$ component of the beam is ignored since it has a negligible effect for oscillations with large $\sin^2 2\theta$.

Figure 6.4 shows the number of electron-like events expected in a 3.3 kiloton exposure of MINOS as a function of Δm^2, assuming $\nu_\mu \to \nu_e$ oscillations with $\sin^2 2\theta = 1$. The contributions from ν_e CC events that are due to $\nu_\mu \to \nu_e$ oscillations, neutral current

events and the intrinsic $\nu_e + \bar{\nu}_e$ beam component are shown separately. The number of electron-like events from $\nu_\mu \rightarrow \nu_e$ oscillations is at least a factor of 10 (or more) larger than the background from NC and beam $\nu_e + \bar{\nu}_e$ events. The expected number of electron-like events that are due to neutral current interactions (39 events for a 3.3 kiloton year exposure) is independent of the neutrino oscillation parameters. The number of electron events from interactions of beam $\nu_e + \bar{\nu}_e$ is actually expected to *decrease* as a function of Δm^2, because they are depleted by $\nu_e \rightarrow \nu_\mu$ oscillations so the 10 events predicted in Figure 6.4 is therefore an upper limit.

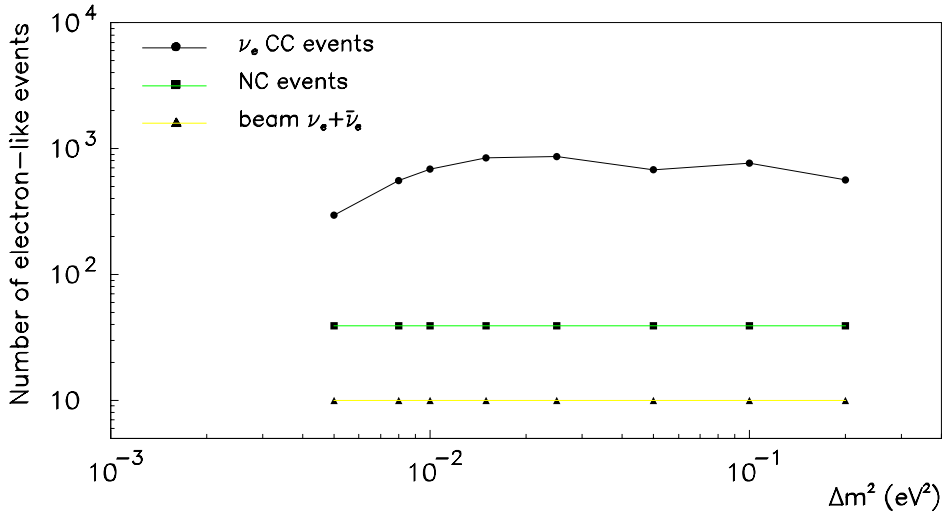

Figure 6.4 – The numbers of events that are classified as electron-like by the cuts described in this chapter, plotted as a function of Δm^2. Neutrino oscillations in the mode $\nu_\mu \rightarrow \nu_e$ with $\sin^2 2\theta = 1$ are assumed. The contributions from ν_e CC events that are the result of $\nu_\mu \rightarrow \nu_e$ oscillations, neutral current events and events due to the intrinsic $\nu_e + \bar{\nu}_e$ component of the beam are shown separately.

Due to the small number of events in the `MCEXP` sample, the number of bins of E_{reco} used in the fit is reduced from 60 to 30. Poisson probabilities, rather than Gaussian probabilities, are assumed for the same reason:

$$P(m(i),n(i)) = \frac{1}{m(i)!} \times n(i)^{m(i)} \times e^{-n(i)}, \quad (6.1)$$

where $m(i)$ and $n(i)$ are the numbers of events in bin i of the MCEXP and MCNO E_{reco} distributions respectively and $P(m(i),n(i))$ is the Poisson probability of observing $m(i)$ events when $n(i)$ are expected.

The log likelihood, neglecting terms in $m(i)!$, is:

$$\ln L = \sum_{i=1}^{n} (m(i) \times \ln n(i, \Delta m^2, \sin^2 2\theta) - n(i, \Delta m^2, \sin^2 2\theta). \quad (6.2)$$

Note that this is the log likelihood and not the log likelihood ratio, that was used in Chapter 4.

Figure 6.5 shows a fit to a MCEXP sample with $\Delta m^2 = 0.01$ eV^2 and $\sin^2 2\theta = 0.7$, assuming $\nu_\mu \rightarrow \nu_e$ oscillations. The left-hand plot shows a comparison between the error contours in neutrino mixing parameter space obtained from this fit to those obtained from the independent ν_μ disappearance fit described in Chapter 4. The thick line denotes the 68%, confidence level contours for ν_e appearance and the thin line is for ν_μ disappearance. The star indicates the true parameters. The right-hand plot shows the distributions of reconstructed electron neutrino energy for the MCEXP sample (error bars) and the best-fit MCNO sample (histogram). The agreement between the two distributions is very good ($\chi^2 = 17/28$).

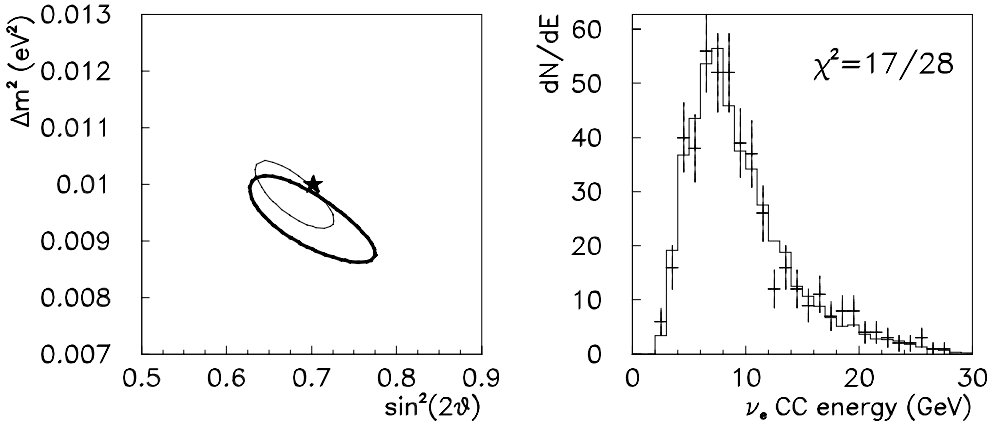

Figure 6.5 - ν_e CC energy test for $\Delta m^2 = 0.01$ eV^2 and $\sin^2 2\theta = 0.7$ and $\nu_\mu \rightarrow \nu_e$ oscillations, assuming fixed normalisation. Left-hand plot: 68% C.L. error contours in neutrino oscillation parameter space. The thick line is for ν_e appearance and the thin line is for ν_μ disappearance. The star represents the true mixing solution. Right-hand plot: reconstructed neutrino energy distributions for the MCEXP sample (error bars) and the best-fit MCNO sample (histogram). A 3.3 kiloton year exposure of MINOS is assumed.

The contours are obviously larger for electron appearance since the ν_e CC selection efficiency (26%) is much smaller than the efficiency for selecting ν_μ CC events (91%). Both fits are consistent with the true parameters and so electron appearance can act as an important cross-check of any result observed with ν_μ disappearance.

Figure 6.6 shows the results of fits to MCEXP samples with several values of Δm^2 and $\sin^2 2\theta = 0.7$. In all four cases, the values of the parameters obtained by ν_e appearance and ν_μ disappearance are consistent with each other and with the true parameters. Both fits produce large errors on the parameters at $\Delta m^2 = 0.005$ eV^2 since there is little neutrino flux below ~3 GeV. The ν_e appearance fit produces large errors at $\Delta m^2 = 0.008$ eV^2, at which point the ν_μ disappearance can measure the parameters to ±10%. This is due to the reduced selection efficiency and hence statistics for electron appearance at low neutrino energy.

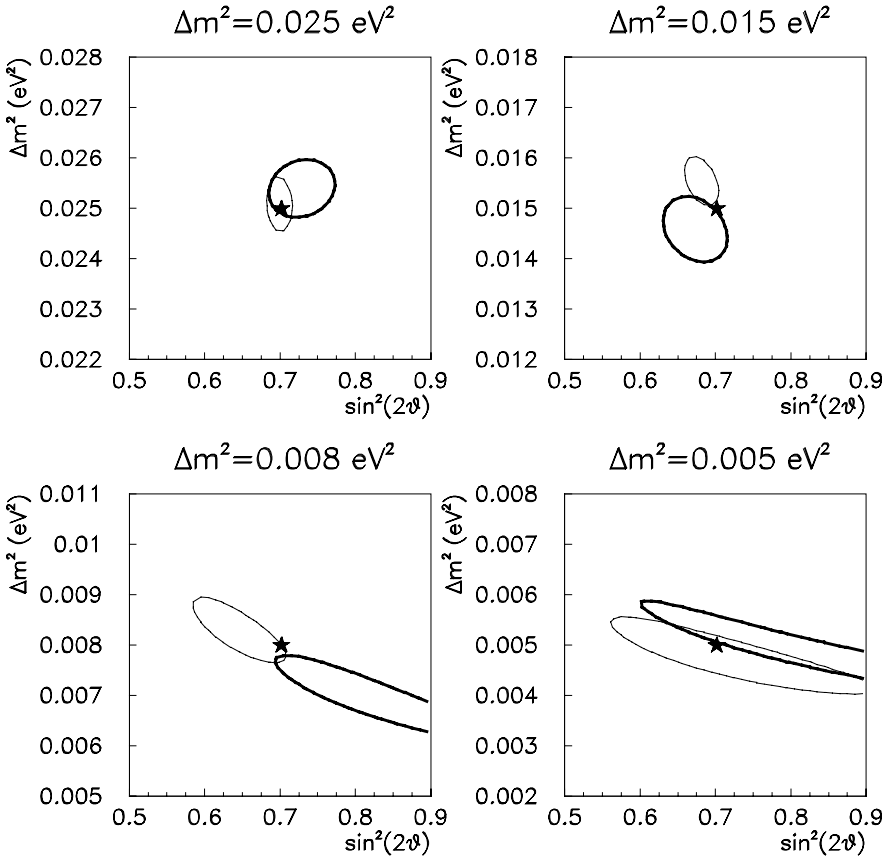

Figure 6.6 – Fits to MCEXP samples with various values of Δm^2 and $\sin^2 2\theta = 0.7$, assuming $\nu_\mu \rightarrow \nu_e$ oscillations and fixed normalisation. The 68% C.L. error contours are drawn. The thick lines are for ν_e appearance fits and the thin lines are for ν_μ disappearance. A 3.3 kiloton year exposure of MINOS is assumed.

Figure 6.7 shows how the errors on the mixing parameters from a fit to the ν_e CC energy distribution compare to those from the fits to the ν_μ CC energy distribution in Chapter 4. The fits assume that the normalisation is perfectly known. The top plot of Figure 6.7 shows that the errors on Δm^2 from the two methods are comparable. The error on

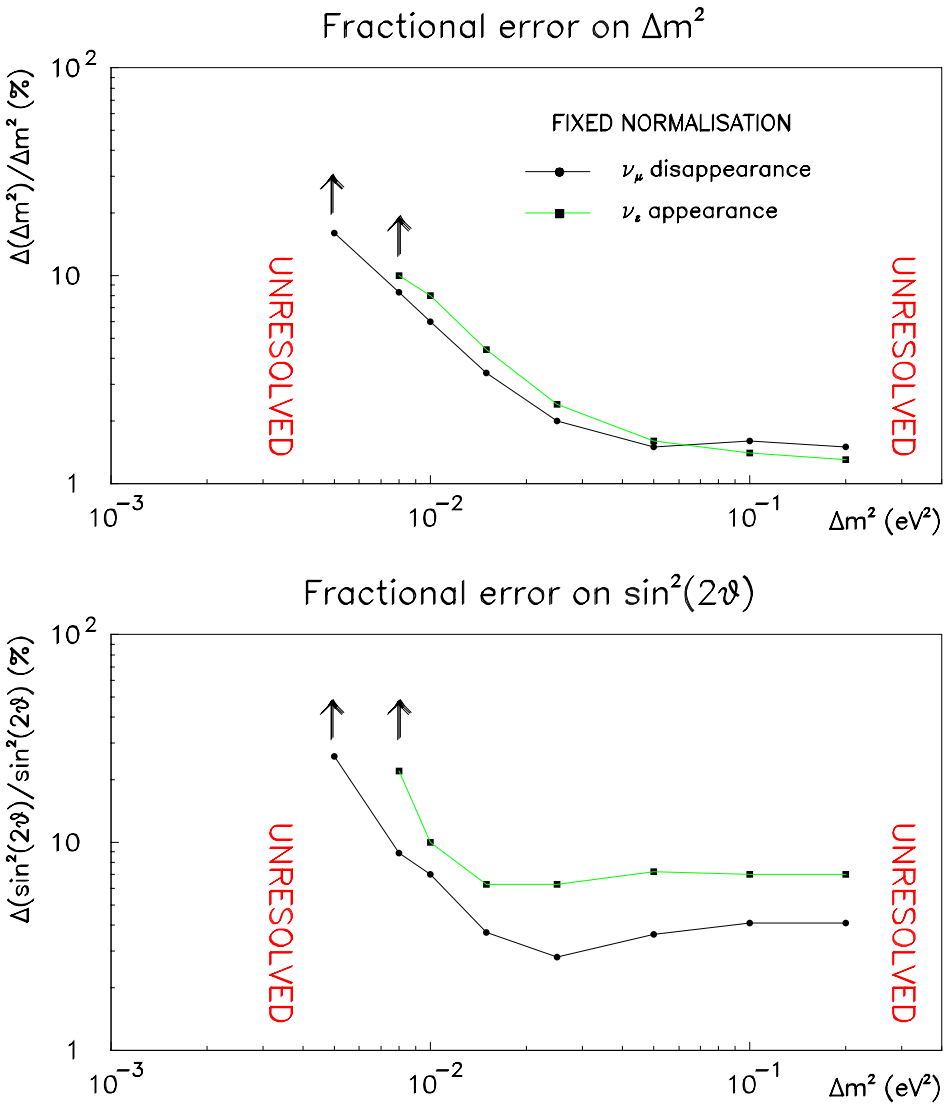

Figure 6.7 – Summary of parameter measurement errors for fits to neutrino oscillations with $\sin^2 2\theta = 0.7$ and various values of Δm^2. The results of independent, fixed normalisation fits to ν_μ CC and ν_e CC energy distributions are compared.

$\sin^2 2\theta$ is typically a factor of two larger for the electron appearance fits. This can be explained by the reduction in statistics for the electron appearance fits compared to the muon disappearance fits. The factor of four difference in the selection efficiencies should result in error contours for electron appearance fits that are twice as large as their muon appearance counterparts. This is what is observed.

If a shape-only fit is performed on any of the ν_e CC energy distributions considered above then it is impossible to extract a value of $\sin^2 2\theta$. This is because the shape of an appearance signal only depends on Δm^2, whereas the shape of a disappearance signal (a dip in the ν_μ CC energy distribution) depends both on Δm^2 and $\sin^2 2\theta$. The normalisation information is therefore crucial to extract a measurement of neutrino oscillation parameters from an appearance signal.

Figure 6.8 summarises the errors on Δm^2 obtained by independent shape-only fits to muon disappearance and electron appearance signals. The plot shows that the errors on Δm^2 are comparable.

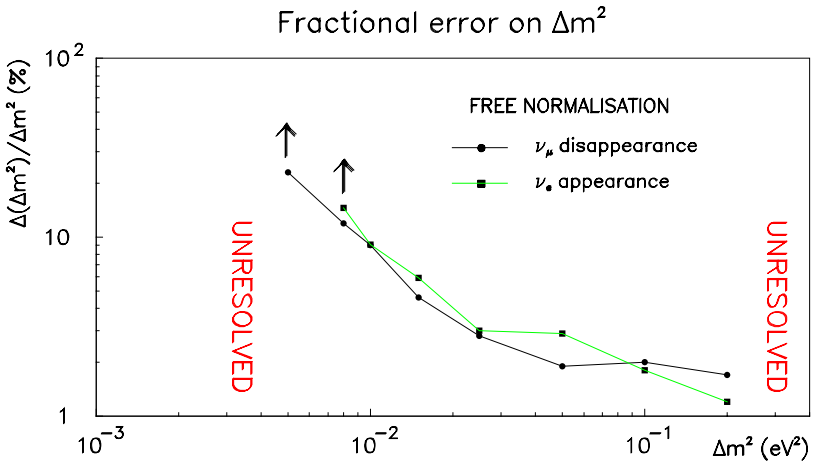

Figure 6.8 – Comparison of errors on Δm^2 from independent, shape-only fits to ν_μ disappearance and ν_e appearance signals.

6.3 Conclusions

This chapter has shown that it is possible to use the energy distribution of electron-like events (mostly ν_e CC interactions) to obtain an independent and complementary measurement of the neutrino mixing parameters to the ν_μ CC analysis described in Chapter 4 if oscillations occur with large $\sin^2 2\theta$. The simple cuts described above select ν_e CC events with 26% efficiency and the background from neutral current and the intrinsic $\nu_e + \bar{\nu}_e$ component of the beam is at least a factor of 10 smaller than the $\nu_\mu \rightarrow \nu_e$ signal if oscillations occur in this mode with $\sin^2 2\theta \sim 1$.

The errors on the mixing parameters obtained from fits to ν_e energy distributions are larger than the corresponding errors from ν_μ disappearance fits because the selection efficiency is a factor of four smaller. This results in errors on $\sin^2 2\theta$ that are larger by a factor of two, assuming the rate normalisation is perfectly known. If the normalisation is not known at all then it is impossible to measure $\sin^2 2\theta$ from ν_e appearance because the shape of the ν_e CC energy distribution is independent of $\sin^2 2\theta$.

If a large effect is observed in the ν_μ disappearance analysis then the study of ν_e CC interactions can provide important additional information on the oscillation mode, since the ν_μ CC energy measurement is largely mode-independent. If two-flavour $\nu_\mu \rightarrow \nu_e$ oscillations occur, then the values of Δm^2 and $\sin^2 2\theta$ obtained from ν_μ disappearance and ν_e appearance fits should be consistent with one another. If two-flavour $\nu_\mu \rightarrow \nu_\tau$ oscillations occur then no effect will be seen in the ν_e appearance analysis[5] . If an oscillation

[5] The contribution from $\tau \rightarrow e$ decays in this analysis is expected to be small and will, in any case, not produce an oscillation signal at the same value of Δm^2 and $\sin^2 2\theta$ as the ν_μ disappearance analysis due to the suppression of the ν_τ CC cross-section and missing energy in the tau decay.

signal is seen in both ν_μ disappearance and ν_e appearance analyses then three-flavour mixing, which is discussed in the following chapter, is indicated.

Chapter 7 Three-flavour analysis in MINOS

A three-flavour analysis is possible in MINOS if it is possible to identify ν_μ CC and ν_e CC events. Chapter 4 and Chapter 6 have shown that this can be achieved in MINOS with 91% and 26% efficiencies respectively. The identification of ν_τ CC events, which is described in Chapter 8, is only possible with much reduced efficiency (~1%). The observation of ν_τCC events does not therefore provide a strong additional constraint on the mixing parameters but can provide a cross-check of the results obtained in this chapter.

This chapter shows how a three-generation analysis in MINOS could work in practice. The expected measurement errors on the mixing parameters are evaluated for several values of Δm^2. Two possible three-generation mixing matrices that are consistent with the recent CHOOZ limit in the mode $\nu_\mu \rightarrow \nu_e$ are investigated to see if they can be distinguished from pure two-generation models. As a part of this work, code to calculate general three-flavour oscillation probabilities has been written and implemented in the GMINOS Monte Carlo package [84].

If the three neutrino species are mixed then there is the potential for a large CP violating effect to be observed in MINOS if the initial ν_μ run is followed by a run with a $\overline{\nu}_\mu$ beam. Section 7.5 evaluates the CP violating amplitudes that could be observed in MINOS for a range of mixing scenarios. The implications of the recent CHOOZ result for the prospects of observing CP violation in MINOS are also discussed.

Six parameters are required to describe generalised three-flavour mixing. These are two Δm^2's and the complex matrix elements $U_{\alpha i}$ that relate the flavour eigenstates α to the mass eigenstates i. These matrix elements can be parameterised by three mixing angles and a CP violating phase, as described in section 2.3.2. It is of interest to be able to determine all of the mixing parameters but analysis in this general space is difficult and intractable to display. The analysis in this section adopts the simplifying one mass-scale dominance (OMSD) model that was introduced in section 2.3.2. This scheme assumes, in analogy with the charged leptons and quarks, a hierarchy of neutrino masses such that $\Delta m^2_{32} >> \Delta m^2_{21}$, as sketched in Figure 7.1. The subscripts refer to particular neutrino mass eigenstates. The relation $\Delta m^2_{32} L / E_\nu \sim O(1)$ is assumed for the MINOS range of E_ν.

Recall that the neutrino oscillation probabilities for the OMSD model assume the

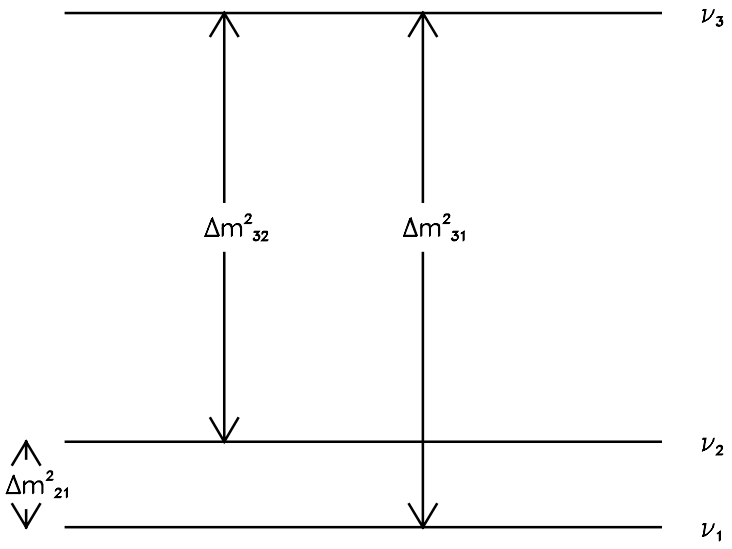

Figure 7.1 – The one mass-scale dominance model.

following simplified form:

$$\begin{aligned} P_{\mu\mu} &= 1 - 4U_{\mu 3}^2(1-U_{\mu 3}^2)\sin^2(1.27\Delta m^2 L/E_\nu), \\ P_{\mu e} &= 4U_{\mu 3}^2 U_{e3}^2 \sin^2(1.27\Delta m^2 L/E_\nu), \\ P_{\mu\tau} &= 4U_{\mu 3}^2 U_{\tau 3}^2 \sin^2(1.27\Delta m^2 L/E_\nu), \end{aligned} \tag{7.1}$$

where Δm^2 is synonymous with Δm^2_{32}. Unitarity requires that $U_{\mu 3}^2 + U_{e3}^2 + U_{\tau 3}^2 = 1$. Section 7.5 will show that CP violation is unobservable in MINOS if OMSD is assumed.

7.1 The triangle representation

Fogli, Lisi and Scioscia have introduced a clear and simple graphical representation of three-generation mixing in the one mass-scale dominance model [86]. The scheme, which is known as the 'triangle representation', is shown in Figure 7.2.

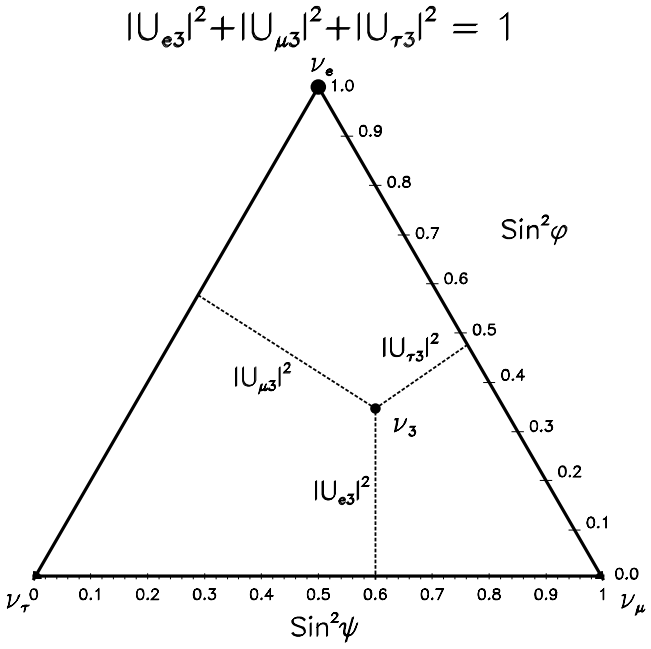

Figure 7.2 – The triangle representation, from [86].

An equilateral triangle of unit height is constructed. The vertices represent the pure flavour eigenstates ν_μ, ν_e and ν_τ. The heavy neutrino mass eigenstate, ν_3 is plotted in this space and the matrix elements $U^2_{\mu 3}$, U^2_{e3} and $U^2_{\tau 3}$ are equal to the perpendicular distances from the point ν_3 to the sides of the triangle. The point ν_3 is also parameterised by the two Euler angles ϕ and ψ, which correspond to the angles θ_2 and θ_3 in the standard Maiani parameterisation of the CKM matrix [17]:

$$\sin^2\phi = U^2_{e3}, \qquad \sin^2\psi = \frac{U^2_{\mu 3}}{1-U^2_{e3}}. \tag{7.2}$$

If ν_3 coincides with one of the flavour vertices then no oscillations take place. Two-generation oscillations are represented by movement along the sides of the triangle. If ν_3 lies within the triangle then true three-flavour mixing is indicated.

7.2 Oscillation mode determination

This section describes the results of a study of the capability of MINOS to determine the neutrino oscillation mode. Simple cuts are used to identify the flavour of neutrinos in the detector. Events are classified exclusively as long (penetrate > 44 × 2 cm steel planes), short (penetrate = 44 × 2 cm steel planes) and electron (penetrate = 44 × 2 cm steel planes; > 80% of total pulse height in first 10 planes; RMS < 20 cm and total pulse height > 1500 photoelectrons). These classes select ν_μ CC events, NC and ν_τ CC events, and ν_e CC

Interaction	LONG	SHORT	ELECTRON
ν_μ CC	91.9%	8.0%	0.1%
NC	8.9%	86.6%	4.4%
ν_e CC	8.4%	65.6%	26.0%
ν_τ CC	24.6%	64.9%	10.5%

Table 7.1 – Average event classification efficiencies.

events respectively. The efficiency of this event classification as a function of true neutrino energy is shown in Figure 7.3. Table 7.1 shows the average efficiencies integrated over the NuMI three horn beam spectrum. This result shows that the contamination of ν_e CC and ν_τ CC events[6] in the ν_μ disappearance analysis of Chapter 4 is always small (< 10%).

For a given set of oscillation parameters $U_{\alpha 3}$ and Δm^2, the numbers of events

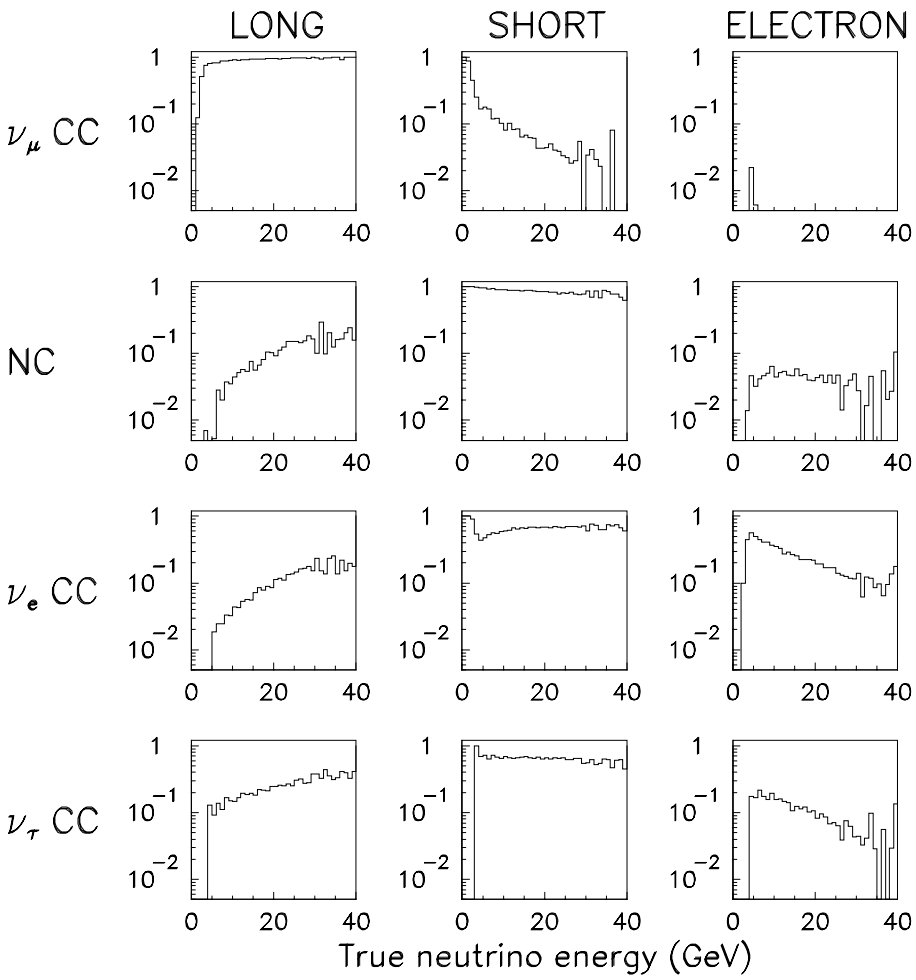

Figure 7.3 – Event classification efficiencies as a function of true neutrino energy.

[6] When the suppression of the ν_τ CC cross section relative to the ν_μ CC cross-section is taken into account.

expected in each class can be calculated by numerical integration over E_ν of the product of the ν_μ flux, the oscillation probability $P_{\mu\alpha}$, the NC or CC cross-section for a neutrino of flavour α and the probability that the interaction is observed in each of the three classes. The number of events in the long class is therefore given by:

$$N_{LONG} = \int_0^\infty \sum_\alpha P_{\mu\alpha}(E_\nu)\sigma_\alpha(E_\nu)\phi_\mu(E_\nu)\varepsilon_{\alpha L}(E_\nu)dE_\nu, \tag{7.3}$$

where α is the flavour of the neutrino interaction (ν_μ, ν_e, ν_τ), $P_{\mu\alpha}$ is the oscillation probability for the transition $\nu_\mu \to \nu_\alpha$, σ_α is the (CC or NC) cross-section for ν_α interactions at energy E_ν, ϕ_μ is the ν_μ flux spectrum and $\varepsilon_{\alpha L}$ is the probability that a neutrino of flavour ν_α is classified as a long event (as shown in Figure 7.3). The numbers of events in the short and electron classes are calculated in the same way as equation (7.3), except $\varepsilon_{\alpha L}$ is replaced by $\varepsilon_{\alpha S}$ and $\varepsilon_{\alpha E}$ respectively.

A χ^2 based on the differences between the observed and expected number of events in each class is calculated as the mixing parameters are varied about their true values, assuming the value of Δm^2 is known precisely[7]:

$$\chi^2 = \frac{(M_L - N_L)^2}{\sigma_L^2} + \frac{(M_S - N_S)^2}{\sigma_S^2} + \frac{(M_E - N_E)^2}{\sigma_E^2}, \tag{7.4}$$

where M refers to the numbers of events in each of the classes for the true hypothesis $(U_{e3}^2, U_{\mu 3}^2, \Delta m^2)$, N is the number of events in each class for a particular pair of $(U_{e3}^2, U_{\mu 3}^2)$ and σ is the error on the expected rate. An error in the CC/total cross section ratio, T, is added in quadrature to the statistical error for the long and short classes. For the three horn WBB, $T = 0.766$ and $\Delta T = 0.0029$ [69]:

[7] Δm^2 is measured by the CC energy test in Chapter 4.

$$\begin{aligned} \sigma_L^2 &= N_L + (0.0029 N_L / 0.766)^2, \\ \sigma_S^2 &= N_S + (0.0029 N_S / 0.234)^2, \\ \sigma_E^2 &= N_E. \end{aligned} \tag{7.5}$$

Figure 7.4 shows how the numbers of events in the long, short and electron classes change as a function of Δm^2 if the threefold maximal mixing hypothesis is assumed. The plot assumes an exposure of 3.3 kiloton years, so 9613 events are expected for no oscillations. At low Δm^2 (~10^{-3} eV^2), where the oscillation probability is small, the numbers of events in the long and electron classes reflect the relative ν_μ CC and NC cross-sections (approximately 75% of events should be CC). The small number of events in the electron class is due to the 0.5% $\nu_e + \overline{\nu}_e$ component of the beam and the 4% of NC events that are mis-identified as electron-like. As Δm^2 is increased, the number of long events decreases as the ν_μ in the beam oscillate to other neutrino species. The number of short and electron events therefore rise as the number of ν_e and ν_τ CC events increases. The total number of events decreases slightly due to the suppression of the ν_τ CC cross section (approximately 8600 events are expected at $\Delta m^2 = 1$ eV^2 where the oscillations are saturated, a loss of 1000 events from the number of events expected for no oscillations).

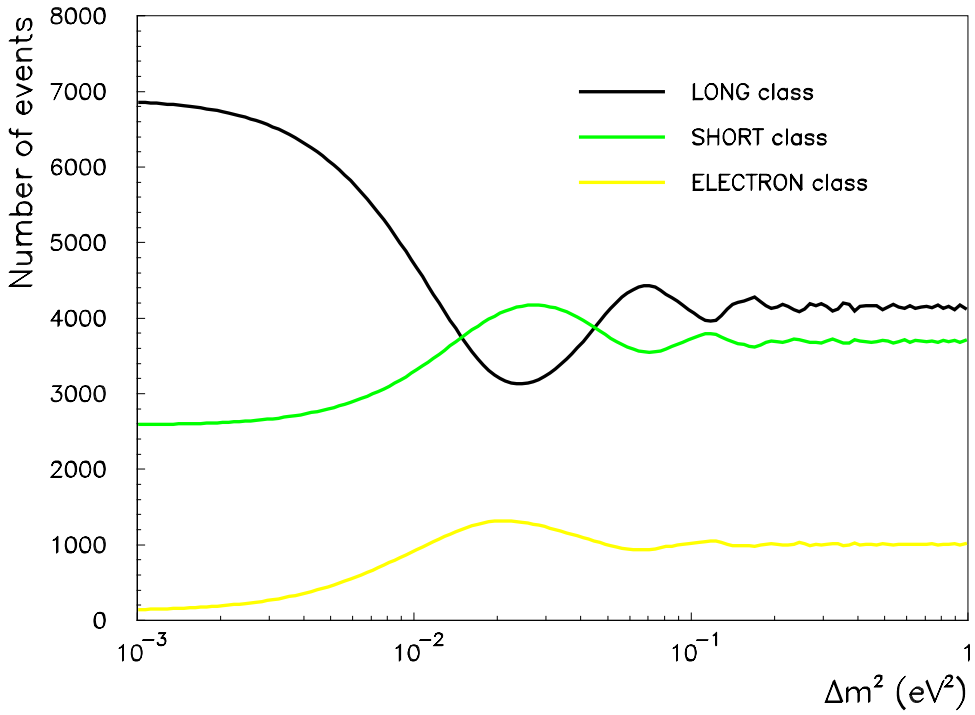

Figure 7.4 – The numbers of events classified as long, short and electron as a function of Δm^2 for the hypothesis of threefold maximal mixing. An exposure of 3.3 kiloton years is assumed.

Figure 7.5 shows a fit to the hypothesis of threefold maximal mixing with $\Delta m^2 = 0.0072$ eV^2 for an exposure of 3.3 kiloton years. The normalisation is assumed to be perfectly known. Contours representing the 68%, 90% and 95% confidence levels relative to the χ^2 minimum are drawn ($\chi^2 = 2.25, 4.5, 6.0$) and the star represents the true values of the mixing parameters. The plot shows that the true parameters are regained although there is a second solution close to the ν_μ vertex of the triangle.

This solution is expected. It results from a quadratic ambiguity in the measurement of the matrix element $U^2_{\mu 3}$ from the ν_μ survival probability $P_{\mu\mu}$. This ambiguity is always present in an experiment which uses a pure flavour neutrino beam unless there are two-

generation oscillations with $\sin^2 2\theta=1$ or no oscillations at all. The reason for this ambiguity can be understood by examining equations (7.1). The average ν_μ survival probability, $\overline{P}_{\mu\mu}$, (averaged over all neutrino energies) is given by:

$$\overline{P}_{\mu\mu} = 4U_{\mu 3}^2(1-U_{\mu 3}^2)\overline{S}, \tag{7.6}$$

where $\overline{S}$ is the quantity defined by equation (4.2):

$$\overline{S} = \frac{\int_0^\infty \phi(E_\nu)\sigma_{CC}(E_\nu)\sin^2(1.27\Delta m^2 L/E_\nu)dE_\nu}{\int_0^\infty \phi(E_\nu)\sigma_{CC}(E_\nu)dE_\nu}.$$

A particular value of $\overline{P}_{\mu\mu}$ therefore results in a two-fold ambiguity in the value of $U_{\mu 3}^2$:

$$U_{\mu 3}^2 = \frac{1}{2}(1 \pm \sqrt{1-(1-\overline{P}_{\mu\mu})/\overline{S}}) \tag{7.7}$$

A measurement of the complementary oscillation probabilities $\overline{P}_{\mu e}$ and $\overline{P}_{\mu\tau}$ does not help to resolve the ambiguity since both depend on $U_{\mu 3}^2$:

$$\begin{aligned} \overline{P}_{\mu e} &= 4U_{\mu 3}^2 U_{e3}^2 \overline{S}, \\ \overline{P}_{\mu\tau} &= 4U_{\mu 3}^2 U_{\tau 3}^2 \overline{S}. \end{aligned} \tag{7.8}$$

The ambiguity *can* be resolved by performing a measurement of oscillation probabilities with a different flavour beam (a ν_e beam in the case of MINOS) that covers the same region of L/E as MINOS. An experiment of this type, such as CHOOZ, will measure the average ν_e survival probability $\overline{P}_{ee}$:

$$\overline{P}_{ee} = 4U_{e3}^2(1-U_{e3}^2)\overline{S}. \tag{7.9}$$

This will produce a two-fold ambiguity for the matrix element U_{e3}^2:

$$U_{e3}^2 = \frac{1}{2}(1 \pm \sqrt{1-(1-\overline{P}_{ee})/\overline{S}}) \tag{7.10}$$

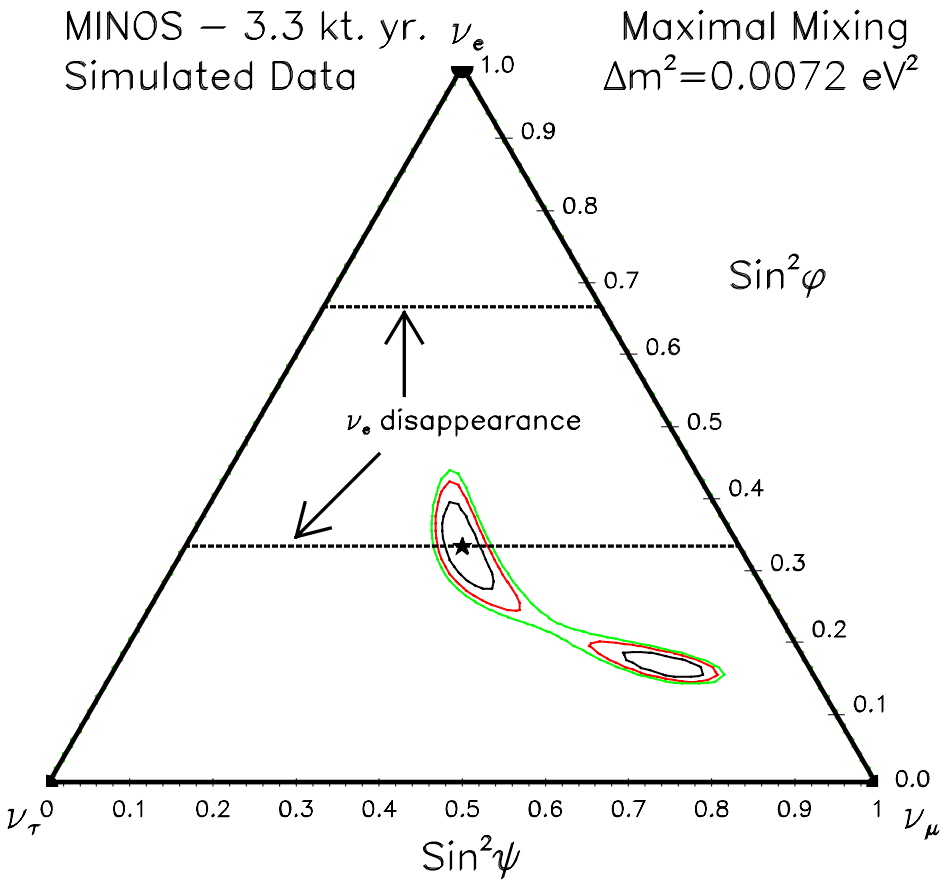

Figure 7.5 – Three-generation parameter measurement for threefold maximal mixing with $\Delta m^2 = 0.0072$ eV^2. The contours represent the 68%, 90% and 95% confidence levels relative to the χ^2 minimum. The true mixing parameters are represented by the star. The dashed lines show the complementary two-fold ambiguity that could be obtained from the measurement of the ν_e disappearance probability.

This ambiguity is different to that found by MINOS from equation (7.7) and the true solution can be obtained by combining measurements from the two experiments. The dashed lines in Figure 7.5 show the two-fold ambiguity that would be seen by a ν_e disappearance experiment if threefold maximal mixing is assumed. The two measurements clearly favour the true solution for the matrix elements.

7.2.1 Effect of event identification

The error contours in the three-generation fits have the following properties: two solutions are found and the correlation between the matrix elements differs between the two solutions. In particular, for $\Delta m^2 < 0.01$ eV^2 the contours describe a crescent shape in the triangle representation.

The fits involve three measurements, the numbers of events in the long, short and electron classes. There are two free parameters for fixed Δm^2, the matrix elements U_{e3}^2 and $U_{\mu 3}^2$. The combination of three measurements and a quadratic ambiguity in the matrix element $U_{\mu 3}^2$ results in two solutions rather than the one expected. There is also redundancy in the measurements because of the unitarity of the mixing matrix. A measurement of $U_{\tau 3}^2$ from the number of short events (which is sensitive to the probability $\overline{P}_{\mu\tau}$) does not give additional information over a measurement of U_{e3}^2 and $U_{\mu 3}^2$ because $U_{e3}^2 + U_{\mu 3}^2 + U_{\tau 3}^2 = 1$.

Figure 7.6 shows how the individual classes contribute to the overall χ^2. The contour lines are $\chi^2 = 2.25, 4.5, 6.0$. The top-left plot, which is for the long class, shows two favoured regions in parameter space. The long class consists mostly of ν_μ CC events which are sensitive to the average disappearance probability $\overline{P}_{\mu\mu}$, defined in equation (7.6). The two-fold ambiguity in $U_{\mu 3}^2$ from a measurement of this probability (according to equation (7.7)) results in two parallel lines in the triangle plot. The fact that the lines of constant χ^2 for the long class are not exactly parallel is a reflection of the contamination due to NC, ν_e CC and ν_τ CC events.

The short and electron contours are similar. The electron class is sensitive to the probability $\overline{P}_{\mu e}$, defined in equation (7.8), which draws a parabolic curve bounding the ν_e-ν_μ side of the triangle. If the short class was only sensitive to ν_τ CC events then it would draw a

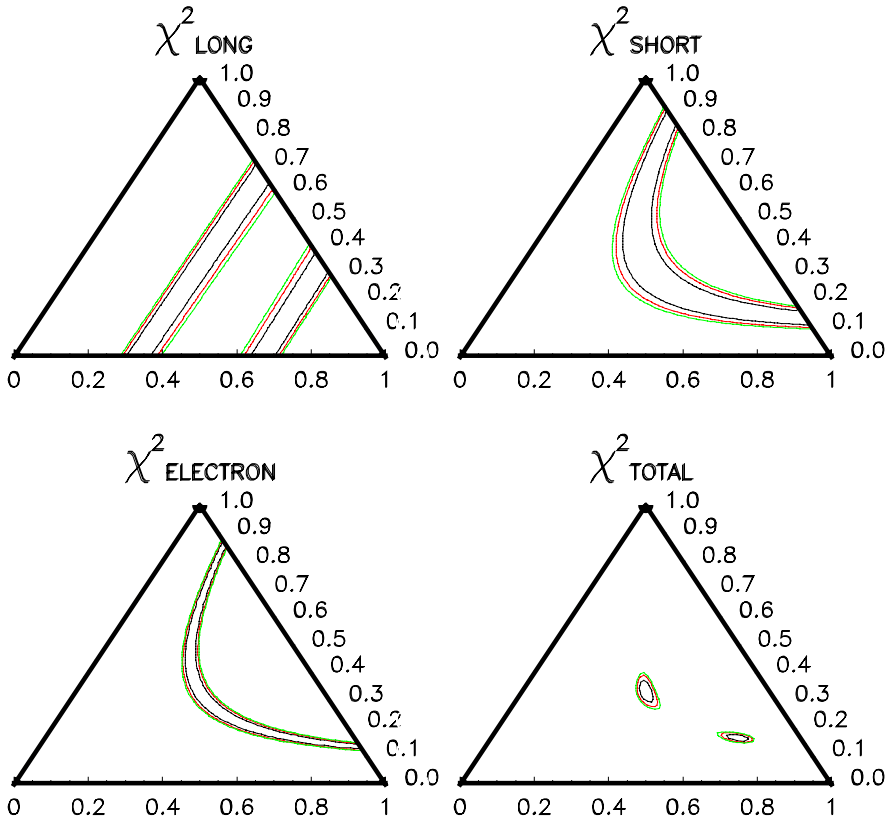

Figure 7.6 – Contributions of individual classes to the total χ^2.

curve that bounds the ν_μ-ν_τ side of the triangle. For this analysis, there is a large ν_e CC contamination of the short sample and the short class favours a similar region of parameter space to the electron class, albeit with inferior statistical precision.

The contours for the total χ^2 (bottom-right plot) are therefore a combination of the two parallel lines obtained from a measurement of $P_{\mu\mu}$ and the curve obtained from a measurement of $P_{\mu e}$. Increased electron neutrino efficiency will therefore result in a more accurate measurement of $P_{\mu e}$ and hence narrower contours.

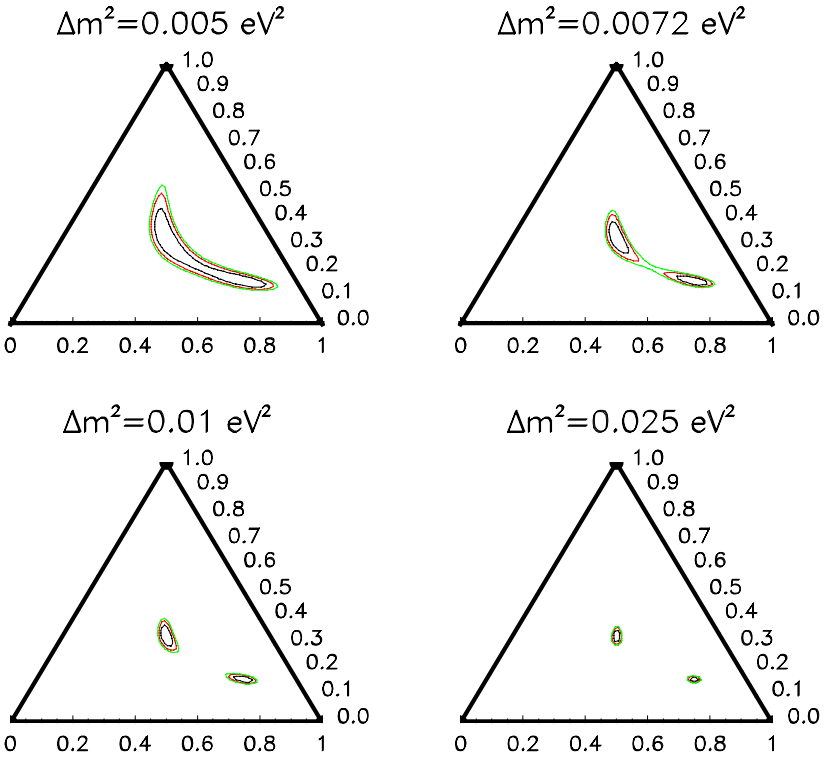

Figure 7.7 – Fits to the threefold maximal mixing hypothesis with several values of Δm^2. A 3.3 kiloton year exposure of MINOS is assumed.

7.2.2 Fits for different values of Δm^2

Figure 7.7 shows the results of fits to the threefold maximal mixing hypothesis with several values of Δm^2. The plot shows that as Δm^2 is increased above 0.01 eV^2 the two solutions become separated as the size of the effect becomes larger. At Δm^2= 0.005 eV^2, the two solutions merge as the signal becomes weak.

The fits described above assume that Δm^2 is perfectly known. In practice there will be measurement errors that need to be included in the fit. A procedure which calculates a χ^2 or likelihood statistic as a function of both the flavour content and observed energy

distributions of neutrino events could simultaneously fit both the matrix elements and Δm^2. This would add an extra (Δm^2) dimension to the triangle plot representation and the error contours shown in this chapter would therefore become three-dimensional surfaces. This all-encompassing analysis is beyond the scope of this study. It is possible, however, to examine how the contours change as Δm^2 is varied with respect to its true value.

Chapter 4 showed that, for large mixing, it is possible to measure Δm^2 to ±6% for the Kamiokande point (Δm^2= 0.01 eV^2). Figure 7.8 shows the results of fits to threefold maximal mixing and Δm^2= 0.01 eV^2 where the fitted value of Δm^2 is assumed to be 0.01 eV^2 - 6% (left-hand plot) and 0.01 eV^2 + 6% (right-hand plot). The plots can be understood in the following way: the appearance (disappearance) probability is proportional to the product of the matrix elements and the quantity $\overline{S}$, defined in equation (4.2). As Δm^2 is decreased below 0.01 eV^2, the value of $\overline{S}$ decreases and hence the matrix elements must increase to provide a good fit to the input hypothesis. This causes the two solutions to move closer together on the triangle plot. On the other hand, increasing Δm^2 results in an increase

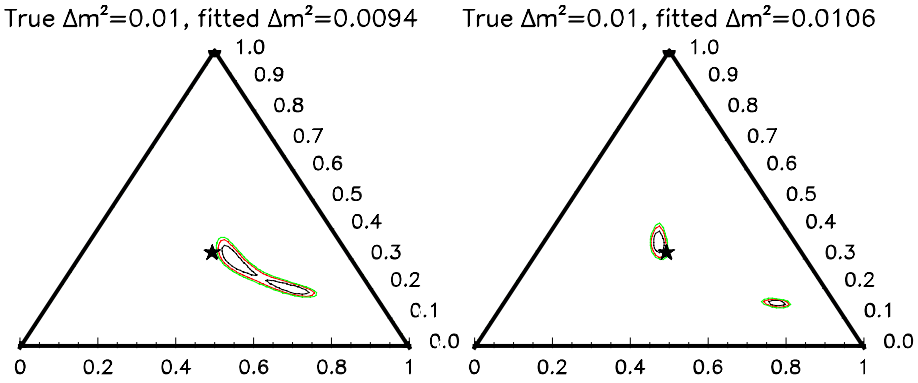

Figure 7.8 – The effect of incorrectly measured Δm^2. The oscillation hypothesis is maximal mixing with Δm^2= 0.01 eV^2. The left-hand plot shows the result of a fit where Δm^2 is assumed to be 0.0094 eV^2 and the right-hand plot assumes Δm^2= 0.0106 eV^2. A 3.3 kiloton year exposure of MINOS is assumed.

in $\overline{S}$, the matrix elements decrease and the favoured solutions move towards the edges of the triangle.

7.3 Systematic effects

The fits described in the previous section assume that the number of neutrino interactions expected for no oscillations is known precisely. It has been shown [71] that an error in the relative normalisation between the near and far detectors of between 2% and 8% is possible due to uncertainties in predicting the neutrino flux at the far detector site. The best

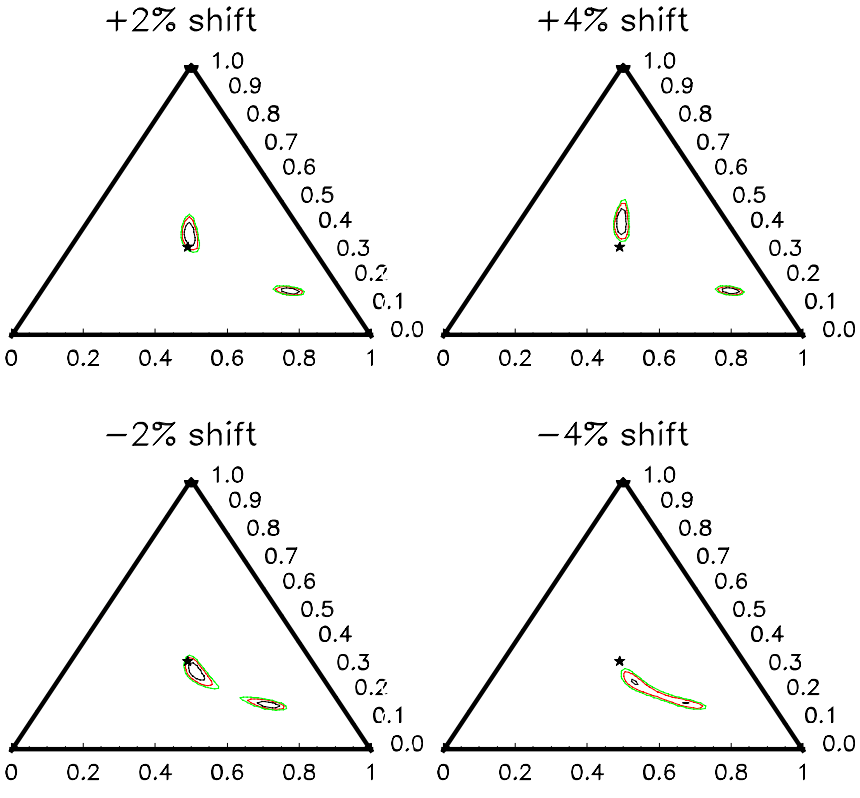

Figure 7.9 – Effect of a shift in the relative near-far rate normalisation for threefold maximal mixing and $\Delta m^2 = 0.01$ eV^2. A 3.3 kiloton year exposure is assumed.

fit oscillation parameters from the ν_μ CC energy analysis described in Chapter 4 deviated from their true values when a difference in the relative rates between near and far detectors was assumed.

Figure 7.9 shows how three-generation fits are affected when a shift in the relative normalisation is assumed. The input hypothesis is threefold maximal mixing with $\Delta m^2 = 0.01$ eV^2. Panels that are marked with a positive shift in Figure 7.9 refer to cases where the expected rate at the far detector site if no oscillations occur is too small. In these cases, the apparent size of the oscillation effect is smaller and the contours move towards the edges of the triangle. The true matrix elements would be regained at a smaller value of Δm^2. A negative shift means that the apparent size of the oscillation effect is larger and the

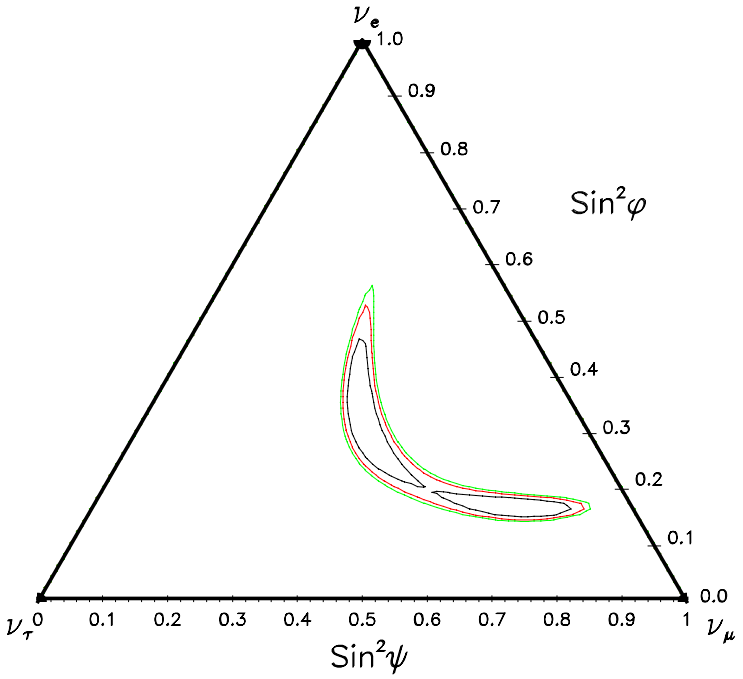

Figure 7.10 – A shape-only fit to maximal mixing and $\Delta m^2 = 0.01$ eV^2 for a 3.3 kiloton year exposure of MINOS..

contours move to larger values of the mixing parameters.

The true matrix elements are excluded at > 95% C.L. if a 4% shift exists between the relative normalisation of the near and far detectors. This source of systematic error can be alleviated if the normalisation is assumed to be completely unknown and only the fractions of events in each of the three classes are measured. The result of a fit of this type for maximal mixing and $\Delta m^2 = 0.01$ eV^2 is shown in Figure 7.10. The contours are significantly larger than those for the fixed normalisation fit shown in Figure 7.5 (as expected) and the two solutions are barely resolved. The error contours for a shape-only fit at $\Delta m^2 = 0.01$ eV^2 are comparable in size to those from a fixed normalisation fit at $\Delta m^2 \sim 0.007$ eV^2.

7.4 Consequences of the CHOOZ result

The recent CHOOZ limit in the mode $\nu_\mu \rightarrow \nu_e$ has serious implications for the prospects of observing three-generation mixing in MINOS. Threefold maximal mixing [57] is ruled out for $\Delta m^2 > 10^{-3}$ eV^2. Two three-generation matrices that are consistent with the CHOOZ limit in the mode $\nu_\mu \rightarrow \nu_e$ and the neutrino oscillation interpretation of the atmospheric neutrino anomaly in the mode $\nu_\mu \rightarrow \nu_\tau$ are investigated in this section to see if they can be distinguished from two-generation models.

CHOOZ sets a limit for $\nu_\mu \rightarrow \nu_e$ oscillations of $\sin^2 2\theta > 0.18$ at 90% C.L. for $\Delta m^2 > 2 \times 10^{-3}$ eV^2 [47]. This sets a limit on the matrix element $U_{e3}^2 < 0.047$ if the one mass-scale dominance model is assumed. This limit, which can be deduced from equation (7.10) by assuming $\overline{P}_{ee} = 0.91$ and $\overline{S} = 0.5$, has also been pointed out in [87]. The two matrices that are considered are defined in the following way (the value of Δm^2 is assumed to be 0.01 eV^2 in both cases):

1. **CHOOZ scenario 1**: This matrix sets $U_{e3}^2 = 0.047$. Here $U_{\mu 3}^2$ and $U_{\tau 3}^2$ are assumed to be equal in magnitude and are set by unitarity to the value 0.4763.

2. **CHOOZ scenario 2**: This matrix sets U_{e3}^2 to 0.0127, corresponding to $\sin^2 2\theta = 0.05$. The matrix elements $U_{\mu 3}^2$ and $U_{\tau 3}^2$ are set to the value 0.4937.

Figure 7.11 shows the error contours expected for a 3.3 kiloton year exposure of MINOS for each of these mixing scenarios. The true parameters are indicated by the stars. The bi-logarithmic representation of Fogli *et. al.* is adopted [86]. This representation allows smaller values of the mixing parameters to be displayed than in the triangle representation. The variables $\tan^2 \phi$ and $\tan^2 \psi$ used in Figure 7.11 are related to the matrix elements in the following way:

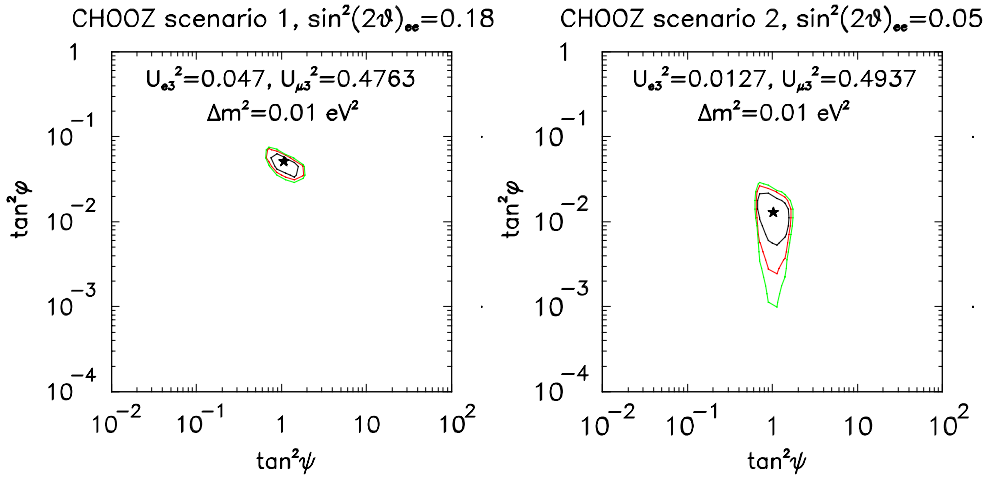

Figure 7.11 – Parameter measurement errors for two three-flavour matrices that are consistent with the CHOOZ result in the mode $\nu_\mu \rightarrow \nu_e$. The matrices are defined in the text. The bi-logarithmic representation of Fogli *et. al.* is adopted [86]. A 3.3 kiloton year exposure is assumed.

$$\tan^2\phi = \frac{U_{e3}^2}{1-U_{e3}^2},$$
$$\tan^2\psi = \frac{U_{e3}^2}{1-U_{e3}^2-U_{\mu 3}^2}, \qquad (7.11)$$

where two-generation $\nu_\mu \to \nu_e$ oscillations with $\sin^2 2\theta=1$ are described by $\tan^2\phi=1$ and large $\tan^2\psi$, and $\nu_\mu \to \nu_\tau$ is given by small $\tan^2\phi$ and $\tan^2\psi=1$. Threefold maximal mixing is given by $\tan^2\phi=½$ and $\tan^2\psi=1$.

The left-hand figure, which is for the larger value of U_{e3}^2 shows that these parameters can be measured by MINOS and are distinct from two-generation $\nu_\mu \to \nu_\tau$ oscillations. The right-hand figure, which is for the smaller value of U_{e3}^2, shows that the parameters are less precisely measured and are more difficult to distinguish from pure two-generation mixing ($\tan^2\psi \sim 1$ and $\tan^2\phi \sim 0$). Note that there is no apparent two-fold ambiguity in these measurements. This is because the models are close to the two-generation limit. The two ambiguous solutions occur at very similar values of $\tan^2\phi$ and $\tan^2\psi$ and so they are unresolved.

7.5 Prospects for observing CP violation in MINOS

If it is established that the three neutrino flavours are mixed, complementary runs made with neutrino and anti-neutrino beams would allow the differences, $D_{\mu e} = P(\nu_\mu \to \nu_e) - P(\overline{\nu}_\mu \to \overline{\nu}_e)$ and $D_{\mu\tau} = P(\nu_\mu \to \nu_\tau) - P(\overline{\nu}_\mu \to \overline{\nu}_\tau)$ to be measured. The CPT theorem demands that $D_{\mu e} = -D_{\mu\tau}$ [16]. The result $D_{\mu e} \neq 0$ or $D_{\mu\tau} \neq 0$ would indicate leptonic CP violation arising from a complex T-violating phase in the mixing matrix. There is no such phase if only two-generations are mixed; the mixing of at least three-generations is required for CP violation to be observable.

The size of any CP violating effect depends on several factors. The difference, $D_{\mu e}$, can be written as:

$$D_{\mu e} = 4J_{CP}(\sin(1.27\Delta m^2_{21}L/E_\nu) + \sin(1.27\Delta m^2_{32}L/E_\nu) - \sin(1.27\Delta m^2_{31}L/E_\nu)).$$

The CP violating parameter, J_{CP}, depends entirely on the mixing matrix elements[8]. The maximum possible value of $|J_{CP}|$ is $1/6\sqrt{3}$ and occurs for threefold maximal mixing. If $\Delta m^2_{21} = 0$ or $\Delta m^2_{32} = 0$ then $D_{\mu e} = 0$ and there is no CP violation.

Two factors therefore determine whether leptonic CP violation could be observed; the magnitude of J_{CP} and the values of $\Delta m^2_{32}L/E_\nu$ and $\Delta m^2_{21}L/E_\nu$. Since CP violation arises from interference between these two Δm^2- dependent phases, an experiment must be sensitive to the smaller of the two Δm^2's to observe a large effect. In general terms, CP violation will be observable in MINOS only if the smaller of the two Δm^2's is of the order 0.01 to 0.1 eV^2 and J_{CP} is sufficiently large.

Since the mixing parameters are, as yet, poorly known, it is not possible to make any very definite predictions of the amount of CP violation to be expected. It is possible, however, to calculate the amount of CP violation that could be observed in MINOS for a number of example mixing matrices and mass hierarchies. Other studies of the potential of long-baseline experiments to measure CP violation have been made [88][89][90]. Table 7.2 lists the four mixing matrices that are examined in this study. These matrices are defined in terms of the three Euler angles $\theta_1, \theta_2, \theta_3$ and the CP-violating phase δ_{CP}, as defined in section 2.3.2. Maximal CP violation ($\delta_{CP} = \pi/2$) is enforced in all four cases, although it is a natural consequence of threefold maximal mixing.

---

[8] $J_{CP} = \mathrm{Im}\{U^*_{\beta k}U_{\alpha k}U_{\beta j}U^*_{\alpha k}\}$.

The matrix labelled CHOOZ assumes that both Δm^2 are below the limit set by CHOOZ for maximal mixing ($\Delta m^2 \sim 10^{-3}$ eV^2). This value of Δm^2 is consistent with the Super-Kamiokande analysis of atmospheric neutrino data (but only marginally consistent with the Kamiokande atmospheric neutrino analysis). If the smaller of the two Δm^2's is greater than 10^{-10} eV^2 then this model predicts an energy independent suppression of the solar neutrino flux of 55%. The matrices labelled CHOOZ OMSD assume that the larger of the two Δm^2's is = 10^{-2} eV^2 and that the smaller Δm^2 is compatible with the MSW or just-so solutions to the solar neutrino problem ($\Delta m^2 \sim 10^{-5}(10^{-10})$ eV^2). These models are compatible with the $\nu_\mu \rightarrow \nu_\tau$ solution to the atmospheric neutrino anomaly and the CHOOZ negative result. The angle θ_2 is fixed by the CHOOZ result and θ_1 is fixed by the MSW best-fit solutions (large and small angle) to the solar neutrino anomaly found by Fogli *et. al.* [59]. The LSND anomaly, which cannot be explained by any of these matrices, is assumed to be spurious in the following discussion.

The most favourable model for observing CP violation in MINOS is threefold maximal mixing with both Δm^2's ~ 10^{-2} eV^2. A large CP violating amplitude is expected in MINOS for these parameters (as shown in Table 7.3). This model is unrealistic, however, because it is inconsistent with the result of the CHOOZ experiment. Figure 7.12 shows an example of the large effects that could be observed for complementary ν_μ and $\overline{\nu}_\mu$ runs. The top plot shows the numbers of identified electron like events expected as a function of

Matrix	Δm^2_{21}	Δm^2_{32}	θ_1	θ_2	θ_3	δ_{CP}	$\lvert J_{CP}\rvert$
Threefold maximal mixing	anything	$=10^{-3}$	$\pi/4$	0.615	$\pi/4$	$\pi/2$	0.096
CHOOZ	$=10^{-3}$	$=10^{-3}$	0.4	0.4	$\pi/4$	$\pi/2$	0.059
CHOOZ OMSD (large angle)	10^{-5}	$=10^{-3}$	0.464	0.219	$\pi/4$	$\pi/2$	0.041
CHOOZ OMSD (small angle)	10^{-5}	$=10^{-3}$	0.045	0.219	$\pi/4$	$\pi/2$	4.65×10^{-3}

Table 7.2 – The four putative three-generation mixing matrices that are used in this analysis. All angles are in radians. The values of Δm^2 (in eV^2) for which these matrices are valid are shown.

reconstructed neutrino energy for a 3.3 kiloton year run with the three horn ν_μ beam. Events are selected using the cuts described in Chapter 6. The open histogram is for electron-like events that are the result of $\nu_\mu \rightarrow \nu_e$ oscillations. The shaded histogram is the contribution of ν_τ CC events that are identified as electron-like (chiefly $\tau \rightarrow e$ decays). The bottom plot shows the same distributions expected for a 20 kiloton year run with a $\bar{\nu}_\mu$ beam. Since the interaction rate of a $\bar{\nu}_\mu$ beam is a factor of six smaller than a ν_μ beam (a factor of three in flux and a factor of two in the cross-sections), the top and bottom plots correspond to the same number of events. The flux spectra of the ν_μ and $\bar{\nu}_\mu$ beams are assumed to be identical.

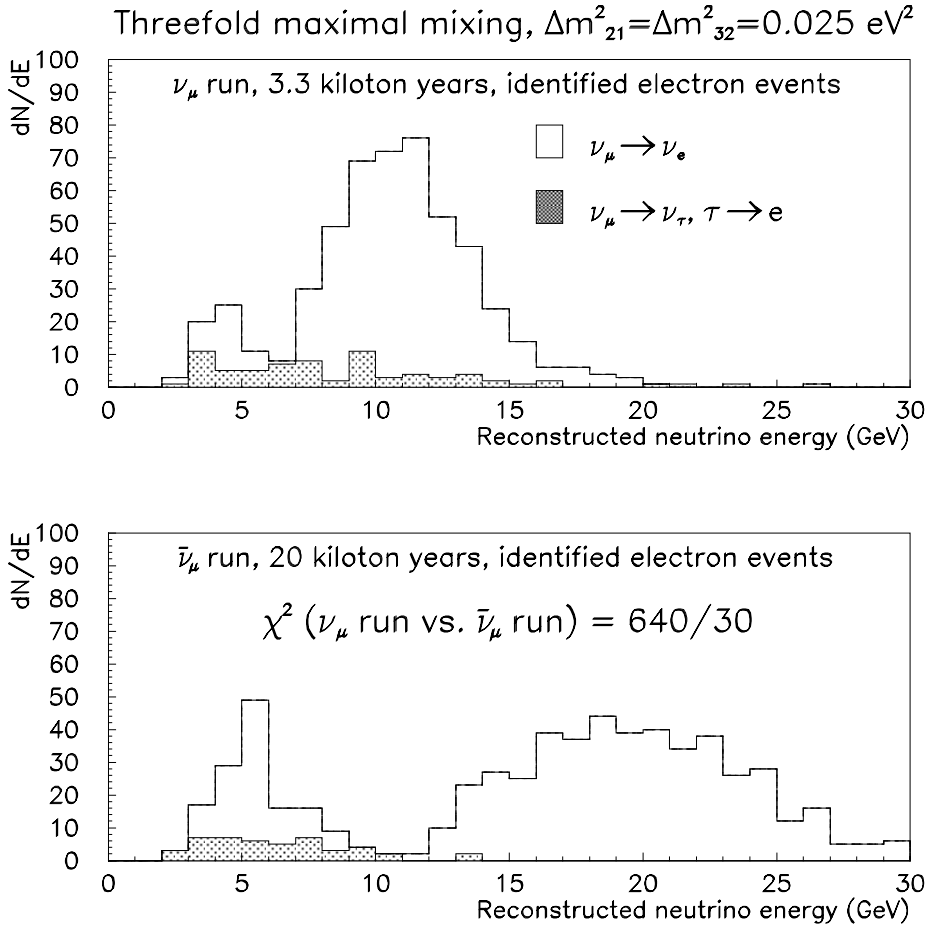

Figure 7.12 – Expected energy distributions of identified electron events for a 3.3 kiloton year ν_μ run (top plot) and a 20 kiloton year $\bar{\nu}_\mu$ run (bottom plot) for a mixing scenario that predicts a large CP violating amplitude in MINOS. Threefold maximal mixing is assumed with both Δm^2's = 0.025 eV^2

The plot shows that, in additional to the difference in oscillation probabilities, there is a significant change in the shape of the energy distributions for these parameters. The contamination due to $\tau \to e$ is small and the contribution of ν_e in the beam is less than 10 events in both distributions.

Table 7.3 shows the value of $D_{\mu e}$ averaged over the NuMI three horn beam ν_μ interaction spectrum for the four matrices defined in Table 7.2. Three mass schemes are considered: both $\Delta m^2 = 0.025$ eV^2 (the most favourable case); both $\Delta m^2 = 8\times10^{-4}$ eV^2 (the most favourable non-hierarchical scheme that is consistent with the CHOOZ result); $\Delta m^2_{32} = 0.01$ eV^2 and $\Delta m^2_{21} = 10^{-5}$ eV^2 (consistent with the solar and atmospheric neutrino anomalies).

Electron identification algorithms have been developed for MINOS that could potentially set a limit on $\sin^2 2\theta$ for $\nu_\mu \to \nu_e$ oscillations of 2-3$\times10^{-3}$ at 90% C.L. for a two year run of MINOS. It is clear that the value of $D_{\mu e}$ must be several times larger than this for a CP violating effect to be observable in MINOS. Table 7.3 shows that this is only the case if neutrino mixing is threefold maximal with both values of $\Delta m^2 \sim 10^{-2}$ eV^2. If the mass hierarchy suggested by the atmospheric and solar neutrino anomalies is assumed ($\Delta m^2_{32} = 0.01$, $\Delta m^2_{21} = 10^{-5}$) then CP violation is unobservable in MINOS, regardless of the

Matrix	$\Delta m^2_{21} = 0.025$ $\Delta m^2_{32} = 0.025$	$\Delta m^2_{21} = 8\times10^{-4}$ $\Delta m^2_{32} = 8\times10^{-4}$	$\Delta m^2_{21} = 10^{-5}$ $\Delta m^2_{32} = 0.01$
Maximal	0.449	7.2×10^{-4}	1.7×10^{-4}
CHOOZ	-	4.4×10^{-4}	1.1×10^{-4}
CHOOZ OMSD (large angle)	-	-	7.3×10^{-5}
CHOOZ OMSD (small angle)	-	-	8.2×10^{-6}

Table 7.3 – The CP violating amplitude, $D_{\mu e}$, averaged over the NuMI neutrino interaction spectrum, for a number of mixing matrices and mass schemes.

values of the mixing matrix elements.

The effect of the CHOOZ result is to push the values of Δm^2 below 10^{-3} eV^2. This suppresses the CP violating effect in MINOS because the default beam is optimised for $\Delta m^2 \sim 0.025$ eV^2. The low energy beam is more suited for a measurement of CP violation if the values of Δm^2 are low although, even if the most favourable matrix elements are considered, it would require more than ten years of running with the proposed low energy beam to measure a 5σ CP violating effect if both values of Δm^2 were 8×10^{-4} eV^2. In conclusion, the CHOOZ result and the mass hierarchy suggested by the solar and atmospheric neutrino results appear to rule out the possibility of observing a large CP violating effect in MINOS for any three-flavour mixing scenario.

Recent studies [88][89][90] of the potential to observe CP violating amplitudes in long-baseline experiments have concluded that, for experiments with baselines = 100 km, large matter effects due to resonant flavour conversion in the Earth's crust are expected. These effects are not CP-symmetric [90] so the transition probabilities of neutrinos and antineutrinos will be different even if CP is conserved. This effect, which has not been considered in the above analysis, further complicates the observation of a CP violating amplitude in MINOS. A prescription to separate the pure CP-violating effect from the matter effect has been proposed in [89] by observing the L/E dependence of the oscillation probabilities (as shown in Figure 7.12) or comparing the results of two experiments with different baselines (e.g MINOS and K2K (KEK to Super-Kamiokande) [67]). It is difficult, however, to extract, the mixing parameters from this analysis; the moduli of the matrix elements and the value of Δm^2 must be known precisely. (This may be one motivating reason for making a precision measurement of the parameters in MINOS.)

A clean CP violating signal may be observed by searching for T-violating effects in long-baseline experiments since the matter effect is symmetric under the time reversal operator [90]. A measurement of T-violation is a non-zero measurement of the asymmetries $T_{\alpha\beta} = P(\nu_\alpha \to \nu_\beta) - P(\nu_\beta \to \nu_\alpha)$ and/or $\overline{T}_{\alpha\beta} = P(\overline{\nu}_\alpha \to \overline{\nu}_\beta) - P(\overline{\nu}_\beta \to \overline{\nu}_\alpha)$ [90]. This requires a mixed flavour beam which is not planned for MINOS or any of the other first-generation long-baseline experiments although it has been suggested that an intense $\nu_\mu + \overline{\nu}_e$ or $\overline{\nu}_\mu + \nu_e$ beam could be produced by a future muon collider [90][91].

7.6 Conclusions for a three-generation analysis of MINOS

A three-generation analysis of MINOS could be performed if it is possible to identify ν_μ CC and ν_e CC events. The results of Chapter 4 have shown that, for the 3 horn WBB, ν_μ CC events can be selected with 91% efficiency and Chapter 6 has shown that electron neutrino events can be identified with an average efficiency of 26%. A three-generation analysis provides more information on the neutrino oscillation mode than the simple two-generation analysis that is commonly used. The complexity of a general three-flavour analysis is avoided if the one mass-scale dominance mass hierarchy, which is suggested by current experimental data on solar and atmospheric neutrinos ($\Delta m^2_{solar} << \Delta m^2_{atm}$), is assumed and the results can be displayed in a clear format.

A three-generation analysis of MINOS will at best give two solutions for the mixing matrix elements, due to the fundamental two-fold ambiguity in the matrix element $U^2_{\mu 3}$ that results from a measurement of the ν_μ disappearance probability. This ambiguity can, in principle, be resolved by an experiment that uses a ν_e beam (such as CHOOZ). The fact that CHOOZ has, as yet, seen no evidence for $\nu_e \to \nu_\mu$ or $\nu_e \to \nu_\tau$ oscillations has important implications for a three-generation analysis of MINOS. The CHOOZ result implies that the

amount of $\nu_\mu \rightarrow \nu_e$ mixing that could be observed in MINOS is small. This chapter has shown, however, that MINOS could distinguish three-generation scenarios that are both consistent with CHOOZ in the mode $\nu_\mu \rightarrow \nu_e$ and the atmospheric neutrino anomaly in the mode $\nu_\mu \rightarrow \nu_\tau$ from pure two-generation $\nu_\mu \rightarrow \nu_\tau$ oscillations.

CP violation, which would indicate that the complex phase $\delta > 0$, could be measured by MINOS if both Δm^2's are = 10^{-3} eV^2 and J_{CP} is large. It appears, however, that it is impossible to simultaneously account for the atmospheric neutrino anomaly, the solar neutrino anomaly and the CHOOZ result and obtain a large CP violating amplitude in MINOS[9].

Chapter 9 discusses the generalities of a three-generation analysis of MINOS and shows how the results of MINOS are complementary to those of other neutrino oscillation experiments.

[9] If four neutrino generations are assumed (the three standard generations plus a sterile neutrino) it has been shown [90] that the results from LSND, CHOOZ, atmospheric and solar neutrinos can be explained in a consistent framework which also allows for large CP violating amplitudes in future long-baseline experiments.

Chapter 8 $\tau \to \pi + X$ analysis in MINOS

8.1 Introduction

The atmospheric neutrino anomaly can be explained by $\nu_\mu \to \nu_\tau$ oscillations with $\Delta m^2 > 10^{-3}$ eV^2 and large $\sin^2 2\theta$. The recent CHOOZ result has effectively ruled out the interpretation of the anomaly in terms of $\nu_\mu \to \nu_e$ oscillations. If the anomaly is not spurious then it appears that $\nu_\mu \to \nu_\tau$ oscillations with parameters that are accessible to MINOS are likely.

The observation of a tau decay signature in MINOS would provide powerful evidence that $\nu_\mu \to \nu_\tau$ oscillations have taken place. This signature would also provide independent and complementary information on the oscillation mode from the ν_μ and ν_e CC analyses of Chapter 4 and Chapter 6 and would provide an important cross-check of the results of the three-generation analysis described in Chapter 7. The observation of characteristic tau decay kinks, which is the goal of emulsion experiments such as CHORUS [65], is impossible in MINOS due to the short lifetime of the tau lepton ($c\tau$=87 μm). It is therefore necessary to devise a test that is sensitive to the topological differences between ν_τ CC events and the background of ν_μ interactions.

The signal for $\tau \to \pi + X$ in MINOS is the observation of pions from tau decays that tend to be of higher momentum than those from ν_μ neutral current interactions. Figure 8.1 shows the output of NEUGEN for the momentum spectrum of leading charged pions from

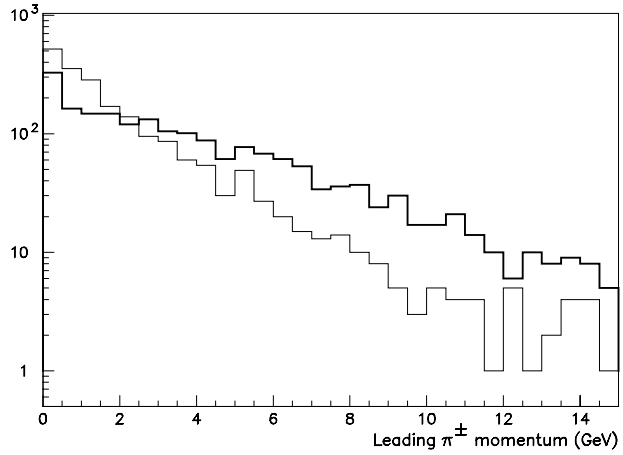

Figure 8.1 - Leading charged pion momentum spectra for 7000 ν_μ NC events (thin line) and 7000 ν_τ CC events (thick line, generated with large Δm^2).

ν_τ CC events and ν_μ NC events. There is a clear excess of high energy pions in ν_τ CC events and this difference is accentuated for low multiplicity final states.

A high energy pion will typically interact after one interaction length in the detector

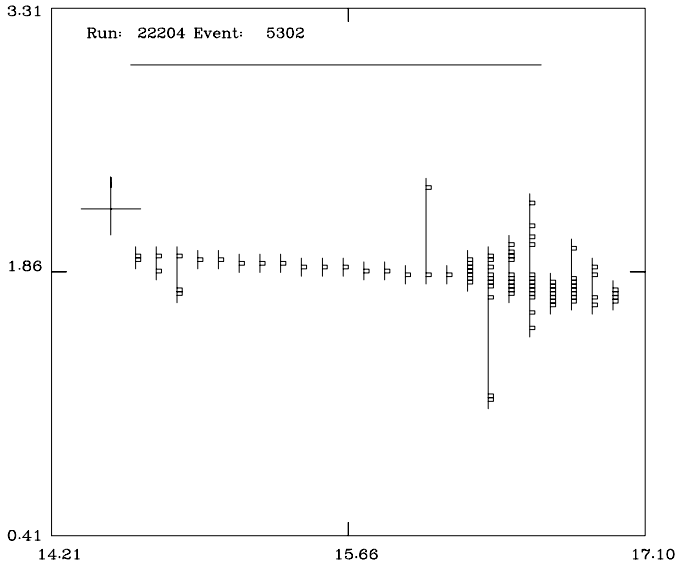

Figure 8.2 – A quasi-elastic track→star event in 2 cm steel. The axis scales are in metres.

(8 planes of 2 cm steel) and produce an energetic shower downstream of the event vertex. An example of this distinctive 'track→star' topology is shown in Figure 8.2.

The statistical power of this test comes from the large τ→hadrons branching ratio (~65%). Modes with low final state multiplicities, such as $\tau \to \pi\nu$ (B.R. 11.31%), are expected to be detected with the greatest efficiency although the test has some sensitivity to the higher multiplicity final states. This test is possible in the wide band beam because the $\tau \to \pi + X$ signal arises from events with small missing energy. The background, mainly from neutral current interactions, has large missing energy and it is possible to devise cuts that reduce the background to the same level as the signal if oscillations occur with large $\sin^2 2\theta$. The search for $\tau \to \mu$ and $\tau \to e$ decays in the wide band beam is much more difficult because the background is larger and tends to obscure the presence of any signal [92].

This chapter describes the $\tau \to \pi + X$ analysis method. In section 8.2, a set of cuts to isolate events with the track→star topology is described. The Hough transform, first introduced in Chapter 5, is used to search for pion tracks in the events. Section 8.3 studies the background to $\tau \to \pi + X$, investigates the uncertainty in this background rate due to imperfect knowledge of charged hadron production and evaluates the possible contamination from ν_e CC events that are produced by three-flavour mixing scenarios. Section 8.4 studies how the sensitivity of the analysis is affected if a pulse height threshold, which may be required to combat noise in the MINOS far detector, is applied to hits in the simulated events. In section 8.5 the potential reach of the $\tau \to \pi + X$ analysis in neutrino oscillation parameter space is calculated. The conclusions of the analysis are drawn in section 8.6. This section includes the major results of Appendix B, which studies how the sensitivity of the

$\tau \to \pi + X$ test to neutrino oscillations is affected as the major parameters of the far detector (steel thickness, transverse pitch, active detector elements) are changed.

8.2 Cuts to isolate quasi-elastic $\tau \to \pi + X$

8.2.1 Objective of cuts

Quasi-elastic track→star events, such as the one shown in Figure 8.2, exhibit a distinctive topology. The main features are:

- short event length compared to ν_μ CC events;
- single track with few extra vertex hits;
- energetic hadronic shower downstream from vertex;
- track and shower are connected.

Two large samples of Monte Carlo events were generated in 2 cm steel and consisted of 51577 ν_μ events with no oscillations and 17794 ν_τ CC events with saturated oscillations. A series of cuts are applied to these two samples to isolate events with track→star topologies. The cuts are applied in two stages; the first stage uses simple cuts to isolate short events with low vertex activity and high downstream activity and the second stage uses the Hough transform to search for a pion track in the event. The objective of the cuts is to produce a pure sample of track→star events that are more common in ν_τ CC events than in the ν_μ background. The distributions and efficiencies that follow are for 2 cm steel with 2 cm liquid scintillator cells unless otherwise stated. Other configurations, with 2 and 4 cm

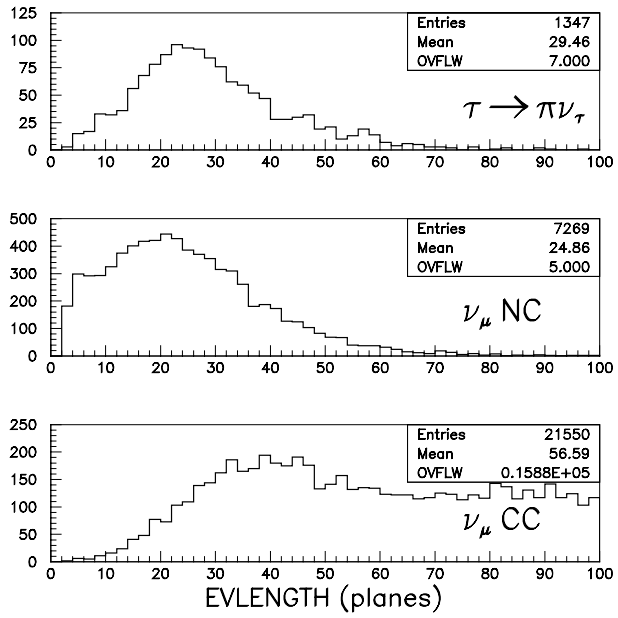

Figure 8.3 - Event length distributions for $\tau \to \pi\nu$, ν_μ NC and CC events. Note the large overflow for the ν_μ CC sample.

steel, 2 and 4 cm transverse pitch and FLS and APT active detectors, are studied in Appendix B.

8.2.2 Event length cut

The transverse and longitudinal extent of $\tau \to \pi + X$ events is governed by the nuclear interaction length, λ_I, in steel (16.7 cm or 8 planes of 2 cm steel). Previous studies [71] have shown that 99% of high energy (24 GeV) hadronic showers have a longitudinal extent of less than $10\lambda_I$ in steel. This allows a good separation between $\tau \to \pi + X$ and ν_μ CC events. In addition, low multiplicity tau decays have, on average, more visible energy

than ν_μ NC events and they will tend to be longer[10]. A minimum and maximum event length cut will therefore provide the optimum selection of signal over background.

The event length, EVLENGTH, is defined by two points: the reconstructed vertex and the end of the event. The event vertex is defined as the first of three contiguous planes containing hits with greater than one photoelectron in the liquid scintillator active detectors. Similarly, the end of the event is defined as the last of three contiguous planes. The event length (in detector planes) is measured between these two points. Figure 8.3 shows distributions of EVLENGTH for $\tau \to \pi\nu$ events, and ν_μ NC and ν_μ CC background events. A cut of 20 < EVLENGTH < 60 accepts 68% of $\tau \to \pi\nu$ events whilst rejecting 86% of ν_μ CC and 47% of ν_μ NC events.

8.2.3 BARREL and FLIGHT cuts

The pion track and hadronic star will be approximately equal in length since they are both governed by the nuclear interaction length. The track and star regions are therefore separated by dividing the event into two equal halves. The two regions are named BARREL and FLIGHT respectively, due to the similarity of a quasi-elastic track→star image to a dart. The event should be track-like in the BARREL region and star-like in the FLIGHT region, as sketched in Figure 8.4.

---

[10] Assuming a flat y distribution, ν_μ NC events will have an average energy of $E_\nu / 2$, where E_ν is the incident neutrino energy. The remaining $E_\nu / 2$ is carried off by the outgoing neutrino. In a $\tau \to \pi + X$ decay, the average visible energy will be $E_\nu / 2$ from the primary vertex plus additional energy due to the pions from the tau decay.

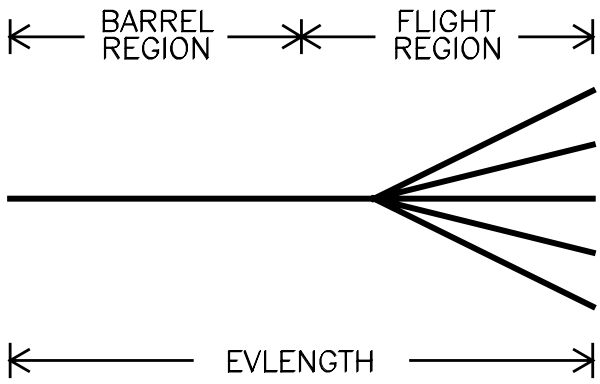

Figure 8.4 - Sketch of a quasi-elastic track→star showing BARREL and FLIGHT regions.

The quantity BARREL is defined as the number of hits per plane in the first half of the event. Similarly, FLIGHT is defined as the number of hits per plane in the second half of the event. Hits in both detector views are summed to calculate these numbers. A small value of BARREL or FLIGHT indicates a track-like region of the event and a large value of BARREL or FLIGHT corresponds to a shower-like region. A track→star event is therefore characterised by a small value of BARREL and a large value of FLIGHT.

Figure 8.5 shows the event topologies expected in particular regions of BARREL versus FLIGHT space. Small BARREL and small FLIGHT indicates a track-like event. Large BARREL and small FLIGHT indicates an event with a shower at the vertex and a downstream track (e.g. a ν_μ CC event). Large BARREL and large FLIGHT indicates a shower-like event (e.g. a NC event). Finally, small BARREL and large FLIGHT indicates a track→star event.

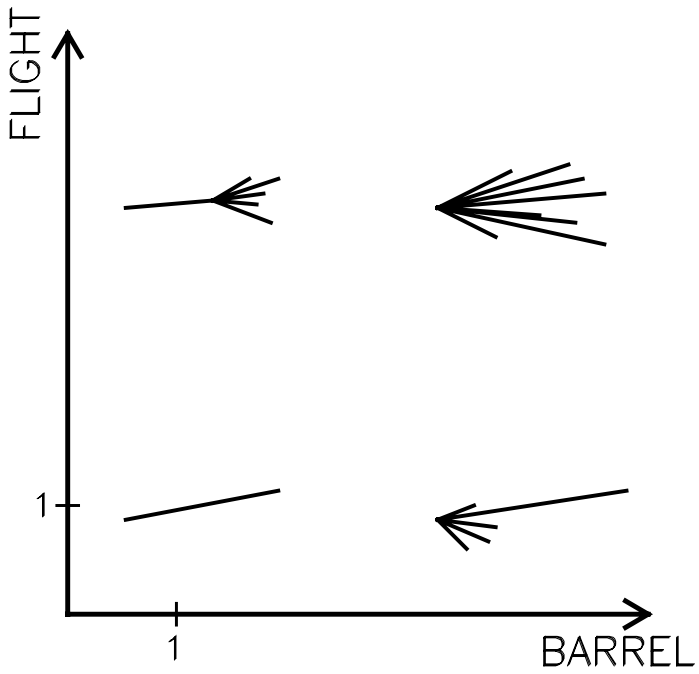

Figure 8.5 - Expected event topologies in BARREL versus FLIGHT space.

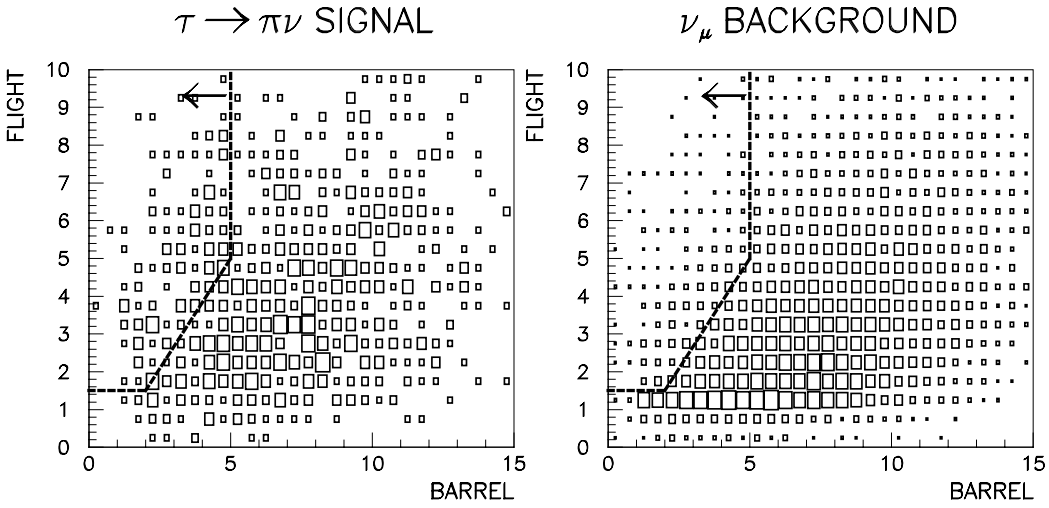

Figure 8.6 - BARREL versus FLIGHT scatter plots for $\tau \to \pi\nu$ and ν_μ NC and CC events.

Figure 8.6 shows distributions of BARREL versus FLIGHT for $\tau \to \pi\nu$ signal and ν_μ background events. There is a relative excess of events with small BARREL and large FLIGHT in the $\tau \to \pi\nu$ sample. Since the background has a broad distribution in BARREL versus FLIGHT space, harsh cuts are required to select quasi-elastic track→star events with small background contamination.

It is important to maximise the acceptance of the BARREL and FLIGHT cuts for $\tau \to \pi\nu$ events because cuts that select only a very small region of BARREL-FLIGHT space are sensitive to uncertainties in the detector response; if the detector response changes then the $\tau \to \pi\nu$ signal may move out of the range of the cuts. The method employed in this analysis is to apply common BARREL and FLIGHT cuts to all of the detector configurations that are studied here and in Appendix B[11]. To do this, it is first necessary to define optimal cuts on BARREL and FLIGHT for all detector configurations. Optimal cuts are defined to

[11] The cuts on EVLENGTH and STARHITS, the number of hits in the FLIGHT region, must be scaled appropriately between 2 and 4 cm steel configurations

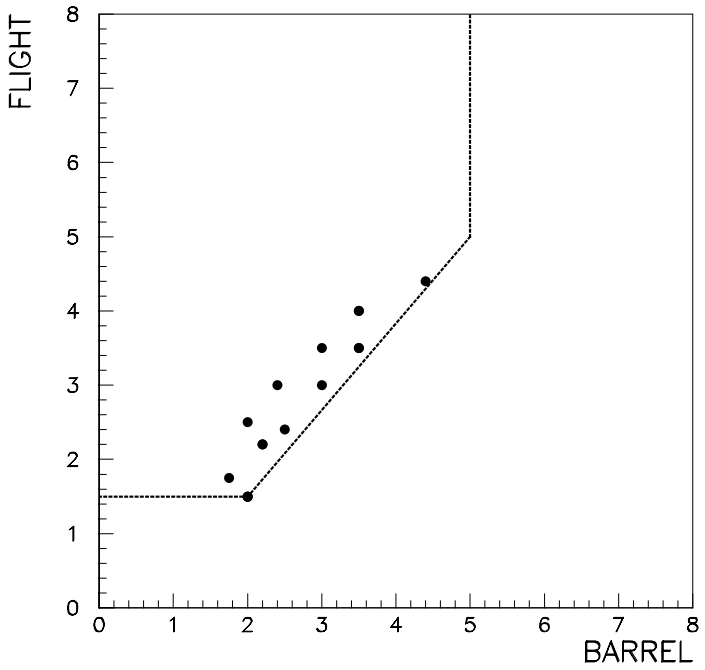

Figure 8.7 - Optimised BARREL and FLIGHT cuts for 16 detector configurations (some cuts are duplicated). The dotted line represents less restrictive cuts on BARREL and FLIGHT that can be applied to all configurations without the need for re-optimisation.

give a $\tau \to \pi\nu$ selection efficiency of approximately 5% and to maximise the ratio of signal over background events that are selected. Figure 8.7 shows optimal cuts on BARREL and FLIGHT that are defined for a number of detector configurations and active detector response functions. The aim is to apply a single cut on BARREL and FLIGHT that will encompass all these points but not seriously degrade the $\tau \to \pi + X$ sensitivity. It is clear from the figure that different BARREL and FLIGHT cuts are required to achieve an optimal signal/background selection ratio in each detector configuration. Events have fewer hits as the detector is degraded, either by increasing the steel thickness or increasing the transverse cell size. The signal and background distributions therefore migrate to smaller values of BARREL and FLIGHT.

It is clear from Figure 8.6 that a rectangular cut that incorporates all of the points in Figure 8.7 will extend into a region of large BARREL and small FLIGHT that is highly populated by background events. The cuts that are applied, shown by the dotted line, eliminate this region. The cuts shown correspond to: FLIGHT > 1.5, BARREL < 5 and FLIGHT > 1.17 × BARREL - 0.84. These cuts accept 16% of $\tau \to \pi\nu$events and reject 98% of ν_μ CC and 92% of ν_μ NC events passing previous cuts.

Some insidious background events also pass through the cuts defined above, in addition to genuine track→star events. Figure 8.8 is an example of one such event, a ν_μ CC event with a slow muon track and a disconnected shower downstream from the vertex. This type of event is effectively rejected by requiring the number of occupied planes, PLANEOCC, to be greater than 0.85 and requiring the *rms* of hits about the *z*- axis for the BARREL and FLIGHT regions, VBAR and VFLI, to be less than 30 and 40 cm respectively. These three cuts accept 73% of $\tau \to \pi\nu$ events and reject 61% of ν_μ CC and 54% of ν_μ NC events passing previous cuts.

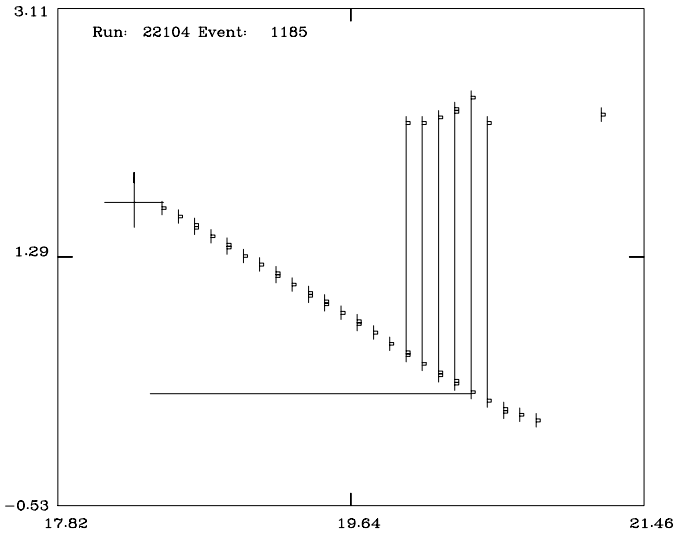

Figure 8.8 – A background ν_μ CC event with a disconnected shower that passes the simple BARREL and FLIGHT cuts.

8.2.4 Application of the Hough Transform to $\tau \to \pi + X$

The cuts described in section 8.2 select short events with few hits in the first half of the event and many hits in the second half. They do not, however, explicitly search for a fast forward pion track emanating from the vertex region. To do this, it is necessary to find tracks in the sample of track→star candidates. In the $\tau \to \pi + X$ analysis, the Hough transform, which was first introduced in Chapter 4, is used as a pattern recognition algorithm. The use of the transform for finding tracks in `GMINOS` events is justified in Appendix A.

Figure 8.9 shows a $\tau \to \pi\nu$ event with a track→star topology. In Hough space, Figure 8.10, this appears as a fairly localised peak superimposed on top of a broad ridge. The two components correspond to the track and star elements of the event respectively.

Clearly the signature of a track in an event is the presence of a localised peak in Hough space. To search for a track, the Hough transform is applied to the track→star candidates that are isolated by the cuts described in Section 8.2 and the Hough space is scanned for the presence of a peak. The Hough Transform is applied only to the hits in the `BARREL` region, since the track is expected to be present in the first half of the event. If there is a straight track in the event, both Hough spaces should contain peaks. The bin locations of the peaks in both spaces are found and the quantity `RMS75`, which is defined in section 5.2, is calculated in each Hough space.

The result of applying the cut `RMS75` < 10 is that, for events passing previous cuts, 46% of $\tau \to \pi\nu$ events are accepted and 19 of 25 ν_μ CC and 80% of ν_μ NC events are rejected.

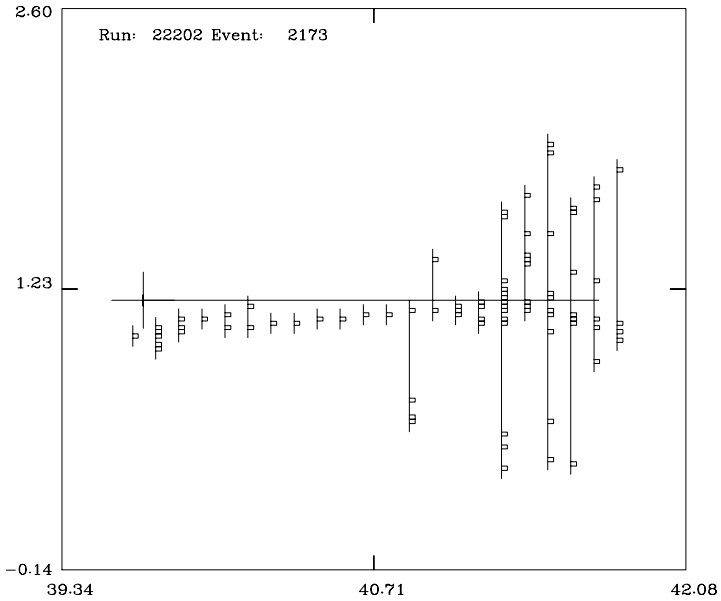

Figure 8.9 - Track→star event topology in 2 cm steel.

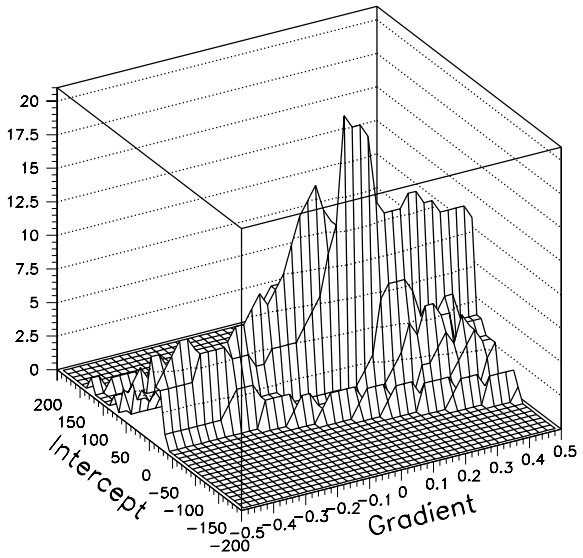

Figure 8.10 - Hough space of the event in Figure 8.9.

8.2.5 Further cuts

Two further cuts are applied to the event samples. The purpose of the first cut is to ensure that the track→star candidates contain an obvious star. The cut requires that the number of hits in the FLIGHT region of the event, STARHITS, be greater than 30. This corresponds to approximately 2.5 GeV of visible energy in 2 cm steel. Figure 8.11 shows distributions of STARHITS for signal $\tau \to \pi\nu$ events and background ν_μ events in 2 cm steel with 2 cm cells. This cut accepts 47 of 50 $\tau \to \pi\nu$ events and rejects 7 out of 30 ν_μ background events passing previous cuts.

The $\tau \to \pi + X$ signal is based upon an excess of high momentum pions in tau decays compared to the ν_μ background. Pions from tau decays tend to be of high momentum and at small angles to the beam direction, whereas pions from the background ν_μ tend to be of low momentum and at large angles. Since events that pass to this stage of the analysis

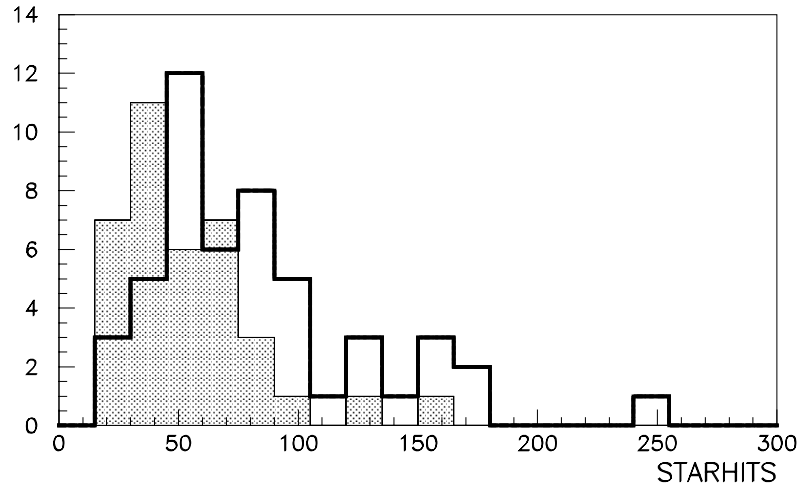

Figure 8.11 - Number of hits in the FLIGHT region, STARHITS, for the $\tau \to \pi\nu$ signal (open histogram) and the ν_μ background (shaded histogram).

have a flagged track, it is possible to use the Hough Space to estimate the angle of the track with respect to the z- axis. The gradients of the peaks in x-z and y-z Hough spaces, GRADXZ and GRADYZ, are related to θ_z, the angle of the track relative to the z- axis by the following expression:

$$\cos\theta_z = \frac{1}{\sqrt{1 + GRADXZ^2 + GRADYZ^2}}. \tag{8.1}$$

Figure 8.12 shows the distributions of $\cos\theta_z$ for the $\tau \to \pi\nu$ signal and the ν_μ background events in 2 cm steel with 2 cm cells. The signal distribution is strongly peaked around $\cos\theta_z = 1$, whereas the background distribution is much broader. The cut $\cos\theta_z > 0.95$ accepts 43 out of 47 $\tau \to \pi\nu$ events and rejects 11 out of 29 ν_μ background events passing previous cuts.

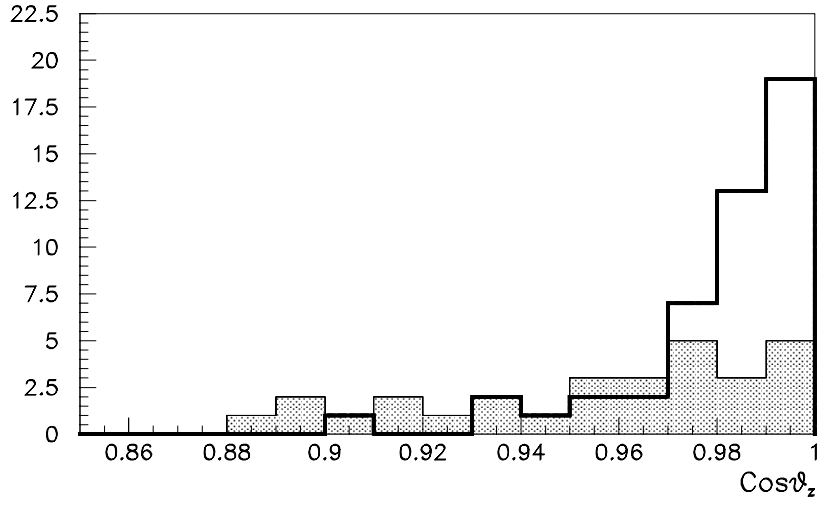

Figure 8.12 - Distributions of $\cos\theta_z$ for the tracks found in $\tau \to \pi\nu$ signal events (open histogram) and ν_μ background events (shaded histogram).

CUTS	SIGNAL		BACKGROUND	
	$\tau \to \pi\nu$	Other ν_τ CC	ν_μ CC	ν_μ NC
NO CUTS	1347	10550	21550	7269
EVLENGTH<60	1300	8865	3229	7098
EVLENGTH>20	920	6054	2965	3875
BARREL<5	261	662	565	978
FLIGHT>1.5	228	410	221	718
FLIGHT>1.17×BARREL-0.84	150	201	64	329
PLANEOCC>0.85	147	177	53	252
VBAR<1000	122	132	38	185
VFLI<1600	108	124	25	152
RMS75<10	50	28	6	30
STARHITS>30	47	27	6	23
$\text{Cos}\theta_z$>0.95	43	26	3	15+1 ν_e NC

Table 8.1 - Breakdown of cuts for 2 cm steel with 2 cm cells. The effects of the cuts are cumulative.

8.2.6 Results

Table 8.1 shows the numbers of signal and background events passing the cuts described above for the detector configuration of 2 cm steel plates and 2 cm pitch liquid scintillator cells. From the table, 69 signal events (43 $\tau \to \pi\nu$ plus 26 higher multiplicity $\tau \to \pi + X$) and 19 background events pass the cuts. This corresponds to a $\tau \to \pi\nu$ selection efficiency of 2.2% with a background rejection ratio of 19/51577 (3.7×10^{-4}). For the Wide Band Beam spectrum, 82200 ν_μ CC and NC events are expected in two years for no oscillations and 9571 ν_τ CC events are expected for $\sin^2(2\theta)$=1 and saturated oscillations (large Δm^2). Normalising the event samples to these numbers yields a signal of 36.8 events with a background of 30.3 events for a two-year exposure. This is equivalent to an 6.7 standard deviation effect or a limit of $\sin^2(2\theta) < 0.19$ @ 90% C.L. if no signal is found.

Figure 8.13 shows the effect of each cut on the signal $\tau \to \pi\nu$ and background ν_μ selection efficiencies. Signal efficiency (the number of $\tau \to \pi\nu$ events passing cuts divided

by the initial number of $\tau \to \pi\nu$ events passing the fiducial and containment cuts) is plotted against background rejection (the initial number of ν_μ events divided by the number of ν_μ events passing the cuts). The effects of the cuts are cumulative. Lines of constant signal/background ratio (i.e. signal efficiency multiplied by background rejection) are shown on the plot. It can be seen that all cuts have the effect of increasing the signal/background ratio. Figure 8.13 also shows the dramatic effect of applying harsh `BARREL` and `FLIGHT` cuts.

Figure 8.14 plots overall ν_τ CC selection efficiency against background rejection. Comparing this plot to Figure 8.13 shows that the signal selection efficiency is lower for ν_τ CC events than for $\tau \to \pi\nu$ events. In particular, the `BARREL` and `FLIGHT` cuts do not significantly improve the signal/background ratio in Figure 8.13, although 35% of ν_τ CC events contain muons or electrons that are efficiently rejected by the `BARREL` and `FLIGHT` cuts. This is because these cuts are optimised for low multiplicity quasi-elastic $\tau \to \pi\nu$ events. The gain in signal/background achieved in Figure 8.13 is offset by inelastic ν_τ CC events that tend to have larger values of `BARREL` and `FLIGHT` than the ν_μ background.

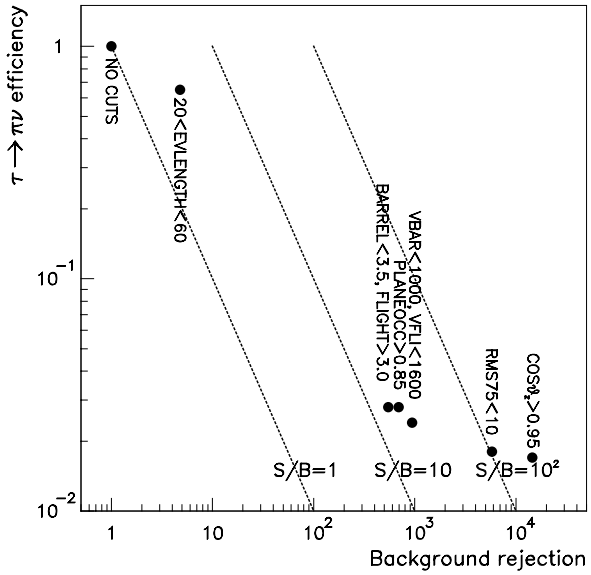

Figure 8.13 - $\tau \to \pi\nu$ selection efficiency versus background rejection as a function of the cuts for 2 cm steel with 2 cm cells. Three lines of constant signal/background selection efficiency are plotted.

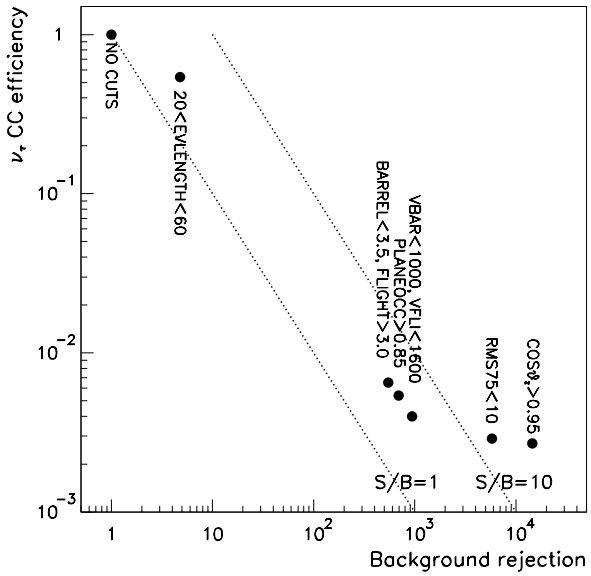

Figure 8.14 - ν_τ CC selection efficiency versus background rejection as a function of the cuts for 2 cm steel with 2 cm cells. Two lines of constant signal/background selection efficiency are plotted.

8.2.7 Track→star purity

To check that the cuts described above are selecting events with a track→star topology, the set of signal and background events that pass all the cuts were scanned using the VINES event display program. The scanning criteria demanded a clear track in both views and a energetic star with greater than 20 hits. Using these rules, 64 out of 69 signal events and 15 out of 19 background events were classified as track→star after scanning. This corresponds to a track→star purity of approximately 90%. All the events that failed the scan contained a clear track but either the star was indistinct or not physically connected to the track (i.e. a less extreme example of the event type shown in Figure 8.8). Note that this scan was only performed to check that the cuts are selecting track→star events and is not an integral part of this analysis.

8.3 Nature of background events

The 19 background events that passed the $\tau \to \pi + X$ cuts should be ν_μ NC events with one energetic charged hadron track that produce the same track→star signal as $\tau \to \pi + X$. The events break down into the following categories: 15 ν_μ neutral current interactions, three ν_μ CC interactions and one ν_e NC interaction. Of the three ν_μ CC events that pass the cuts, two are slow (< 1 GeV) muons with a few extra hits at the end of the track (possibly $\mu \to e$ decays). These could be eliminated by a stronger cut on the number of `STARHITS`, at the expense of a lower overall efficiency for selecting true $\tau \to \pi + X$ events. The third CC event is a 8 GeV muon which suffers a catastrophic energy loss (probably bremsstrahlung) producing a high energy electromagnetic shower and hence a track→star topology.

The neutral current events selected by the cuts possess the following features:

- low average hadron multiplicity = 3.7;
- one high (>2 GeV) momentum hadron;
- leading charged hadron: proton (60%), π^- (33%), π^+ (7%).

These neutral current events therefore possess the features expected from the background to $\tau \to \pi + X$ and the number of ν_μ CC events faking the track→star topology is small.

8.3.1 Comparison of Monte Carlo hadro-production with data

One weakness in this analysis is that it is sensitive to the model of hadron production that is implemented in NEUGEN. If the Monte Carlo is significantly underestimating the rate of production of high momentum pions in ν_μ NC events then the size of the background to $\tau \to \pi + X$ may be larger than indicated in this analysis. Of course, the definitive measurement of the ν_μ NC background to the $\tau \to \pi + X$ signal will be made in the near detector. It is possible, however, to perform a check of the Monte Carlo by comparing its predictions with published data on hadro-production in νN, ep and e^+e^- experiments.

The quark-parton model describes the process of deep-inelastic lepton nucleon scattering in terms of the variables x and Q^2 but it does not explain the process of hadronization of the struck quark fragments. Fragmentation functions, which give the probability of producing a hadron of a particular type, with a fraction z of the total energy of the quark system, are predicted by models such as that of Field and Feynman [93] or the Lund model [94]. The predictions of the fragmentation functions from the models are in good agreement with data. Experimental data also shows that the fragmentation functions are largely independent of x and Q^2 and depend only on the scaling variable z [95].

A number of experimental collaborations have published data on neutrino and electro-production of hadrons and it is possible to directly compare the experimental data with the output of NEUGEN. Figure 8.15 shows the measured z dependence of the charged hadron fragmentation function from a variety of data sources compared with the predictions of the Monte Carlo. The quantity plotted on the ordinate is $1/N_{ev}dN^{\pm}/dz$, where N_{ev} is the total number of events in the data sample and $dN^{\pm}/dz$ is the number of positive and negative charged hadrons produced in these N_{ev} events per bin of .

The solid histogram is the prediction of NEUGEN for ν_μ CC events. The dotted and dashed histograms are the 1σ statistical errors on the 7818 Monte Carlo ν_μ CC events. The data points are derived from measurements from νp, ep and e^+e^- experiments over the

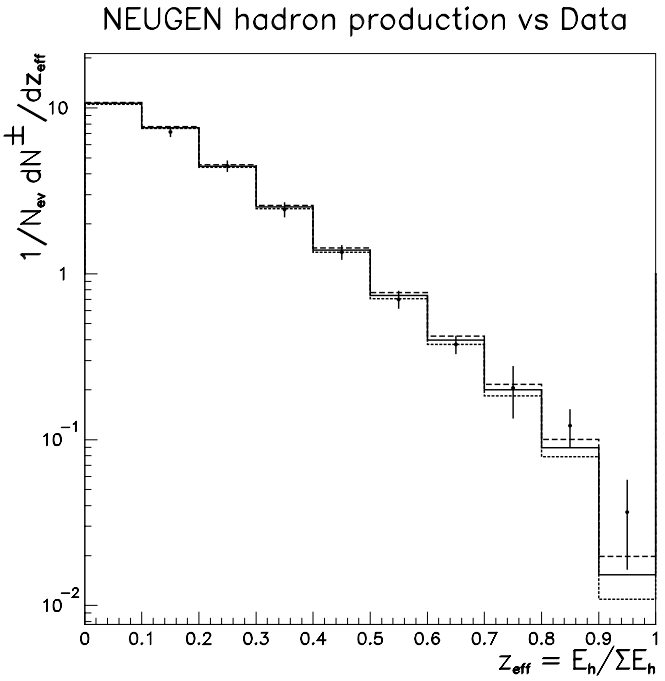

Figure 8.15 - Comparison between the NEUGEN z distribution for ν_μ CC events and published data on hadro-production in νp, e^+e^- and ep interactions. The solid histogram is the prediction of NEUGEN, the dotted lines represent the Monte Carlo statistical errors and the points are the combination of the experimental measurements that are derived from [96].

range $0.1<z<1.0$ [96]. The data points used are from ep scattering at DESY [97], e^+e^- interactions at DORIS [98] and νp interactions at BEBC [96]. The 50 experimental data points are grouped into 9 equidistant bins of z from 0.1 to 1.0. In each bin, the weighted mean of the data points is calculated. The error is the *rms* of the points in each bin. The agreement between measurements and NEUGEN is very good ($\chi^2 = 3.7$ for 9 D.O.F.) and the two distributions agree over more than 2 decades in $1/N\, dN/dz$.

It is possible to use Figure 8.15 to constrain the normalisation of the hadron production spectrum predicted by NEUGEN. Figure 8.16 shows how the value of χ^2, calculated between the prediction of NEUGEN and the experimental data, changes as the overall normalisation of the NEUGEN z distribution is varied about its true value. The plot shows that the data constrains the normalisation of NEUGEN to within ±10% of its true value at 90% confidence and that the minimum value of χ^2 occurs for a normalisation scale factor of 1.0 (i.e. the true value).

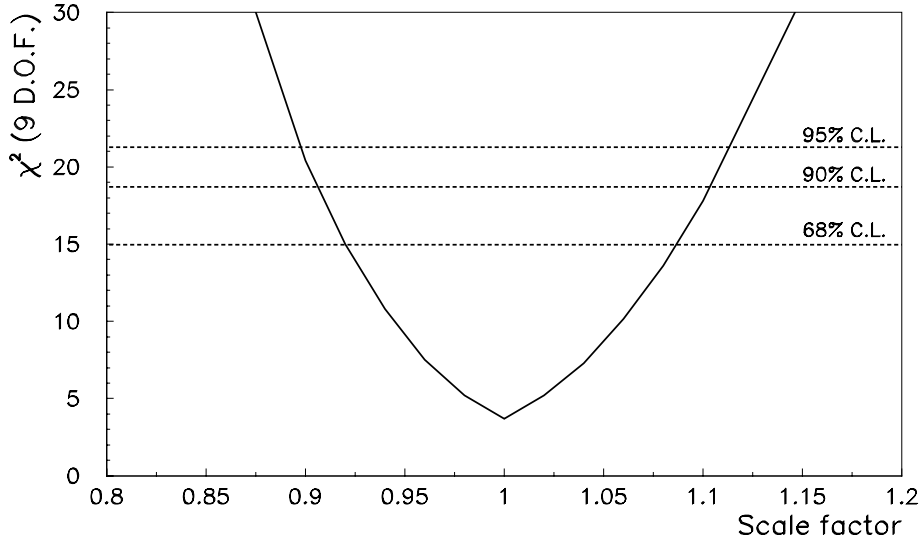

Figure 8.16 – The quality of fit between the z distribution predicted by NEUGEN and that measured by experiment when a normalisation scale factor is applied to the NEUGEN prediction.

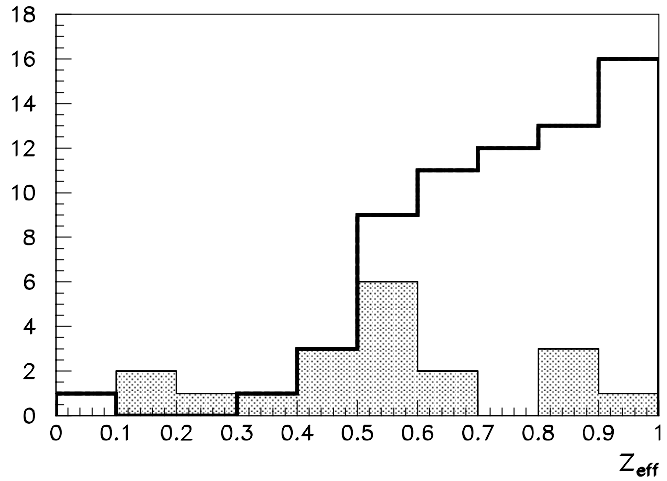

Figure 8.17 – Distributions of z_{eff} for the leading charged hadrons in the 69 ν_τ CC signal events (open histogram) and the 19 ν_μ background events (shaded histogram) that pass the $\tau \to \pi + X$ cuts.

The shapes of the two distributions are in good agreement although there is a factor of two difference between NEUGEN and measured data in the final bin of Figure 8.15 (z=0.9-1.0). The statistical and systematic errors on the data, however, are large in this bin. Figure 8.17 shows the distributions of z_{eff} for the leading charged hadrons in the 69 signal ν_τ CC signal events (open histogram) and the 19 ν_μ background events (shaded histogram) that pass the $\tau \to \pi + X$ cuts[12]. Both the signal and background distributions are broad although the signal events tend to have higher values of z_{eff}. Only one of the 19 background events lies in the bin with z_{eff} = 0.9-1.0 where the uncertainty in the background prediction is greatest. Uncertainties in the shape and normalisation of the z distribution for charged hadrons are therefore small in comparison to the size of the $\tau \to \pi + X$ signal expected for $\nu_\mu \to \nu_\tau$ oscillations with large mixing, which produces a signal to background ratio of

[12] $z_{eff} = E_h / \sum E_h$.

approximately 1:1. The comparison of hadro-production between NEUGEN and experimental data that is described in this section has therefore shown that this signal to background ratio has an uncertainty of less than ±10% at 90% confidence.

8.3.2 Electron contamination of track→star samples

The analysis presented above has focused on $\nu_\mu \to \nu_\tau$ oscillations. In certain three-flavour models, however, there will be large fractions of both ν_τ and ν_e in the beam. In the case of threefold maximal mixing [57], 22% of the beam will be ν_e and 22% will be ν_τ. The number of ν_τ interactions in the detector will be fewer because of the suppression of the ν_τ CC cross-section. For a two-year exposure, 82200 ν_μ interactions are expected in the far detector. In the case of maximal mixing and large Δm^2, there will be 82200×0.22×0.766 = 13852 ν_e CC interactions[13].

A set of 40635 ν_e CC Monte Carlo events, generated in 2 cm steel with 2 cm cells, were subjected to the cuts described above in order to check whether ν_e CC events represent a large contamination to the $\tau \to \pi + X$ signal. The results are shown in Table 8.2. Six of the 40635 events survive the cuts. There is a 10% probability of observing 9 events or more due to statistical fluctuations. The cuts in BARREL-FLIGHT space are effective in rejecting electron events because ν_e CC events are dense and tend to have large values of BARREL and FLIGHT. The table also shows the effectiveness of the Hough transform in rejecting this type of event since only 7 of 189 events passing previous cuts survive RMS75 < 10. For maximal mixing and large Δm^2, 36.8×4/9 = 16.3 track→star candidates from $\tau \to \pi + X$ interactions are expected with a ν_e CC contamination of less than 9×13852/40635 = 3.1 events at 90% C.L. In this worst case scenario, the ν_e fraction of the signal is at the level of ~

[13] $T = \sigma_{CC}/\sigma_{TOTAL} = 0.766$

CUTS	ν_e CC events
NO CUTS	27713
EVLENGTH<60	27710
EVLENGTH>20	16166
BARREL<5	640
FLIGHT>1.5	517
FLIGHT>1.17×BARREL-0.84	323
PLANEOCC>0.85	254
VBAR<1000	193
VFLI<1600	189
RMS75<10	7
STARHITS>30	7
$\text{Cos}\theta_z$>0.95	6

Table 8.2 – The effect of $\tau \to \pi + X$ cuts on ν_e CC events *after* fiducial and containment cuts have been applied. The effects of the cuts are cumulative.

20% or less. The recent CHOOZ result, which sets a limit on $\sin^2 2\theta$ of 0.18 at 90% C.L. for large Δm^2 [47], implies that the number of ν_e CC events that fake the track→star signature in a 20 kiloton year exposure of MINOS is expected to be less than 1.3 events at 90% C.L.

8.4 Effect of pulse height threshold on $\tau \to \pi + X$

In addition to neutrino-induced events, the MINOS detector will also record signals due to radioactive and electronic noise. These noise signals will generally be single hits with small pulse heights. They may present unrealistic demands on the readout electronics if they occur at too high a rate.

It may therefore be necessary to apply a pulse height threshold to events in the detector to reduce the noise rate to a manageable level. Hits with pulse heights below this threshold will be ignored. Figure 8.18 shows the distribution of pulse heights for 1000 ν_μ CC and NC events in 2 cm steel with 2 cm cells and liquid scintillator active detector elements. The broad maximum centred at seven photoelectrons represents the response of liquid scintillator to a minimum ionising particle. The pulse heights have not been corrected for attenuation.

Table 8.3 shows the effect of applying several pulse height thresholds to the $\tau \to \pi + X$ analysis. The second column represents the percentage of hits that are rejected when a particular threshold is applied. The third and fourth columns show the numbers of signal and background events expected in a two-year exposure for each value of the threshold. Column five shows the signal to noise ratio. The table shows that the sensitivity of

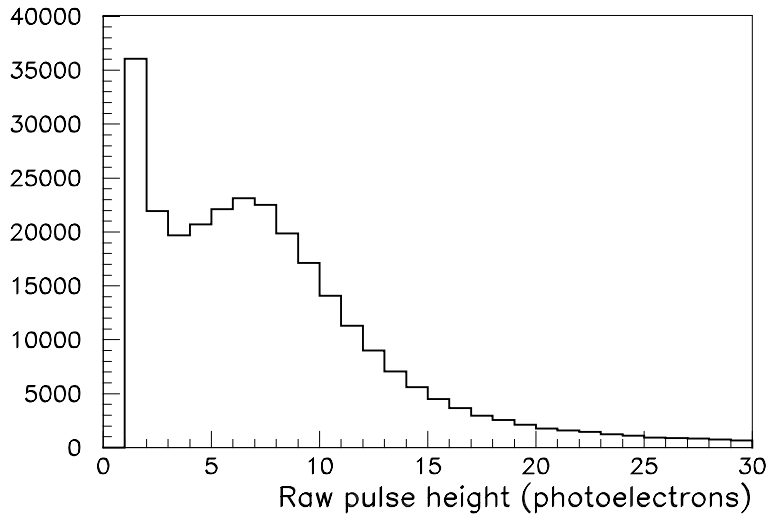

Figure 8.18 – Pulse height distribution for 1000 ν_μ CC and NC events in 2 cm steel with 2 cm cells and liquid scintillator active detectors.

Threshold	% hits rejected	2 year signal	2 year background	Signal/Noise
0	0	36.9	30.3	6.7
> 1 p.e.	12%	43.8	39.9	6.9
> 2 p.e.	20%	43.3	48.4	6.2
> 4 p.e.	34%	39.5	44.0	6.0

Table 8.3 – Effect of a pulse height threshold on the sensitivity of the $\tau \to \pi + X$ test to neutrino oscillations.

the $\tau \to \pi + X$ test is not strongly affected by the application of a pulse height threshold of up to four photoelectrons (equivalent to half a m.i.p.) in 2 cm steel. A four photoelectron threshold should be more than sufficient to reduce the noise rate in MINOS to an acceptable level, since any noise hits are generally expected with pulse heights of only one or two photoelectrons.

8.5 Sensitivity of $\tau \to \pi + X$ analysis to neutrino oscillations

It is possible to compute the sensitivity of the $\tau \to \pi + X$ test as a function of neutrino oscillation mixing parameters $\sin^2(2\theta)$ and Δm^2, given the $\tau \to \pi + X$ selection efficiency as a function of true neutrino energy. The solid line in Figure 8.19 shows the limit that could be set on neutrino oscillation parameters in 2 cm steel with 2 cm cells for a two-year exposure if the background expectation is assumed to be 30.3 events.

The 69 signal events obtained in 2 cm steel with 2 cm cells in section 8.2.6 corresponds to saturated oscillations (large Δm^2 and $\sin^2(2\theta)=1$). The number of signal and background events in a 2 year exposure are 36.8 and 30.3 respectively. Given these numbers, the 90% C.L. limit that can be set on $\sin^2(2\theta)$ is $\sin^2(2\theta) = 1.29 \times \sqrt{30.3} / 36.8 = 0.19$. To calculate the limit on $\sin^2(2\theta)$ for other values of Δm^2 it is necessary to predict the number of signal and background events for each Δm^2. The background sample consists

predominantly of ν_μ NC events and, since the number of neutral current interactions is independent of oscillations, the calculation that follows assumes that the background expectation is independent of Δm^2.

The number of ν_τ CC events flagged as track→star candidates by the cuts is given by:

$$N_{track \to star} = \int_0^\infty \phi(E_\nu)\sigma(E_\nu)\eta(E_\nu)\varepsilon(E_\nu)\sin^2(2\theta)\sin^2(1.27\Delta m^2 L / E_\nu)dE\,, \qquad (8.2)$$

where $\phi(E_\nu)$ is the ν_μ flux spectrum as a function of true neutrino energy, $\sigma(E_\nu)$ is the ν_μ CC interaction cross-section, $\eta(E_\nu)$ is the ratio of ν_τ CC/ν_μ CC cross-sections and $\varepsilon(E_\nu)$ is the efficiency of the cuts (as a function of E_ν) in selecting ν_τ CC events.

At large Δm^2 and $\sin^2(2\theta)$=1, 36.8 signal track→star events are obtained in a two-year exposure. Equation (8.2) then becomes:

$$\sin^2(2\theta)/2 \times \int_0^\infty \phi(E)\sigma(E)\eta(E)\varepsilon(E)dE = 36.8\,, \qquad (8.3)$$

where the term $\sin^2(1.27\Delta m^2 L / E_\nu)$ has been averaged to 1/2 since $\Delta m^2 L / E >> 1$.

The 90% C.L. limit on $\sin^2(2\theta)$ for any Δm^2 is obtained when the signal excess is equal to 1.29 multiplied by the square root of the background expectation. For a background of 30.3 events, this number is $1.29 \times \sqrt{30.3} = 7.1$. Substituting this result into equation (8.2) and rearranging yields:

$$\sin^2(2\theta)_{\min} = \frac{7.1}{\int_0^\infty \phi(E)\sigma(E)\eta(E)\varepsilon(E)\sin^2(1.27\Delta m^2 L / E)dE}. \qquad (8.4)$$

The quantity $\phi(E)\sigma(E)\eta(E)\varepsilon(E)$ in the above equation is simply the E_ν distribution of the set of ν_τ CC events that pass the $\tau \to \pi + X$ cuts. Therefore the integral in equation (8.4) can be replaced by a sum, over the 69 track→star events, of the weight $\sin^2(1.27\Delta m^2 L / E)$:

$$\sin^2(2\theta)_{\min} = \frac{7.1}{\sum_{i=1}^{69} A \times \sin^2(1.27\Delta m^2 L / E_i)}, \tag{8.5}$$

where A is a numerical factor that normalises the sum such that the denominator is equal to 36.8 for large Δm^2. This condition means that $69 \times A \times 1/2 = 36.8$ which yields $A = 1.07$. Therefore, the final expression for the 90% C.L. limit on $\sin^2(2\theta)$ for any Δm^2 is:

$$\sin^2(2\theta)_{\min} = \frac{7.1}{\sum_{i=1}^{69} 1.07 \times \sin^2(1.27\Delta m^2 L / E_i)}. \tag{8.6}$$

The limit plot (Figure 8.19) was obtained by simply evaluating equation (8.6) for a range of Δm^2 values and plotting the resultant limit on $\sin^2(2\theta)$. The wiggles at large Δm^2 in Figure 8.19 are due to the low statistics of the track→star sample.

Figure 8.19 shows that for Δm^2 greater than 0.01 eV^2, the $\tau \to \pi + X$ test in 2 cm steel with 2 cm cells could set a limit on $\sin^2(2\theta)$ of approximately 0.2. A signal of approximately five standard deviations could be observed for a 20 kiloton year exposure of MINOS if the Kamiokande atmospheric neutrino parameters ($\sin^2(2\theta) \sim 1$, $\Delta m^2 \sim 0.01$ eV^2) [41] are correct. In isolation this is not a particularly convincing discovery signal although, in conjunction with large signals from other tests, such as the NC/CC ratio and the ν_μ CC energy distribution etc, it would provide corroborating evidence for $\nu_\mu \to \nu_\tau$ oscillations. On the other hand, the value of Δm^2 is not well measured by atmospheric neutrino experiments and may well be larger than 0.01 eV^2. The $\tau \to \pi + X$ test has maximum sensitivity at $\Delta m^2 \sim 0.03$ eV^2, where a 9 or 10 standard deviation effect could be observed for $\nu_\mu \to \nu_\tau$ oscillations with $\sin^2 2\theta = 1$. The test is not sensitive, however, to the threefold

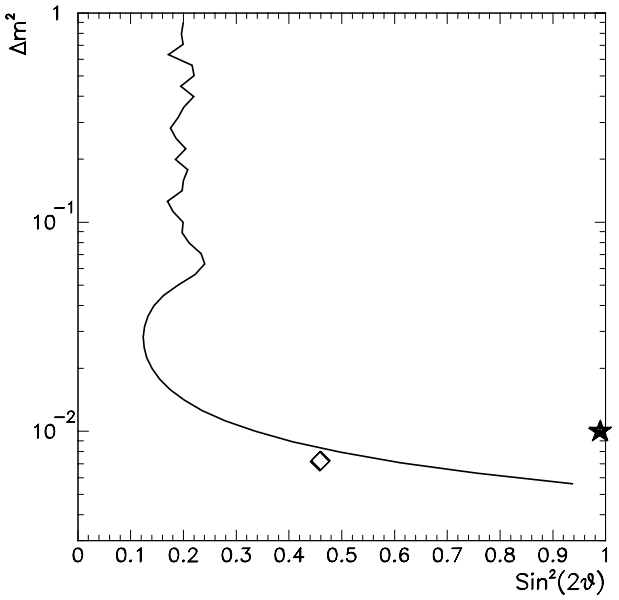

Figure 8.19 – Predicted 90% confidence limit that could be set in the mode $\nu_\mu \to \nu_\tau$ for a two-year run of MINOS in the WBB. The thick line shows the limit that could be set for a detector with 2 cm steel with 2 cm cells. The star corresponds to the Kamiokande best-fit point [41] and the diamond represents the Harrison, Perkins, Scott solution for threefold maximal mixing [57].

maximal mixing hypothesis of Harrison, Perkins and Scott ($\sin^2(2\theta) = 4/9$, $\Delta m^2 = 0.0072$ eV^2) [57] or the preliminary results from Super-Kamiokande which suggest a value of $\Delta m^2 \sim 2 \times 10^{-3}$ eV^2 [36].

8.6 Conclusions

The previous sections have shown that the mode $\tau \to \pi + X$ can provide a test of $\nu_\mu \to \nu_\tau$ oscillations in the Wide Band Beam. The track→star topology that forms the basis of the test is distinctive and is selected with high purity with the cuts detailed above. It has been shown that:

- a signal/noise ratio that is equivalent to ~ 6 standard deviations is expected in the configuration of 2 cm steel and 2 cm cells for a 20 kiloton exposure of MINOS;
- a signal to noise ratio of between 4 and 5 standard deviations is expected for the Kamiokande atmospheric neutrino parameters ($\Delta m^2 = 0.01$ eV^2 and $\sin^2 2\theta = 1$). The test has maximal sensitivity (signal/noise ~10) at $\Delta m^2 \sim 0.03$ eV^2 but is not sensitive to the low values of Δm^2 (~10^{-3} eV^2) suggested by the Super-Kamiokande atmospheric neutrino analysis.

The sensitivity of the $\tau \to \pi + X$ test has been evaluated for a number of possible configurations of the MINOS far detector. The detailed results are contained in Appendix B and the important conclusions are:

- the signal to background ratio is highest for a detector with 2 cm steel with 2 cm cells;

- the $\tau \to \pi + X$ sensitivity is not strongly affected by degrading the transverse granularity for a constant steel thickness;
- four centimetre steel with 2 co-ordinates per plane produces a similar signal to noise ratio to either of the 2 cm steel configurations;
- the configuration of 4 cm steel with 1 co-ordinate readout per steel plane is not favourable to the $\tau \to \pi + X$ analysis. Four centimetre steel configurations with 1D readout produce low signal to noise and signal to background ratios;
- using pulse height information instead of simply counting the number of hits improves the signal to background ratio, but not the sensitivity to neutrino oscillations;
- applying a pulse height threshold of up to four photoelectrons in configurations with liquid scintillator active detectors does not significantly affect the sensitivity of the $\tau \to \pi + X$ test to neutrino oscillations;
- aluminium proportional tube and fibre liquid scintillator active detector technologies have a comparable sensitivity to neutrino oscillations.

One possible weakness of this test is that it is very sensitive to the high energy tail of the leading pion momentum spectrum in ν_μ NC events. An error in this distribution could lead to a large increase in the background to $\tau \to \pi + X$. An estimate of the possible scale of this uncertainty has been obtained by comparing the output of NEUGEN to published data on hadron production. The results show that the scale of the uncertainty is not large enough to pose a significant problem if oscillations occur with large $\sin^2 2\theta$. The possible contamination of the track→star sample with ν_e CC events is small for any three-flavour

scenario with appreciable $\nu_\mu \to \nu_\tau$ mixing and is further constrained by the recent CHOOZ limit in the mode $\nu_\mu \to \nu_e$.

In summary, the $\tau \to \pi + X$ test is a method to search for $\nu_\mu \to \nu_\tau$ with $\Delta m^2 \geq 10^{-2}$ eV^2 and $\sin^2 2\theta > 0.2$ in the Wide Band Beam. The optimum detector configurations are 2 cm steel plates with 1D readout or 4 cm steel plates with 2D readout. APT and FLS active detector technologies produce the same results. Any detector configuration involving 4 cm steel plates and only 1D readout is not favourable to this analysis.

Chapter 9 Conclusions

9.1 Summary of results

The MINOS experiment has been designed with a baseline of 731 km and a mean neutrino interaction energy of 17 GeV. These parameters have been chosen to explore the region of neutrino oscillation parameter space suggested by the atmospheric neutrino anomaly.

The neutrino mixing parameters are not well measured by the atmospheric neutrino experiments if the anomaly is interpreted in terms of neutrino oscillations. The size of the discrepancy between the experiments and the Monte Carlo predictions indicates that the mixing matrix elements are large although flux uncertainties, large statistical errors and measurement errors on the direction of the incoming neutrino mean that it is difficult to distinguish between $\nu_\mu \rightarrow \nu_e$ and $\nu_\mu \rightarrow \nu_\tau$ oscillations. In addition, the value of Δm^2 is not well measured (it is uncertain to ±1 decade or more). This uncertainty in Δm^2 means that the average MINOS L/E might not be optimal to measure the mixing parameters responsible for the atmospheric neutrino anomaly. It is therefore essential that there is flexibility in the MINOS beam design, and that the capability exists to switch to a lower energy beam if required.

This thesis has shown how well the mixing parameters could be measured by MINOS if the atmospheric neutrino anomaly is due to neutrino oscillations. The most important (and convincing) measurement that MINOS could make is the observation of an

energy-dependent suppression of the ν_μ flux. For large mixing, this would be an unambiguous demonstration of neutrino oscillations. It has been shown in Chapter 4 that MINOS could provide a precision measurement of Δm^2 (< 10% error) if the true value lies between $0.005 < \Delta m^2 < 0.2$ eV^2 for the default WBB. The performance of a proposed low energy beam, which is designed to confront the new Super-Kamiokande atmospheric neutrino results, has been studied in Chapter 5. This beam allows a measurement of Δm^2 down to approximately 0.002 eV^2. Further results are needed before the optimal beam design for MINOS becomes clear. The results from atmospheric neutrino experiments are subject to large systematic uncertainties and they may not provide decisive information before 2002. The long-baseline K2K experiment, however, is expected to run in 1998-1999 and could see a statistically significant L / E dependent effect if $\Delta m^2 \sim 0.01$ eV^2.

The low energy beam has a much reduced flux compared to the default three horn WBB, which would limit the potential reach in parameter space. In addition, switching from the default beam design to the low energy beam would require a major redesign of the beam line and has serious implications for the COSMOS experiment (the number of neutrinos above tau production threshold and hence the sensitivity of COSMOS to $\nu_\mu \rightarrow \nu_\tau$ oscillations would be greatly reduced). It may be too late to implement the low energy beam for 2002 but it should remain an option as a possible upgrade path. For the three horn beam, work on reducing both the rate uncertainties to < 4% and the uncertainties in the prediction of the far detector spectrum for no oscillations to less than 20% of their current value would reduce parameter measurement errors and minimise the risk of observing spurious neutrino oscillation signals if the atmospheric neutrino anomaly is not explained by neutrino mixing.

The second important measurement that MINOS could make is of the matrix elements that relate the flavour and mass eigenstates. It has been shown in Chapter 6 that it is

possible to identify electron neutrino events in MINOS so a three-generation analysis of MINOS data is possible. The nature of the analysis depends on the results of other experiments and the value of Δm^2 measured by MINOS, as will be explained in the following section. A general three-flavour analysis involving six free parameters most easily explains the current data (although even this may be insufficient if the LSND result is confirmed) but an analysis of MINOS (or any other experiment) in this space is difficult. The analysis described in Chapter 7 assumes the simplifying one mass-scale dominance model. This model, which assumes a neutrino mass hierarchy that is similar to the charged leptons and quarks, is suggested by the results of the atmospheric and solar neutrino experiments. The analysis has indicated how well the parameters could be measured and has shown that, for any three-flavour mixing hypothesis, MINOS (or any other experiment with a single flavour beam) will at best isolate two solutions for the mixing matrix elements. This uncertainty is a fundamental property of three-generation mixing in the OMSD model. Since the CHOOZ result has effectively ruled out the prospect of observing large $\nu_\mu \rightarrow \nu_e$ mixing in MINOS, the role of MINOS (in addition to checking the CHOOZ result) is to measure or constrain the amount of $\nu_\mu \rightarrow \nu_e$ mixing. It has been shown in Chapter 7 that it is possible in principle to distinguish between two-generation $\nu_\mu \rightarrow \nu_\tau$ and three-generation mixing and still be consistent with the CHOOZ limit.

General three-flavour mixing allows for the possibility of leptonic CP violation. Chapter 7 has studied the prospects of observing a CP violating effect in MINOS. For favourable values of the parameters (threefold maximal mixing and both Δm^2's ~10^{-2} eV^2) it has been shown that the energy distributions of electron-like events for ν_μ and $\overline{\nu}_\mu$ runs are a more convincing demonstration of CP violation than the difference in oscillation probabilities. The prospects for observing CP violation, however, depend critically on the values of Δm^2 and the mixing matrix elements. MINOS could only observe CP violation if

both Δm^2's > 10^{-3} eV^2 and all the matrix elements are large. The prospects for this are not favourable due to the value of Δm^2 obtained by fits to solar neutrino results and the CHOOZ limit, which appear to rule out the prospects of observing any significant CP violation in MINOS for any three-flavour mixing scenario.

If the evidence from CHOOZ is combined with that from the atmospheric neutrino experiments then it appears that large $\nu_\mu \rightarrow \nu_\tau$ mixing is likely. If this is the case then it is important for MINOS to have the ability to detect tau leptons. Since MINOS is relatively coarsely grained, it is impossible to do this on an event by event basis. Chapter 8 describes a statistical method to observe tau leptons by relying on differences in event topologies between tau? hadrons and NC events (the major source of background). While this test has low efficiency ($\tau \rightarrow \pi\nu$ efficiency ~ 2%) and a signal to background ratio of one, it benefits somewhat from finer transverse and longitudinal granularity. Since the ratio of ν_τ / ν_μ charged-current cross sections depends on neutrino energy, the $\tau \rightarrow \pi$ analysis is strongly dependent on the value of Δm^2. If $\Delta m^2 \sim 10^{-3}$ eV^2 (as suggested by the preliminary Super-Kamiokande atmospheric neutrino results) then the $\tau \rightarrow \pi$ test will not observe a signal because almost all of the ν_τ are below tau production threshold. On the other hand, if $\Delta m^2 \geq 10^{-2}$ eV^2 then a five standard deviation or greater effect may be observed.

Figure 9.1 summarises many of the results presented in this thesis. The figure shows how the expected size of measurement errors and ν_τ appearance signals depend on the value of Δm^2 if oscillations are assumed with large $\sin^2 2\theta$. The top two lines in Figure 9.1 show the range of Δm^2 for which a precision measurement (< 10% error) of the mixing parameters is possible in the low energy beam, as described in Chapter 5. The lines assume neutrino oscillations with $\sin^2 2\theta = 0.7$ and a 20 kiloton year exposure of MINOS. The third and fourth lines show the range of Δm^2 for which a precision measurement is possible in the

three horn wide band beam for the ν_μ CC energy analysis that is described in Chapter 4. These lines assume neutrino oscillations with $\sin^2 2\theta = 0.7$ and a 3.3 kiloton year exposure of MINOS. The fifth and sixth lines are the analogue of the fourth and fifth lines for the ν_e appearance analysis that is described in Chapter 5. The bottom line shows the range of Δm^2 for which a five standard deviation or greater effect in the $\tau \rightarrow \pi$ analysis is expected, assuming an exposure of 20 kiloton years. All the lines assume that the number of events expected for no oscillations is perfectly known.

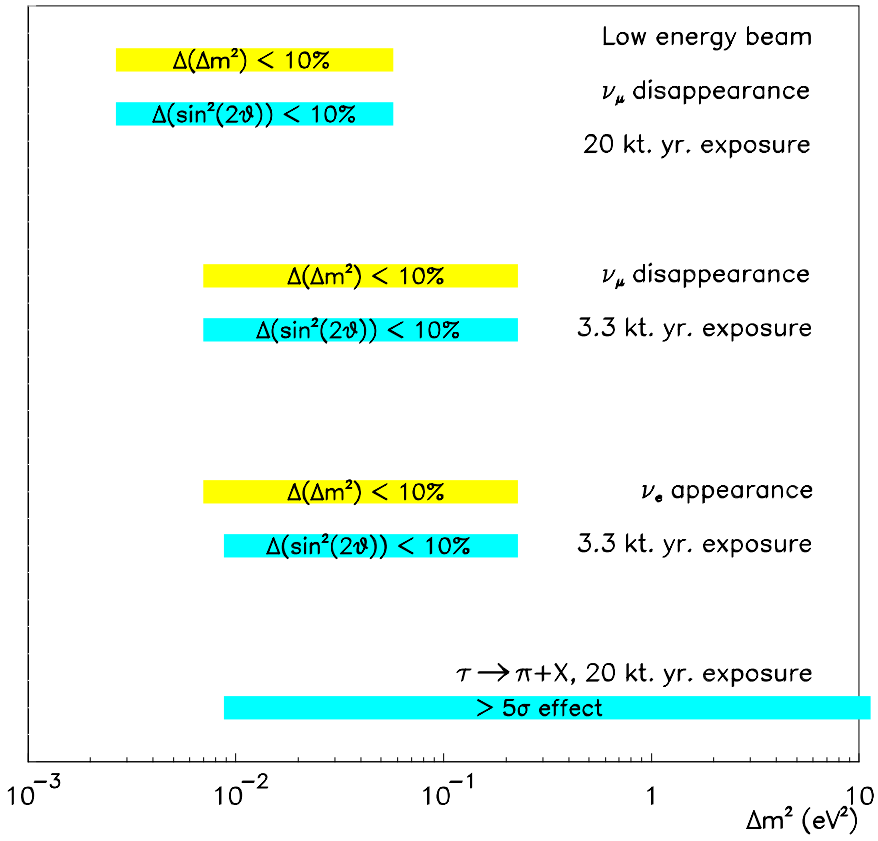

Figure 9.1 – A summary of the major results of this thesis. The lines are explained in the accompanying text.

The figure shows that, if the results of the three horn wide band beam and the possible low energy beam are combined, the MINOS experiment could measure the mixing parameters with < 10% errors if neutrino oscillations occur with $\sin^2 2\theta \geq 0.7$ and $0.003 \leq \Delta m^2 \leq 0.1$ eV^2. This range covers much of the region of parameter space suggested by the atmospheric neutrino anomaly although the low energy beam is vital for a measurement of the lowest values of Δm^2 suggested by the anomaly ($\Delta m^2 \sim 0.003$ eV^2). The $\tau \rightarrow \pi$ analysis can provide complementary information on the oscillation mode if $\Delta m^2 > 0.01$ eV^2.

It is clear that an all-encompassing fit that combines the energy information from the ν_μ and ν_e CC energy tests (and possibly the rate and energy information from the $\tau \rightarrow \pi$ test) in a three-generation framework will use the flavour and energy information from MINOS in the most efficient way and produce the smallest errors on the mixing parameters. The strategy of dividing the analysis into a number of discrete but complementary parts (Chapter 4-8 of this thesis) is useful in a) testing the no-oscillation hypothesis, b) measuring (or setting limits on) the mixing parameters and the oscillation mode and c) understanding and correcting for any sources of systematic error which may be different for the various analyses. The all-encompassing analysis can be performed in the future when the results of the simpler analyses are understood.

9.2 MINOS and neutrino oscillation phenomenology

This section briefly reviews the current experimental hints of neutrino oscillations and explains how they are related to the future results of MINOS. Four possible mixing scenarios are presented that can explain most, if not all, of these hints and the consequences of these scenarios for MINOS are discussed.

9.2.1 Recap of experimental hints for neutrino oscillations

The LSND excess

LSND observes an excess of events that are consistent with $\overline{\nu}_e$ CC interactions, as described in section 2.5.4. This can be explained by $\overline{\nu}_\mu \to \overline{\nu}_e$ oscillations with $P(\overline{\nu}_\mu \to \overline{\nu}_e) \sim 0.3\%$ [49]. Much of the allowed region in neutrino oscillation parameter space has been excluded by other experiments although a small region survives at $\Delta m^2 \sim 1$ eV^2 and $\sin^2 2\theta \sim 10^{-2}$.

The atmospheric neutrino anomaly

The anomalous flavour ratio of atmospheric neutrinos can be interpreted in terms of $\nu_\mu \to \nu_\tau$ or $\nu_\mu \to \nu_e$ oscillations with $\sin^2 2\theta \sim 1$ and $\Delta m^2 > 10^{-3}$ eV^2, as described in section 2.5.2. The $\nu_\mu \to \nu_e$ solution has recently been ruled out by the CHOOZ experiment which has set a limit of $\sin^2 2\theta < 0.18$ at 90% C.L. for $\nu_\mu \to \nu_e$ oscillations with $\Delta m^2 > 10^{-3}$ eV^2 [47].

The Kamiokande and Super-Kamiokande atmospheric neutrino experiments both observe that the flavour ratio of atmospheric neutrinos depends on the zenith angle, and hence L/E. The best-fit values of Δm^2 are $\Delta m^2 \sim 10^{-2}$ eV^2 for the Kamiokande data [41] and $\Delta m^2 \sim 2-3\times10^{-3}$ eV^2 for the Super-Kamiokande data [36]. The combined results of these two experiments suggest that Δm^2 lies in the range $10^{-3} < \Delta m^2 < 10^{-1}$ eV^2.

The solar neutrino problem

Five experiments observe a flux of solar neutrinos that is significantly lower than the prediction of the standard solar model (the suppression is between a factor of two and a

factor of four). The suppression of the neutrino flux also appears to depend on neutrino energy (as shown in Table 2.1).

These observations can be explained by $\nu_e \rightarrow \nu_x$ oscillations with large mixing strength. There are three possible regions of Δm^2:

1. $\Delta m^2 \sim 10^{-3}$ eV^2: this assumes vacuum oscillations with $\sin^2 2\theta \sim 1$. The suppression of neutrino flux is energy independent, and hence somewhat inconsistent with the results of Table 2.1, because:

$$\frac{\Delta m^2 L}{E} \sim \frac{10^{-3} \times 10^{11}}{1} >> 1.$$

2. $\Delta m^2 \sim 10^{-5}$ eV^2: this assumes MSW resonant neutrino oscillations, as described in section 2.5.1.2. Two solutions are possible; the small angle solution with a vacuum mixing angle of $\sin^2 2\theta \sim 10^{-2}$, and the large angle solution with $\sin^2 2\theta \sim 1$. The suppression of neutrino flux can be energy dependent and the current data is therefore well-described by these models.

3. $\Delta m^2 \sim 10^{-10}$ eV^2: this assumes vacuum oscillations with $\sin^2 2\theta \sim 1$. The value of Δm^2 is tuned to the Sun-Earth distance ($\Delta m^2 L / E \sim 1$) so the suppression of neutrino flux is energy dependent. This solution predicts a seasonal variation in the neutrino flux over and above that expected from the eccentricity of the Earth's orbit, as described in section 2.5.1.2.

9.2.2 Implications of current results for MINOS

LSND and MINOS

The LSND excess suggests $\overline{\nu}_\mu \rightarrow \overline{\nu}_e$ oscillations with $\Delta m^2 \sim 1$ eV^2 and $\sin^2 2\theta \sim 10^{-2}$. MINOS is expected to be sensitive to $\nu_\mu \rightarrow \nu_e$ oscillations with $\sin^2 2\theta > 3\times10^{-3}$ [72] and so the size of any possible $\nu_\mu \rightarrow \nu_e$ signal in MINOS from the LSND result is small.

If the value of Δm^2 from the LSND analysis is also responsible for the atmospheric neutrino anomaly (i.e. the anomaly is explained by $\nu_\mu \rightarrow \nu_\tau$ oscillations with $\Delta m^2 \sim 1$ eV^2 and $\sin^2 2\theta \sim 1$) then MINOS would observe a large suppression in the ν_μ CC event rate but would not be able to measure Δm^2 because the oscillation phase would be smeared out by experimental energy resolution (see section 4.5.3). This scenario would require the Kamiokande and Super-Kamiokande zenith angle distributions of atmospheric neutrinos to be wrong.

The atmospheric neutrino anomaly and MINOS

This has been discussed in detail in the preceding chapters of this thesis. If the atmospheric neutrino anomaly is due to neutrino oscillations and the CHOOZ result is taken into account then $\nu_\mu \rightarrow \nu_\tau$ oscillations with $\sin^2 2\theta \sim 1$ and $\Delta m^2 > 10^{-3}$ eV^2 are implied. In this case MINOS should see a large suppression of the ν_μ CC event rate and measure the mixing parameters to better than 10% accuracy, as demonstrated in Chapter 4.

The solar neutrino problem and MINOS

The solar neutrino data is well-described by neutrino oscillations with $\Delta m^2 \sim 10^{-5}(10^{-10})$ eV^2. These values of Δm^2 have implications for MINOS; they imply that, even if the atmospheric neutrino anomaly is explained by neutrino mixing with $\Delta m^2 \sim 10^{-2}$ eV^2, the expected CP violating amplitude in MINOS cannot be larger (and is expected to be much smaller) than $10^{-5}(10^{-11})/10^{-2} < 10^{-3}$ and is hence unobservable.

9.2.3 Implications for MINOS of possible neutrino oscillation scenarios

Several example neutrino oscillation scenarios that can explain most, if not all, of the hints that are summarised in section 9.2.1 are listed in Table 9.1. The values of the independent Δm^2's for each scenario are listed in the top row of the table. The table shows whether the scenarios can explain the three experimental hints of neutrino oscillations listed in the first column; the LSND excess, the atmospheric neutrino anomaly and the solar neutrino problem. It is also shown whether or not the scenarios are consistent with the zenith angle distribution of atmospheric neutrinos from Kamiokande and Super-Kamiokande. This is indicated by a tick or a cross in the fourth row of the table. The oscillation modes for each of the hints are shown in the table if they can be explained by the scenarios and a cross is shown if they cannot. The prospect of observing a CP violating in MINOS for each of the scenarios is shown in the sixth row of the table; a cross indicates that the predicted CP violating amplitude is unobservable in MINOS ($D_{\mu e} < 10^{-3}$). The seventh row suggests the appropriate analysis for MINOS; 'OMSD' means that the three-flavour one mass-scale dominance model can be adopted, '6 parameter' means that a generalised three-flavour framework with three mixing angles, a complex phase and two independent values of Δm^2 is necessary, and '> 3 flavour' means that a complex analysis involving the three standard generations plus a sterile neutrino is required.

	Scenario 1 $\Delta m^2_{32} \sim 0.01$ $\Delta m^2_{21} \sim 10^{-5}$ **or** (10^{-10})	**Scenario 2** $\Delta m^2_{32} \sim 1$ $\Delta m^2_{21} \sim 10^{-5}$	**Scenario 3** $\Delta m^2_{32} \sim 10^{-3}$ $\Delta m^2_{21} \sim 10^{-3}$	**Scenario 4** $\Delta m^2_{43} \sim 1$ $\Delta m^2_{32} \sim 0.01$ $\Delta m^2_{21} \sim 10^{-5}$ **or** 10^{-10}
LSND	×	$\overline{\nu}_\mu \rightarrow \overline{\nu}_e$	×	$\overline{\nu}_\mu \rightarrow \overline{\nu}_e$
Atmospheric neutrino anomaly	$\nu_\mu \rightarrow \nu_\tau$	$\nu_\mu \rightarrow \nu_\tau$	$\nu_\mu \rightarrow \nu_\tau$ 3 flavour	$\nu_\mu \rightarrow \nu_\tau$ or $\nu_\mu \rightarrow \nu_{sterile}$
Kamiokande and Super-K zenith angle distributions	✓	×	✓	✓
Solar neutrinos	$\nu_e \rightarrow \nu_\mu$ MSW or vacuum oscillations	$\nu_e \rightarrow \nu_\tau$ small angle MSW oscillations	Vacuum oscillations, three-flavour mixing	$\nu_e \rightarrow \nu_{\tau,sterile}$ MSW or vacuum oscillations
CP violation in MINOS	×	×	×	Possible [90]
MINOS analysis	OMSD	OMSD	6 parameter	> 3 flavour

Table 9.1 – Four possible neutrino oscillation scenarios.

Figure 9.2 shows how the values of Δm^2 chosen in the four scenarios correspond to the experimental data. The abscissa of the plot is L/E, which corresponds to $(\Delta m^2)^{-1}$. The labels below the axis show the regions of L/E that are relevant to the experimental hints for neutrino oscillations. There are two regions for solar neutrinos, corresponding to the MSW and vacuum oscillation solutions respectively. The thick line between $10 < L/E < 10^3$ km/GeV shows the region of Δm^2, and hence L/E, suggested by the Kamiokande and Super-Kamiokande zenith angle distributions of atmospheric neutrinos. The values of Δm^2 or L/E that explain the various experimental hints for the four scenarios are shown by the markers. If a marker for a particular hint is absent then the hint cannot be explained by the particular scenario (for example, scenario 1 cannot explain the LSND excess and hence the open circle, which represents LSND, is absent). In some scenarios (one and four), the solar neutrino problem can be solved by either of two values of Δm^2. The

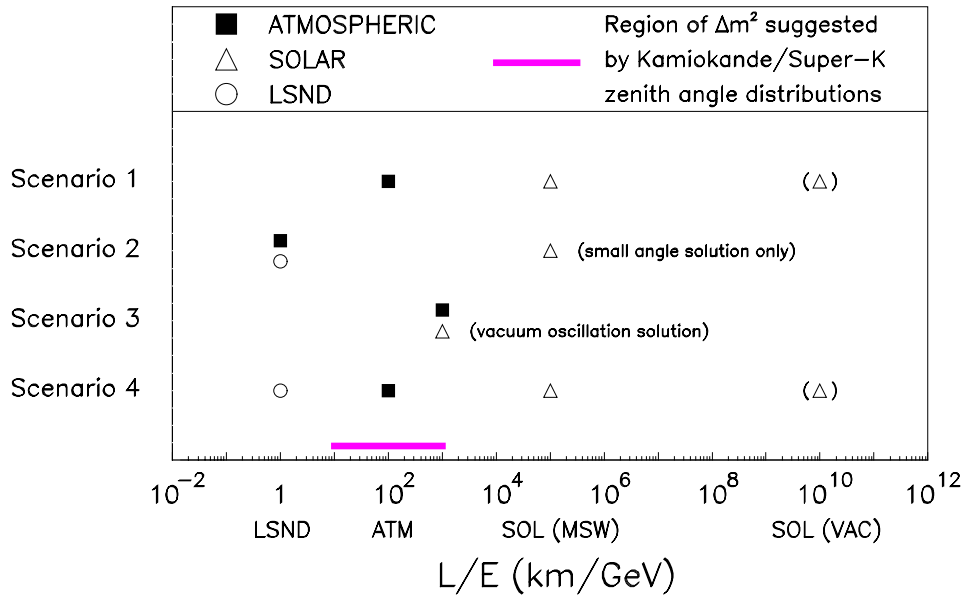

Figure 9.2 – The values of L/E (or $(\Delta m^2)^{-1}$) required to solve the experimental hints of neutrino oscillations, for the scenarios listed in Table 9.1.

second value of Δm^2 is indicated in parentheses for these cases. In scenario 2, the atmospheric neutrino anomaly is explained by oscillations with large Δm^2 (~ 1 eV^2) and the fact that the black square, which represents the atmospheric neutrino anomaly, is inconsistent with the range of L/E suggested by the zenith angle distributions of Kamiokande and Super-Kamiokande (the thick line) means that these distributions are assumed to be spurious in this model.

The first scenario can be regarded as the most plausible three-generation solution, given the current weight of evidence and assuming that the LSND excess is spurious. The second and third scenarios are other three-generation solutions that require at least one piece of evidence for neutrino oscillations to be wrong. The fourth scenario assumes that three independent mass-scales are required to explain all the data. This requires at least four neutrino generations. All of the scenarios assume that the atmospheric neutrino anomaly is genuine and therefore a large neutrino oscillation effect is expected to be observed in MINOS. If the neutrino masses are strongly ordered ($m_3 >> m_2 >> m_1$), as suggested by the charged lepton and quark sectors, then scenarios 2 and 4 imply neutrino masses that are cosmologically interesting ($m_\nu \sim 1$ eV^2). If the masses are degenerate, then all the scenarios may imply that neutrinos possess a significant fraction of the mass density of the universe.

The detailed predictions and consequences of the four scenarios are described in the following sections.

Scenario 1: LSND spurious, hierarchical mass spectrum

$$\Delta m^2_{32} \sim 10^{-2} \text{ eV}^2, \Delta m^2_{21} \sim 10^{-5} (10^{-10}) \text{ eV}^2$$

LSND: the LSND excess is assumed to be spurious.

ATMOSPHERIC: the atmospheric neutrino anomaly is explained by $\nu_\mu \rightarrow \nu_\tau$ oscillations with $\Delta m^2 \sim 10^{-2}$ eV^2 and $\sin^2 2\theta \sim 1$.

SOLAR: the solar neutrino problem is solved by either MSW enhanced neutrino oscillations with $\Delta m^2 \sim 10^{-5}$ eV^2 (large or small angle solution) or vacuum oscillations with $\Delta m^2 \sim 10^{-10}$ eV^2 and $\sin^2 2\theta \sim 1$. The suppression of solar neutrino flux can (in principle) be energy dependent.

MINOS ANALYSIS STRATEGY: the values of the two independent Δm^2's allows the one mass-scale dominance (OMSD) model to be applied. MINOS is expected to observe large $\nu_\mu \rightarrow \nu_\tau$ mixing and small or zero $\nu_\mu \rightarrow \nu_e$ mixing, due to the CHOOZ result.

CP VIOLATION: the values of Δm^2 assumed here rule out the possibility of observing a CP violating amplitude in MINOS.

Scenario 2: Large Δm^2 atmospheric neutrino oscillations, hierarchical mass spectrum

$$\Delta m^2_{32} \sim 1 \text{ eV}^2, \Delta m^2_{21} \sim 10^{-5} \text{ eV}^2$$

LSND: the LSND excess is explained by $\bar{\nu}_\mu \rightarrow \bar{\nu}_e$ oscillations with $\Delta m^2 \sim 1$ eV^2 and $\sin^2 2\theta \sim 10^{-2}$.

ATMOSPHERIC: the atmospheric neutrino anomaly is explained by $\nu_\mu \rightarrow \nu_\tau$ oscillations with $\Delta m^2 \sim 1$ eV^2 and $\sin^2 2\theta \sim 1$. This value of Δm^2 is not consistent with the zenith angle distributions of atmospheric neutrinos observed by the Kamiokande and Super-Kamiokande experiments and they are thus assumed to be spurious.

SOLAR: the solar neutrino problem is solved by $\nu_e \to \nu_\tau$ oscillations with $\Delta m^2 \sim 10^{-5}$ and $\sin^2 2\theta \sim 10^{-2}$ (the small angle MSW solution). The suppression can be energy dependent.

MINOS ANALYSIS STRATEGY: the OMSD model can be applied in this case. The value of Δm^2 is too large to be measured directly by MINOS but large effects will be seen in many of the MINOS oscillation tests. The $\tau \to \pi + X$ test is also expected to yield a six standard deviation effect here.

CP VIOLATION: the value of Δm^2 required to solve the solar neutrino problem rules out the possibility of observing CP violation in MINOS.

Scenario 3: LSND spurious, non-hierarchical mass spectrum

$$\Delta m^2_{32} \sim 10^{-3}\ \text{eV}^2,\ \Delta m^2_{21} \sim 10^{-3}\ \text{eV}^2$$

LSND: the LSND excess is assumed to be spurious.

ATMOSPHERIC: the atmospheric neutrino anomaly is explained by neutrino oscillations with $\Delta m^2 \sim 10^{-3}\ \text{eV}^2$ and large mixing. The oscillation mode ($\nu_\mu \to \nu_e$, $\nu_\mu \to \nu_\tau$ or three-flavour mixing) is not constrained because the value of Δm^2 is below the limit set by the CHOOZ experiment. The value of Δm^2 is consistent with the Super-Kamiokande zenith angle distribution and marginally consistent with that for Kamiokande.

SOLAR: the solar neutrino problem is solved by vacuum oscillations with $\Delta m^2 \sim 10^{-3}\ \text{eV}^2$ and large mixing (the oscillation mode is not constrained). This solution predicts that the oscillation probability is energy independent and so is somewhat inconsistent with the current solar neutrino data (as shown by Table 2.1).

MINOS ANALYSIS STRATEGY: since the two values of Δm^2 are comparable and both are (marginally) within the MINOS range of sensitivity, the OMSD model cannot be assumed and a generalised three-flavour analysis that involves six free parameters must be performed. The dependence of the oscillation probabilities on neutrino energy will be complex due to interference between the two Δm^2's. The proposed low energy beam for MINOS will be required to measure Δm^2.

CP VIOLATION: the CP violating amplitude that could be observed in MINOS if this scenario is assumed has been calculated in section 7.5 to be less than 10^{-3} and therefore unobservable.

Scenario 4: Three mass-scales, hierarchical mass spectrum

$$\Delta m^2_{43} = 1 \text{ eV}^2,\ \Delta m^2_{32} = 10^{-2} \text{ eV}^2,\ \Delta m^2_{21} = 10^{-5}(10^{-10}) \text{ eV}^2$$

LSND: the LSND excess is explained by $\bar{\nu}_\mu \to \bar{\nu}_e$ oscillations with $\Delta m^2 \sim 1$ eV^2 and $\sin^2 2\theta \sim 10^{-2}$.

ATMOSPHERIC: the atmospheric neutrino anomaly is explained by neutrino oscillations with $\Delta m^2 \sim 10^{-2}$ eV^2 and $\sin^2 2\theta \sim 1$. Oscillations in the mode $\nu_\mu \to \nu_\tau$ or $\nu_\mu \to \nu_s$ are possible, where ν_s is a sterile neutrino.

SOLAR: the solar neutrino problem can be solved by MSW or vacuum oscillations with $\Delta m^2 \sim 10^{-5}$ or $\Delta m^2 \sim 10^{-10}$ eV^2. An energy-dependent suppression of the neutrino flux is possible. It is possible to solve the solar neutrino problem with $\nu_e \to \nu_\tau$ or $\nu_e \to \nu_s$ oscillations.

MINOS ANALYSIS STRATEGY: this scenario assumes three independent mass scales so neither the OMSD model nor a generalised three-flavour framework can be assumed. A complex analysis involving four neutrino flavours (the three normal generations plus a sterile neutrino) which uses the oscillation probabilities observed by MINOS together with results from other experiments is therefore necessary.

CP VIOLATION: it has been shown [90] that the constraints on observing CP violation that are studied in section 7.5 are relaxed and a large CP violating effect could be observed in MINOS.

9.3 Implications of MINOS results

This thesis has demonstrated that it is possible to accurately measure the mixing parameters in MINOS if a large oscillation effect exists. It is interesting to consider what these results would imply for the underlying physics.

There are many theoretical models of neutrino mass and mixing that attempt to explain the current neutrino oscillation data in a consistent framework, for example [99][100][101][102] and the models described in [91]. This proliferation of models is due in part to the relative freedom in constructing physics beyond the Standard Model and also because the mixing parameters are not well-established by current experimental data. This second point is obviously an area in which MINOS could make a significant contribution. It is important to note that the models suppose that the current experimental hints of neutrino oscillations are in fact genuine effects. Many models assume the best-fit parameters from the Kamiokande atmospheric neutrino analysis ($\Delta m^2 \sim 0.01$ eV^2 and $\sin^2 2\theta \sim 1$ [41]) are correct and, although the recent Super-Kamiokande result is suggestive of oscillations [36], it cannot

be said that the parameters (especially Δm^2) have been *measured* by either experiment. This thesis has shown that MINOS would be able to convincingly demonstrate the existence of neutrino oscillations with these parameters and measure the values of Δm^2 and $\sin^2 2\theta$.

Once oscillations have been established, the more detailed predictions of the models can be tested. This will be carried out by a number of experiments, including MINOS. The most recent models, for example [99], assume that the LSND effect, the atmospheric neutrino anomaly and the solar neutrino problem are all due to neutrino oscillations. This scenario is most easily explained by the mixing of four neutrino species (the three standard generations plus a sterile neutrino). A three-generation solution can be found although this requires that the atmospheric neutrino anomaly is due to large Δm^2 oscillations [56]. This result will be completely checked by MINOS, which can provide a direct measurement of Δm^2 up to 0.2 eV^2 and can also indicate whether Δm^2 is larger than this value.

The LSND result will be checked by the KARMEN experiment within the next few years and this will indicate whether three-generation or four-generation mixing models are appropriate. Several of the four-generation models make different predictions for the oscillation mode responsible for the atmospheric neutrino anomaly. This freedom is due to the poor discrimination between $\nu_\mu \rightarrow \nu_\tau$ and $\nu_\mu \rightarrow \nu_e$ oscillations offered by atmospheric neutrino experiments. The recent CHOOZ result [47] has already ruled out several mixing schemes that predict large $\nu_\mu \rightarrow \nu_e$ mixing for atmospheric neutrinos [57][102]. MINOS, which will have electron and tau identification abilities, will also be in a situation to discriminate between models that predict large $\nu_\mu \rightarrow \nu_\tau$ mixing [100][101] and those that

predict large $\nu_\mu \rightarrow \nu_s$ mixing, where ν_s is a sterile neutrino[14] [99]. MINOS should also be able to probe $\nu_\mu \rightarrow \nu_e$ mixing below the CHOOZ limit and provide further constraints on possible oscillation models.

The spectrum of neutrino masses is not well-determined by current experiments. MINOS will be able to measure or constrain the value of one Δm^2 but, since a measurement of Δm^2 is only sensitive to the *differences* between neutrino mass eigenstates, this does not automatically distinguish between models with a strongly-ordered see-saw mass hierarchy or models with almost degenerate neutrino masses. It has recently been pointed out, however, [103] that neutrino oscillation experiments can provide strong constraints on the mass of possible Majorana neutrinos (even though oscillations do not distinguish between Dirac and Majorana neutrinos). The effective Majorana mass, $|\langle m \rangle|$, which is proportional to the matrix element for double-beta decay, is related to the matrix element U_{e3}^2 and the value of Δm^2 by the following expression, if the neutrino masses are strongly-ordered [103]:

$$|\langle m \rangle| \approx |U_{e3}|^2 \sqrt{\Delta m^2} \,. \tag{9.1}$$

An analysis of current neutrino oscillation data sets a limit of $|\langle m \rangle| < 3 \times 10^{-2}$ eV [103]. This limit depends on the value of Δm^2 and can therefore be further refined if a precision measurement of Δm^2 is made by MINOS together with a measurement or limit on the matrix element U_{e3}^2 from a search for $\nu_\mu \rightarrow \nu_e$ oscillations. Future double-beta decay experiments are only sensitive to $|\langle m \rangle| > 10^{-1}$ eV so if they observe a signal the pattern of neutrino masses is not hierarchical and the masses cannot be generated by the see-saw mechanism [103].

---

[14] If $\nu_\mu \rightarrow \nu_s$ oscillations occur with $\Delta m^2 \sim 10^{-2}$ eV^2 and $\sin^2 2\theta \sim 1$ then MINOS is expected to observe a large, energy dependent, suppression of the ν_μ flux (as shown in the bottom-right plot of Figure 4.12) but no electron or tau appearance signals.

It is therefore clear that MINOS will be able to provide important information which will a) either establish or refute neutrino oscillations with parameters similar to those suggested by the Kamiokande atmospheric neutrino analysis; b) measure or set limits on the oscillation parameters which will test current models of neutrino mass and mixing and possibly indicate what lies beyond the Standard Model and c) indicate (when combined with the results of other experiments) what future experiments should be performed to further explore neutrino oscillation parameter space.

In conclusion, the future results of MINOS, in particular the ability to measure the mixing parameters, as described in this thesis, are of central relevance to the resolution of the atmospheric neutrino problem. The outcome of a search for neutrino oscillations in MINOS, whether positive or negative, will have far-reaching consequences for neutrino oscillation phenomenology.

Appendix A The Hough Transform

The Hough transform is used in Chapter 5 and Chapter 8 to find tracks in GMINOS simulated neutrino interactions. In Chapter 5 the transform is used to identify ν_μ CC events in the putative low energy neutrino beam and in Chapter 8 it is used to search for pion tracks in $\tau \to \pi + X$ events.

The definition of the Hough transform and its application in this thesis is described in section 5.2. The purpose of this appendix is to justify and study the performance of the Hough transform as a track finding algorithm in MINOS.

The Hough Space

Recall that the Hough transform defined in equation (5.1):

$$H(m,c) = \sum_{hits} \Delta(y_i - mx_i - c),$$

transforms two-dimensional co-ordinates in MINOS events into lines in m, c, or Hough, space. If the points in x, y space form a straight line, the lines in Hough space will converge at a particular value of m and c. The presence of a peak in the Hough space of an event is therefore a signal that the event contains a straight track.

The dimensions of the Hough space are the same in both physics analyses presented in this thesis. The Hough space must be large enough to intercept all the lines that result from the co-ordinates in a typical MINOS event. The value of m, or gradient, ranges from –1 to +1 in Hough space. This corresponds to an angle relative to the z axis of ±45° (the beam is

orientated at an angle of +3° relative to the positive z axis). Pions from $\tau \to \pi + X$ events and muons from ν_μ CC events tend to be within 20° of the positive z axis. The value of c, or intercept, ranges from –200 to +200 cm. This is several times larger that the expected transverse size of a typical neutrino interaction in MINOS (~1 m). This range also allows for an error of ±1 metre in the x or y vertex position of an event without affecting the efficiency of the transform.

The Hough space used in this thesis is a two-dimensional histogram with $n \times n$ bins. The bin size must be small enough to ensure that the overlap between lines in Hough space due to points with different co-ordinates in x, y space is always small. On the other hand, the effects of coulomb scattering and magnetic bending may result in lines that do not overlap at a single accumulation point in Hough space if the bin size is *too* small. It is important to note that the speed of any selection algorithm based on the Hough transform depends on the number of bins used in Hough space. The time to fill the Hough space is proportional to $N_{hits} \times n$, where n is the number of bins in each dimension of Hough space and N_{hits} is the number of hits in the event. The time to scan the Hough space for the presence of an accumulation point is proportional to n^2. The choice of bin size in general applications is therefore a trade-off between accuracy, which increases with larger n, and speed, which decreases with larger n. The accuracy of the Hough transform as a function of the bin size is discussed below in the context of MINOS, where the low trigger rate does not place a premium on the speed of the track finding algorithm.

Track estimator RMS75

Section 5.2 explains how the estimator RMS75 is defined for both the $x-z$ and the $y-z$ Hough spaces that result from the two orthogonal views of a GMINOS simulated neutrino interaction. The condition RMS75 < 10 must hold for an event to be classified as a track in a 160×160 bin Hough space. The requirement on RMS75 must scale as a function of the number of bins in order for the size of the peak to be a constant fraction of the area of the total Hough space. Specifically:

$$RMS75 < \sqrt{\frac{n}{160}} \times 10, \tag{A.1}$$

where n is the number of bins in each dimension of Hough space. The following conditions are therefore required in order to flag the presence of a track in an event:

- 20×20 bin Hough space → RMS75 < 3.5;
- 40×40 bin Hough space → RMS75 < 5;
- 80×80 bin Hough space → RMS75 < 7.1;
- 160×160 bin Hough space → RMS75 < 10;

A less restrictive cut of RMS75 < 10 is applied to the 40×40 bin Hough space used in the low energy ν_μ CC analysis in Chapter 5 in order to maximise the efficiency of the selection algorithm for low momentum muon tracks.

Efficiency as a function of track length

In Chapter 5 the Hough transform is used to search for muon tracks in simulated low energy neutrino interactions in MINOS. The typical muon energy in these events is approximately 2.5 GeV, which corresponds to a track length of about 3.8 m in a detector with 2 cm steel plates and a 3 cm gap between successive planes. The shortest track length that is used in the analysis is 50 cm. In Chapter 8 the transform is used to search for high momentum pion tracks that are common to $\tau \to \pi + X$ events. The length of these tracks is governed by the nuclear interaction length in steel and the pion tracks are typically 30 to 40 cm in length. The bin size in Hough space must be chosen so that tracks with these lengths are selected with high efficiency.

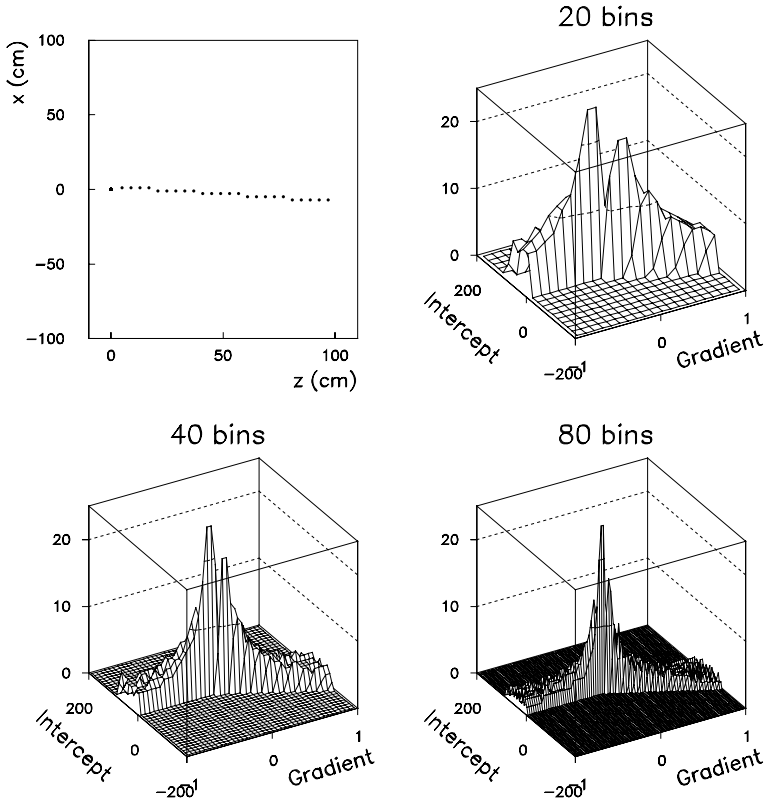

Figure A.1 – The Hough spaces of a 100 cm track (top-left plot) for different bin sizes.

A simple track generator has been written to investigate the efficiency of the Hough transform as a function of track length. The generator assumes a detector with 2 cm thick passive planes interleaved with planes of 2 cm × 2 cm active detectors. The detectors are assumed to be 100% efficient. The effects of coulomb scattering and magnetic bending are not modelled; these are studied below using `GMINOS` simulated events.

The top-left panel of Figure A.1 shows a track generated with the simple generator. The track is 100 cm long and is orientated at an angle of -5° relative to the positive z axis. The other three panels show the Hough space of this event with 20×20, 40×40 and 80×80 bins respectively. The Hough spaces show that the peak becomes narrower and more pronounced when the number of bins is increased. This is because co-ordinates that are in close proximity in x, y space produce lines in Hough space that are also close together. The lines will fall in the same bins in Hough space if the binning is coarse and the peak will be broader as a result.

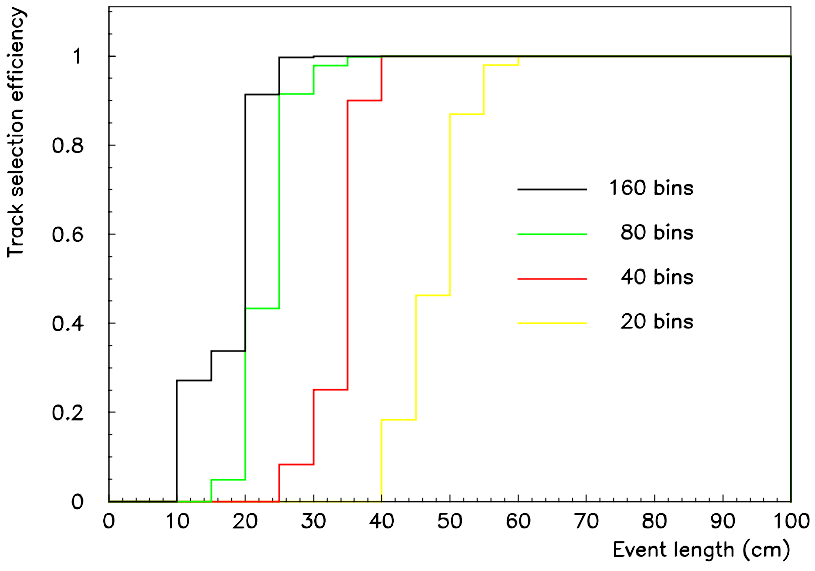

Figure A.2 – The track finding efficiency as a function of event length and Hough space bin size for 10000 generated tracks.

Figure A.2 shows the efficiency of the track finding algorithm (Hough transform followed by a cut on RMS75) as a function of event length and bin size in Hough space. Four samples of 10,000 events (one sample for each bin size) were generated with a flat event length distribution between 10 and 100 cm and orientated within ±30° relative to the positive z axis). The vertices of the events are assumed to be perfectly known.

The figure shows that the algorithm is 100% efficient at finding tracks that are longer than 70 cm, even for a Hough space with 20×20 bins. The advantage of fine binning in Hough space is apparent for short tracks; it is impossible to identify tracks that are shorter than 40 cm with a 20×20 Hough space. A 160×160 Hough space retains some efficiency for tracks that are only 10 cm in length. The cut-off in efficiency for short tracks that is evident from Figure A.2 is due to lines from different co-ordinates in x, y space falling in the same bins in Hough space. This effect is less pronounced if finer bins are used and hence the cut-off occurs at shorter track length. The overall selection efficiencies, integrated over all track lengths, are the following: 58.2% (20×20 bins), 73.9% (40×40 bins), 85.8% (80×80 bins) and 91.5% (160×160 bins).

These results suggest that the $\tau \to \pi + X$ analysis, which deals with tracks that are 30 to 40 cm in length, should use 80×80 or 160×160 bins in Hough space. The ν_μ CC analysis for low energy events is concerned with track lengths that are greater than 50 cm. A Hough space with 40×40 bins is therefore adequate.

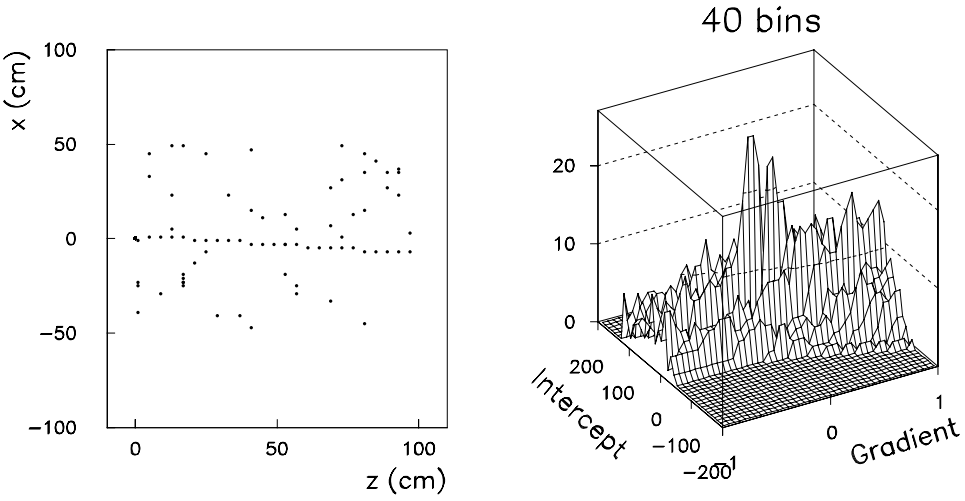

Figure A.3 – The track from Figure A.1 with 50 randomly generated noise hits.

Effect of detector noise

The Hough transform, which examines the macroscopic structure of events, is expected to be less sensitive to noise and gaps in tracks than algorithms such as least squares fitting, that examine the microscopic structure of events. The effect of noise on the efficiency of the Hough transform is studied by generating noise hits randomly with co-ordinates –50 cm < x < 50 cm and 0 < z < 100 cm on top of the tracks produced by the simple track generator.

The left-hand plot of Figure A.3 shows the same event as Figure A.1 with 50 randomly generated noise hits. The distribution of lines in Hough space produced by the noise hits is roughly flat between –1 < *gradient* < +1 and –50 cm < *intercept* < +50 cm. The right-hand plot shows that the peak in Hough space due to the track is less distinct as a result.

The average track selection efficiencies as a function of the number of bins in Hough space and the number of noise hits in each event are shown in Table A.1. As in the previous section, 10,000 events with 10 cm < *event length* < 100 cm and -30° < θ_z < 30° are generated for each scenario.

The general features of Table A.1 are that the presence of noise degrades the efficiency of the Hough transform and that the degradation is less pronounced as the number of bins in Hough space is increased. The table shows that, even for a severe noise rate of 50 hits in a 1 m^3 region, the Hough transform is still >60% efficient at finding tracks if 40×40 or more bins are used. The efficiency appears to *increase* if ten noise hits are present when 80×80 bins or less are used. This paradoxical result occurs for very short tracks which produce indistinct peaks in Hough space. There is a small probability that the line in Hough space from a random hit could overlap with this peak and hence reduce `RMS75` to a point whereby the event is classified as a track. This effect diminished as the bin size is reduced and is in any case outweighed by the negative effects of more noise hits as the noise rate is increased.

# bins	No noise	10 noise hits	50 noise hits	100 noise hits
20×20	58.2%	60.9%	43.8%	24.0%
40×40	73.9%	77.7%	62.3%	43.8%
80×80	85.8%	86.7%	73.4%	59.1%
160×160	91.5%	90.4%	77.8%	64.7%

Table A.1 – Average track selection efficiencies as a function of the noise rate.

Effect of Coulomb scattering and magnetic bending

Multiple coulomb scattering and magnetic bending change the angle of a track and will therefore broaden the resulting peak in Hough space. These effects depend on muon momentum and hence track length. If the Hough space is finely binned, these effects may smear the peak from a track to such an extent that the event fails the RMS75 cut. It is therefore expected that Hough spaces with coarse binning are less sensitive to the effects of magnetic bending and coulomb scattering.

The left-hand plot of Figure A.4 shows a GMINOS neutrino interaction in which the muon track is deflected by the influence of a magnetic field. The right-hand plot shows the Hough space of this event for 80×80 bins. The smearing of the accumulation point is clearly seen.

GMINOS events have been used to investigate how the effects of magnetic bending and multiple scattering affect the efficiency of the Hough transform as a track-finding algorithm. The low energy beam sample from Chapter 5, which contains a significant

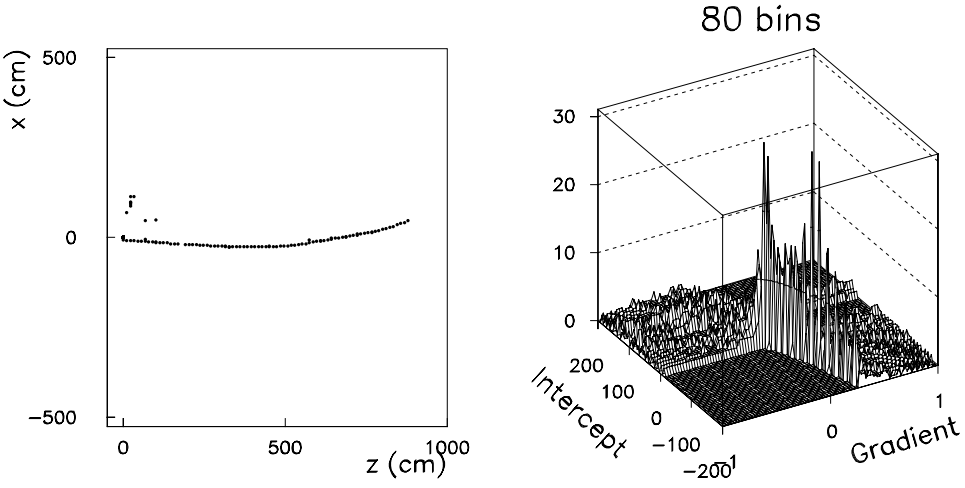

Figure A.4 – A GMINOS simulated neutrino interaction showing the effect of magnetic bending.

fraction of quasi-elastic ν_μ CC events, has been used with the following cuts:

- ν_μ CC interaction;
- event is contained within detector volume;
- event length < 100 planes in 2 cm steel;
- event is quasi-elastic ($E_{hadrons}$ < 0.5 GeV).

A sample of 3415 neutrino interactions pass these cuts.

Figure A.5 shows the track selection efficiency as a function of event length and the number of bins in Hough space for these events. The detector configuration that is used to generate these events is 2 cm steel plates with 2 cm pitch liquid scintillator active detectors. The distance between successive active detector planes is approximately 5 cm so the x axis

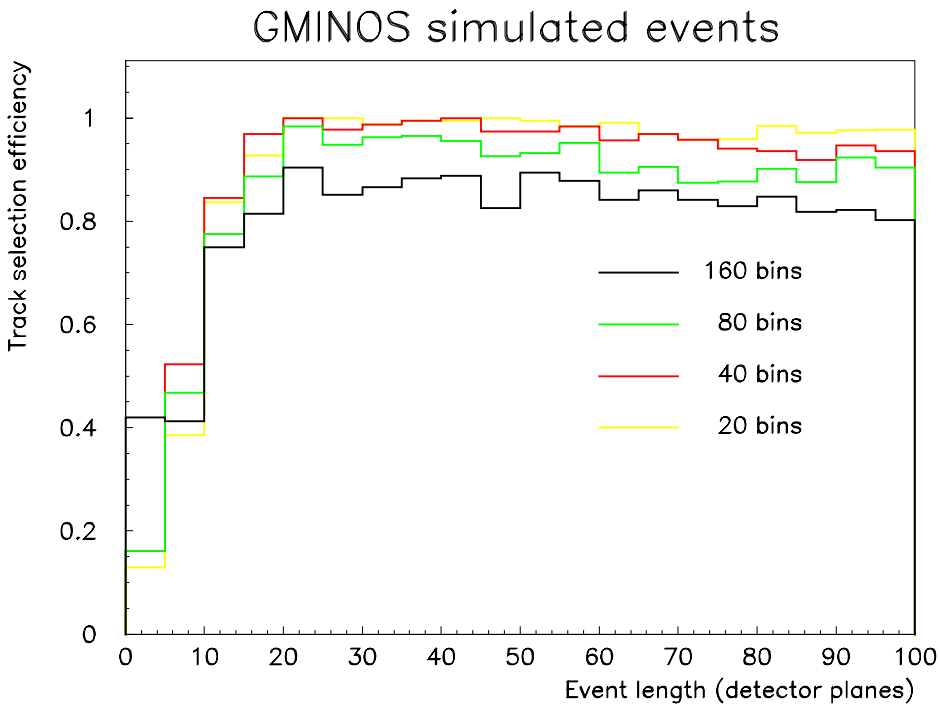

Figure A.5 – Track selection efficiency as a function of event length for GMINOS events.

scale is 0 to 500 cm, rather than the 0 to 100 cm scale used in Figure A.1. The plot shows that fine bins give the best efficiency for short (< 15 planes) events and that coarse bins give the best efficiency for long (> 30 planes) events. Figure A.1 showed that fine bins are intrinsically more efficient for short tracks but Figure A.5 shows that they are more susceptible to the effects of magnetic bending, especially for long tracks.

Table A.2 shows the average efficiencies integrated over all event lengths (second column) and for events shorter than 100 cm (third column). The third column should be compared to the results of the simple track generator in Table A.1. It shows that the efficiency of the track finding algorithm for Hough spaces with 80×80 bins or greater is degraded for tracks < 100 cm when the effects of coulomb scattering and magnetic bending are included.

# bins in Hough space	All events	Event length< 100 cm
20×20	94.9%	66.0%
40×40	93.8%	71.9%
80×80	89.3%	65.7%
160×160	82.8%	63.5%

Table A.2 – Average track selection efficiencies for a sample of GMINOS neutrino interactions.

Conclusions

The performance of the Hough transform as a track finding algorithm has been studied and the following conclusions have been drawn:

- the selection efficiency for straight tracks improves as the number of bins in Hough space is increased. This is especially true for short (< 40 cm) tracks;
- the transform can still function in the presence of large noise rates. Hough spaces with finer binning are less susceptible to the effects of noise;
- the effects of magnetic bending and multiple scattering favour coarse bin sizes.

The ν_μ CC analysis at low neutrino energy in Chapter 5 uses the Hough transform to identify tracks that are greater than 50 cm in length and are typically 2-3 metres. The analysis uses a 40×40 bin Hough space. The choice of 40 bins results in a greater efficiency to short tracks than 20 bins (improving the sensitivity to low values of Δm^2) and is less sensitive to the effects of magnetic bending than either 80 or 160 bins.

The $\tau \to \pi + X$ analysis uses the Hough transform to identify pion tracks that are between 20 cm and 1 metre in length. The analysis uses a 160×160 bin Hough space. The choice of 160 bins provides the greatest sensitivity to short (< 40 cm) tracks and the pion tracks are short enough to ensure that the effects of magnetic bending are not a problem. The analysis could work equally well with 80×80 bins although a 160 bin Hough space is slightly more robust to the effects of noise.

Appendix B τ→π+*X* Results and Detector Optimisation

Chapter 8 has shown that the $\tau \to \pi + X$ analysis is possible in MINOS. The purpose of this appendix is to investigate how the sensitivity of the analysis changes as the major parameters of the detector are varied. These results were used, along with other considerations, to decide the optimum detector parameters for the MINOS near and far detectors in September 1997.

The following variables have been investigated to determine their effect on the $\tau \to \pi + X$ analysis:

- 2 and 4 cm plate thickness;
- 2 and 4 cm transverse cells;
- 1D versus 2D readout;
- liquid scintillator (FLS) and aluminium proportional tube (APT) active detector elements;
- application of a pulse height threshold to the data in order to combat detector noise;
- using pulse height information instead of counting the number of hits.

Detector configurations

The analysis in Chapter 8 uses a two samples of simulated events that were generated with 2 cm steel plates and 2 cm pitch liquid scintillator active detector cells. These samples contain 51577 ν_μ events with no oscillations and 17794 ν_τ CC events with saturated oscillations. They correspond to exposures of 12.5 and 37.2 kiloton years[15] respectively. The configuration of 2 cm steel with 4 cm pitch cells is simulated by ganging together adjacent cells of the 2 cm steel, 2 cm pitch events. These two configurations are therefore not independent.

Two additional Monte Carlo samples were generated to study the performance of the $\tau \rightarrow \pi + X$ test in 4 cm steel. The signal sample consisted of 24539 ν_τ CC events (an exposure of 51.3 kiloton years) and the background sample contained 27058 ν_μ NC and CC interactions (an exposure of 6.6 kiloton years). The 4 cm steel files have two crossed scintillator readout planes per passive steel plane (i.e. two co-ordinates per steel plane). Since the effective nuclear interaction length in this configuration is the same as the configuration of 2 cm steel and 2 cm cells, the applied cuts (including `EVLENGTH` and `STARHITS`) are the same.

Simulated events have also been generated with the response function of the aluminium proportional tube (APT) active detectors. Samples consisting of 28490 ν_μ events (an exposure of 6.9 kiloton years) and 15238 ν_τ CC events (an exposure of 31.8 kiloton years) were generated in 4 cm steel with two-dimensional readout (cathode strips and anode wires). No data was available for 2 cm steel.

---

[15] The ν_τ exposure corresponds to $\nu_\mu \rightarrow \nu_\tau$ oscillations with $\sin^2 2\theta = 1$ and large Δm^2.

Figure B.1 shows distributions of pulse height for wires and strips from a sample of 100 ν_μ events in 4 cm steel with APT active detectors. There is clear evidence of pulse sharing on the strips. A muon passing through a strip generally induces a signal on the two adjacent strips. These extra hits will affect many of the cuts used in the $\tau \rightarrow \pi + X$ analysis so they are eliminated by requiring that the pulse height recorded on the strips and wires is greater than 0.005 (equivalent to 0.6 m.i.ps). One-dimensional readout is simulated by discarding the strip readout and using only the wire information.

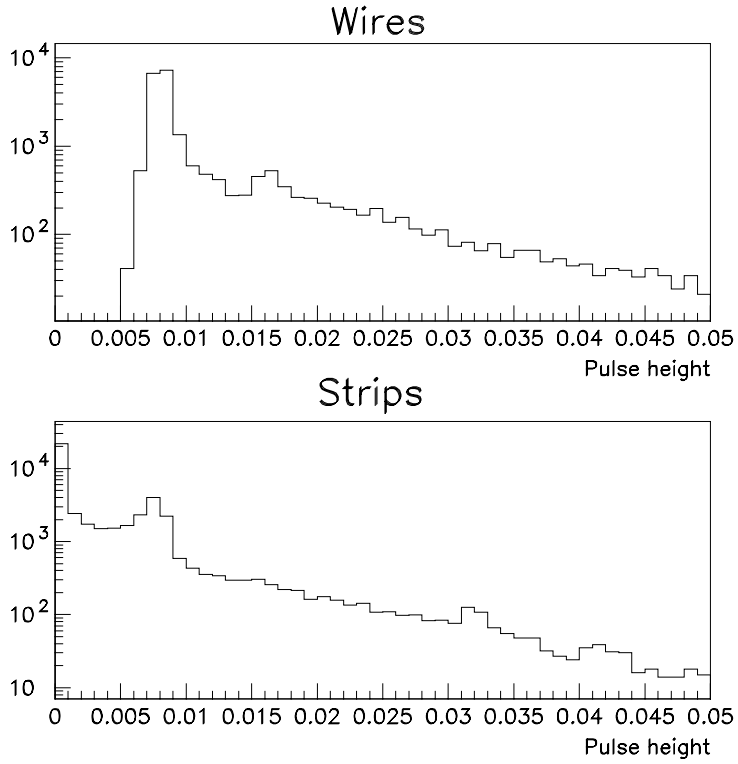

Figure B.1 – Pulse height distributions for 100 simulated ν_μ CC and NC events with APT active detectors. The top plot shows the pulse height distribution from the wire readout, and the bottom plot is for strip readout. A cut on the pulse height of 0.005 eliminates much of the pulse sharing on the strips.

Comparison between FLS and APT

The aim of this section is to compare the results of the $\tau \to \pi + X$ analysis in APT and FLS active detectors over a range of steel thickness and transverse cell size. The relative merits of the two technologies are the following:

1. APTs can, in principle, provide better transverse resolution than FLS detectors with the same transverse pitch by analysing the pulse heights induced on adjacent strips. Pulse sharing is eliminated in this analysis because it affects the `BARREL` and `FLIGHT` cuts and the Hough transform. The effect of improved transverse resolution is, however, studied in general in this Appendix to discover whether or not it is beneficial to the $\tau \to \pi + X$ analysis.

2. Scintillator based detectors provide better energy resolution than gas detectors (by a factor of 1.5) because they sample a larger fraction of the hadron shower (the cross-section for low energy neutron/proton scattering in the scintillating medium is higher than that in gas). This is the reason why simulated data with FLS active detectors produce approximately twice the number of hits per GeV as APT detectors with the same detector configuration, as shown in Table B.1

Configuration	Hits/GeV	Pulse height/GeV	1 m.i.p response
FLS22	19.3	549	22.5
FLS24	15.8	549	22.5
FLS42	19.5	541	22.5
FLS44	15.9	541	22.5
FLS42 (1D)	9.8	274	22.7
FLS44 (1D)	8.0	274	22.7
APT42	9.3	0.13	0.0178
APT44	8.3	0.13	0.0178
APT42 (1D)	4.6	0.094	0.0109
APT44 (1D)	3.7	0.094	0.0109

Table B.1 – Detector response for various configurations of active and passive detector. The first column lists the configuration, following the format: active detector (FLS or APT); steel thickness (cm); transverse cell size (cm); (readout). The second column lists the mean number of hits per GeV for NC events. The third column lists the mean pulse height per GeV for NC events and the final column lists the mean pulse height per plane (in arbitrary units) produced by a minimum ionising particle. These arbitrary units are different for the APT and FLS configurations.

Four variations of the cuts are applied to the data samples.

1. events are selected using BARREL and FLIGHT variables. The number of STARHITS must be equivalent to 2 GeV of visible energy or more. Column 2 of Table B.1 lists the number of hits/GeV for each detector configuration;

2. events are selected using BARREL and FLIGHT variables as above but the energy of the star is estimated from the summed pulse height in the FLIGHT region. Column 3 of Table B.1 lists the summed pulse height/GeV for each configuration. The energy of the star must be greater than 2 GeV. Figure B.2 shows distributions of the star energy for signal and background events, calculated from hits and pulse height information, for the FLS22 configuration;

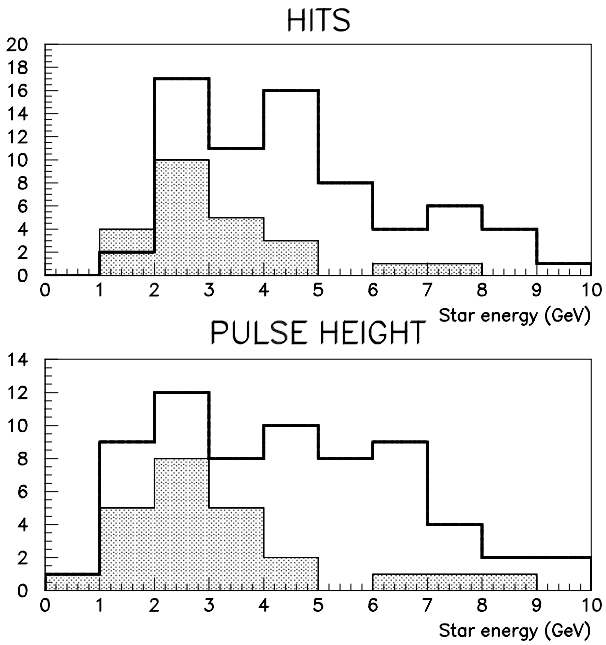

Figure B.2 – The energy of the hadronic star estimated from counting the number of hits (top plot) and from summing the total pulse height (bottom plot) in the FLIGHT region. The open histograms are for ν_τ events passing all cuts and the shaded histograms are for ν_μ events.

3. BARREL and FLIGHT variables are not used to select events. Pulse height information is used to construct the number of mips per plane in the BARREL and FLIGHT regions. Column 4 of Table B.1 shows the mean pulse height per plane produced by a minimum ionising particle. The number of mips per plane in the BARREL region is the summed pulse height per plane in the first half of the event divided by the mean pulse height per plane produced by a mip. Figure B.3 shows BARREL versus FLIGHT distributions for signal and background events in the FLS22 configuration above the corresponding distributions in BARREL MIPS versus FLIGHT MIPS space. The following cuts are applied in mip space:

   - BARREL MIPS < 5;

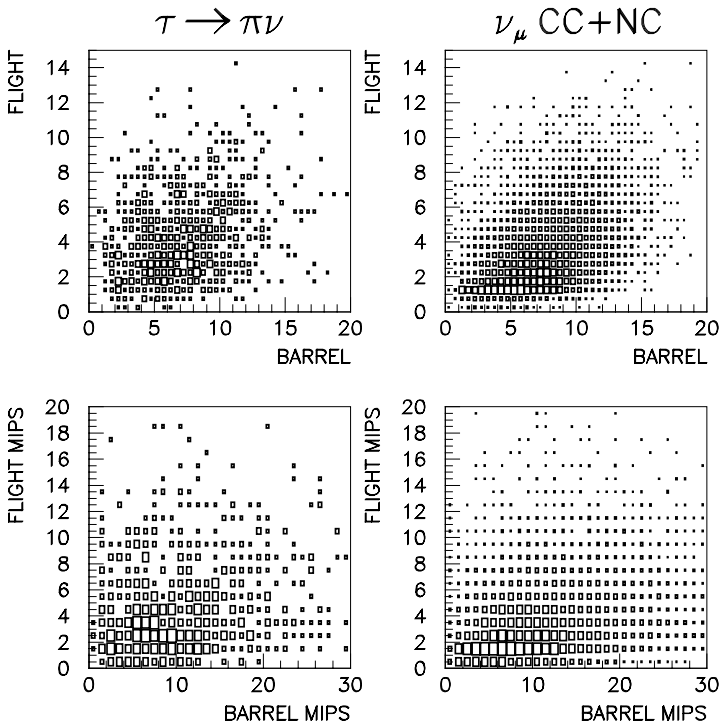

Figure B.3 - Track→star event selection in 2 cm steel, 2 cm cells with FLS active detectors. The left-hand plots show distributions for $\tau \rightarrow \pi\nu$ events and the right hand plots show distributions for ν_μ NC and CC events. The top plots are distributions of BARREL and FLIGHT, which are defined using hit information. The bottom two plots are distributions of the number of minimum ionising particles per plane in the BARREL and FLIGHT regions, which are defined using pulse height information. Track→star events lie in the top left hand sectors of each plot.

- FLIGHT MIPS > 1.5;
- FLIGHT MIPS > 1.17 × BARREL MIPS – 0.84.

The energy of the star, as estimated by pulse height, is required to be greater than 2 GeV;

4. a minimal set of cuts is applied to the data. Figure 8.13 in Chapter 8 shows that some of the cuts have a large effect on signal/background selection efficiency

whereas others have only a small effect. Only those cuts which have a large effect are applied to the data. These cuts are:

- $20 <$ `EVLENGTH` < 60;
- `BARREL MIPS` and `FLIGHT MIPS` cuts;
- `RMS75` < 10;
- $\cos\theta_z > 0.95$.

Event selection: hits, Star energy: hits

Figure B.4 shows the signal expected for the $\tau \to \pi + X$ test in a two-year run of MINOS, assuming $\nu_\mu \to \nu_\tau$ oscillations with $\sin^2(2\theta) = 1$ and large Δm^2, in a number of detector configurations. Event selection and star energies are based on hits information. The left-hand plot, which shows the signal/noise ratio (signal/vbackground) that could be obtained in each configuration, indicates that FLS active detectors (filled circles) and APT detectors (open circles) produce very similar numbers. The signal/noise ratio is not a strong function of either steel thickness or transverse granularity. One dimensional readout with 4 cm steel produces a smaller signal/noise ratio than the other configurations.

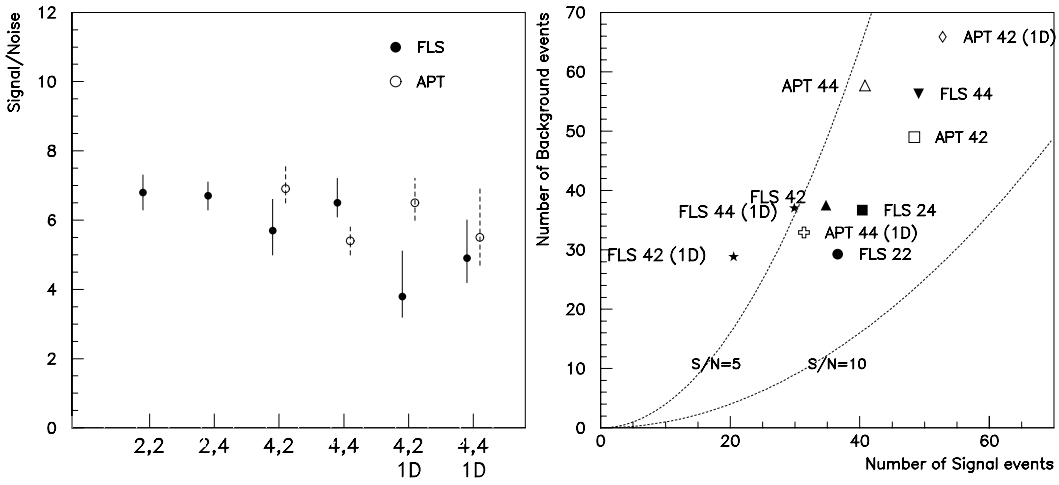

Figure B.4 - $\tau \rightarrow \pi + X$ sensitivity for various detector configurations. Events are selected using hits and the star energy is estimated from counting the number of hits in the FLIGHT region. The leftmost plot shows the signal to noise ratio that could be obtained in a two-year run of MINOS for various configurations. The error bars are at 90% C.L. The right-hand plot shows the normalised numbers of signal and background events expected in a two-year run for all configurations. Two lines of constant signal to noise ratio are also plotted.

The right-hand plot in Figure B.4 shows the numbers of signal ν_τ CC events and background ν_μ events expected in a two-year exposure of MINOS for each detector configuration. The errors on these numbers are omitted for clarity. A line drawn from the origin to the top right-hand corner of the plot indicates a signal to background ratio of 1.0. The best signal/background ratio is obtained in 2 cm steel with 2 cm transverse granularity. In general, increasing the steel thickness, decreasing the transverse granularity and switching from 2D readout to 1D readout reduces the signal/background ratio. The left-hand plot indicates that the FLS22 and APT42 (1D) configurations have the same signal/noise ratio but the right-hand plot shows that more than double the number of background events pass the cuts in the APT42 (1D) configuration. The signal/background ratio is therefore worse than for the FLS22 configuration.

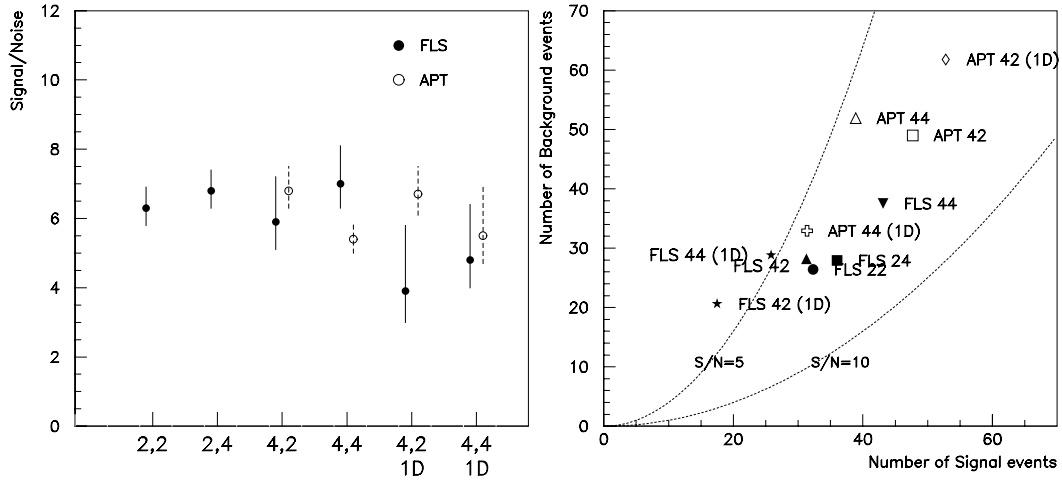

Figure B.5 - $\tau \rightarrow \pi + X$ sensitivity for various detector configurations. Events are selected using hits and the star energy is estimated from pulse height information.

Event selection: hits, Star energy: pulse height

Figure B.5 shows the signal to noise ratios and normalised numbers of signal and background events expected if pulse height is used to estimate the energy of the star. The signal/noise ratios obtained in each configuration are similar to those of Figure B.4. Four centimetre steel with 1D readout produces lower signal/noise ratios than the other configurations.

The effect of using pulse height to estimate the energy of the star instead of using hit information can be seen by comparing the right-hand plots of Figure B.4 and Figure B.5. The numbers of signal and background events passing the cuts are fewer when pulse height information is used, i.e. the absolute $\tau \rightarrow \pi + X$ selection efficiency is reduced. Pulse height information does, however, improve the signal/background ratio; more of the points have a signal/background ratio of 1.0 or better.

Event selection: pulse height, Star energy: pulse height

Figure B.6 shows the signal/noise and normalised numbers of signal and background events expected if the events are selected by cutting on the number of mips per plane in the BARREL and FLIGHT regions and pulse height is used to estimate the energy of the star. The left-hand plot shows the same features as the previous two figures although the absolute level of signal/noise is reduced somewhat. This is purely an acceptance issue; a cut of 5 mips/plane is not the same as 5 hits/plane since two particles passing through one cell will produce a pulse height signal equivalent to two mips but only one hit. The acceptances for FLS and APT active detectors will be slightly different since the 1 mip peak is wider in the APT simulation than in the FLS (30% versus 10%). The plot indicates that 4 cm steel with 1D readout is again inferior to the other configurations but the points are consistent with a constant value of signal/noise due to the large statistical errors.

The right-hand plot of Figure B.6 shows that the absolute selection efficiency is

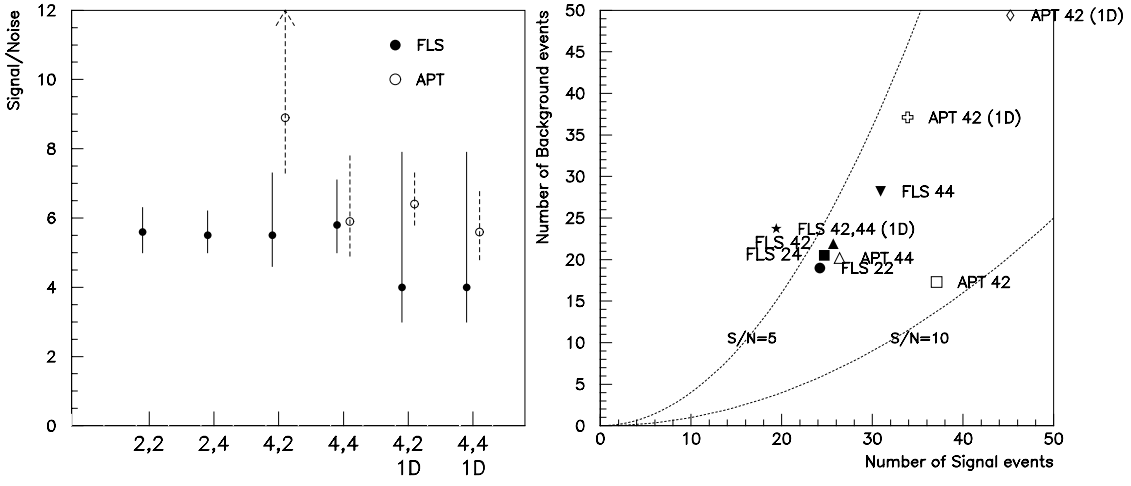

Figure B.6 - $\tau \to \pi + X$ sensitivity for various detector configurations. Events are selected using pulse height and the star energy is estimated from pulse height information.

reduced when pulse height is used to select events (note the different scale to the other plots). The benefit of using pulse height is that almost all the configurations produce a signal/background ratio of 1.0 or greater. In Figure B.4, there are significant differences in acceptance for closely similar configurations. The points `FLS22` and `FLS24` are separated in Figure B.4; degrading the transverse resolution increases the acceptance but reduces the signal/background ratio since there is a higher probability that two particles will pass through the same cell. When pulse height is used to select events, it is possible to resolve mips passing through the same cell and the acceptances for `FLS22` and `FLS24` are practically identical in Figure B.6.

Event selection: pulse height, minimal cuts

Figure B.7 shows the signal/noise ratio and normalised numbers of signal and background events expected if events are selected using pulse height information and only cuts that have a large effect on the signal/background ratio are applied. Comparing Figure B.7 to Figure B.6 shows that the signal/noise ratio is increased when only the minimal cuts are applied. The smaller statistical errors in Figure B.7 show more clearly the loss in sensitivity for the configurations with 4 cm steel and 1D readout. The FLS data is slightly worse than the APT data for these configurations.

The right-hand plot of Figure B.7 shows that the acceptance is indeed larger when the minimal cuts are applied although, in contrast to Figure B.6, most of the configurations produce a signal/background ratio of less than 1.0. It is interesting to note that the acceptance for the APT configurations does not change significantly between Figure B.6 and Figure B.7 whereas the FLS configurations show a marked increase in acceptance. This indicates that the cuts which have been applied in Figure B.6 but not in Figure B.7 are cutting on properties of the events that are more common to FLS data than APT data. One example of this is the presence of 'scattered hits' in FLS events, due to neutrons scattering off hydrogen in the scintillator, which are not present in the APT data.

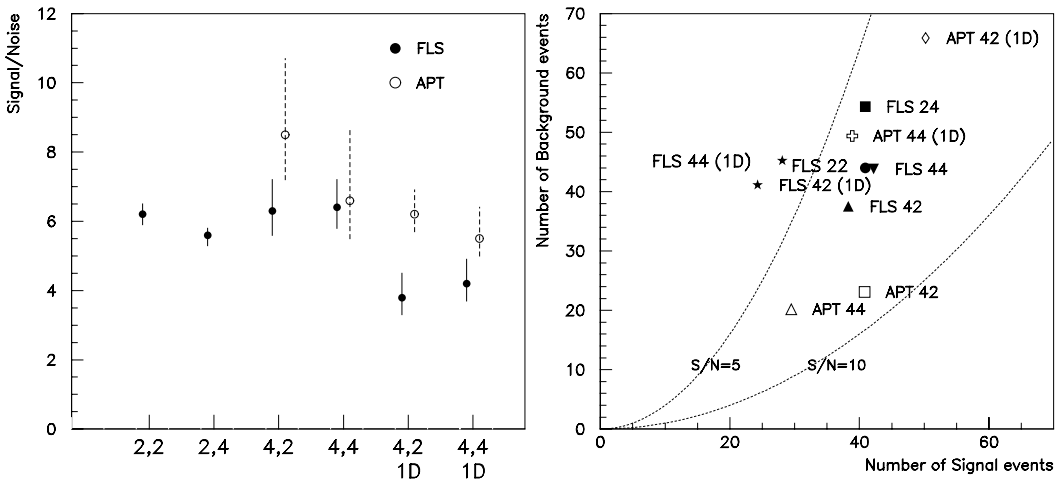

Figure B.7 - $\tau \to \pi + X$ sensitivity for various detector configurations. Events are selected using pulse height and only cuts that have a large effect on signal/background selection efficiency are applied.

Sensitivity to neutrino oscillations

The $\tau \to \pi + X$ analysis, which relies on the observation of a high momentum pion track that subsequently creates an energetic hadron shower, is clearly energy dependent. The analysis will be relatively inefficient at low neutrino energy, reducing the sensitivity of the analysis to oscillations with low Δm^2. Figure B.8 shows the low Δm^2 segment of six limit plots for different FLS detector configurations (the APT limits are practically identical and are not plotted). The low Δm^2 behaviour of the 6 limit plots is very similar.

The sensitivity of the $\tau \to \pi + X$ test to the Kamiokande parameters can be estimated by reading off the limits on $\sin^2(2\theta)$ shown in Figure B.8. At $\Delta m^2 = 0.01$ eV^2 the $\tau \to \pi + X$ analysis is predicted to set a limit on $\sin^2(2\theta)$ of between 0.275 and 0.375,

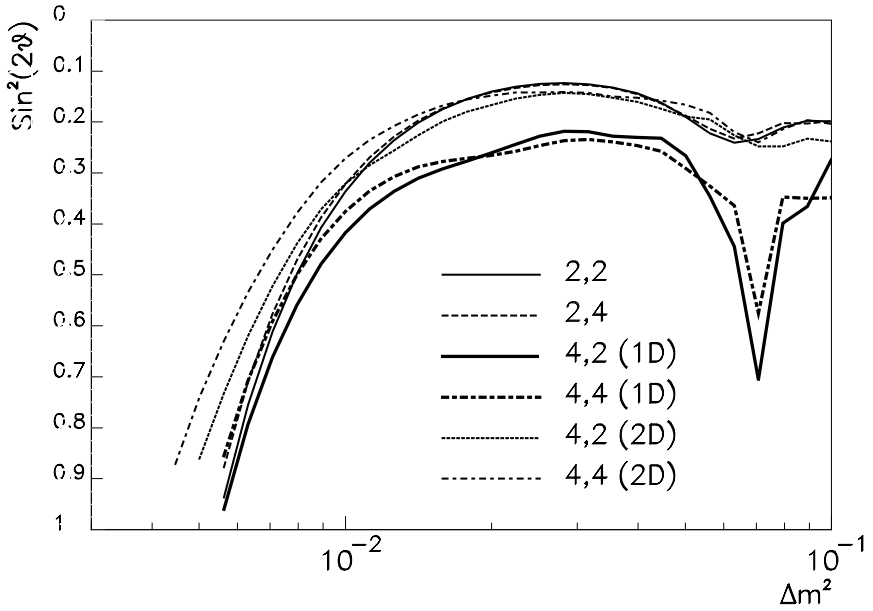

Figure B.8 – Predicted 90% confidence limits at low Δm^2 in the mode $\nu_\mu \to \nu_\tau$ for a 2 year run in the WBB for 6 detector configurations. The thin solid line shows the limit that can be set in 2 cm steel with 2 cm cells.

depending on the detector configuration. The significance of the oscillation signal, $signal / \sqrt{background}$, is related to $\sin^2(2\theta)_{\min}$ by:

$$S / \sqrt{B} = 1.29 / \sin^2(2\theta)_{\min}. \quad \text{(B.1)}$$

This equation yields a significance of between 3.4 and 4.7 standard deviations for $\Delta m^2 = 0.01$ eV^2

Conclusions for detector optimisation

Transverse granularity

The sensitivity of the $\tau \to \pi + X$ test to neutrino oscillations is not affected when the transverse cell size is increased from 2 cm to 4 cm because the signal/noise ratio is the same in both configurations. If hits are used to select events then there is an increase in acceptance when the transverse cell size is increased since there is a higher probability for two particles to pass through the same cell. The acceptance for 2 cm and 4 cm cells is the same if pulse height is used to select events.

Longitudinal granularity

The sensitivity of the $\tau \to \pi + X$ test to neutrino oscillations is not affected when the steel thickness is increased from 2 cm (with 1D readout) to 4 cm (with 2D readout). For liquid scintillator active detectors, these two configurations have the same effective interaction length so this result is not surprising. Comparing the results of 4 cm steel with 1D readout to 2 cm steel with 1D readout shows a reduction in sensitivity to oscillations.

1D readout versus 2D readout

One-dimensional readout with 4 cm steel plates produces lower signal/noise and signal/background ratios than 2D readout with the same steel thickness. This is because there are fewer hits per GeV for 1D readout, producing a poorer estimate of the star energy, and the number of hits in a track is reduced by a factor of two, resulting in a poorer track finding efficiency.

Pulse height versus hits

Pulse height can be used to select events on the basis of the number of hits per plane in the `BARREL` and `FLIGHT` regions and to estimate the energy of the star. The use of pulse height instead of counting the number of hits reduces the selection efficiency somewhat but improves the signal/background ratio. This is because multiple mip crossings can be resolved in a single cell.

APT versus FLS

APT data and FLS data produce similar values of signal/noise in all configurations with 4 cm steel (no APT data was available in 2 cm steel). The two technologies produce somewhat different acceptances because the response to a mip is different (the APT simulations show a wider mip peak) and the APT data has fewer hits/GeV for neutral current events than the FLS data. The sensitivity to neutrino oscillations, however, is the same in both active detectors.

Optimal detector configurations for $\tau \to \pi + X$

The absolute efficiency of the $\tau \to \pi + X$ test for $\tau \to \pi\nu$ events is small (2.2%) and only a few tens of track→star events are expected in a two year run for maximal neutrino

oscillations at large Δm^2. The test is therefore limited by statistics and is only believable if it produces a large signal/noise ratio (greater than 5) and a good signal/background ratio (about 1.0 or better). Given these conditions, the best detector for $\tau \rightarrow \pi + X$ is fine-grained (2 cm steel with 2 cm transverse pitch). Configurations with 4 cm transverse pitch and/or 4 cm steel (with 2D readout) produce the same signal to noise ratio as 2 cm steel with 2 cm transverse pitch, albeit with a slightly worse signal/background ratio. 4 cm steel with 1D readout produces a low signal/noise ratio and a poor signal/background ratio, therefore it is not favourable to this analysis. Good pulse height capabilities can help to increase the signal/background ratio, although there appears to be no advantage for scintillator over gas detectors or *vice versa* when pulse height information is used.

Appendix C The MINOS Collaboration

E. Ables[10], S. Afanasjev[4], G. Alexeev[4], W.W.M. Allison[14], G.J. Alner[17], I. Ambats[1], Yu. Antipov[16], C. Arroyo[18], D.S. Ayres[1], B. Baller[5], B. Barish[2], P.D. Barnes Jr.[10], W.L. Barrett[23], V. Batarin[16], A. Bazilevsky[16], R. H. Bernstein[5], V. Bezzubov[16], R. Bionta[10], R.E. Blair[1], D.J. Boehnlein[5], D. Bogert[5], P.M. Border[12], S. Borodin[4], C. Bower[7], V. Brudanin[4], W.L. Bryan[13], D. Burke[2], J. Byrne[19], D. Carey[5], R. Carney[10], T. Chase[12], V.A. Chechin[9], G. Chelkov[4], B. Choudhary[2], J.H. Cobb[14], J. Conboy[11], D. Cossairt[5], R.J. Cotton[17], H. Courant[12], P. Cushman[12], P.G. Dawber[19], J.W. Dawson[1], A. Denisov[16], N. Diaczenko[20], G. Drake[1], A. Durum[16], R. Edgecock[17], O. Eroshin[16], O. Fackler[10], R. Fakhrutdinov[16], T.H. Fields[1], W.S. Freeman[5], H.R. Gallagher[14], A. Gara[3], G. Gavrilov[15], M. Gebhard[7], Yu. Gilitsky[16], S. Golovkin[16], M.C. Goodman[1], Yu. Gorin[16], Yu. Gornushkin[4], J. Guo[6], K. Green[19], V.J. Guarino[1], M.J. Hansen[12], J. Hanson[2], P.G. Harris[19], E. Hartouni[10], R. Hatcher[2], R. Heinz[7], K. Heller[12], N. Hill[1], Y. Ho[3], T. Hu[6], J. Hylen[5], M. Ignatenko[4], G. Irwin[18], V. Ivochkin[15], U. Jagadish[13], V. Jakutovich[15], C. James[5], T. Joffe-Minor[1], D. Johnson[5], T. Kafka[22], N. Khovanski[4], J. Kilmer[5], H. Kim[2], V. Kochetkov[16], G. Koizumi[5], A. Kozhevnikov[16], A. Krivshich[15], Z. Krumstein[4], V. Kubarovsky[16], A. Kulyavtsev[16], V. Kurshetsov[16], E.P. Kuznetsov[9], A. Ladran[10], Y.F. Lai[6], L. Landsberg[16], K. Lang[21], W. Lee[3], J. Li[6], M. Libkind[10], P.J. Litchfield[17], N.P. Longley[2], A. Makeev[16], V. Makeev[16], V. Maleev[15], W.A. Mann[22], H.S. Mao[6], M.L. Marshak[12], D. Maxam[12], E.N. May[1], V. Medovikov[16], E. Melnikov[16], S. Menary[5], D.G. Michael[2], R.H. Milburn[22], L. Miller[7], W.H. Miller[12], G. Mitselmakher[5], V. Molchanov[16], J. Morfin[5], S. Mrenna[1], S. Mufson[7], V. Mukhin[16], J. Musser[7], A. Nadtochi[15], A. Napier[22], J. Nelson[12], F. Nezrick[5], S. O'Day[5], W. Oliver[22], H. Olsan[10], A. Olshevski[4], V. Onuchin[16], L. Ott[10], A. Para[5], E. Parker[10], G.F. Pearce[17], C.W. Peck[2], C. Perry[14], E.A. Peterson[12], S. Petrenko[16], A. Petruchin[16], D.A. Petyt[14], P. Pitukhin[16], L.E. Price[1], D.R. Pushka[5], R.A. Rameika[5], A.L. Read[5], K. Ruddick[12], R. Rusack[12], A. Sadovski[4], J. Schneps[22], P.V. Schoessow[1], R. Schwienhorst[12], V. Semenov[16], V. Shelichov[16], B.W. Shen[6], P.D. Shield[14], A. Sisakian[4], W. Smart[5], V. Smotriaev[8], A. Soldatov[16], V. Solyanik[16], V. Startcev[16], J. Swan[10], R. Talaga[1], J. Thomas[11], K.M. Thompson[1], J.L. Thron[1], V. Timofeev[4], L. Tkatchev[4], T. Toohig[5], D. Tovee[11], I. Trostin[8], V. Tsarev[9], L.R. Turner[1], N. Tyurin[16], A. Usachev[16], M. Vakili[20], V. Vaneev[16], D. Vavilov[16], V. Victorov[16], L.S. Wang[6], M. Wang[6], R.C. Webb[20], A. Wehmann[5], S.J. Werkema[5], N. West[14], R.F. White[19], S.G. Wojcicki[18†], D. Wright[10], C. Wuest[10], X.M. Xia[6], W.G. Yan[6], T. Yokota[10], J.C. Yun[5], J.Q. Zhang[6], S. Zimin[16], and A. Zinchenko[4]

[†] **Spokesman**

Argonne[1] - Caltech[2] - Columbia[3] - Dubna[4] - Fermilab[5] - IHEP-Beijing[6] - Indiana[7] - ITEP[8] - Lebedev[9] - Livermore[10] - UC-London[11] - Minnesota[12] - Oak Ridge[13] - Oxford[14] - PNPI[15] - Protvino[16] - Rutherford[17] - Stanford[18] - Sussex[19] - Texas A&M[20] - Texas Austin[21] - Tufts[22] - Western Washington[23]

Bibliography

[1] C. L. Cowan *et. al.*, Science **124,** p103 (1956).

[2] C. S. Wu *et. al.*, Phys. Rev. **105**, p1413 (1957).

[3] M. Goldhaber, L. Gradzins and A. Sunyar, Phys. Rev. **109**, p1015 (1958).

[4] Particle Data Group, Phys. Rev. **D54**, p1 (1996).

[5] C. W. Kim, hep-ph/9607391, submitted to KOSEF-JSPS Winter School on Recent Developments in Particle and Nuclear Theory, Seoul, Korea; 21-28 Feb 1996. Publ. In Proceedings J. Korean Phys. Soc., Suppl. (1996).

[6] H. V. Klaptor-Kleingrothaus, Neutrino '96, Proceedings of the 17th International Conference on Neutrino Physics and Astrophysics, Helsinki, Finland, 1996, eds. K. Enqvist, K. Huitu and J. Maalampi, World Scientific, p317.

[7] J. Bonn, Neutrino '96, p264.

[8] V. M. Lobashov, Neutrino '96, p264.

[9] K. S. Hirata *et. al.*, Phys. Rev. Lett. **58**, p1490 (1987).

[10] R. M. Bionta *et. al.*, Phys. Rev. Lett. **58**, p1494 (1987).

[11] J. N. Bahcall and S. L. Glashow, Nature **326**, p476 (1987).

[12] K. Assamagan *et. al.*, Phys Rev. **D53**, p6065 (1996).

[13] A. Gregorio, Neutrino '96, p283.

[14] D. Spergel, astro-ph/9603026.

[15] R. N. Mohapatra and G. Senjanović, Phys. Rev. Lett. **44**, p912 (1980).

[16] S. M. Bilenky and S. T. Petcov, Rev. Mod. Phys. **59**, p671 (1987).

[17] L .Maiani, Phys. Lett. **B62**, p183 (1976).

[18] A. De Rújula, M. Lusignoli, L. Maiani, S. T. Petcov and R. Petronzio, Nucl. Phys. **B168**, p54 (1980).

[19] J. N. Bahcall, http://www.sns.ias.edu/ jnb/Snviewgraphs/snviewgraphs.html.

[20] J. N. Bahcall and M. H. Pinsonneault, Rev. Mod. Phys. **67**, p781 (1995).

[21] J. N. Bahcall, Neutrino '96, p56.

[22] A. Yu. Smirnov, Neutrino '96, p38.

[23] R. Davis, Prog. Nucl. Phys. **32**, p13 (1994).

[24] K. Lande, Neutrino '96, p25.

[25] V. N. Gavrin, Neutrino '96, p14.

[26] T. Kirsten, Neutrino '96, p3.

[27] Y. Suzuki, Neutrino '96, p73.

[28] L. Wolfenstein, Phys. Rev. **D17**, p2369 (1978); S. P. Mikheyev and A. Yu. Smirnov, Sov. J. Nucl. Phys. **42**, p913 (1986).

[29] G. L. Fogli, E. Lisi and D. Montanino, hep-ph/9709473.

[30] B. Faïd, G. L. Fogli, E. Lisi and D. Montanino, hep-ph/9608311.

[31] SNO Collaboration, G. T. Ewan *et. al.*, "Sudbury Neutrino Observatory Proposal", Report No. SNO-87-12 (1987) (unpublished).

[32] G. Bellini (BOREXINO collaboration) in TAUP'95, Proceedings of the 4th International Workshop on Theoretical and Phenomenological Aspects of Underground Physics, Toledo, Spain, 1995, eds. A. Morales, J. Morales and J. A. Villar, [Nucl. Phys. B, Proc. Suppl. **48**, p547 (1996)].

[33] G. Barr, T. K. Gaisser and Todor Stanev, Phys. Rev. **D39**, p3572 (1989); M. Honda, K. Kasahara, K. Hidaka and S. Midorikawa, Phys. Lett. **B248**, p193 (1990).

[34] R. Becker-Szendy *et. al.*, Phys. Rev. **D46**, p3720 (1992).

[35] K. S. Hirata *et. al.*, Phys. Lett. **B280**, p146 (1992).

[36] K. Martens, Invited talk at HEP 97, International Europhysics conference on High Energy Physics, Jerusalem, Israel, August 1997, to appear in the proceedings.

[37] M. Aglietta *et. al.*, Europhys. Lett. **8**, p611 (1989).

[38] Ch. Berger *et. al.*, Phys. Lett. **B227**, p489 (1994).

[39] W. W. M. Allison *et. al.*, Phys. Lett. **B391**, p491 (1997).

[40] S. Kasuga, "A study of the PID capability with a water Čerenkov detector", Masters thesis, Univ. Tokyo (1995).

[41] Y. Fukuda *et. al.*, Phys. Lett. **B335**, p237 (1994).

[42] A. Stassinakis, *"A Study of the Atmospheric Neutrino Flavour Content using the Soudan 2 detector"*, D. Phil. Thesis, University of Oxford, 1997.

[43] J. Brunner, CERN-PPE/97-38, to be published in Progress of Physics.

[44] O. G. Ryazhskaya, JETP Lett. **60**, p617 (1994).

[45] Y. Fukuda *et. al.*, Phys. Lett. **B388**, p397 (1996).

[46] The CHOOZ proposal, avaliable via WWW at http://duphy4.physics.drexel.edu/chooz_pub/index.htmlx.

[47] M. Apollonio *et. al.*, CHOOZ collaboration, University of Pisa report, hep-ex/9711002.

[48] Nuclear Instruments and Methods **A338**, p149 (1997).

[49] C. Athanassapoulos *et. al.,* Phys. Rev.**C54**, p2685 (1996).

[50] C. Athanassapoulos *et. al.*, Los Alamos preprint LA-UR-97-1998, submitted to Phys. Rev. C.

[51] J. Kleinfeller, Neutrino '96, p193; B. Armbruster *et. al.*, hep-ex/9801007.

[52] L. Borodovsky *et. al.*, Phys. Rev. Lett. **68**, p274 (1992).

[53] B. Achkar *et. al.*, Nucl. Phys. **B434**, p503 (1995).

[54] S. M. Bilenky, C. Giunti and W. Grimus, hep-ph/9607372.

[55] R. N. Mohapatra, Neutrino '96, p290.

[56] G. L. Fogli, E. Lisi, D. Montanino and G. Scioscia, hep-ph/9706230.

[57] P. F. Harrison, D. H. Perkins and W. G. Scott, Phys. Lett. **B349**, p137 (1995).

[58] P. F. Harrison, D. H. Perkins and W. G. Scott, hep-ph/9702243.

[59] G. L. Fogli, E. Lisi, D. Montanino and G. Scioscia, hep-ph/9607251; G. L. Fogli, E. Lisi and D. Montanino, Phys. Rev. **D54**, p2048 (1996).

[60] NOMAD Collaboration, CERN-PPE-97-059.

[61] G. Gratta (Palo Verde collaboration), Neutrino '96, p248; Palo Verde Collaboration, "Review of Progess", avaliable via WWW at http://www.cco.caltech.edu/songhoon/Palo-Verde/Palo-Verde.html.

[62] N. Ushida *et. al.*, Phys. Rev. Lett. **57** p2897 (1986).

[63] F. Dydak *et. al.*, Phys. Lett. **B134**, p281 (1984).

[64] Ch. Berger *et. al.*, Phys. Lett. **B245**, p305 (1990).

[65] CHORUS collaboration, CERN-PPE-97-033; CHORUS collaboration, CERN-PPE-97-149.

[66] R. A. Sidwell, Neutrino '96, p237.

[67] Y. Suzuki, Neutrino '96, p237.

[68] F. Cavanna, CERN-PPE/95-133.

[69] The MINOS Collaboration, *"A Long-baseline Neutrino Oscillation Experiment at Fermilab"*, Fermilab Proposal P875, February 1995; "Addendum to *P-875: A Long-Baseline Neutrino Oscillation experiment at Fermilab"*, Fermilab report NuMI-L-79, April 1995.

[70] M. Goodman *et. al.*, *"Proposal for a Long-baseline Neutrino Oscillation Experiment using the Soudan 2 Neutrino Detector"* Fermilab Proposal P-822 (withdrawn).

[71] J. Hylen *et. al.*, Fermilab report NuMI-B-285, September 1997.

[72] The MINOS Collaboration, *"MINOS Progress Report to the Fermilab PAC"*, Fermilab report NuMI-L-300, October 1997.

[73] The UK MINOS Collaboration, *"The MINOS Long-baseline Neutrino Experiment"*, submitted to the UK PPESP, November 1997.

[74] G. D. Barr, *"The Separation of Signals and Background in a Nucleon Decay Experiment"*, D.Phil. thesis, University of Oxford, 1987; H. M. Gallagher, *"Neutrino Oscillation Searches with the Soudan 2 Detector"*, Ph.D. thesis, University of Minnesota, 1996.

[75] `ADAMO` users guide, avaliable via WWW at: http://www1.cern.ch/Adamo/.

[76] S. Jadach, Z. Was and J. H. Kuehn, Comp. Phys. Commun., **64**, p275, (1991).

[77] R. Hatcher, *"Numbering Conventions and Co-ordinate Systems in* `GMINOS`*"*, Fermilab report NuMI-L-243, February 1997.

[78] D. A. Petyt, *"Hadron and Muon energy resolution in the far detector"*, Fermilab report NuMI-L-66, February 1995.

[79] J. Thomas, A. Para and D. Tovee, *"The Principles of Muon Tracking in MINOS"*, Fermilab report NuMI-L-301, October 1997.

[80] D. Ayres, *"The MINOS Detector Instrumented with APT's"*, Fermilab report NuMI-L-293, September 1997.

[81] J. H. Cobb, Nuclear Instruments and Methods, **A372**, p 501 (1996).

[82] J. Thomas, "*Muon Tracking in MINOS using* `GMINOS`", Fermilab report NuMI-L-311, in preparation.

[83] P. Ballester, *"Hough Transform for Robust Regression and Automated Detection"* Astronomy and Astrophysics, **286**, p1011 (1994).

[84] D. A. Petyt, http://mimosa.astro.indiana.edu:80/minos/code_mgt/threegen.readme.

[85] D. G. Michael, L. Miller and S. Mufson, *"Event Type Identification and Systematic Errors for numu to nue Oscillations"*, Fermilab report NuMI-L-101.

[86] G. L. Fogli, E. Lisi and G. Scioscia, Phys. Rev. **D52**, p5334 (1995).

[87] G. L. Fogli, E. Lisi, A. Marrone and D. Montanino, hep-ph/9711421; M. Narayan, G. Rajasekaran and S. Uma Sankar, hep-ph/9712409.

[88] M. Tanimoto, Phys. Rev. **D55**, p1653 (1997).

[89] J. Arafune and J. Sato, Phys. Rev. **D55**, p1653 (1997); J. Arafune, M. Koike and J. Sato, Phys. Rev. **D56**, p3093 (1997).

[90] S. M. Bilenky, C. Giunti and W. Grimus, hep-ph/9712537.

[91] R. N. Mohapatra, hep-ph/9711444.

[92] The MINOS collaboration, *"Status Report on Tau Identification in MINOS"* , Fermilab report NuMI-L-228.

[93] R. D. Field and R. P. Feynman, Nucl. Phys. **B136**, p1 (1978).

[94] B. Andersson *et. al.*, Nucl. Phys. **B135**, p273 (1978).

[95] P. Renton and W. S. C. Williams, Ann. Rev. Nucl. Part. Sci. **31** p193 (1981).

[96] P. C. Bosetti *et al*. Nucl. Phys. **B149**, p13 (1979).

[97] J. M. Scarr *et. al.*, Nucl. Phys. **B135**, p224 (1977).

[98] R. Bandelik *et. al.*, Phys. Lett. **B67**, p358 (1977).

[99] Q. Y. Liu and A. Yu. Smirnov, hep-ph/9712493.

[100] M. Drees, S. Pakvasa, X. Tata and T. ter Veldhuis, hep-ph/9712439.

[101] V. Barger, T. J. Weiler and K. Whisnant, hep-ph/9712495.

[102] C. D. Froggatt, hep-ph/9711506.

[103] S. M. Bilenky, C. Giunti, C. W. Kim and M. Monteo, hep-ph/9711400.